UNIVERSIDADE DA BEIRA INTERIOR

Engenharia

Development of an Open Source Software Tool for Propeller Design in the MAAT Project

Desenvolvimento de uma Ferramenta Computacional de Código Aberto para Projeto de Hélices no Âmbito do Projeto MAAT

João Paulo Salgueiro Morgado

Tese para obtenção do Grau de Doutor em

Engenharia Aeronáutica

(3º ciclo de estudos)

Orientador: Prof. Doutor Miguel Ângelo Rodrigues Silvestre

Coorientador: Prof. Doutor José Carlos Páscoa Marques

Covilhã, março de 2016

Aos meus pais e às minhas irmãs

This page has been intentionally left blank
for double side copying

Agradecimentos

A execução deste trabalho só foi possível devido à colaboração, disponibilidade e empenho de algumas pessoas às quais quero desde já manifestar o meu mais sincero agradecimento.

Ao Professor Miguel Silvestre, pela orientação neste trabalho, pelos conhecimentos que me transmitiu, pelo rigor científico com que sempre desenvolveu o trabalho e por me ter incutido um espírito crítico. Agradeço-lhe também pela sua amizade, por toda a disponibilidade e atenção que sempre dispensou ao longo destes anos.

Ao Professor José Páscoa, pela sua co-orientação neste trabalho, pela sua constante disponibilidade, pelos conhecimentos que me transmitiu e pelos conselhos que me deu. Quero ainda agradecer-lhe o espaço que me disponibilizou no ClusterDEM, permitindo que este trabalho fosse desenvolvido num ambiente calmo e confortável.

Ao Sr. Rui, ao Pedro Santos e ao Pedro Alves pelo apoio prestado na parte experimental deste trabalho e pelo seu empenho na resolução dos problemas que foram surgindo.

Ao Carlos, à Galina, ao Shyam, ao Jakson e ao Frederico, com quem partilhei o espaço de trabalho do ClusterDEM, pela disponibilidade sempre demonstrada e ainda pela possibilidade de ter partilhado estes anos com pessoas de diferentes culturas e costumes.

Ao Amilcar, ao Rui, ao Mahdi e ao Luís por tudo o que partilhámos ao longo destes anos, pelo apoio que sempre me deram nos momentos menos bons, pelas discussões mais ou menos científicas que tivemos e sobretudo pela vossa amizade.

A ti, Andreia, por tudo. Por me fazeres sorrir, por estares sempre a meu lado por me aturares e por me ajudares a ver sempre o lado mais positivo das coisas. O meu obrigado não é suficiente por todo o carinho que demonstras por mim.

À minha Mãe, ao meu Pai e às minhas Irmãs pois sem vocês nada disto teria sido possivel. Obrigado por estarem sempre presentes, pela compreensão, pelo constante apoio e pelo encorajamento ao longo destes anos. Não é possível agradecer tudo o que fazem por mim.

A todos o meu Muito Obrigado!

Support

The present work was performed as part of Project MAAT (Ref. No. 285602) supported by European Union Seventh Framework Programme. Part of the work was also supported by C-MAST – Center for Mechanical and Aerospace Sciences and Technologies, Portuguese Foundation for Science and Technology Research Unit No. 151.

This page has been intentionally left blank
for double side copying

Resumo

Nesta tese é apresentado o desenvolvimento de um novo código para projeto e análise de hélices, capaz de prever adequadamente o desempenho a baixos números de Reynolds. O JBLADE foi desenvolvido partindo dos códigos QBLADE e XFLR5 e utiliza uma versão aperfeiçoada da teria do elemento da pá que contém um novo modelo que considera o equilíbrio tridimensional do escoamento. O código permite que a pá seja introduza como um número arbitrário de secções, caracterizadas pela sua posição radial, corda, ângulo de incidência, comprimento, perfil e ainda pela polar 360º associada ao perfil. O código permite uma visualização gráfica em 3D da pá, ajudando o utilizador a detetar possíveis inconsistências. O JBLADE também permite uma visualização direta dos resultados das simulações através de um interface gráfico, tornado o código acessível e de fácil compreensão. Além disso, a interligação entre os diferentes módulos do JBLADE evita operações demoradas de importação e exportação de dados, diminuindo assim possíveis erros criados pelo utilizador. O código foi desenvolvido como um código aberto, para a simulação de hélices, e que tem a capacidade de estimar o desempenho de uma determinada geometria de hélice nas condições de operação do seu ponto de projeto e fora do seu ponto de projeto. O trabalho de desenvolvimento aqui apresentado foi focado no projeto de hélices para dirigíveis de grande altitude no âmbito do projeto MAAT (Multibody Advanced Airship for Transportation). O *software* foi validado para diferentes tipos de hélice, provando que pode ser utilizado para projetar e otimizar hélices para diferentes finalidades.

São apresentadas a derivação e validação do novo modelo de equilíbrio tridimensional do escoamento. Este modelo de equilíbrio 3D tem em conta o possível movimento radial do escoamento ao longo do disco da hélice, melhorando as estimativas de desempenho do *software*. O desenvolvimento de um novo método para a estimativa do coeficiente de arrasto dos perfis a 90º, permitindo uma melhor modelação do desempenho pós-perda é também apresentado. Diferentes modelos de pós perda presentes na literatura e originalmente desenvolvidos para a indústria das turbinas eólicas foram implementados no JBLADE e a sua aplicação a hélices para melhorar a estimativa do desempenho foi analisada. Os resultados preliminares mostraram que a estimativa de desempenho das hélices pode ser melhorada, utilizando estes modelos de pós-perda. Uma metodologia de projeto inverso, baseada no mínimo das perdas induzidas foi implementado no JBLADE, de modo a ser possível obter hélices com geometrias otimizadas para um dado ponto de projeto. Além disto, um módulo de cálculo estrutural foi também implementado, permitindo estimar o peso das pás, a deformação das mesmas, quer em termos de flexão, quer em termos de torção, devido à tração gerada pela própria hélice e aos momentos do perfil. Para validar as estimativas de desempenho do JBLADE foram utilizadas hélices originalmente apresentadas nos relatórios técnicos NACA, nomeadamente no relatório técnico 594 e 530. Estas hélices foram simuladas no JBLADE e os resultados foram comparados com os dados experimentais e com as estimativas de desempenho

obtidas através de outros códigos numéricos. O módulo de projeto inverso e o módulo estrutural foram também validados, através da comparação com outros resultados numéricos.

De modo a verificar a fiabilidade do código XFOIL usado no JBLADE para previsão das características dos perfis das pás, o modelo de turbulência *k-ω Shear Stress Transport* e uma versão reformulada do modelo de transição *k-kl-ω* foram utilizados em simulações *RANS* para comparação dos resultados do desempenho aerodinâmico de perfis. Os resultados mostraram que o código XFOIL dá uma estimativa de desempenho mais próxima dos dados obtidos experimentalmente do que os modelos *RANS CFD*, provando que pode ser utilizado no JBLADE como ferramenta de estimava de desempenho aerodinâmico dos perfis.

Em vez da tradicional prescrição do coeficiente de sustentação ao longo da pá para melhor L/D, foi utilizado os pontos de melhor $L^{3/2}/D$ para o projeto de uma hélice para o dirigível cruzador do projeto MAAT. Os procedimentos de otimização empregados ao longo do processo de projeto destas hélices para utilização em grandes altitudes são também descritos. As hélices projetadas com o JBLADE foram analisadas e os resultados obtidos foram comparados com simulações convencionais de dinâmica de fluidos computacional, uma vez que não existem dados experimentais para estas geometrias em particular. Foram utilizadas duas aproximações diferentes de modo a obter duas geometrias finais. Foi mostrado que esta nova abordagem de projeto de hélices leva à minimização da corda necessária ao longo da pá, enquanto a tração e a eficiência da hélice são maximizadas.

Foi desenvolvida uma nova instalação experimental para ensaio e caracterização de hélices de baixo número de Reynolds no âmbito do projeto MAAT, que foi posteriormente utilizada para desenvolver e validar ferramentas numéricas para projeto destas hélices. Além da descrição do desenvolvimento da instalação experimental, é também apresentada a validação da mesma, através da comparação das medições de diferentes hélices com dados experimentais presentes na literatura, obtidos em diferentes instalações de referência. Foi construída e testada uma réplica da hélice APC 10”x7” SF, fornecendo dados adicionais para a validação do JBLADE. É ainda apresentado o processo de desenho da réplica no *software* CAD e de construção dos moldes e do protótipo da hélice. Os resultados mostraram uma boa concordância entre as estimativas do JBLADE e as medições experimentais. Assim, conclui-se que o JBLADE pode ser utilizado para projetar e estimar o desempenho das hélices que poderão ser utilizadas pelo dirigível cruzador do MAAT bem como em outras aplicações.

Palavras-chave

JBLADE Software, Teoria do Elemento de Pá, Correções Pós-Perda, Equilíbrio 3D do escoamento, Projeto Inverso de Hélices, Simulação de Hélices em Dinâmica de Fluidos Computacional, Testes de Hélices em Túnel de Vento.

Abstract

This thesis presents the development of a new propeller design and analysis software capable of adequately predicting the low Reynolds number performance. JBLADE software was developed from QBLADE and XFLR5 and it uses an improved version of Blade Element Momentum (BEM) theory that embeds a new model for the three-dimensional flow equilibrium. The software allows the introduction of the blade geometry as an arbitrary number of sections characterized by their radial position, chord, twist, length, airfoil and associated complete 360º angle of attack range airfoil polar. The code provides a 3D graphical view of the blade, helping the user to detect inconsistencies. JBLADE also allows a direct visualization of simulation results through a graphical user interface making the software accessible and easy to understand. In addition, the coupling between different JBLADE modules avoids time consuming operations of importing/exporting data, decreasing possible mistakes created by the user. The software is developed as an open-source tool for the simulation of propellers and it has the capability of estimating the performance of a given propeller geometry in design and off-design operating conditions. The current development work was focused in the design of airship propellers. The software was validated against different propeller types proving that it can be used to design and optimize propellers for distinct applications.

The derivation and validation of the new 3D flow equilibrium formulation are presented. This 3D flow equilibrium model accounts for the possible radial movement of the flow across the propeller disk, improving the performance prediction of the software. The development of a new method for the prediction of the airfoil drag coefficient at a 90 degrees angle of attack for a better post-stall modelling is also presented. Different post-stall methods available in the literature, originally developed for wind turbine industry, were extended for propeller analysis and implemented in JBLADE. The preliminary analysis of the results shows that the propeller performance prediction can be improved using these implemented post-stall methods. An inverse design methodology, based on minimum induced losses was implemented in JBLADE software in order to obtain optimized geometries for a given operating point. In addition a structural sub-module was also integrated in the software allowing the estimation of blade weight as well as tip displacement and twist angle changes due to the thrust generation and airfoil pitching moments. To validate the performance estimation of JBLADE software, the propellers from NACA Technical Report 530 and NACA Technical Report 594 were simulated and the results were checked against the experimental data and against those of other available codes. The inverse design and structural sub-module were also validated against other numerical results.

To verify the reliability of XFOIL, the XFOIL Code, the Shear Stress Transport k-ω turbulence model and a refurbished version of k-kl-ω transition model were used to estimate the airfoil aerodynamic performance. It has been shown that the XFOIL code gives the closest prediction

when compared with experimental data, providing that it is suitable to be used in JBLADE Software as airfoil's performance estimation tool.

Two different propellers to use on the MAAT high altitude cruiser airship were designed and analysed. In addition, the design procedure and the optimization steps of the new propellers to use at such high altitudes are also presented. The propellers designed with JBLADE are then analysed and the results are compared with conventional CFD results since there is no experimental data for these particular geometries. Two different approaches were used to obtain the final geometries of the propellers, since, instead of using the traditional lift coefficient prescription along the blade, the airfoil's best $L^{3/2}/D$ and best L/D were used to produce different geometries. It was shown that this new first design approach allows the minimization of the chord along the blade, while the thrust and propulsive efficiency are maximized.

A new test rig was developed and used to adequately develop and validate numerical design tools for the low Reynolds numbers propellers. The development of an experimental setup for wind tunnel propeller testing is described and the measurements with the new test rig were validated against reference data. Additionally, performance data for propellers that are not characterized in the existing literature were obtained. An APC 10"x7" SF replica propeller was built and tested, providing complementary data for JBLADE validation. The CAD design process as well as moulds and propeller manufacture are also described. The results show good agreement between JBLADE and experimental performance measurements. Thus it was concluded that JBLADE can be used to design and calculate the performance of the MAAT project high altitude cruiser airship propellers.

Keywords

JBLADE Software, Blade Element Momentum Theory, Post-Stall Corrections, 3D Flow Equilibrium, Propeller Inverse Design, CFD Propeller Simulation, Wind Tunnel Testing

Resumo Alargado

Este trabalho apresenta o desenvolvimento de um nova ferramenta para projeto e análise do desempenho de hélices operando a baixos números de Reynolds. A ferramente desenvolvida é um *software* que contém uma interface gráfica e que foi desenvolvido tendo como base os *softwares* QBLADE e XFLR5, já existentes. A inovação deste código consiste na implementação de uma versão melhorada da teoria do elemento de pá, normalmente utilizada por outros códigos de projeto e análise de desempenho de hélices, que tem em conta um equilíbrio tri-dimensional do escoamento, contabilizando assim a rotação da esteira, e melhorando as previsões de desempenho das hélices.

Este trabalho foi desenvolvido no âmbito do projeto europeu *Multibody Advanced Airship for Transport (MAAT)*, que envolveu mais de 15 entidades, e que pretende implementar um novo modelo de transporte através da utilização de dirigíveis. Neste modelo são utilizados 2 tipos de dirigíveis: um crusador, que operará entre os 15 000- 16 000 *m* de altitude e um outro tipo de dirigivel que será responsável por fazer a ligação entre o solo e o crusador. Ora, como apresentado ao longo do documento, as hélices têm vindo a ser utilizadas em veículos com uma altitude de operação semelhante, pelo que é essencial o desenvolvimento de uma ferramenta fiável para projectar e analisar as hélices do crusador do projeto MAAT.

Durante o estudo e análise do estado atual das teorias aplicavéis a hélices, chegou-se à conclusão que era possível melhorar essas teorias. Este modelo de equilíbrio tri-dimensional tem em conta o possível movimento radial do escoamento ao longo do disco da hélice, melhorando as estimativas de desempenho do *software* Além disto, como as hélices têm ângulos de torção bastante elevados, principalmente na zona da raíz, os perfis das pás estão muitas vezes a operar em regime pós-perda, e os códigos númericos utilizados para prever o seu desempenho nem sempre fornecem dados fidedignos acerca do desempenho dos mesmos. O JBLADE utiliza um método que consiste na extrapolação dos valores do coeficiente de sustentação e do coeficiente de arrasto apresentado na literatura. Neste modelo, a previsão do valor do coeficiente de arrasto tem uma importância vital para uma correcta extrapolação deste mesmo coefficiente, podendo levar a diferenças significativas na previsão de desempenho da hélice. Assim, de modo a melhorar a previsão de desempenho da hélice foi desenvolvido um novo método para estimar o coeficiente de arrasto de um perfil a um angulo de ataque de 90º. Este método baseia-se no raio do bordo de ataque do perfil e foi também incorporado no JBLADE. Foram também implementados no JBLADE diferentes modelos de pós perda, originalmente desenvolvidos para a indústria de turbinas eólicas que como demonstrados, melhoram a previsão de desempenho para baixas razões de avanço. Foram comparados diferentes modelos e os resultados foram analisados e discutidos. Estes modelos estão disponíveis no JBLADE, podendo ser utilizados ou não na simulação da hélice, conforme as preferências do utilizador.

De formar a agilizar o processo de projeto de uma hélice, foi implementado um método de projeto inverso descrito na literatura. Foram feitas algumas modificações ao método original, nomeadamente através da utilização do ponto de melhor L/D e $L^{3/2}/D$ dos perfis, permitindo que a corda necessária para produzir uma determinada tração seja menor. Este processo foi validado através da comparação dos dados obtidos no JBLADE com outros dados disponíveis na literatura bem como com outros códigos disponíveis. Esta implementação do método de projeto inverso foi depois utilizado para projetar uma hélice para aplicação no dirigível crusador do projeto MAAT.

Uma vez que as hélices que serão utilizadas no dirigível do projeto MAAT serão bastante grandes, é importante assegurar que não sofrerão uma deformação excessiva, que poderá levar à sua destruição. Assim, foi implementado um módulo de cálculo estrutural, no qual a pá da hélice é considerada uma viga encastrada. Esta viga está sujeita a um momento flector e a um momento torsor, que surgem devido à geração de tração pela própria pá. Depois de uma análise aerodinâmica da pá, o utilizador pode definir um material para a mesma, bem como selecionar um conceito de construção entre os disponíveis e escolher o ponto para o qual quer analizar a deformação a que a pá está sujeita. Os resultados são apresentados na forma de gráficos de deslocamento e incremento ao ângulo de torção ao longo da envergadura da pá. Este módulo estrutural permite que o utilizador leve a cabo uma iteração adicional durante o projecto, e que garante que a pá não deformará excessivamente quando estiver em operação. O módulo estrutural permite ainda estimar o peso e o volume de cada pá, algo importante para o caso concreto do dirigível MAAT, uma vez que terá um grande número de hélices.

O JBLADE é um *software*, desenvolvido como um código *open source*, escrito em linguagem C++/QML e compilado utilizando *Qt® Creator*. O *software* mantém todas as funcionalidades originais do módulo XFOIL originalmente desenvolvidas no XFLR5, que permitem o projecto e a optimização de perfis para um dado ponto de projecto. O JBLADE possui uma interface gráfica e através da qual é possível executar todos os passos necessários ao projeto e análise de desempenho de uma hélice. O *software* permite que a pá seja introduza como um número arbitrário de secções, caracterizadas pela sua posição radial, corda, ângulo de incidência, comprimento, perfil e ainda pela polar 360º associada ao perfil. Este *software* permite também uma visualização e manipulação gráfica em 3 dimensões da pá/hélice, ajudando o utilizador a detetar possíveis inconsistências. O JBLADE também permite uma visualização direta e gráfica dos resultados das simulações de desempenho da hélice, tornado o código acessível e intuitivo. Uma vez que todos os módulos internos do JBLADE estão interligados, são evitadas operações demoradas de importação e exportação de dados, diminuindo assim possíveis erros criados pelo utilizador durante este processo. O código foi desenvolvido como um código aberto, para a simulação de hélices, e que tem a capacidade de estimar o desempenho de uma determinada geometria nas condições de operação do seu ponto de projeto e fora desse ponto de projeto. Como explicado anteriormente, uma vez que este trabalho foi desevolvido no âmbito do projecto MAAT, o desenvolvimento do *software* foi focado no projeto de hélices para dirigíveis

de grande altitude. Para validar as modificações e os modelos desenvolvidos neste *software* foram utilizadas diferentes geometrias, provando que o JBLADE pode ser utilizado para projetar e otimizar hélices para diferentes finalidades.

O procedimento de simulação de uma hélice foi validado, garantindo que pode ser utilizado um ponto intermédio e a distribuição correspondente dos números de Reynolds e de Mach. Foi ainda validado o número de pontos necessário para definir um perfil no sub-módulo XFOIL, mostrando que acima de 200 pontos não existem diferenças significativas no cálculo do desempenho do perfil, para um dado número de Reynolds. O novo método anteriormente apresentado para estimativa da previsão do coeficiente de arrasto foi também validado, e o seu efeito na previsão do desempenho das hélices foi demonstrado. O JBLADE foi ainda extensivamente validado através da comparação com dados experimentais apresentados na literatura, nomeadamente e com outros códigos numéricos disponíveis.

Para garantir que o XFOIL poderia ser utilizado como ferramenta de previsão do desempenho de um perfil para um dado ponto de operação, foram feitas simulações para os perfis E387 e S1223 e comparadas com dados obtidos através de simulações de dinâmica dos fluidos computacional. Nestas simulações foram utilizados o modelo de turbulência *k-ω Shear Stress Transport (SST)* e uma versão remodelada do modelo de transição *k-kl-ω*. O modelo de transição *k-kl-ω* foi utilizado uma vez que prever o ponto de transição ao longo da corda é essencial para conseguir calcular correctamente o desempenho dos perfis que operam a baixos números de Reynolds (60 000<*Re*<500 000). Os resultados mostraram que o XFOIL consegue prever o desempenho dos perfis tão bem quanto os modelos de turbulência e de transição utilizados nas simulações de dinâmica dos fluidos computacional. Além disso, o XFOIL tem ainda a vantagem de as simulações serem mais rápidas e de necessitar de muito menos recursos computacionais quando comparado com as simulações de dinâmica dos fluidos computacional. O XFOIL pode, assim, continuar a ser utilizado como ferramenta de cálculo para o desempenho dos perfis que serão utilizados ao longo das pás da hélice.

Durante este trabalho foi ainda desenvolvida uma nova instalação experimental, que foi posteriormente utilizada na validação do JBLADE. Esta instalação experimental, aplicada no túnel de vento do Departamento de Ciências Aeroespaciais da Universidade da Beira Interior foi validada através da comparação das medições obtidas para uma hélice com dados experimentais obtidos para essa mesma hélice noutras instalações experimentais. Além da validação da instalação experimental, foi construída e testada uma réplica da hélice APC 10”x7” SF, fornecendo dados adicionais para a validação do JBLADE. É apresentado todo o processo de desenho da réplica da hélice APC 10”x7” SF no *software* CAD bem como os passos necessários para a construção dos moldes. Foram desenhados 2 moldes fémea no *software* CATIA e posteriormente maquinados utilizando uma fresadora controlada por computador. Para obter a hélice final foi colocada fibra de carbono no interior dos moldes, sendo estes posteriormente fechados. Foi então introduzida resina epoxy, de modo a preencher todas as

cavidades e obter uma hélice tão próxima quanto possível da hélice original. Os resultados experimentais foram depois comparaddos com as simulações efectuadas no JBLADE, mostrarando uma boa concordância entre as estimativas do JBLADE e as medições experimentais. Através de tudo o que foi anteriormente apresentado foi possivel concluir que que o JBLADE pode ser utilizado para projetar e estimar o desempenho de hélices, que entre outras aplicações, poderão ser utilizadas pelo dirigível cruzador do projecto MAAT.

Table of Contents

List of Figures

List of Tables

This page has been intentionally left blank
for double side copying

Nomenclature

Latin Terms

A	=	Area of the actuator disk, m^2
A_0	=	$k-kl-\omega$ model freestream vortex surface area
A_1	=	Cross-section area of the settling chamber, m^2
A_2	=	Cross-section area of the test section, m^2
a_a	=	Axial induction factor
$a_{a_{old}}$	=	Axial induction factor of the previous iteration
A_{core}	=	Area of core airfoil
A_{ext}	=	Area of exterior airfoil, m^2
A_{int}	=	Area of interior airfoil, m^2
a_t	=	Tangential induction factor
$a_{t_{old}}$	=	Tangential induction factor of the previous iteration
B	=	Number of blades
b	=	Length of the beam, m
c	=	Blade local chord, m
C_a	=	Axial force coefficient
C_D	=	Airfoil drag coefficient
$c_{d_{2D}}$	=	Two dimensional drag coefficient
$c_{d_{3D}}$	=	Three Dimensional drag coefficient
$C_{D_{90}}$	=	Airfoil drag coefficient at 90°
$C_{D_{Ref}}$	=	Reference airfoil drag coefficient
C_{INT}	=	$k-kl-\omega$ model intermittency damping constant
C_L	=	Airfoil lift coefficient
$C_{l_{max}}$	=	Maximum lift coefficient of the airfoil
$c_{l_{pot}}$	=	Potential flow lift coeficient
$c_{l_{non\_rot}}$	=	airfoil lift coefficient of non-rotating airfoil
c_r	=	Blade local chord, m
$c_{l_{rot}}$	=	Airfoil lift coefficient of rotating airfoil
$c_{l_{3D}}$	=	Three Dimensional lift coefficient
$c_{l_{2D}}$	=	Two dimensional lift coefficient
c_p	=	power coefficient
C_t	=	Tangential force coefficient
c_t	=	Thrust coefficient
C_ω	=	Turbulent kinetic energy dissipation
C_{ω_1}	=	Specific turbulent kinetic energy dissipation

C_{ω_2} = Rate of the turbulent kinetic energy dissipation

C_{ω_3} = Scale of the turbulent kinetic energy dissipation rate

C_{ω_R} = Constant to control the turbulent kinetic energy dissipation rate

$C_{\lambda,y}$ = Calibration constant to control the influence of the distance to the wall

C_{μ} = $k-kl-\omega$ model turbulent viscosity coefficient

C_{SS} = Shear-Sheltering constant

D = Drag, N

D' = Component of drag force on the original system of coordinates

D_L = $k-kl-\omega$ model laminar fluctuations kinetic energy destruction term

D_p = Propeller diameter, m

D_T = $k-kl-\omega$ model turbulent kinetic energy destruction term

D_{ω} = Cross diffusion term

E = Young Modulus, GPa

F = Prandtl's correction factor

F_a = Axial blade force, N

f_{INT} = $k-kl-\omega$ model intermittency damping function

f_{INT}^{new} = $k-kl-\omega$ model new intermittency damping function

F_t = Tangential blade force, N

f_v = $k-kl-\omega$ model viscous damping function

f_W = $k-kl-\omega$ model viscous wall damping function

f_{ω} = $k-kl-\omega$ model kinematic wall effect damping function

f_{SS} = $k-kl-\omega$ model shear-sheltering damping function

F_1, F_2 = Blending functions

G = Circulation function

g = Gravity acceleration, m/s^2

g_{c_l} = Lift coefficient correction function

G_{ω} = Generation of ω

$\tilde{G}_k$ = Turbulence kinetic energy generation due to mean velocity gradients

I_{xx} = Moment of inertia, m^4

I_{yy} = Moment of inertia, m^4

J = Advance Ratio

k = Turbulent kinetic energy

kl = $k-kl-\omega$ model laminar fluctuations kinetic energy

k_L = $k-kl-\omega$ model laminar kinetic energy

$k_{T,s}$ = $k-kl-\omega$ model effective small-scale turbulent kinetic energy

k_{TOT} = $k-kl-\omega$ model total fluctuatin

L = lift force, N

L' = Component of lift force on the original system of coordinates

LE_{Radius} = Airfoil leading edge radius calculated with least square method

M	=	Bending moment, N.m
$\dot{m}$	=	Mass flow rate, kg/s
M_{Blade}	=	Blade's Mass, kg
$\dot{m}_e$	=	Mass flow rate at the exit, kg/s
$\dot{m}_0$	=	Mass flow rate at the unperturbed flow, kg/s
N	=	Amplification factor
n	=	Rotation speed , rps
P	=	Power, W
p_1	=	Pressure at settling chamber
p_2	=	Pressure at test section
P_i	=	Arbitrary load applied to a beam, N
P_c	=	Power coefficient, $2P/\rho V^3 \pi R^2$
$P_c{}'$	=	Power coefficient derived with respect to the non-dimensional radius
P_k	=	$k-kl-\omega$ model turbulent production term
P_{kl}	=	$k-kl-\omega$ model laminar fluctuations kinetic energy production term
$P_{k_{t,s}}$	=	$k-kl-\omega$ model turbulent kinetic energy production term
Q	=	Torque, N.m
R	=	Propeller tip radius, m
r	=	radius of blade element position, m
R_{BP}	=	$k-kl-\omega$ model bypass transition energy transfer function
R_{hub}	=	Propeller hub radius, m
R_{LE}	=	airfoil leading edge radius
R_{NAT}	=	$k-kl-\omega$ model natural transition energy transfer function
Re_{exp}	=	Exponential value for Reynolds number correction
Re_T	=	Turbulence Reynolds number
Re_T^{new}	=	New turbulence Reynolds number
Re_r	=	Local Reynolds number
Re_{Ref}	=	Reference Reynolds number
S	=	Mean flow shear
S_k, S_ω	=	Dissipation of k and ω
T	=	Thrust, N
t	=	airfoil thickness
T/A	=	Disk Loading, N/m^2
T_c	=	Thrust coefficient, $2T/\rho V^2 \pi R^2$
$T_c{}'$	=	Thrust coefficient, derived with respect to non dimensional radius
Tu	=	Absolute turbulent intensity
V_{Blade}	=	Blade Volume, m^3
$V_{Blade_{Core}}$	=	Volume of the core of the blade, m^3
$V_{Blade_{skin}}$	=	Volume of the skin of the blade, m^3

V_e = Induced Velocity at the far wake, m/s

V_p = Velocity at propeller's disk, m/s

V_{skin} = Volume of the skin of the blade, m^3

$V_{t_{75}}$ = Tangential velocity at 75% of the blade radius, m/s

V_x = Axial or tangential flow velocity components at the disk

V_{x_w} = Axial or tangential flow velocity components at the wake

V_0 = Velocity of the unperturbed flow, m/s

V_1 = Velocity at the settling chamber, m/s

V_2 = Velocity at the test section, m/s

W = element relative velocity, m/s

W_a = element axial velocity, m/s

$\overline{W}_a$ = Average axial velocity, m/s

W_r = Local freestream speed, m/s

W_t = Element tangential velocity, m/s

x = Non-dimensional distance, $\Omega r/W$

x/c = non dimensional x position

$X_{centroid}$ = Horizontal coordinate of the airfoil centroid, mm

$Y_{centroid}$ = Vertical coordinate of the airfoil centroid, mm

y^+ = Non-dimensional wall distance

$(y/c)_{(x/c)=0.0125}$ = non dimensional y position at $x/c = 0.0125$

Y_k, Y_ω = Dissipation of k and ω

z_1 = Height of settling chamber center line

z_2 = Height of test section center line

Greek Symbols

α = angle of attack, deg

α^* = Damping turbulent viscosity coefficient

$\alpha_{c_{l_{max}}}$ = Angle of attack of maximum lift coefficient, deg

$\alpha_{c_{l_0}}$ = Angle of attack of zero lift coefficient, deg

α_T = $k - kl - \omega$ model effective turbulent diffusivity

Δr = Width of the annulus, m

Δc_l = Difference between lift coefficient with and without separation

Δc_d = Difference between drag coefficient with and without separation

δ = Bending displacement, m

Γ = Circulation

Γ_k, Γ_ω = Effective diffusivity of k and ω

ε = Drag-to-lift ratio, D/L

ε_{conv} = User-defined convergence criterion

ζ = Displacement velocity ratio, v'/V

η	=	Propeller efficiency
θ	=	incidence angle, deg
θ_{75}	=	Propeller twist angle at 75 % of the blade span
θ_{Axis}	=	incidence angle coincident with airfoil axis
$\theta_{LowerSurface}$	=	incidence angle coincident with airfoil lower surface
λ	=	Speed ratio, $W/\Omega R$
λ_{eff}	=	$k-kl-\omega$ model effective turbulent length scale
λ_T	=	$k-kl-\omega$ model turbulent length scale
μ	=	Dynamic viscosity ,N.s/m^2
μ_t	=	Turbulent viscosity
$\nu_{T,s}$	=	$k-kl-\omega$ model small scale turbulent kinematic viscosity
$\nu_{T,l}$	=	$k-kl-\omega$ model large scale turbulent kinematic viscosity
ξ	=	Non-dimensional radius, $r/R=\lambda x$
ρ	=	air density, kg/m^3
ρ_{mat}	=	Material density, kg/m^3
σ_k, σ_ω	=	Turbulent Prandtl numbers for k and ω
σ_r	=	rotor solidity ratio
ϕ	=	inflow angle, deg
ϕ_t	=	Tip inflow angle
Ω	=	rotation speed, RPM
Ω_v	=	Mean flow vorticity
ω	=	Specific dissipation rate
ω_{relax}	=	User-defined relaxation factor

Acronyms

AoA	=	Angle of Attack
APC	=	Advanced Precision Composites – Commercial brand of propellers
BEM	=	Blade Element Momentum
CFD	=	Computational Fluid Dynamics
FEM	=	Finite Element Method
FVM	=	Finite Volume Method
MAAT	=	Multibody Advanced Airship for Transportation
MRF	=	Multiple Reference Frames
NACA	=	National Advisory Committee for Aeronautics
RANS	=	Reynolds-Averaged Navier Stokes
SF	=	Slow Flyer
TR	=	Technical Report
UBI	=	University of Beira Interior
VTOL	=	Vertical Take Off and Landing
XFLR5	=	Software Developed by Deperrois, A.

This page has been intentionally left blank
for double side copying

Chapter 1

Introduction

1.1 - Motivation

The problems caused by growth in the transportation sector, e.g. the rise of fuel consumption and cost, as well as pollution and consequent climate change led to a reconsideration of the transportation systems by the most economically advanced nations (Wilson, 2004). Nowadays, despite all technologic developments, as we proceed in the 21st century, we may be about to witness the return of slower air transport as a means of increasing energy efficiency and business profitability. Slowing down aircrafts can take us towards the airship. After the initial developments until the 1930s, and during some decades, the airships were only considered as a mere curiosity. At their peak, in the late 1930s, airships were unrivaled in transoceanic transportation. Nowadays, they can be used effectively as platforms for different purposes (van Eaton, 1991; Liao & Pasternak, 2009; Morgado *et al.*, 2012; Wang *et al.*, 2009) especially activities that require long endurance or hovering for long time.

In Europe, the development of new airships is being supported by European Union through the Multibody Concept for Advanced Airship for Transport (MAAT (Dumas *et al.*, 2011)) project. The MAAT Project was funded by European Union through the 7th Framework Programme and it aims to investigate the possibilities to develop a new stratospheric airship as a global transportation system. This collaborative project aims to develop a heavy lift cruiser-feeder airship system in order to provide middle and long range transport for passengers and goods. The MAAT system is composed by the cruiser and the feeder modules. The feeder is a Vertical Take Off and Landing (VTOL) Vehicle which ensures the connection between the ground and the cruiser. It can go up and down by the control of buoyancy force and displace horizontally to join to the cruiser. The cruiser is conceived to move mostly in a horizontal way at high

altitude. Since the MAAT project has the objective of operating airships at stratospheric altitudes, propellers are a valid option to the airships' propulsion.

The presented work was integrated in the Multibody Advanced Airship for Transport (MAAT) project. A distributed propulsion concept for the MAAT cruiser airship based on very low tip speed propellers can bring advantages in terms of minimizing the needed propulsion power for this solar powered airship. The problem is the very low average Reynolds number of the propellers' blade, resulting from the extremely low air density at the cruising altitude of *16 km*. The existing design tools suited for the development of such low Reynolds propellers show limitations that cannot be overran.

1.2 - Objectives

The objective of the thesis is to develop a software tool capable to design and optimize propellers for the MAAT project airship application. A detailed literature review and state of the art research is to be carried out. Appropriate analysis and optimization computational tools must be developed and/or integrated. Furthermore, a complete validation of the tool should be performed, through the comparison with numerical and experimental data available in the literature. In order to achieve these goals the following topics must be addressed:

- Development of a software capable to design and optimize propellers suitable to high-altitude/low Reynolds usage;
- Integration of an inverse design methodology in order to design new propellers for distinct applications;
- Estimation of the blade tip displacement and torsional angle change due to the thrust, blade sweep and pitching moment at a given operating condition;
- Validation of the software through different comparisons with both numerical and experimental data;
- Design and analysis of a propeller to use in the MAAT cruiser airship.

1.3 - Contributions

The main contributions of this dissertation lie on the characteristics of the new software tool suitable for the design and optimization of new propellers. Although the computational tool partly uses well established methods for both airfoil and propeller aerodynamic analysis, it also embeds new models that improve its accuracy and applicability to the particular low Reynolds numbers propeller design making it very useful and powerful.

A new model for the 3D flow equilibrium (see Section 2.4.1) was developed to account with the real 3D flow passing the propeller disk. In addition, a new method to predict the airfoil drag

coefficient at an angle of attack of 90º C_{D90} based on the airfoil leading edge (see Section 2.4.2) was developed and it proved to be more accurate than the methods previously used in other BEM's based Software.

An inverse design capability was integrated in the software, allowing a faster propeller design from the known propeller operating point as presented in Section 3.2.5. In addition, a *Structural sub-module* (see Section 3.2.7) was also integrated in the software, providing the capability of propeller weight estimation depending on the material and the structural concept used in the propeller. This sub-module also allows the determination of tip displacement at different propeller operating conditions. Furthermore, this sub-module also allows the computation of the twist angle change due to the propeller operating conditions, allowing an additional layer of iteration during the propeller design.

Since the software is an in-house development code, further enhancements can be easily implemented in order to account for the complete propulsion system. The long term goal of the JBLADE Software development is to provide a user-friendly, accurate, and validated open-source code that can be used to design and optimize propellers for distinct applications.

1.4 - Thesis Outline

After this introductory chapter, in which the motivation, objectives and contributions of this thesis were described, the present work is divided in the sections described below.

Chapter 2 presents the historical development of propeller theory. Furthermore, this chapter presents a state of the art of the low Reynolds number propeller design. In addition, this chapter also includes the detailed description of the formulations theories used inside the JBLADE Software. Chapter 2 includes the contributions to the state of the art of propeller theory developed during this thesis. Two different main contributions are presented and discussed in detail: the 3D flow equilibrium and the new method to predict the airfoil drag coefficient based on the airfoil's leading edge radius.

Chapter 3 presents the JBLADE Software architecture in detail. The chapter begins with the overview of the XFOIL and BEM Modules interaction. Furthermore, each sub-module and their capabilities are described and discussed in detail. In addition, Chapter 3 also presents the different JBLADE validations. The data from NACA TR 594 was used to validate the simulation procedure as well as the JBLADE performance prediction. NACA TR 530 Report data were used to validate the new methods for the airfoil C_{D90} prediction. This chapter also presents the validation of the inverse design sub-module through the comparison with the original Adkins and Liebeck implementation. Furthermore, the validation of the structural sub-module is presented by comparing the bending and torsional predictions of some operation loaded blades with Finite Element Method (FEM) simulations in CATIA V5 ®.

Chapter 4 presents a comparison between XFOIL and conventional turbulence and transition models. The chapter describes the theoretical formulation of each model as well as the numerical procedure used along the simulations. Two different airfoils were used to verify the accuracy of XFOIL against conventional Computational Fluid Dynamics (CFD).

Chapter 5 presents the development and optimization of a new propeller suitable for the MAAT cruiser airship. In this chapter the development of the airfoil used in the propeller is also described. Two different propellers were developed, following different methodologies and their geometries are shown is Chapter 5.

Chapter 6 presents the Computational Fluid Dynamics simulations of different propellers. It shows the numerical procedure used to simulate the APC 10"x7" SF propeller and the propellers developed in Chapter 5. The APC 10"x7" SF was also used to validate the new 3D flow equilibrium, presented in Chapter 2. Furthermore, the performance prediction of JBLADE is also compared with CFD predictions and experimental data from UIUC propeller data site. The propellers developed for the MAAT cruiser airship were simulated and their performance was compared with the JBLADE predictions.

Chapter 7 presents the experimental work developed in the University of Beira Interior's subsonic wind tunnel. The development and validation of the experimental procedure is shown, followed by the uncertainty analysis of the data obtained from the experiments. In addition, the process of replication of the APC 10"x7" SF propeller is described in detail. To finalize, the original APC 10"x7" SF propeller is tested and compared with the performance of its replica.

Chapter 8 presents the general discussion and conclusions of the work developed during the present dissertation. At the end of the chapter future works are proposed for the continuous development of the JBLADE Software as well as possible improvements in the test rig, in order to keep developing more accurate tools and more efficient propellers.

Chapter 2

Propeller Design Theory

2.1 - Historical Developments of Propeller Theory

Propellers are being used to generate thrust from the beginning of powered flight (Colozza, 1998; Dreier, 2007). The first developments related to the theory of propellers occurred in the 19th century with Rankine & Froude (1889) and Froude (1920) through a work mainly focused on marine propellers. They established the essential momentum relations governing a propulsive device in a fluid medium. Later, Drzewiecki (1892) presented a theory of propeller action where blade elements were treated as individual lifting surfaces moving through the medium on a helical path. However, he did not take into account the effect of the own propeller induced velocity at each element. In 1919, Betz & Prandtl (1919) stated that the load distribution for lightly loaded propellers with minimum energy loss is such that the shed vorticity forms regular helicoidal vortex sheets moving backward undeformed behind the propeller. Thus, the induced losses of propellers will be minimized if the propeller slipstream has a constant axial velocity and if each cross section of the slipstream rotates around the propeller axis like a rigid disk (Eppler & Hepperle, 1984). Prandtl, as described in Glauert (1935) found an approximation to the flow around helicoidal vortex sheets which is good if the advance ratio is small and improves as the number of blades increases. The approximation presented by Prandtl is still applied in simple mathematical codes.

Goldstein (1929) found a solution for the potential field and the distribution of circulation for propellers with small advance ratios. This solution was still limited to lightly loaded propellers. Theodorsen (1948), through his study on the vortex system in the far field of the propeller, concluded that the Goldstein's solution for the field of a helicoidal vortex sheet remains valid, even for moderate/highly loaded propellers. In 1935 Welty & Davis (1935) described the steps needed to design and produce a new propeller according to the available material properties and introduce the light alloy propeller. Later, in 1936, Biermann (1936) developed one of the

first parametric studies, analysing the influence of some parameters during propeller design. He analysed the reduction in the design pitch angle as a function of the propeller operating speed and the thrust and/or power increase. In 1937, Caldwell (1937) studied the effect of the propeller's diameter and rotational speed on its efficiency for different operating conditions. McCoy (1939) presented a study in which he mentioned the improvement of the propeller's efficiency that can be expected if the engines are enclosed within the airplane or within the wing structure and driving shafts are used to drive the propellers. He concluded that the reduction in drag, the increase in lift, *L/D* ratio and in the propeller efficiency associated with extension shaft drives give for equal power a substantial improvement in entire aircraft's operation. Later, in 1944, he presented the functional requirements that have formed the basis for propeller development by the United States Army at that time (McCoy, 1944). In addition, he presented experimental results showing that reverse pitch propellers can be used to help the aircraft landing in shorter distances.

In 1948, Ribner & Foster (1990) developed a computer code that allowed to determine the ideal efficiency of an ideal propeller. Approximately 10 years later, during 1955, Mccormick (1955) presented a Goldestein's propeller analysis, satisfying the Minimum Induced Losses (MIL) propeller wake condition but extended it to account for the hub radius influence. The MIL propeller wake condition is attributed to Betz in what he called the solid wake condition. The author shows that for a trailing vortex sheet of a given propeller pitch, when the hub's influence is included it increases the value of the bound circulation of the line vortex generating the sheet. In addition the author notices that the change varies inversely with the number of blades. During 1965, de Young (1965) derived the force and moment equations covering the propeller range of angle of attack from 0º to 90º. He made the expression independent of the blade shape, using a solidity based on an average blade chord. Additionally, he verified that his formulation shows an accuracy adequate to establish design criteria, to perform trend studies, to develop preliminary configuration and to estimate the propeller performance.

During 1968, Hall (1969) developed a new method to analyse propeller blades at high angles of attack similar to the classical Prandtl's (Glauert, 1935) tip loss model. The developed tip loss factor is also a function of the number of the blades, nondimensional propeller radius and wake helix geometry. During 1974, Fanoe (1974) presented an expression for the aerodynamic pitch angle, valid for a propeller with an arbitrary number of blades in viscous flow to be used in the design of moderately loaded propellers. In 1978, Azuma & Kawachi (1979) derived a new momentum theory. This theory was based on the instantaneous momentum balance of the fluid with the blade elemental lift at each local station in the propeller disk. When they applied the theory to both steady and unsteady flow cases they achieved good results, with lower computational costs when compared with the vortex theory. In 1980, Larrabee (1979) analysed the steady air loads on the propeller and presented a practical design theory for minimum induced loss propellers. The method presented by Larrabee is a combination between

momentum theory, blade element theory and vortex theory. In 1986, Johnson (1986) presented a study in which the progress in development of advanced computational methods for rotary-wing aerodynamics was examined. In the same year, Rizk & Jou (1986a, 1986b) developed a preliminary design code based on the finite volumes for solving the potential flow about a propeller by line relaxation. Although the code was able to calculate the transonic flow field around the propellers during the initial phase of the research, the authors decided to limit the investigation to subsonic flow calculations. They combined an analysis code with the single-cycle optimization approach to produce an efficient design code (Rizk, 1983, 1985).

In 1989, Favier *et al.* (1989) investigated the isolated propeller aerodynamics both numerically and experimentally. They studied the propeller aerodynamic field over a large range of operating conditions of the axial flight regime. They concluded that their code predictions of both local and global aerodynamic coefficients were in good agreement with the experiments for the different propeller axial flight conditions. During 1988, Strash *et al.* (1998) presented a multi-grid Euler technique with a coupled blade element momentum module that can be used in the analysis of the propeller slipstream interference effects. Later on, Adkins & Liebeck (1994) presented improvements with small angle approximations and light load approximations, overcoming the restrictions in the method developed by Larrabee (1979). In 2002, Miley *et al.* (2002) analysed the design methods applied by the Wright brothers to their propeller. Additionally, the experimental investigation conducted by Miley showed that the Wright brothers developed a high efficiency low rotational speed propellers early in 1911.

2.2 - Present Status of Propeller Aerodynamics

Although the literature of propeller aerodynamics is, in some aspects, dispersed and incomplete (Wald, 2006), the theories describing the propeller aerodynamics have been improved during the past decades. There are several methods available for the propeller design and analysis depending on the desired level of fidelity (Benini, 2004). The Computational Fluid Dynamics (CFD) is the most sophisticated method, consisting in three dimensional viscous flow models, including incompressible Reynolds-Averaged Navier Stokes (RANS) equations solved in an iterative way. However, as it is possible to observe in Chapter 4, if the airfoils are working at low Reynolds number environments the RANS CFD methods present some limitations in the prediction of the laminar flow region, leading to worst results when compared with other computational tools or even with experimental data. Between the most advanced methods is also the lifting surface methods. Some of the implementations can calculate near-wall effects since they contain the RANS equations to account for the viscous effects in this region (Black, 1997; Feng *et al.*, 1998; Hsiao & L., 1998). Nevertheless, the previously mentioned methods are difficult to implement and they require too much computational resources. In addition, it is not easy to apply them to the different geometries when performing practical parametric studies in propeller design due to the necessary meshing process. Since the design process is

known by the iterative geometry manipulation, a simpler approach is needed. The Blade Element Momentum (BEM) theory is inherently two-dimensional and it is the less sophisticated method. However, it does not require expensive computational power when compared to CFD. In addition, the BEM theory also presents good agreement when compared with experimental data. Moreover it can be easily applied to the above mentioned iterative geometry process (Benini, 2004) making it suitable to be used during the design phase.

2.3 - Available Propeller Design Codes

Some codes suitable for the design and analysis of high altitude/low Reynolds propellers were found. Namely QPROP (Drela, 2006), QMIL (Drela, 2005b), XROTOR (Drela & Youngren, 2003) and JAVAPROP (Hepperle, 2010). QPROP, XROTOR and QMIL share the same BEM formulation described in Drela (2006). The first two are used for propeller analysis and the third is used for design with minimum induced losses using a different set of unknown variables than that used for analysis. QPROP/XROTOR major limitations are that the blade airfoil lift is assumed to be linear within the minimum and maximum lift coefficient stall limits and the post stall lift coefficients are not specified. Additionally, the drag polar of the airfoils are modelled with 2-piece parabolas within the linear lift region and an extra drag term is added if the angle of attack surpasses the stall limit. These simplifications in the airfoil performance modelling lead to a modest accuracy in the propeller performance predictions.

JAVAPROP (Hepperle, 2010) propeller analysis and design code is based on the blade element momentum theory. The blade is modelled considering independent sections along the span and the formulation does not account with any three dimensional effects correction. Only four distinct airfoils can be defined along the blade and the airfoils characteristics are then interpolated in the sections between those four sections. The airfoils are modelled as pre inserted lift and drag versus angle of attack tables files making hard any iteration of the airfoils Reynolds number during the propeller design iterations or even the previous modelling of the post stall airfoils characteristics to produce the complete tables. No insight is given by the author regarding the formulation used for blade design optimization by JAVAPROP.

2.4 - Propeller Theory

2.4.1 - Momentum Theory

The simplest and classical methodology that describes a propeller working is the momentum theory, also known as actuator disk theory which was originally developed by Rankine & Froude (1889). The control volume for the momentum theory can be assumed as a stream tube that just surrounds the propeller (see Figure 2.1). This 1-D theory considers the flow as inviscid,

incompressible and irrotational. The flow enters the stream tube, is accelerated trough the rotor disk and then is exhausted from the end of the stream tube.

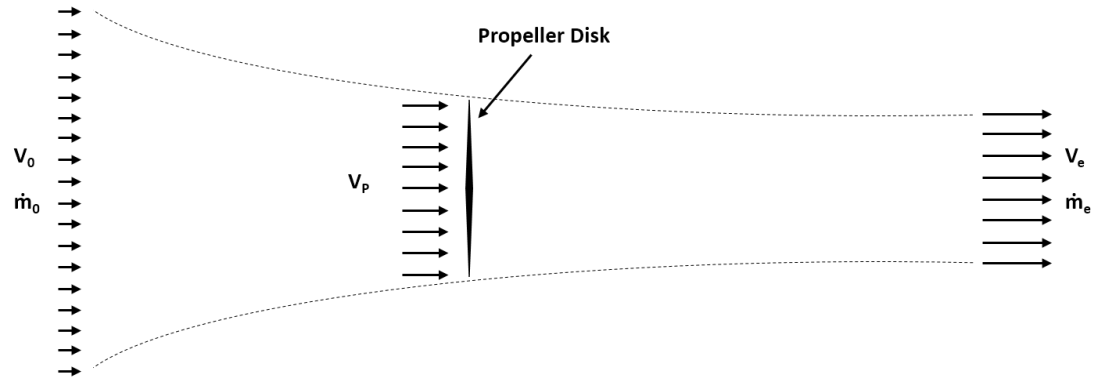

Figure 2.1 - Propeller Stream-tube (Rwigema, 2010).

The change in momentum of the flow along the stream-tube starting far upstream, passing through the propeller disk and just after moving off into the slipstream must be equal to the thrust produced by the propeller (Glauert, 1935). It means that the thrust produced by the propeller depends on the mass flow rate and the velocity change through the propeller. This allows the calculation of the propeller's produced thrust according to Eq. 2.1:

$$T = \dot{m}_e V_e - \dot{m}_0 V_0 \tag{2.1}$$

Since the propeller rotates, it is possible to define *its* mass flow rate from continuity as:

$$\dot{m}_0 = \dot{m}_e = \dot{m} = \rho V_p A \tag{2.2}$$

replacing Eq. 2.2 in Eq. 2.1:

$$T = \rho V_p A (V_e - V_0) \tag{2.3}$$

Since the thrust is related to the pressure jump across the propeller disk, applying the Bernoulli's equation far upstream and downstream it becomes:

$$T = \frac{1}{2}\rho A (V_e^2 - V_0^2) \tag{2.4}$$

with Eq. 2.3 and 2.4 for the propeller disk velocity:

$$V_p = \frac{1}{2}(V_e + V_0) \tag{2.5}$$

Thus, the airspeed through the propeller disk is simply the average between freestream velocity and final slipstream velocity.

The Momentum Theory can be extended to 2D dividing the disk into annulus as shown in Figure 2.2. The increment of thrust on each annulus can be calculated as:

$$T = \rho V_p 2\pi r \Delta r V_e \qquad 2.6$$

where $2\pi r\Delta r$ is the area of the annulus and V_p represents the induced velocity at the propeller disk and V_e is the induced velocity at the far wake.

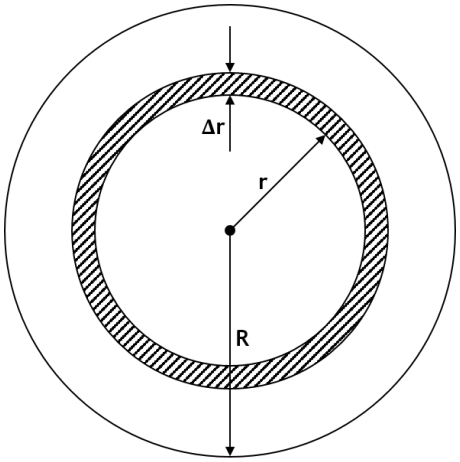

Figure 2.2 – Geometry of rotor annulus (Prouty, 2003).

As in the original derivation of the momentum equation, it may be shown that:

$$V_e = 2V_p \text{ or } V_{x_w} = 2V_x \qquad 2.7$$

where V_x can be the axial or tangential flow velocity components, V_a and V_t respectively (see Figure 2.3). So, the annulus thrust becomes:

$$T = 4\rho\pi V_p^2 r\Delta r \qquad 2.8$$

2.4.2 - Blade Element Theory

The Blade Element Theory was first developed by Drzewiecki (1892). This theory is used to determine the thrust and torque at an arbitrary radial location along the blade and it takes into account the geometry of the propeller blades, such as airfoil's shape and chord and also the incidence angle at that specific location. The blade is divided into n elementary sections along the span and it is assumed that no aerodynamic interactions occur between different blade elements. In addition, the forces on the blade elements are determined using only the two-dimensional lift and drag data of the blade element airfoil according to the local angle of attack

that results from its orientation to the incoming flow. Each blade element is characterized by having a given chord and length as shown in Figure 2.3. At each element, blade geometry and flow-field properties can be related to a finite propeller thrust, dT, and torque, dQ. The overall performance characteristics of the propeller blade can be obtained by integration along the radius of the blade.

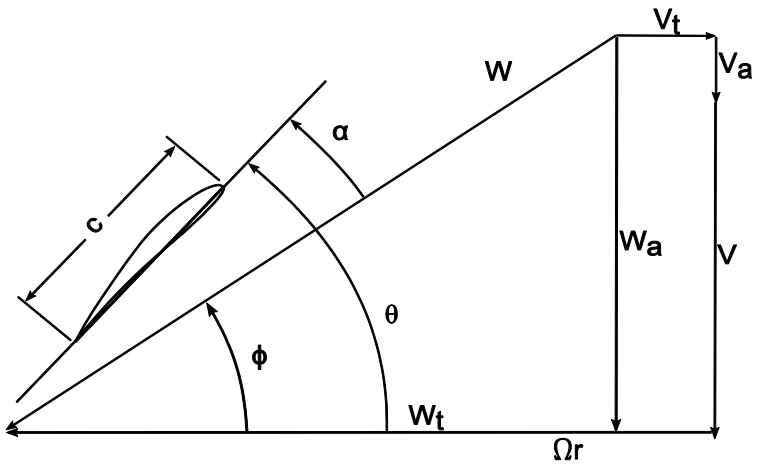

Figure 2.3 - Blade element geometry and velocities at an arbitrary radius position (Drela, 2006)

Analysing Figure 2.3, the inflow angle based on the two components of the local velocity vector can be calculated as:

$$\tan\phi = \frac{W_a}{W_t} = \frac{V + V_a}{\Omega r - V_t} = \frac{V(1 + a_a)}{\Omega r(1 - a_t)} \tag{2.9}$$

where:

$$a_a = \frac{V_a}{V} \tag{2.10}$$

$$a_t = \frac{V_t}{\Omega \mathrm{r}} \tag{2.11}$$

also, the following relation can be obtained:

$$W = \frac{V + V_a}{\sin\phi} = \frac{V(1 + a_a)}{\sin\phi} \tag{2.12}$$

The induced velocity components, V_a and V_t in Eq. 2.9 and in Eq. 2.12 are a function of the forces on the blades and are calculated through the blade element momentum theory as presented in Section 2.5.3 The thrust produced by each elemental annulus of the disk is calculated as:

$$dT = \frac{1}{2} B\rho W^2 (C_L cos\phi - C_D sin\phi) c dr \tag{2.13}$$

where B represents the number of the blades of the propeller. The torque produced by each element is given by Eq. 2.14:

$$dQ = \frac{1}{2} B\rho W^2 (C_L sin\phi + C_D \cos\phi) crdr \quad 2.14$$

2.4.3 - Blade Element Momentum Theory

Combining the previous presented theories (see Section 2.5.1 and Section 2.5.2), it becomes possible to determine the performance of a given propeller with the known blade number, rotational speed and distributions of chord, incidence and airfoils. The blade element relative velocity and respective inflow angle are computed through the axial and tangential velocity components W_a and W_t. The axial velocity results from the sum of the freestream airspeed to the induced axial velocity, V_a, at the propeller disk. The tangential velocity results from the sum of the velocity of the element due to the propeller rotation, with the induced tangential velocity, V_t. The induced velocity components are determined from the momentum theory (see Section 2.5.1), for the annulus swept by the rotating blade element and used to calculate the angle of attack, α, as the difference between the inflow angle, ϕ and the incidence angle, θ. With α, the element's lift and drag coefficients can be determined from the airfoil characteristics. With these coefficients, the axial and tangential force coefficients are obtained according to the local ϕ:

$$C_a = C_L \cos\phi - C_D \sin\phi \quad 2.15$$

$$C_t = C_L \sin\phi + C_D \cos\phi \quad 2.16$$

To describe the overall propeller performance, the forces are obtained from the force coefficients according to:

$$F_x = \frac{1}{2} \rho W^2 c C_x \quad 2.17$$

where the subscript x corresponds to axial or tangential components. The total thrust and torque of the propeller are calculated by numerical integration:

$$T = B \sum_{i=1}^{n} F_{a_i} \quad 2.18$$

$$Q = B \sum_{i=1}^{n} F_{t_i} r \quad 2.19$$

with the total torque given by Eq. 2.19, the necessary shaft power is obtained.

$$P = \Omega Q \quad 2.20$$

and dimensionless thrust and power coefficients are calculated from their definitions:

$$c_t = \frac{T}{\rho n^2 D_p^4} \quad 2.21$$

$$c_p = \frac{P}{\rho n^3 D_p^5} \quad 2.22$$

where the advance ratio is defined as:

$$J = \frac{v}{nD} \quad 2.23$$

and the propeller efficiency is computed according Eq. 2.24:

$$\eta = J\frac{c_t}{c_p} \quad 2.24$$

Since the induced velocity components depend on the element´s forces and vice-versa, the iteration variables of the classical Blade Element Momentum method are the axial and tangential induction factors:

$$a_a = \frac{W_a - V}{V} \quad 2.25$$

$$a_t = \frac{\Omega r - W_t}{\Omega r} \quad 2.26$$

Including their dependence on the element´s force coefficients according to the results from momentum theory:

$$a_a = \left(\frac{4\sin^2\phi}{\sigma_r C_a} - 1\right)^{-1} \quad 2.27$$

$$a_t = \left(\frac{4\sin\phi\cos\phi}{\sigma_r C_t} + 1\right)^{-1} \quad 2.28$$

where σ_r is the ratio of the blade element area to the annulus sweep by the element in its rotation and it is defined as:

$$\sigma_r = \frac{cB}{2\pi r} \quad 2.29$$

2.4.3.1 Prandtl Tip and Hub Losses Corrections

The original blade element momentum theory does not take into account the influence of vortices shed from the blade tips into the slipstream on the induced velocity field. However, since the blade creates a pressure difference in the flow, at the tip, that flow tends to move

from the lower blade surface to the upper blade surface, reducing the resultant force in the neighbourhood of the tip. Prandtl, as described in Glauert (1935), derived a correction factor that compensates for the amount of work that can actually be performed by the element according to its proximity to the blade's tip (it is widespread the use of this correction for the blade root too). The factor is calculated as:

$$F = \frac{2}{\pi}\cos^{-1}(e^{-f}) \tag{2.30}$$

where f for the tip region:

$$f_{tip} = \frac{B}{2}\frac{R-r}{r\sin\phi} \tag{2.31}$$

Similarly to the f_{tip} presented in Eq. 2.31, the f_{hub} can be calculated by:

$$f_{hub} = \frac{B}{2}\frac{r-R_{hub}}{r\sin\phi} \tag{2.32}$$

If the element is affected by both tip losses and hub losses, the total factor is obtained by multiplying those factors. Thus, this factor F is used to modify the momentum segment of the Blade Element Momentum equations (Eq. 2.27 and Eq. 2.28) as presented in Eq. 2.33 and Eq.2.34:

$$a_a = \left(\frac{4F\sin^2\phi}{\sigma_r C_a} - 1\right)^{-1} \tag{2.33}$$

$$a_t = \left(\frac{4F\sin\phi\cos\phi}{\sigma_r C_t} + 1\right)^{-1} \tag{2.34}$$

2.4.3.2 Post Stall Models

The rotational motion of the blade affects the element's boundary layer such that the airfoil stall is delayed, shifting to higher angles of attack. Besides this, the post stall behaviour of the airfoil is affected by the rotation motion condition and plays an important role in the overhaul propeller performance. In order to complement the available tools in JBLADE, and make the predictions more accurate, five models to correct the airfoil characteristics after stall were implemented. For all models presented in this subsection, except the model of Corrigan & Schillings (1994) were implemented as:

$$c_{l_{3D}} = c_{l_{2D}} + g_{c_l}\,\Delta c_l \tag{2.35}$$

$$c_{d_{3D}} = c_{d_{2D}} + g_{c_d}\,\Delta c_d \tag{2.36}$$

where g_{c_l} and g_{c_d} are the functions associated with each model, while Δc_l and Δc_d represent the difference between the obtained lift and drag coefficients in case of no separation occurrence. The remaining $c_{l_{2D}}$ and $c_{d_{2D}}$ are the lift and drag coefficients measured or calculated for the airfoil.

Snel et al. Model

The model of Snel *et al.* (1994) emerged from the solution of a simplified form of the 3D boundary layer equations on a rotating blade, resulting in:

$$g_{c_l} = 3\left(\frac{c}{r}\right)^2 \tag{2.37}$$

This model only changes the lift coefficient, while 2D airfoil drag coefficient is maintained unchanged.

Du and Selig Model

The model developed by Du & Selig (1998) is an extension of the work done by Snel *et al.* (1994) which accounts also for changes in drag coefficient due to the rotation of the blade. The two dimensional coefficients are modified by:

$$g_{c_l} = \frac{1}{2\pi}\left[\frac{1.6(c/r)a - (c/r)^{\frac{dR}{\Lambda r}}}{0.1267b - (c/r)^{\frac{dR}{\Lambda r}}} - 1\right] \tag{2.38}$$

$$g_{c_d} = \frac{1}{2\pi}\left[\frac{1.6(c/r)a - (c/r)^{\frac{dR}{\Lambda r}}}{0.1267b - (c/r)^{\frac{dR}{\Lambda r}}} - 1\right] \tag{2.39}$$

where:

$$\Lambda = \frac{\Omega R}{\sqrt{W^2 + (\Omega R)^2}} \tag{2.40}$$

In their original work, Du and Selig kept the constants $a = b = d = 1$. The same values of *a*, *b* and *d* were kept herein. Although in JBLADE it is possible to change the values of these constants, to do so, the user needs to have some knowledge about their possible values.

Dumitrescu and Cardos Model

The model proposed by Dumitrescu & Cardos (2007) presents a correction in the lift coefficient. Similarly to the work of Snel *et al.* the function to correct the lift coefficient due to blade rotation came from an analysis of the momentum equations for the three dimensional boundary layer.

$$g_{c_l} = 1 - e^{-\frac{\gamma}{(r/c)-1}} \quad 2.41$$

The correction presented in Eq. 2.41 assumes a viscous decay of the vortex lift in the span wise direction. The authors concluded that the best comparisons with experimental data occur for $\gamma = 1.25$. The same value of γ is used in JBLADE.

Chaviaropoulos and Hansen Model

The model formulated by Chaviaropoulos & Hansen (2000) uses a system of simplified equations which were obtained by the integration of the three dimensional incompressible Navier-Stokes equations in the radial direction of the blade. This method was extended in order to account the influence of the blade's twist.

$$g_{c_l} = a\left(\frac{c}{r}\right)^h \cos^n(\theta) \quad 2.42$$

$$g_{c_d} = a\left(\frac{c}{r}\right)^h \cos^n(\theta) \quad 2.43$$

The values used in the work of Bouatem & Mers (2013) which best compare with the experimental data are: $a = 2.2$, $h = 1$ and $n = 4$ whereby the same values were used in the simulations of the present work.

Corrigan and Schillings Model

The model developed by Corrigan & Schillings (1994) correlates the stall delay to the ratio of the local blade chord to radial position. The authors analysed the pressure gradients in the boundary layer and combining with the work of Banks & Gadd (1963) they developed the correction function for the lift coefficient as presented in Eq. 2.44:

$$c_{l_{rot}} = c_{l_{non_{rot}}}\left(\frac{\partial c_{l_{pot}}}{\partial \alpha}\Delta\alpha\right) \quad 2.44$$

The function is expressed as a shift in the angle of attack as presented in Eq. 2.45:

$$\Delta\alpha = \left[\left(\frac{K\left(\frac{c}{r}\right)}{0.136}\right)^n - 1\right]\left(\alpha_{c_{l_{max}}} - \alpha_{c_{l_0}}\right) \quad 2.45$$

and the separation point is related with the velocity gradient, K through:

$$\left(\frac{c}{r}\right) = 0.1517K^{-1.084} \quad 2.46$$

The authors recommend using a n value within 0.8 and 1.6. The value $n = 1$ proved to give good results throughout different comparisons with experimental data.

2.4.4 - Propeller Momentum Theory with Slipstream Rotation

The major objection to these results has been the failure of the method to account for rotation of the fluid within the slipstream. There appears to be no physical basis for neglecting slipstream rotation. Clearly, torque must be applied to turn the propeller and that torque must result in rotation of the fluid within the slipstream. Because some of the power supplied to the propeller must go to support this rotation, the propulsive efficiency will be reduced as a result of slipstream rotation. In the following analysis we shall examine the magnitude of this effect.

Phillips (2002) has shown that the solution obtained from the classical propeller momentum theory (see Eq. 2.47 and Eq. 2.48) does not satisfy the angular momentum equation. In dimensionless form, the induced velocity from the momentum theory can be written as:

$$\frac{V_i}{(\omega/2\pi)\,2R_{tip}} = \sqrt{\frac{J^2}{4} + \frac{2C_t}{\pi}} - \frac{J}{2} \qquad 2.47$$

with C_t as defined in Eq. 2.21 and J as defined in Eq. 2.23. Following the momentum theory analysis, the propulsive efficiency for the propeller was then defined as:

$$\eta = \frac{TV_\infty}{Q\omega} = \left(\frac{1}{2} + \sqrt{\frac{1}{4} + 2C_t/\pi J^2}\right)^{-1} \qquad 2.48$$

The author (Phillips, 2002) presented the formulae to obtain a new induced velocity (see Eq. 2.49) and the respective propeller efficiency (see Eq. 2.50) considering the slipstream rotation.

$$\frac{V_i}{(\omega/2\pi)\,2R_{tip}} = \sqrt{\frac{J^2}{4} + \frac{\pi^2}{4}\left(1 - \sqrt{1 - \frac{16\,C_t}{\pi^3}}\right)} - \frac{J}{2} \qquad 2.49$$

$$\eta = \frac{TV_\infty}{Q\omega} = \left[\frac{1}{2} + \sqrt{\frac{1}{4} + \frac{\pi^2}{4J^2}\left(1 - \sqrt{1 - 16\frac{C_t}{\pi^3}}\right)}\right]^{-1} - \frac{J^2}{2}\left[\sqrt{1 + \frac{\pi^2}{J^2}\left(1 - \sqrt{1 - \frac{16\,C_t}{\pi^3}}\right)} - 1\right] \qquad 2.50$$

Phillips (2002) showed that the slipstream rotation increases the induced velocity and decreases the propulsive efficiency. The author states that the major difference between the induced velocity predicted from momentum theory and that predicted from vortex theory is that momentum theory predicts a zero circumferential component of induced velocity on the

upstream side of the propeller while the vortex theory accounts for that circumferential component of induced velocity.

2.4.5 - Propeller Inverse Design Methodology

In 1994, Adkins & Liebeck (1994) developed a new design methodology in which the momentum equations needed to be equivalent to the circulation equations. Thus, the induction factors can be related to the displacement velocity ratio, ζ, according to Eq.2.51 and Eq. 2.52:

$$a_a = \frac{\zeta}{2}\cos^2\phi\ (1 - \varepsilon\tan\phi) \tag{2.51}$$

$$a_t = \frac{\zeta}{2x}\sin\phi\ \cos\phi\left(1 + \frac{\varepsilon}{\tan\phi}\right) \tag{2.52}$$

Analyzing Eq. 2.51 and Eq. 2.52 together with the geometry of Figure 2.3 the relation presented in Eq. 2.53 can be obtained:

$$\tan\phi = \frac{\left(1 + \frac{\zeta}{2}\right)}{x} \tag{2.53}$$

If the condition $r\tan\phi = const.$ (Betz & Prandtl, 1919) needs to be satisfied, Eq. 2.53 proves that ζ must be a constant independent of the radius, for a propeller shed vortex to be a minimum induced loss regular screw surface.

To each new propeller design it is necessary to provide the needed thrust or shaft power. The non-dimensional thrust and power coefficients for design purposes are:

$$T_c = \frac{2T}{\rho V^2 \pi R^2} \tag{2.54}$$

$$P_c = \frac{2P}{\rho V^3 \pi R^2} = \frac{2Q\Omega}{\rho V^3 \pi R^2} \tag{2.55}$$

which, when applied to the Thrust and Power per unit of radius result in Eq. 2.56 and Eq. 2.57:

$$T_c' = I_1'\,\zeta - I_2'\,\zeta^2 \tag{2.56}$$

$$P_c' = J_1'\,\zeta + J_2'\,\zeta^2 \tag{2.57}$$

where:

$$I_1' = 4\xi G(1 - \varepsilon\tan\phi) \tag{2.58}$$

$$I_2' = \lambda\left(\frac{I_1'}{2\xi}\right)\left(1 + \frac{\varepsilon}{\tan\phi}\right)\sin\phi\cos\phi \tag{2.59}$$

$$J_1' = 4\xi G\left(1 + \frac{\varepsilon}{\tan\phi}\right) \quad 2.60$$

$$J_2' = \left(\frac{J_1'}{2}\right)(1 - \varepsilon\tan\phi)\cos^2\phi \quad 2.61$$

Since ζ is constant for an optimum design, a required thrust results in the following constraints at Eq. 2.62:

$$\zeta = \left(\frac{I_1}{2I_2}\right) - \sqrt{\left(\frac{I_1}{2I_2}\right)^2 - \frac{T_c}{I_2}} \quad 2.62$$

$$P_c = J_1\zeta + J_2\zeta^2 \quad 2.63$$

On the other hand, if the power is specified along the design process, the constraints result as in Eq. 2.64:

$$\zeta = -\left(\frac{J_1}{2J_2}\right) - \sqrt{\left(\frac{I_1}{2I_2}\right)^2 - \frac{T_c}{I_2}} \quad 2.64$$

$$T_c = I_1\zeta - I_1\zeta^2 \quad 2.65$$

To obtain the blade geometry, each element, dr, is considered to have a known position, a given chord and a local lift coefficient. Thus, the lift per unit radius of one blade can be calculated according to:

$$\frac{\rho W^2 c C_L}{2} = \rho W\Gamma \quad 2.66$$

where Γ is given by Eq. 2.67:

$$\Gamma = \frac{2\pi V^2\zeta F\cos\phi\sin\phi}{B\Omega} \quad 2.67$$

Simplifying, it results in:

$$Wc = \frac{4\pi\lambda GVR\zeta}{C_L B} \quad 2.68$$

Assuming that ζ is known, the local value of the ϕ is also known from Eq. 2.53 and Eq. 2.68, becoming a function of the local lift coefficient only.

The Reynolds number is calculated according to Eq. 2.69:

$$Re = \frac{Wc}{\nu} \quad 2.69$$

The selection of a lift coefficient from the airfoil data, allows the determination of the drag-to-lift ratio and the total velocity can be calculated as presented in Eq.2.70:

$$W = \frac{V(1 + a_a)}{\sin \phi} \tag{2.70}$$

where a_a is given by Eq. 2.51.

Even considering only one C_L the blade geometry can be determined. Since α is known from airfoil data, the blade element incidence with respect to the disc can be calculated as in Eq. 2.71:

$$\theta = \alpha + \phi \tag{2.71}$$

This design methodology also takes into account the tip losses according to Prandtl's formulation. The formulation of the Prandtl tip losses (see Eq. 2.30 and Eq. 2.31) according to the inverse design methodology is described in Eq. 2.72:

$$f = \frac{B}{2} \frac{1 - \xi}{\sin \phi_t} \tag{2.72}$$

where:

$$\tan \phi_t = \lambda \left(1 + \frac{\zeta}{2}\right) \tag{2.73}$$

The inflow angle is calculated using ζ and the tip's inflow angle, as presented in Eq. 2.74:

$$\tan \phi = \frac{\tan \phi_t}{\xi} \tag{2.74}$$

Eq. 2.74 represents the condition in which the vortex sheet in the wake is nothing more but a rigid screw surface ($r \tan \phi = const.$). The inverse design methodology is summarized in Figure 2.4.

2.5 - Forces acting on a Propeller

When a propeller is subjected to the rotation, the interaction between the flow and the blades, and the blades' mass inertial forces, causes loads and strains. Thus, twisting and bending forces appear throughout the propeller blades (AC65-12A, 1976; Curtiss-Wright, 1944). These forces and their location along the blade can be calculated with Blade Element Momentum theory presented above and the magnitude and location of the forces can then be used to calculate the blade deformations.

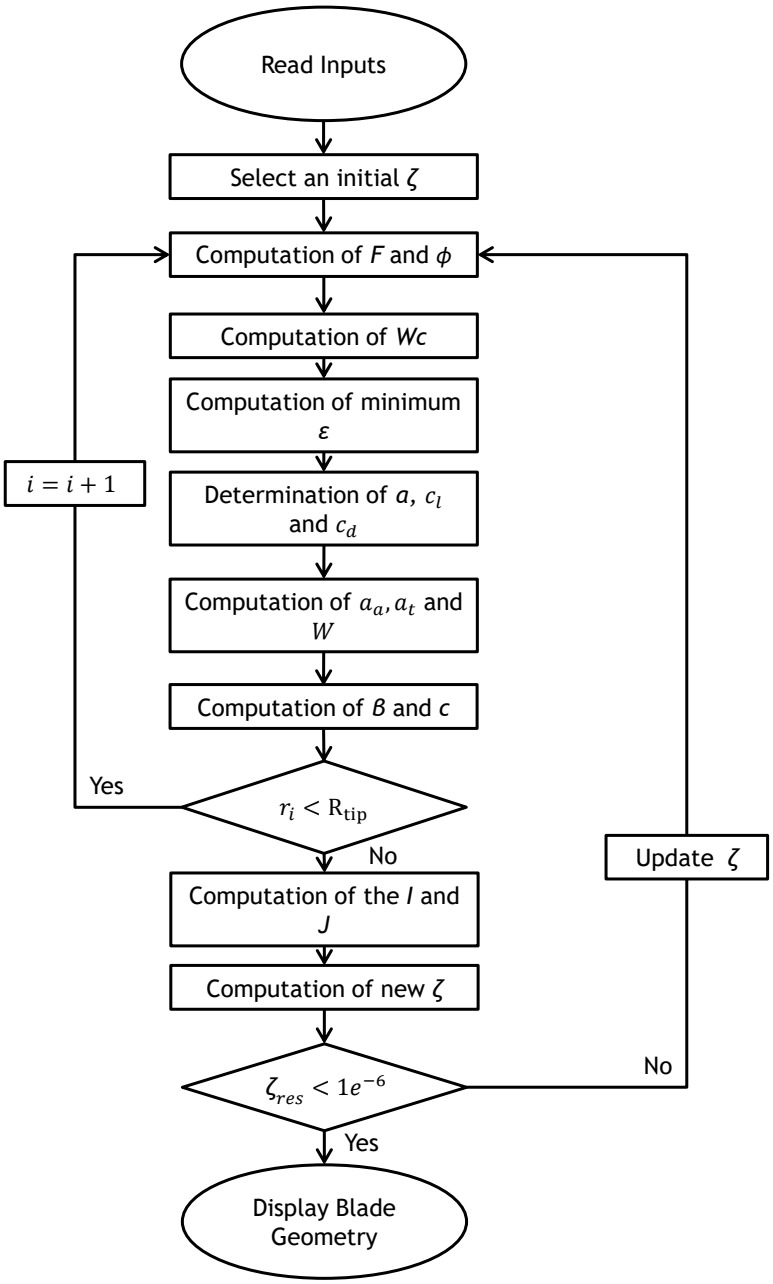

Figure 2.4 - Flowchart of inverse design procedure in JBLADE.

During the rotational motion, the centrifugal force acts from the hub to the tip of the blade, tending to pull the blades from the hub (see Figure 2.5 (a)). The greater the propeller rotational speed, the greater the centrifugal forces will be. The thrust bending force (see Figure 2.5 (b)) attempts to bend the propeller blades forward at the tips, because the lift toward the tip of the blade flexes the thin blade sections forward. The torque bending forces, as presented in Figure 2.5 (a) try to bend the propeller blade back in the opposite direction at which the propeller is rotating.

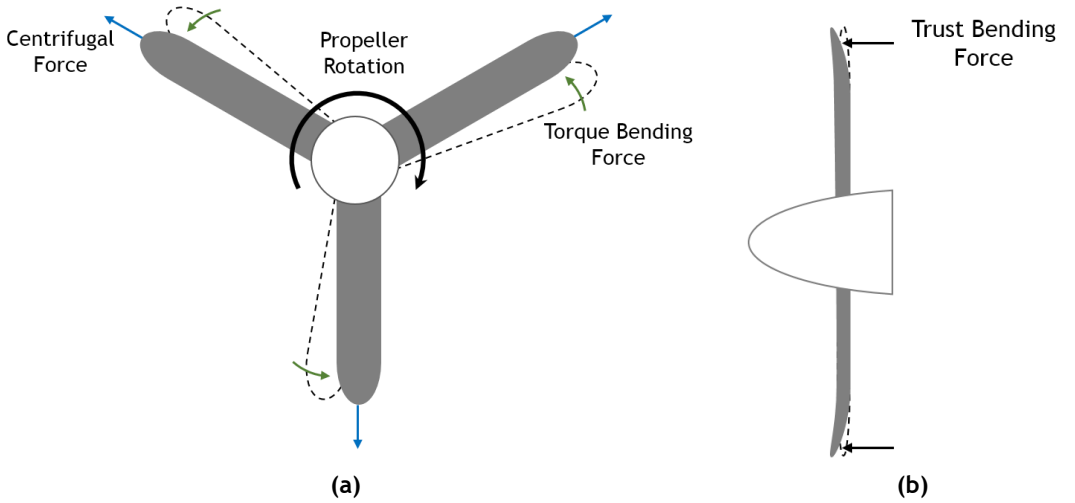

Figure 2.5 - (a) Illustration of propeller torque bending force and propeller centrifugal force. Reproduced from *Mechanics Powerplant Handbook* (1976) (b) Illustration of propeller trust bending force.

Besides the bending and centrifugal forces mentioned above, the propellers' blades are also subjected to aerodynamic and centrifugal twisting moments (AC65-12A, 1976; Curtiss-Wright, 1944).

2.5.1 - Volume and Blade Mass Estimation

The estimation of the blade mass was implemented and its validation is presented in this section. To calculate the volume of the blade, an integration along each station of the airfoil is performed. For the completely solid structure and for the case of the skin thickness concepts the volume of the blade is calculated as:

$$V_{Blade} = \sum_{i=1}^{n} \frac{A_i + A_{i+1}}{2} \Delta r \qquad 2.75$$

If the blade is solid, the mass of the blade is calculated as:

$$M_{blade} = V_{Blade} \rho_{mat} \qquad 2.76$$

In the case of the skin thickness the mass is calculated as:

$$M_{blade} = V_{Skin} \rho_{mat} \qquad 2.77$$

where:

$$V_{Skin} = \sum_{i=1}^{n} \frac{\left(A_{ext_i} - A_{int_i}\right) + \left(A_{ext_{i+1}} - A_{int_{i+1}}\right)}{2} \Delta r \qquad 2.78$$

If the blade concept contains a skin and an additional core material, the blade volume is calculated as:

$$V_{Blade} = V_{Blade_{Skin}} + V_{Blade_{Core}} \quad (2.79)$$

where

$$V_{Blade_{Skin}} = \sum_{i=1}^{n} \frac{\left(A_{ext_i} - A_{int_i}\right) + \left(A_{ext_{i+1}} - A_{int_{i+1}}\right)}{2} \Delta r \quad (2.80)$$

and

$$V_{Blade_{Core}} = \sum_{i=1}^{n} \frac{A_{core_i} + A_{core_{i+1}}}{2} \Delta r \quad (2.81)$$

To calculate the blade mass it is just needed to simply multiply the volume by the density of the desired material. For the cases where the blade is solid or just have a skin, the blade mass is calculated as:

$$M_{Blade} = V_{Blade}\rho_{mat} \quad (2.82)$$

If the third concept is chosen, then the blade mass is calculated as:

$$M_{Blade} = V_{Blade_{skin}}\rho_{mat_{skin}} + V_{Blade_{core}}\rho_{mat_{core}} \quad (2.83)$$

2.5.2 - Blade Bending Estimation

To calculate the blade's tip displacement due to the normal force produced in the propeller's operation, it was necessary firstly to calculate the inertia modulus of each airfoil section. The second moments of area were obtained according:

$$I_{xx} = \int_A y^2 \, dA \quad (2.84)$$

$$I_{yy} = \int_A x^2 \, dA \quad (2.85)$$

In order to simplify the simulations, it was considered a simple cantilevered beam (see Figure 2.6), with the constraint located at the root and the forces applied at 25% of the chord, in order to produce a pure bending moment.

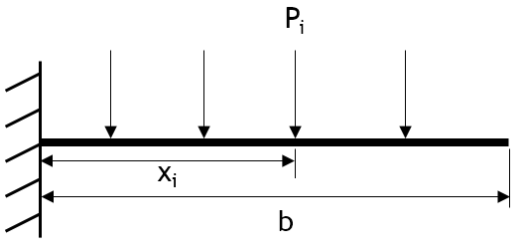

Figure 2.6 – Scheme of a cantilevered beam with a group of arbitrary positioned loads.

In order to calculate the angle and the displacement at each element of the blade, it is necessary to determine the bending moment at each element. The bending moment was calculated according to Eq. 2.86 :

$$M_{(x)} = M_0 - \sum_{i=1}^{n(x)} P_i \, x_i \qquad 2.86$$

Then, the angle and the displacement at each element of the blade were calculated according to Eq. 2.87 and Eq. 2.88, respectively.

$$\theta_i = \theta_{i-1} - \frac{M_{(x)}}{EI_{(x)}} \Delta x \qquad 2.87$$

$$\delta_i = \delta_{i-1} + \theta_{i-1}\Delta x - \frac{M_{(x)}}{2EI_{(x)}} \Delta x^2 \qquad 2.88$$

In the cases that the blades are composed with more than one material, like the case "Skin + Core Material", the equivalent bending stifness is determined according to:

$$EI_{(x)} = E_1 I_{1_{(x)}} + E_2 I_{2_{(x)}} \qquad 2.89$$

2.5.3 - Blade Twist Deformation

To calculate the twist deformation during propeller operation, the concept illustrated in Figure 2.7 was used. The twisting moment *T*, was calculated according to the next steps:

- The angle of attack at each blade section was computed, in JBLADE's aerodynamic sub-module.
- The airfoil's pressure centre location computed during XFOIL calculations was used and the distance between this pressure centre and the section's 25% chord was determined.
- The Moment is calculated by multiplying the Force previously computed in JBLADE aerodynamic sub-module and the distance calculated above.

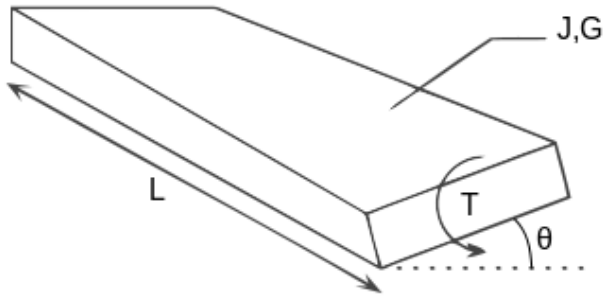

Figure 2.7 – Illustration of a beam subjected to a twisting moment.

The torsion angle can be calculated according to Eq. 2.90:

$$\theta_i = \theta_{i-1} + \frac{T\,\Delta x}{JG} \tag{2.90}$$

where according to Young *et al.* (2002) J can be defined as:

$$J_s = \frac{4I_{xx}}{1 + \frac{16I_{xx}}{Ac^2}} \tag{2.91}$$

2.6 - Present Research Contributions to Propeller Aerodynamics Modelling

2.6.1 - New 3D Flow Equilibrium Model

The theoretical formulation presented in Section 2.5.3 assumes that the flow in the propeller annulus is two-dimensional, meaning that radial movement of the flow is neglected. However, for such condition, three-dimensional equilibrium must exist as discussed in Section 2.5.4 for the Momentum Theory. Furthermore, the classical Blade Element Momentum formulation assumes that neighbouring blade elements induced velocities are independent, which lacks physical reasoning (Wald, 2006). In JBLADE (see Figure 2.3) this issue is addressed by a new model based on 3D flow equilibrium, as presented by Saravanamuttoo *et al.* (1996) considering that before the propeller disk, the enthalpy is radially uniform across the flow and the entropy gradient is null as well:

$$W_a \frac{\partial W_a}{\partial r} + W_t \frac{\partial V_t}{\partial r} + \frac{W_t^2}{r} = 0 \tag{2.92}$$

where W_a is the axial flow velocity across the disk, V_t is the tangential flow velocity in the disk and r is the radial position in the disk.

The case where W_a is maintained constant across the propeller annulus, reduces Eq. 2.92 to Eq. 2.93:

$$\frac{dW_t}{dr} = -\frac{W_t}{r} \leftrightarrow W_t r = const. \tag{2.93}$$

In this case, the whirl varies inversely with radius, which is best known as the free vortex condition. Although this differs substantially from the ordinary BEM approach, where the momentum theory applied to the tangential velocity induction totally disregards the neighbour elements to determine the element's V_t, it makes sense when one considers that from far upstream down to the propeller disk, the flow should be isentropic or close to irrotational, thus

respecting the free vortex condition. To implement this equilibrium condition, in the first iteration the forces coefficients are computed assuming no tangential induction factor, which means that $a_t = 0$. The mass flow rate at an arbitrary annulus element *i* and total mass flow rate are calculated as presented in Eq. 2.94 and Eq. 2.95 respectively.

$$\dot{m}_i = 2\rho W_a \pi r dr \tag{2.94}$$

$$\dot{m}_{total} = \int_{R_{hub}}^{R} \dot{m}_i \tag{2.95}$$

To satisfy the momentum conservation, the total propeller torque will be the result of a free vortex induced tangential velocity profile with an average axial velocity, $\overline{W_a}$ across the propeller disk. A reference value of tangential induced velocity is used that corresponds to that at 75% of the blade radius, $V_{t_{75}}$. The average axial velocity is calculated according to:

$$\bar{W}_a = \frac{\dot{m}_{total}}{\pi \rho R^2} \tag{2.96}$$

At a given element V_t is calculated as:

$$V_t = \frac{0.75R\, V_{t_{75}}}{r} \tag{2.97}$$

The total torque of the blade can be calculated as presented in Eq. 2.98:

$$Q = \int 4\pi\rho \bar{W}_a V_t r dr \tag{2.98}$$

Thus, replacing Eq. 2.96 and Eq.2.97 in Eq.2.98 and solving for $V_{t_{75}}$, we get Eq. 2.99:

$$V_{t_{75}} = \frac{2}{3} \frac{Q}{\pi\rho \bar{W}_a R(R^2 - R_{hub}^2)} \tag{2.99}$$

The tangential induction factor can be updated and the coefficients will be calculated again with the updated tangential induction factor.

$$a_t = \frac{V_t}{\Omega r} \tag{2.100}$$

2.6.2 - New Methods for CD_{90} Prediction

Sometimes, the data required for rotary wing performance estimation codes need to be extrapolated from the available wind tunnel data (Worasinchai et al., 2011). In addition, during the extrapolation process one of the aspects with major weight, as referred by Montgomerie (1996), is the airfoil drag coefficient at an angle of attack of 90 degrees. The developments to

predict the drag coefficient at 90 degrees began with Gault (1957), who presented the low speed stalling characteristics of airfoils and correlated them with a single specific upper thickness coordinate located at $x/c = 0.0125$. The results presented by Gault are restricted to airfoils without high-lift devices and to airfoils with aerodynamically smooth surfaces, and he considered also the Reynolds number influence on airfoils stalling characteristics.

Later, in 1995, Montgomerie (1996, 2004) presented two different methods to predict the value of the drag coefficient and its distribution along a wind turbine blade. The first method considers a constant drag coefficient distribution along the entire blade and represents the most widely used method by wind turbine manufacturers. The second method consists of a curvilinear distribution of drag coefficient at 90 degrees.

In 2000, Lindenburg (2000) presented an empirical relation to calculate $C_{D_{90}}$ based in a similar approach used by Montgomerie. To make valid the assumption that the airfoil acts as a flat plate in the 90 degrees angle of attack condition, Lindenburg assumed that the flow on one side of the airfoil is fully separated. Recently, Timmer (2010) presented a correlation to predict the value of drag coefficient at 90 degrees based on Gault's approach. He correlated the same airfoil coordinate, $(y/c)_{x/c=0.0125}$, with experimentally measured drag coefficients at 90 degrees and presented a linear correlation for drag coefficient prediction at 90 degrees. Initially, the method described by Montgomerie (2004) was used in JBLADE, but it was found that different extrapolated 360 degrees polars will lead to significant differences on final predicted power and thrust forces (see Figure 3.21) for the same propeller.

2.6.2.1 Airfoil Leading Edge Radius Method

In this new proposed method, CD_{90} is correlated with the airfoil leading-edge radius. The leading-edge radius of an arbitrary airfoil was calculated using an approximation by the least-square method on its set of contour coordinates. For a NACA four-digit-series airfoil, it is possible to calculate the leading-edge radius through:

$$R_{LE} = 1.109\, t^2 \qquad 2.101$$

The leading-edge radius was calculated for different NACA airfoils, and the results are presented in Table 2.1.

Table 2.1 - Leading edge radius calculations and errors due to the least square method approximation

Airfoil Name	LE Radius w/ Eq. 2.101	LE Radius w/ Least Square Method	Error, %
NACA 0012	0.01597	0.01596	0.06
NACA 0015	0.02495	0.02472	0.93
NACA 0018	0.03593	0.03525	1.93
NACA 4409	0.00898	0.00933	3.75
NACA 4412	0.01597	0.01629	1.96
NACA 4415	0.02495	0.02511	0.64
NACA 4418	0.03593	0.03597	0.11

The greatest difference occurs for an airfoil with 9% thickness, and it is 3.75%, which is a reasonably low value. The drag coefficient at 90 degrees of specific airfoils was then calculated (see Table 2.2) and plotted against their experimentally measured values of drag coefficient at 90 degrees, as presented in Figure 2.8. The linear correlation that was found to fit the data is:

$$C_{D_{90}} = 2.0772 - 3.978\, LE_{Radius} \qquad 2.102$$

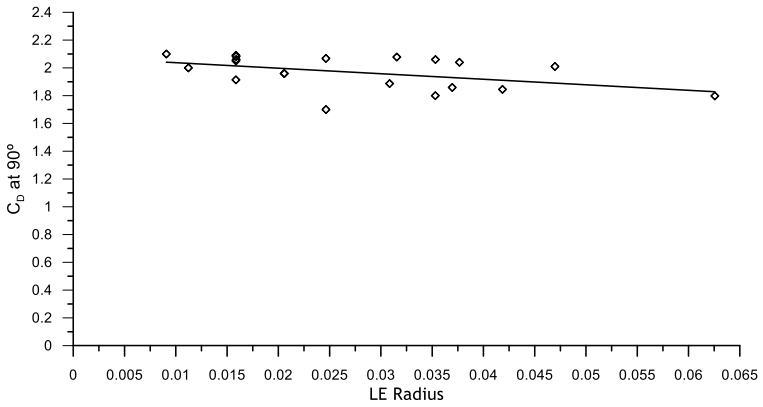

Figure 2.8 - Measured airfoil drag coefficient at 90 degrees AoA *vs* airfoil leading edge radius. The airfoil data correspond to those of Table 2.2.

2.6.2.2 Airfoil $\left(\frac{y}{c}\right)$ at $\frac{x}{c} = \mathbf{0.0125}$ Method

An improvement to the fitting previously presented by Timmer (2010) was also implemented. The airfoil y coordinate at *x/c = 0.0125* for more airfoils (see Table 2.2) was calculated and airfoils were added to the originally considered database. The comparison between new and original correlations can be observed at Figure 2.9. This new correlation was also implemented in the JBLADE software providing a second option for the calculation of $C_{D_{90}}$.

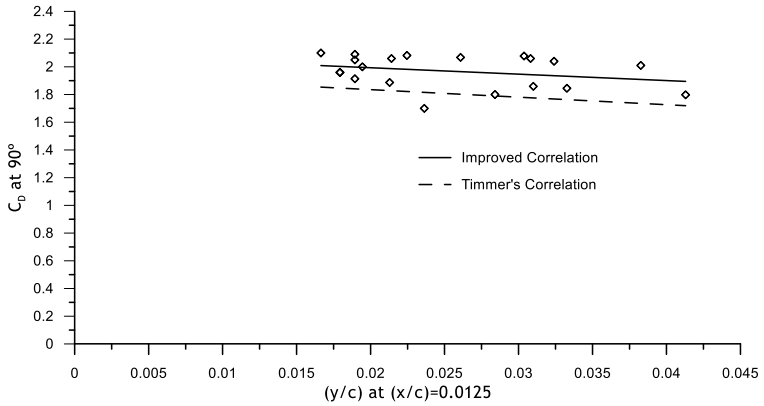

Figure 2.9 - Comparison between original correlation, described by Timmer (2010) and improved correlation. The airfoil data correspond to those of Table 2.2.

The new correlation obtained with the y coordinate at $x/c = 0.0125$ is given by:

$$C_{D_{90}} = 2.086 - 4.6313 \left(\frac{y}{c}\right)_{\left(\frac{x}{c}=0.0125\right)} \qquad 2.103$$

Table 2.2 – Drag coefficient at 90 degrees measured and calculated by the two developed methods for a set of airfoils.

Airfoil Name	Reference	Measured CD 90	Calculated CD90 w/ LE_{Radius}	Calculated CD90 w/ $y/c_{\left(\frac{x}{c}\right)=0.0125}$
DU 91-W2-250	(Timmer, 2010)	1.859	1.9302	1.9424
DU-97-W-300	(Timmer, 2010)	1.845	1.9107	1.9319
FX 84-W-127	(Massini *et al.*, 1988)	2.000	2.0325	1.9959
FX 84-W-218	(Massini *et al.*, 1988)	2.040	1.9274	1.9359
LS-417	(Timmer, 2010)	1.887	1.9545	1.9874
LS-421-MOD	(Massini *et al.*, 1988)	2.010	1.8903	1.9088
NACA 0012 (1)	(Lindenburg, 2000)	2.090	2.0141	1.9983
NACA 0012 (2)	(Massini *et al.*, 1988)	2.050	2.0141	1.9983
NACA 0012 (3)	(Timmer, 2010)	1.914	2.0141	1.9983
NACA 0015	(Miley, 1982)	1.700	1.9779	1.9766
NACA 0018	(Timmer, 2010)	1.800	1.9368	1.9544
NACA 4409	(Ostowari & Naik, 1984)	2.100	2.0411	2.0089
NACA 4412	(Ostowari & Naik, 1984)	2.060	2.0140	1.9868
NACA 4415	(Ostowari & Naik, 1984)	2.068	1.9792	1.9652
NACA 4418	(Ostowari & Naik, 1984)	2.060	1.9367	1.9433
NACA 23012	(Massini *et al.*, 1988)	2.082	2.0140	1.9820
NACA 23017	(Massini *et al.*, 1988)	2.078	1.9517	1.9453
NACA 23024	(Lindenburg, 2000)	1.798	1.8283	1.8948
NACA 63-215	(Lindenburg, 2000)	1.959	1.9954	2.0030

This page has been intentionally left blank
for double side copying

Chapter 3

JBLADE Software Development

JBLADE is a numerical open-source propeller design and analysis software written in the C++/QML programming language, compiled with Qt® toolkit (Digia, 2014). The code is based on QBLADE (Marten & Wendler, 2013; Marten et al., 2013) and XFLR5 (Deperrois, 2011) codes. It uses the classical Blade Element Momentum (BEM) theory modified to account for 3D flow equilibrium. The airfoil performance figures needed for the blades simulation come from the XFOIL (Drela, 1989) sub-module. This integration, allows the fast design of custom airfoils and computation of their lift and drag polars. The software can estimate the performance curves of a given propeller for off-design analysis. It has a graphical user interface (GUI) making easier the task of designing the propeller and analysing the simulations. The long term goal of JBLADE is to provide a user-friendly, accurate, and validated open-source code that can be used to design and optimize propellers for a large spectrum of applications.

3.1 - Software Overview

Figure 3.1 shows the JBLADE software structure with the different sub-modules and their iteration routines in which the airfoil polars, blades, propellers and simulations are defined, executed and stored. Furthermore, it can be seen how the BEM module is coupled with the *XFOIL sub-module*. JBLADE software allows a direct visualization of simulation results through a GUI making the software accessible and easy to understand by willing users. In addition, the coupling between different JBLADE modules avoids time consuming operations of importing/exporting data, decreasing possible mistakes created by the user. The simulation starts by importing the blade's sections airfoils coordinates into the *XFOIL sub-module*. A direct analysis for each airfoil performance over the largest possible angle of attack range is performed. These XFOIL airfoil performance polars are used in the 360º Polar Object, where a full 360º range of angle of attack airfoil polar for each blade section airfoil is built. Each 360º polar is defined by its name and parent XFOIL polar. After at least one 360º Polar is stored in

the *360º Polar Object database sub-module*, a blade can be defined in the *Blade object sub-module*. This sub-module stores the blade's geometric data as well as which 360º polar is associated to each of the blade sections previously defined in the Blade Object. After the creation of the blade, a propeller can be defined in the *Propeller Object sub-module*. This sub-module is used to store the propeller data as well as the simulation parameters associated to each propeller. The simulation results, which characterize the propeller performance are obtained in the *BEM simulation sub-module* and stored in the *Blade Data Object sub-module* for each element along the blade and added to the Propeller Simulation Object database.

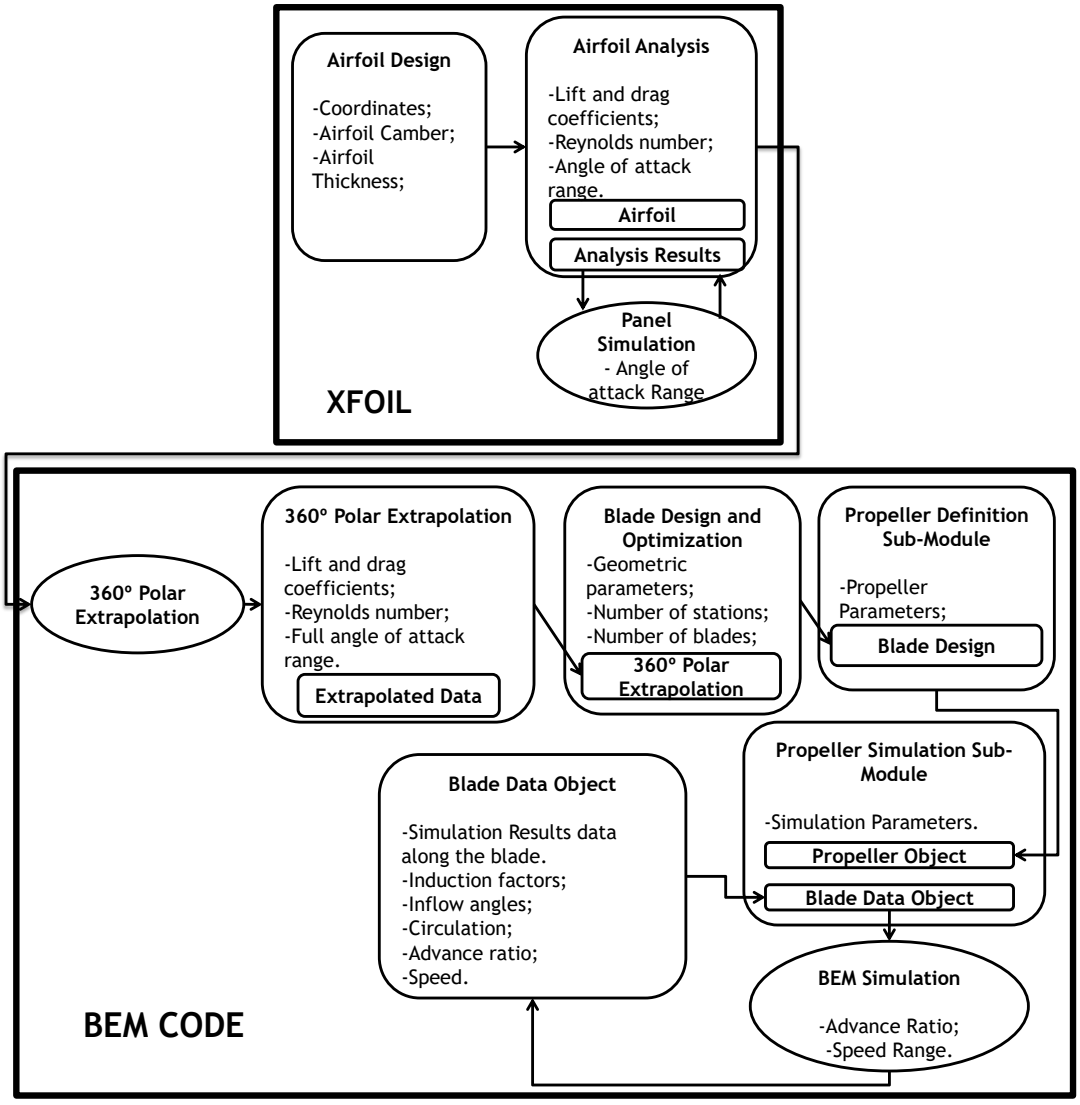

Figure 3.1 - JBLADE software structure representing the internal sub-modules interaction.

3.1.1 - Airfoil design and analysis

To perform a new propeller design or performance analysis it is necessary to import the needed airfoils that will be used along the blades sections. Subsequently, the performance of the airfoils should be computed over the largest angle of attack range. The XFOIL (Drela, 1989)

code is used to compute and analyse the flow around the airfoils. The XFOIL most relevant features for JBLADE are the inviscid/viscous analysis of an airfoil with forced or free transition. In addition, the XFOIL capacity to calculate transitional separation bubbles and predict the airfoil performance just beyond the stall make the code helpful and useful in JBLADE (Drela, 1988). In order to obtain accurate results with JBLADE software, it is essential that the correct Reynolds and Mach numbers are defined in the airfoil simulation settings (see Figure 3.2). The achievement of correct Reynolds and Mach numbers along the blade may take some iteration until the propeller analysis process is finished. The *XFOIL sub-module* allows the simulations for a given Reynolds number over an angle of attack (AoA) range and the simulation for a given angle of attack over different Reynolds numbers. In addition, depending on the number of the points of an imported airfoil, a global refinement of the airfoil's panels is needed to ensure good convergence during the airfoil analysis. Furthermore, the *XFOIL sub-module* allows direct modifications of the airfoils by changing the airfoil thickness and its position as well as airfoil camber and its position. Regarding the inverse design capabilities of this sub-module, it maintains all the functionalities originally developed for XFLR5 (Deperrois, 2011). Each time that one of the previous mentioned parameters is modified a new airfoil will be generated.

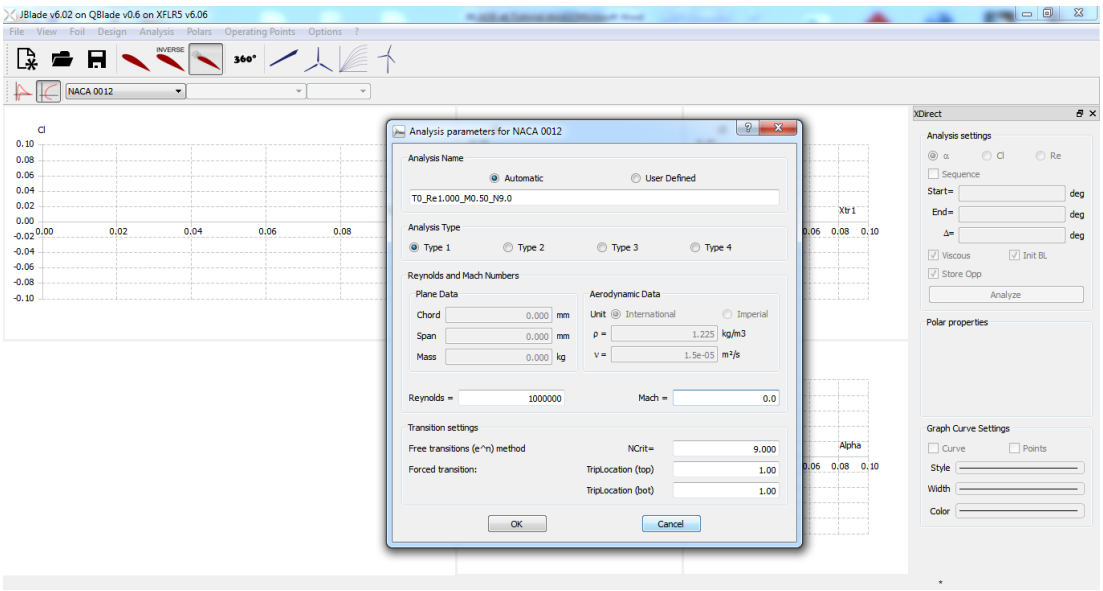

Figure 3.2 - XFOIL sub-module in JBLADE.

Figure 3.2 shows the settings that user needs to define in a typical airfoil simulation in JBLADE. The data obtained in this *XFOIL sub-module* will be used in the *360º Polar Extrapolation sub-module*, where a full 360º range of angle of attack airfoil polar for each blade section airfoil will be built.

3.1.2 - 360º AoA Polar extrapolation

Since the propeller blade sections can achieve high angles of attack during their operation, the available airfoil performance data need to be extrapolated to become available for the full

360º of angle of attack. In this sub-module the previously calculated data for each airfoil is extended to the full range of angle of attack (see Figure 3.3). As shown in Section 3.2.3 different values of drag coefficient at 90º of angle of attack may lead to different extrapolated airfoil polars, which in turn, will lead to different propeller performance prediction. Originally, the method described by Montgomerie (2004) was used in JBLADE, but, later, the methods described in Section 2.4.2 were integrated. These methods proved to improve the extrapolation process leading to a decrease of the errors introduced by the user. The polars calculated in *XFOIL sub-module* can be selected in the drop-down menu and an extrapolation can be conducted. The Montgomerie's (2004) extrapolation procedure uses a blending function to make the transition between the XFOIL prediction curve and the flat plate curve. In this procedure the user can modify the resulting coefficients modifying the sliders present in this sub-module (see Figure 3.3). Additionally, the user should specify the 2D drag coefficient of the airfoil at 90º. The complete extrapolation procedure of airfoils' polar extrapolation is described by Montgomerie (2004). The Viterna & Janetzke (1982) extrapolation procedure consists on empirical equations. In this procedure the user should specify the aspect ratio of the future blade as described in the work of Viterna & Corrigan (1982). In addition, there are 2 more methods available to extrapolate the airfoil polars to 360º of angle of attack. Both LE Radius and Y Coordinate are based in Montgmerie's extrapolation process. In the LE Radius option, the $C_{D_{90}}$ is calculated as described in Section 2.4.2.1 while in the Y Coordinate the airfoil $C_{D_{90}}$ is calculated as presented in Section 2.4.2.2. The polars generated in the *360 Polar Extrapolation sub-module* will be used in the propeller performance calculations. Furthermore, these polars data will be used also to determine the drag-to-lift ratio in the *Inverse Design sub-module*.

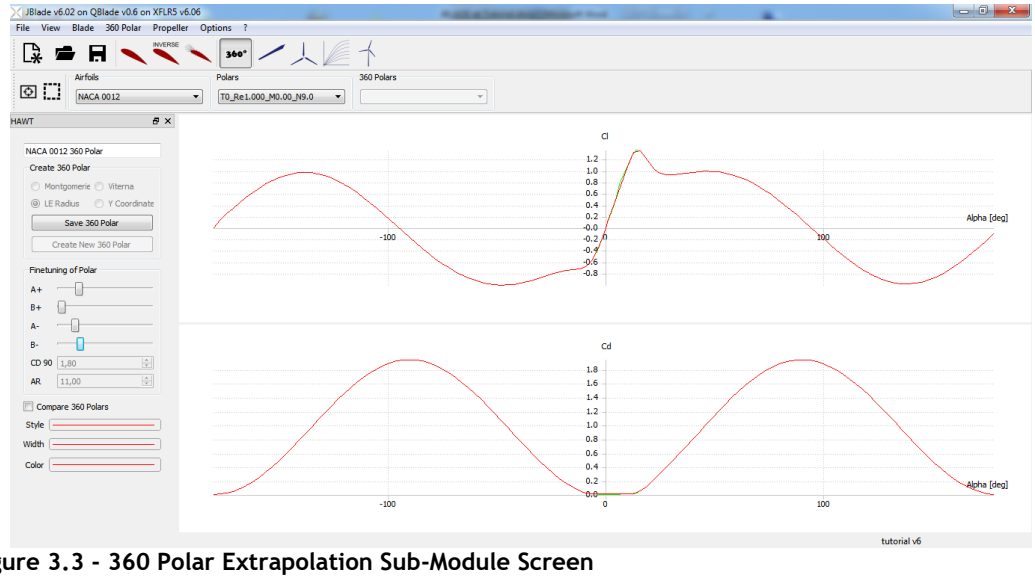

Figure 3.3 - 360 Polar Extrapolation Sub-Module Screen

3.1.3 - Blade definition

The JBLADE software allows the introduction of the blade geometry as an arbitrary number of sections characterized by their radial position, chord, twist, airfoil and airfoil's associated 360 AoA polar. The user should specify the number of blades and the hub radius of the propeller.

The software provides a 3D graphical representation of the blade/propeller to the user (see Figure 3.4), helping the user to identify possible issues, e.g. a conflict between blades at root region if the hub radius is too small for the root section chord. Furthermore, this sub-module allows the blade's geometry exporting to use in a conventional CAD software. Whenever a blade is deleted or overwritten, all associated simulations and propellers are deleted as well.

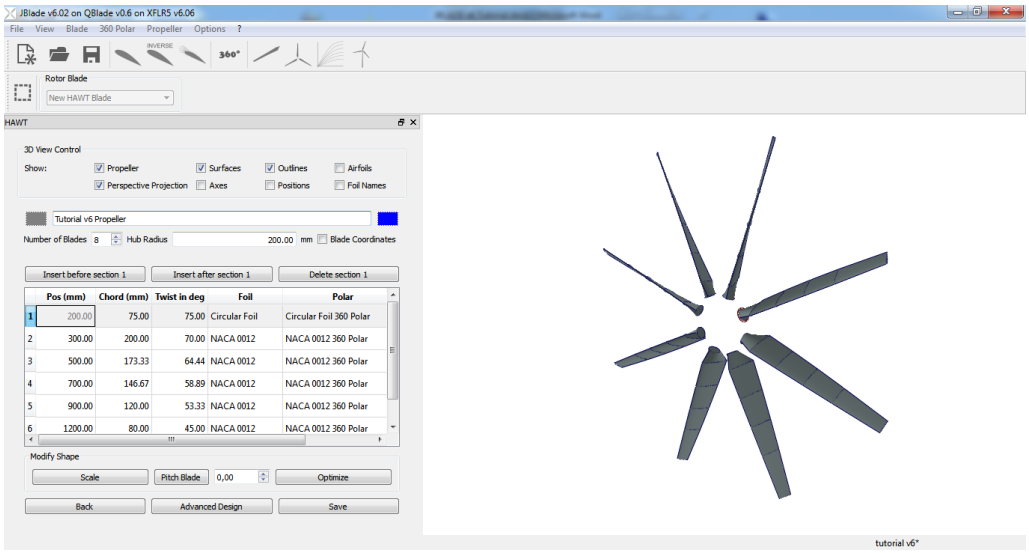

Figure 3.4 - Blade Definition Sub-Module

3.1.3.1 Propeller inverse design

The propeller inverse design methodology was implemented in JBLADE as presented in Section 2.5.5. The user should specify the operating condition of the propeller, namely air density in which the propeller will operate, the free stream speed, the propeller rotational speed and the power (or torque) delivered to the propeller or thrust produced by the propeller.

To use the inverse design tool, the user should previously specify the number of blades, the blade hub radius, the radial position of each station, as well as station's airfoil and its associated polar (see Figure 3.5). After the introduction of these parameters, the inverse design procedure (see Figure 2.4) is applied and the on-design optimal blade geometry is achieved. In addition the user should specify the criteria to minimize the drag-to-lift ratio. There are 3 options available: specify a constant C_L over the blade or specify the airfoil's best $L^{3/2}/D$ or airfoil's best L/D. After the inverse design procedure, the obtained blade can be saved and used normally in the *Simulation sub-module*.

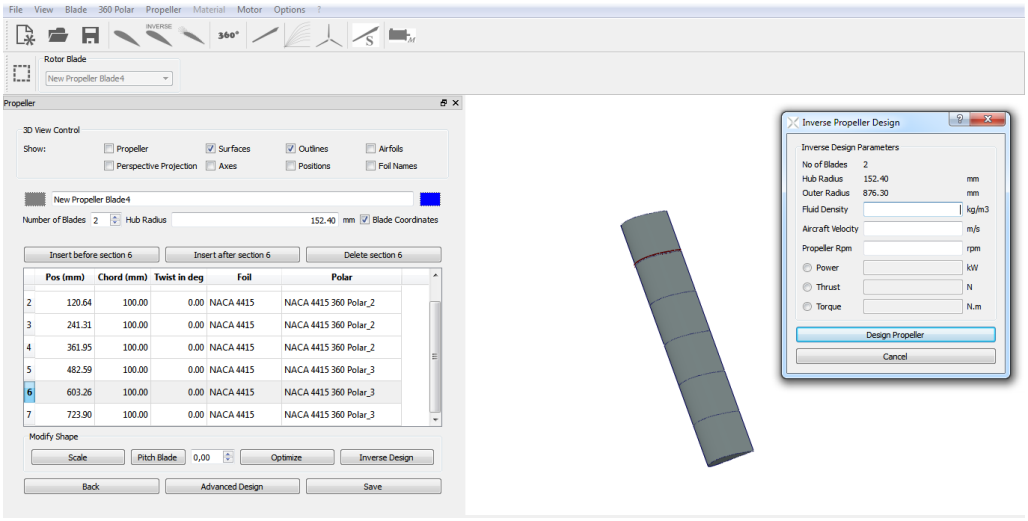

Figure 3.5 - Blade definition/inverse design sub-module in JBLADE.

3.1.4 - Parametric simulation

In the *Parametric Simulation sub-module* the propeller can be simulated using a multi-parameter simulation. This sub-module (see Figure 3.6) allows simulations by defining the interval and incremental values of the propeller operational parameters speed, rotational speed and pitch angle. These variations in different parameters allow performing parametric studies of the propeller. Whenever a simulation is defined, all simulation parameters need to be specified. For analysing the results of the simulations, the four graphs show the simulation results. By double-clicking on a graph, it is possible to change the plotted variables and by right-clicking on a graph, is possible to change the graph type.

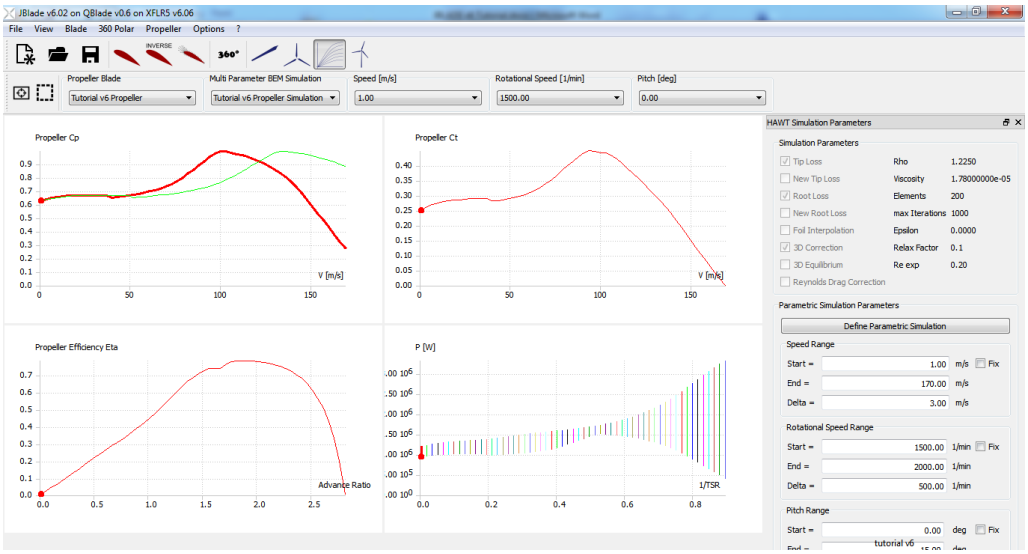

Figure 3.6 - Parametric Simulation Sub-Module in JBLADE.

3.1.5 - Propeller definition and simulation

In the *Propeller Definition and Simulation sub-module* the user can create new propellers composed by the previously defined blades (see Figure 3.7). This sub-module allows simulations within a speed interval, for a fixed rotational speed and fixed pitch angle. To define a new propeller simulation the user should specify the propeller rotational speed and the minimum and maximum free stream speeds to be calculated. Each propeller can have more than one associated simulations. To create and perform the simulation for a given propeller, the user should specify the number of elements along the blade, the convergence criteria, the density and viscosity of the fluid and maximum number of iterations (see Figure 3.9). The propeller performance estimation is then obtained with a BEM simulation routine (see Figure 3.8) and stored in the blade data object (see Figure 3.1) for each element along the blade. Furthermore, the user can improve the accuracy of the simulations using other tools also available in the JBLADE software (see Figure 3.9) such as: Root and Tip Losses (see Section 2.5.3.1), Post Stall Models (see Section 2.5.3.2), Foil Interpolation (see Section 3.1.5.2), 3D Equilibrium (Morgado *et al.*, 2015) (see section 2.4.1) and Reynolds Drag Correction (see Section 3.1.5.6) (Marten *et al.*, 2013).

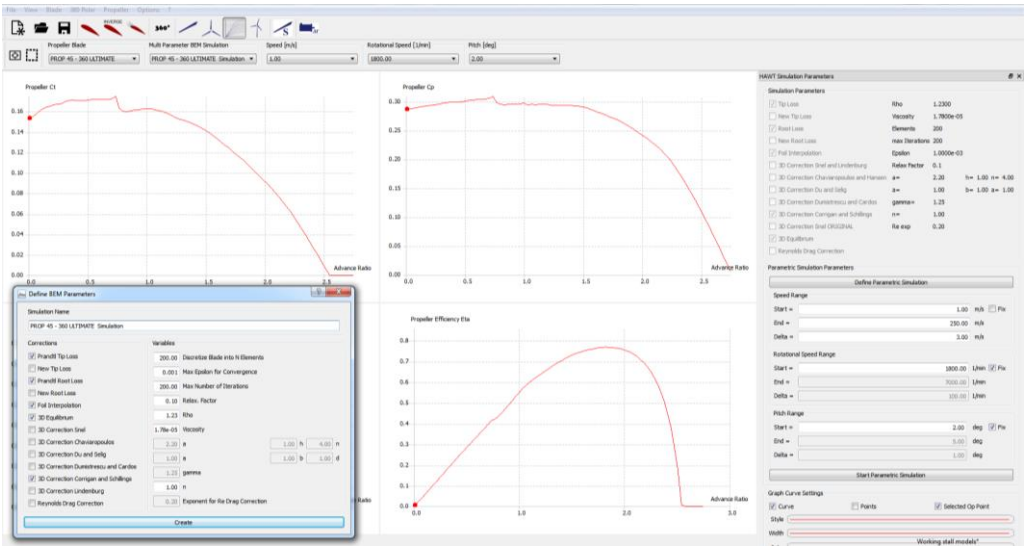

Figure 3.7 – Simulation sub-module overview.

When 3D Equilibrium formulation is enabled the formulation presented in Section 2.4.1 is applied and an initial layer of iteration in which $a_t = 0$ appears. After solving this additional iteration layer, the radial induction factor can be updated and the coefficients will be calculated again with the updated radial induction factor. This sub-module also allows the comparison between different propellers and between different simulations for the same propeller as well.

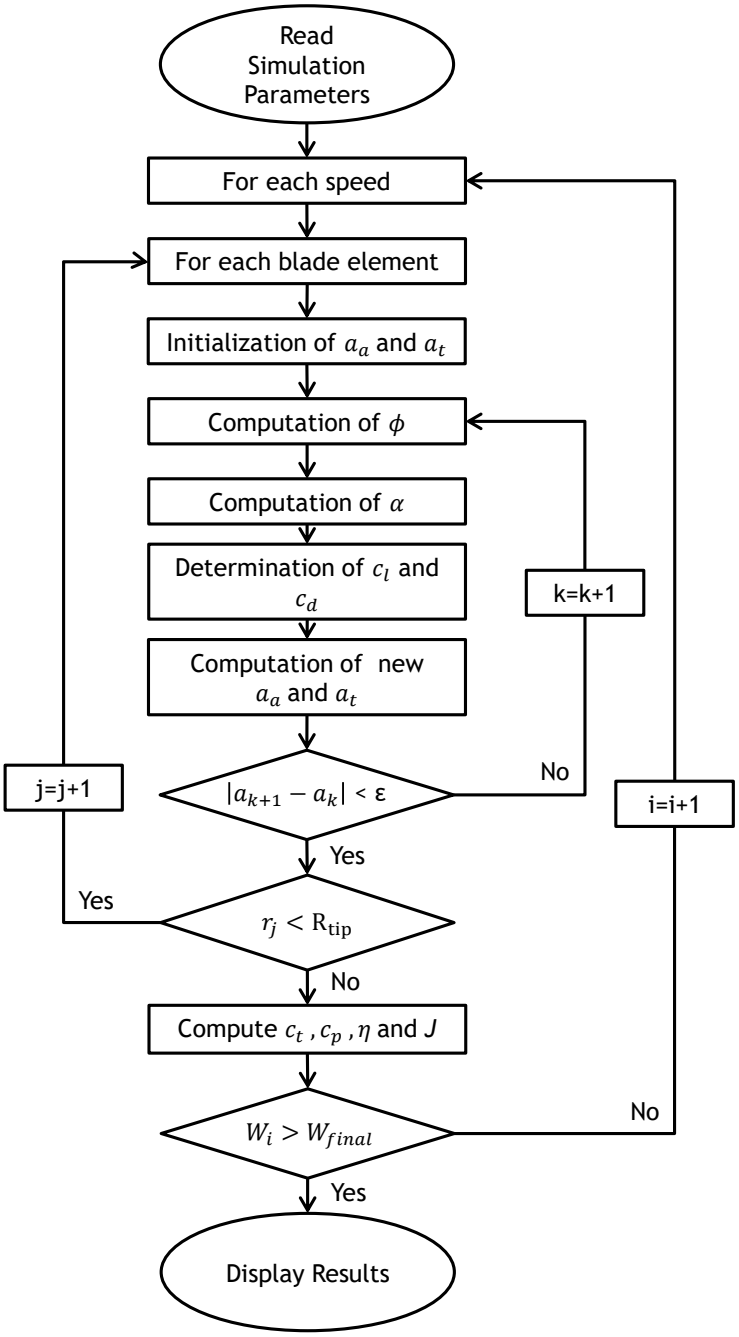

Figure 3.8 - Flowchart of simulation procedure in JBLADE.

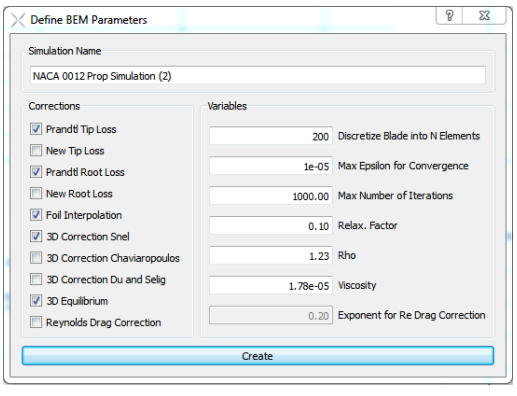

Figure 3.9 - Simulation definition dialog box.

3.1.5.1 Number of blade elements

As mentioned in Section 3.1.3 each blade is composed by an arbitrary number of sections that are introduced by the user. Additionally, the blade is divided in elements, sinusoidally spaced along the blade's span and used to perform BEM calculations. The number of elements represents the divisions that will be used during the simulation procedure and is independent of the blade's sections number (see Figure 3.10). The elements are sinusoidally spaced along the blade, ensuring a smooth change between the elements' parameters all over the blade radius.

When an analysis is being performed, the BEM algorithm is executed once for every element. The input values of chord and twist are interpolated between the blade sections, where they were previously defined, and computed for the centres of each element. All the variables used in the BEM simulation are computed for the centre of each element and are treated as the average values over the element.

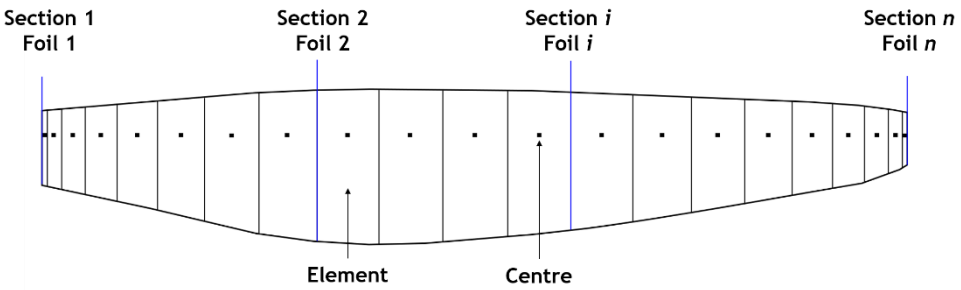

Figure 3.10 – Representation of the sections and the sinusoidal spaced elements along the blade.

3.1.5.2 Foil interpolation

A linear interpolation of the section parameters between the two closest sections with defined airfoils is available. When the Foil Interpolation is selected, the polar data used for the BEM's calculations of each element is a linear interpolation between the polar data of the bounding Sections' airfoils (see Figure 3.10). If the Foil Interpolation is not selected, all blade elements laying between position 1 and 2 are linked to the airfoil polar data from Section 1. Thus, the last airfoil at Section *n*, is not included in the simulation. Furthermore, a discontinuity between the elements may appear, since the airfoil in Section 1 can be different from the airfoil in Section 2 and thus they may have different performances. Although the linear interpolation between two airfoil polars never represents the true behaviour of the intermediate elements, the interpolation represents a better approximation to the real polar on the intermediate elements.

3.1.5.3 Fluid density and viscosity

The fluid density is used to calculate the power and thrust of the propeller, while the dynamic viscosity of the flow is needed to compute the local Reynolds number along the blade according to Eq. 3.1:

$$Re_r = \frac{W_r c_r \rho}{\mu} \tag{3.1}$$

3.1.5.4 Convergence criteria

The convergence criterion ε_{conv} defines when the iteration has converged and it is used to stop the iteration on that element. The convergence is achieved when the difference between actual and last iteration induction factors are smaller than the convergence criterion. The user should specify the value for ε_{conv} that is defined as presented in Eq. 3.2.

$$\max\left(\left|a_a - a_{a_{old}}\right|, \left|a_t - a_{t_{old}}\right|\right) < \varepsilon_{conv} \tag{3.2}$$

3.1.5.5 Relaxation factor

A common problem during the iteration loop of a BEM computation is the fluctuating behaviour of the axial induction factor (Marten & Wendler, 2013). This may lead to a stop of the iteration after the maximum number of iterations is reached and impacts both on the code's performance and accuracy. The relaxation factor is introduced in the iteration after a new value, a_{k+1}, for the axial induction factor has been calculated:

$$a_{k+1} = \omega_{relax}\, a_{k+1} + (1 - \omega_{relax}) a_k \tag{3.3}$$

3.1.5.6 Reynolds Number Correction

The changes in lift and drag polars due to Reynolds number effects are not included in JBLADE. The polars are always computed for a fixed Reynolds number. During the simulation of a propeller, the Reynolds number is changing for every operational point. The user should carefully check how large the deviation is for each case. Hernandez & Crespo (1987) suggested a correction in which the lift polar remains unchanged and the drag polar is corrected by scaling the drag coefficient inversely with the Reynolds number.

$$c_D = c_{D_{Ref}} \left(\frac{Re_{Ref}}{Re}\right)^{Re_{exp}} \tag{3.4}$$

3.1.6 - Structural sub-module

In the *Structural sub-module* (see Figure 3.11) the user can create new materials that will be used to perform the structural analysis to the propeller's blades. Furthermore, the structural analysis can be defined in this sub-module as well. It is possible to estimate the mass of the blade according to the previously defined blade's material. In addition, it is possible to calculate the tip displacement, due to the thrust produced by the propeller, and the torsional deformation, due to aerodynamic twisting.

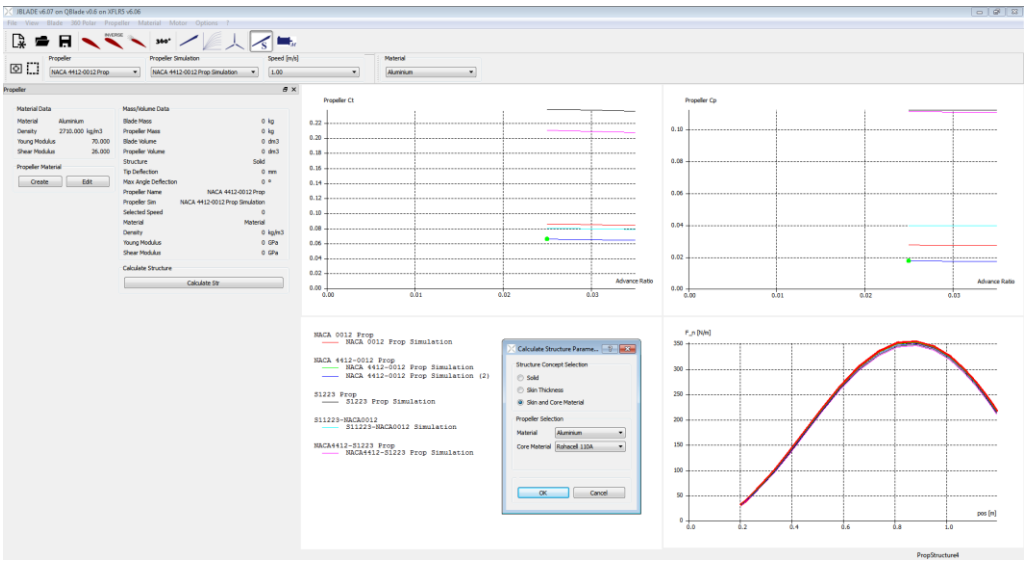

Figure 3.11 - Structural sub-module overview.

3.1.6.1 Creating and editing materials

To define a new material (see Figure 3.12), the user should specify the name, the density and the Young Modulus. After defining these properties, the material is added to the Material database and stored. In addition, each material can be modified or deleted. To maintain the software's consistency, when a material is deleted, all the structural simulations using that specific material are deleted as well.

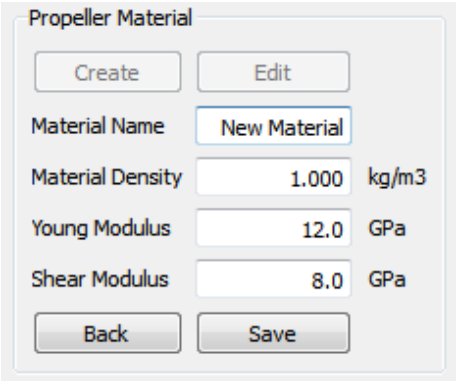

Figure 3.12 - New material definition dialog box.

3.2 - JBLADE Software Validation

3.2.1 - Propeller Geometries

The data from NACA Technical Reports (Gray, 1941; Theodorsen *et al.*, 1937) were used to validate the simulation procedures, the methodologies presented in Sections up to 2.6 and in Section 2.9 and also the Software performance predictions. The propeller presented by Adkins & Liebeck (1994) was used to validate the inverse design methodology (see Section 2.5.5) as well as the JBLADE performance predictions. The APC 11"x4.7" propeller was also used to validate the JBLADE aerodynamic predictions.

3.2.1.1 NACA Technical Report 594

The propeller used to validate JBLADE Software corresponds to the NACA Technical Report No. 594 (Theodorsen *et al.*, 1937) configuration "Nose 6 – Propeller C". The propeller has 3 blades and a diameter of 3.054 m (see Figure 3.13(a) and (b)).

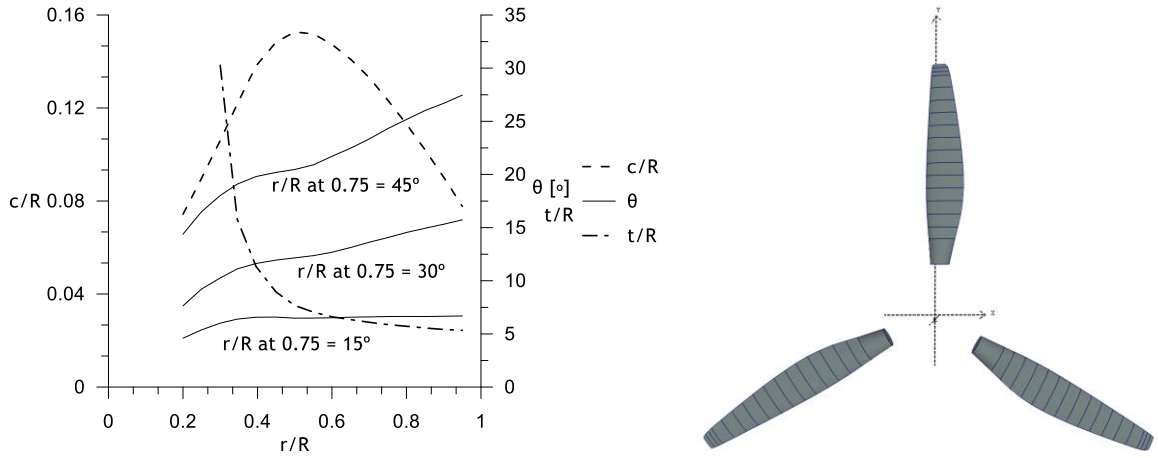

Figure 3.13 - NACA Technical Report No. 594 (Theodorsen *et al.*, 1937) propeller (a) propeller geometry (b) propeller visualization in JBLADE.

3.2.1.2 NACA Technical Report 530

The propeller 6267A-18 presented in NACA Technical Report No. 530 (Gray, 1941) uses the Clark Y airfoil along the entire span. This propeller was originally tested with a 0.711 meters diameter spinner with a rotational speed of *520* RPM. The propeller has 3 blades and a diameter of *3.073 m*. Its geometry and visualization are represented in Figure 3.14 (a) and (b), respectively.

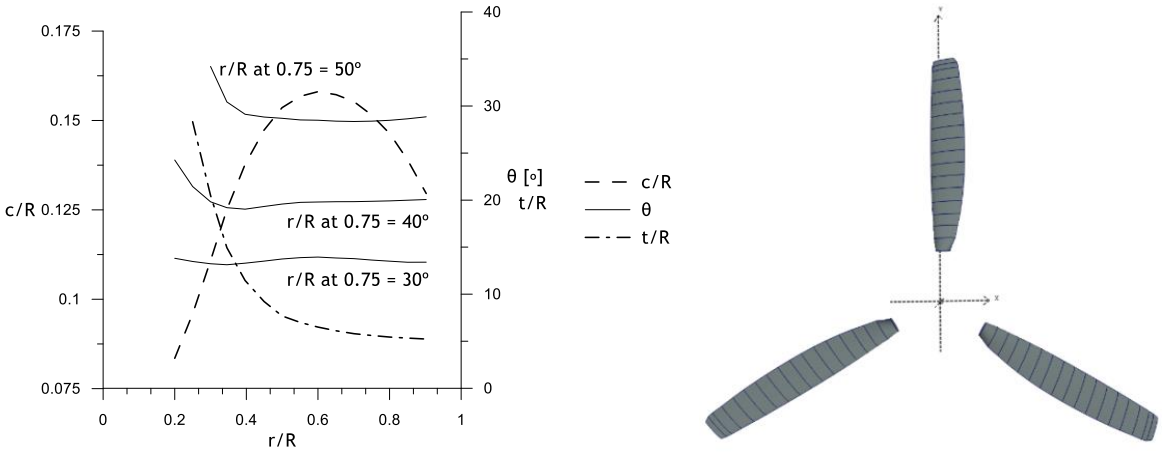

(a) **(b)**

Figure 3.14 - NACA Technical Report No. 530 (Gray, 1941) 6267A-18 propeller (a) propeller geometry (b) propeller visualization in JBLADE.

3.2.1.3 Adkins and Liebeck Propeller

The propeller presented by Adkins & Liebeck (1994) has 2 blades and a diameter of *1.75 m*. The propeller's section consists of NACA 4415 airfoils from root to tip. The blade geometry is presented in Figure 3.15 (a) and its visualization inside JBLADE is presented in Figure 3.15 (b).

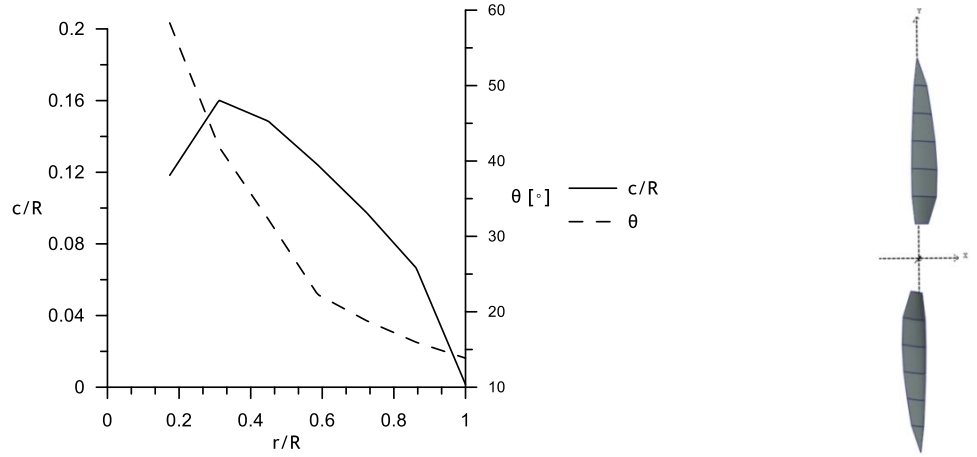

(a) **(b)**

Figure 3.15 - Propeller geometry presented by Adkins & Liebeck (1994) (a) propeller geometry (b) propeller visualization in JBLADE

3.2.1.4 APC 11"x4.7"

The APC 11"x4.7" propeller was also used to validate JBLADE for low Reynolds number predictions. The propeller was replicated according to the data found at UIUC Propeller Database (Brandt *et al.*, 2014). Figure 3.16 (a) shows the chord and pitch angle distribution

along the blade radius. The propeller has 2 blades and 0.28 m of diameter, and when replicated in JBLADE it becomes as in Figure 3.16 (b).

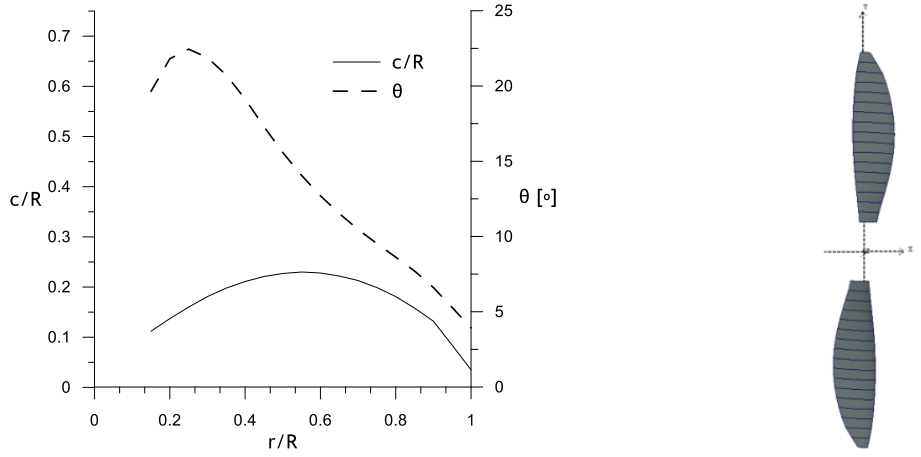

(a) (b)

Figure 3.16 - APC 11"x4.7" propeller(Brandt *et al.*, 2014) (a) propeller geometry (b) Illustration of the propeller inside JBLADE

3.2.2 - Simulation Procedure Validation

With the presented architecture of the JBLADE Software, a simulation using the propeller described in Section 3.2.1.1 was conducted. To start the simulation procedure the airfoil polars were obtained in the *XFOIL sub-module*. The polars were then extrapolated such that the lift and drag coefficients became available for post stall angles of attack. Geometry presented on Figure 3.13 (a) was replicated in order to define the propeller blades in JBLADE and the corresponding airfoil for each blade section was used, obtaining the propeller represented at Figure 3.13 (b). The blade pitch angle was adjusted to the given angle at 75% of the radius and the propeller performance was computed.

In order to understand how to perform a correct propeller simulation in JBLADE, the number of points necessary to define an airfoil was studied. This procedure allows the optimization of the XFOIL numerical accuracy and the different polars obtained with different number of points are presented in Figure 3.17 (a). It can be observed that, for more than 200 points XFOIL does not show a significant difference in the airfoil polars. Thus, in the simulations performed along this thesis each airfoil was refined in order to have, at least, 200 points.

Since each section of the blade has a specific Reynolds and Mach number, the capability to correctly predict the airfoil performance plays a key role on the propeller analysis, a study was also conducted and the results are presented in Figure 3.17 (b). It can be concluded, as the existing literature suggests (Selig, 2003), that XFOIL can correctly predict the airfoil performance for Reynolds and Mach numbers intervals of interest to high altitude propellers.

Therefore, since the capability of XFOIL correctly predicts the airfoil performance, a detailed study was conducted and is described in Chapter 4.

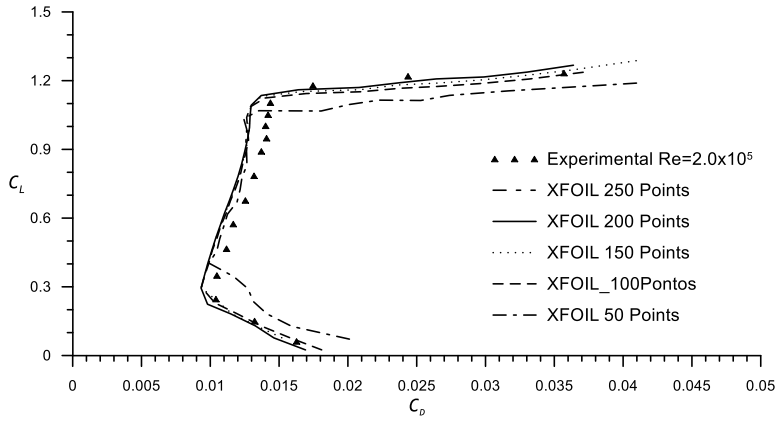

(a)

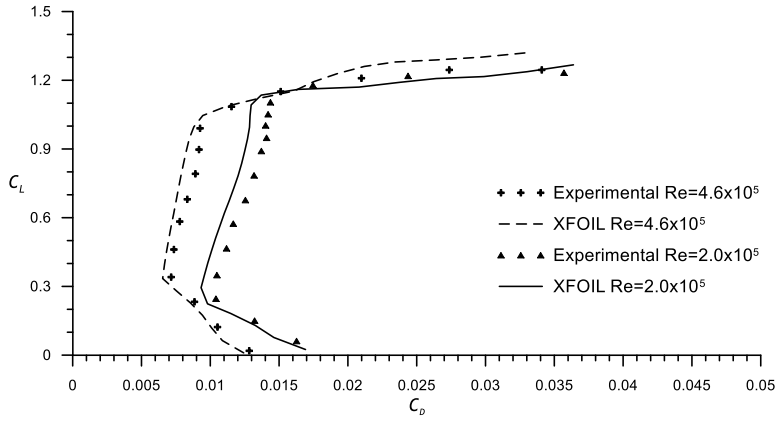

(b)

Figure 3.17 – E387 airfoil polars. (a) Validation of polar calculation using different number of points to define the airfoil in XFOIL (b) Comparison between XFOIL and experimental studies (Selig & Guglielmo, 1997) different Reynolds numbers

To correctly replicate the geometries presented in both NACA Reports, a search was conducted to find how the blade pitch angle was measured in the original NACA Reports. However, there are no clear indications about how the blade angle was measured at each radial position.

Analysing the two common reference lines (see Figure 3.18), it was concluded that NACA tests refer to the lower surface of the blade, the usual practice at that time. Regarding the difference on a Clark Y airfoil having 12% thickness it becomes:

$$\theta_{Axis} - \theta_{Lower_{Surface}} \approx 2° \qquad 3.5$$

Since JBLADE considers the pitch angle equivalent to the θ_{Axis}, these extra 2° were thus added to the geometries from NACA Reports to ensure the agreement between the tests and the JBLADE simulations. This procedure was also adopted by other authors as presented by Hepperle (2010).

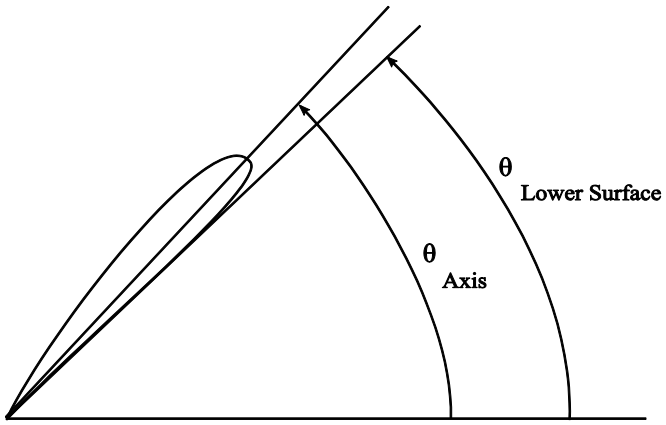

Figure 3.18 - Possible reference lines for blade pitch angle measurements.

To validate the computations for a wide range of advance ratios, independent simulations for small, medium and large advance ratios were performed and compared with the previously calculated curve using the average distribution of Reynolds and Mach numbers along the blade (see Figure 3.19). For each of the blade's defining section the average Reynolds and Mach number was set as the mean value corresponding to half the advance ratio that corresponded to the propeller operating conditions used to collect the experimental data. The propeller rotational speed was constant at *1800* RPM.

The "*VMIN*" points were obtained with the distribution of Reynolds and Mach numbers for a low advance ratio operating condition. The airfoil polars were calculated using the Reynolds and Mach number distribution for the advance ratio about 0.1 and the propeller performance was only analysed for this specified advance ratio.

The "*COMPUTED*" curves were calculated with the Reynolds and Mach numbers distributions for an intermediate advance ratio, close to the maximum efficiency of the propeller. The "VMED" simulations were performed using the same Reynolds and Mach numbers as the "COMPUTED" curves. The "*VMAX*" points were obtained with the same procedure but for an advance ratio close to the zero thrust condition of the respective propeller. Observing Figure 3.19 it is possible to conclude that the averaged Reynolds and Mach numbers distribution "*VMED*", which correspond to an intermediate advance ratio, allow a close approximation for the full range of advance ratios simplifying the simulation procedure.

In addition, the influence of the improvements made on the theoretical formulation of JBLADE were studied and the results can be observed in Figure 3.20. The *"Original BEM"* curve corresponds to the initial formulation described in Section 2.5.3 and, as it was incorporated in QBLADE for wind turbines but here extended to simulate propellers. The "*Mod. BEM*" curve corresponds to the modification of the classical BEM with the 3D Equilibrium described in Section 2.4.1. Analysing Figure 3.20, it can be observed that the 3D Equilibrium implementation had resulted in significant improvements throughout the complete advance ratio range.

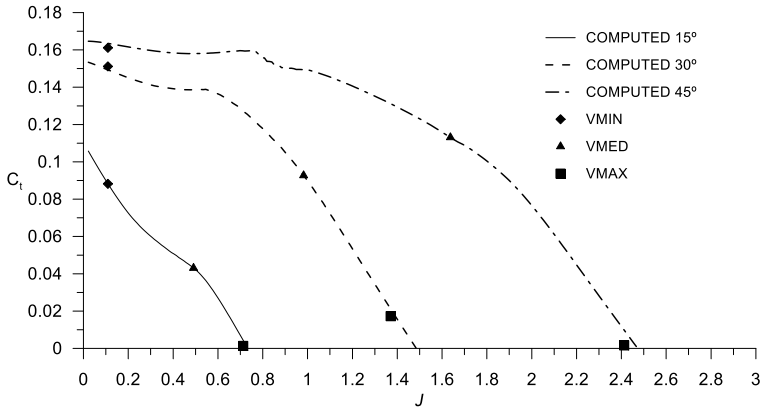

(a)

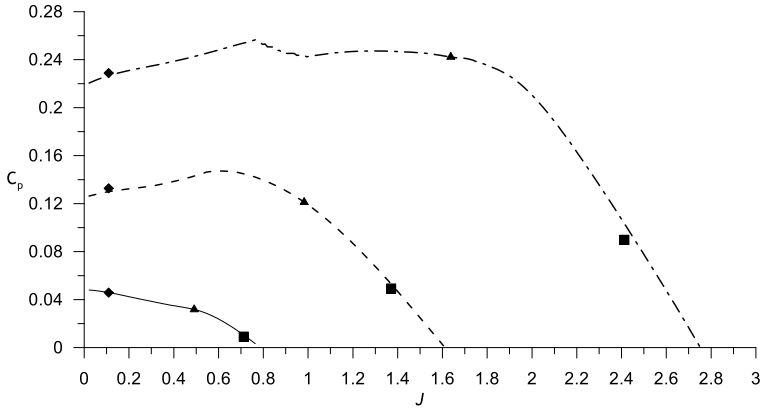

(b)

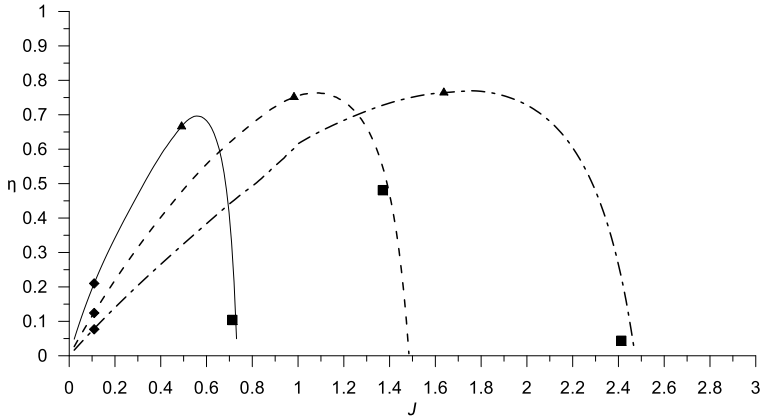

(c)

Figure 3.19 - Validation of calculations for the Propeller "C" of NACA TR 594 (Theodorsen *et al.*, 1937) using a distribution of averaged Reynolds and Mach Numbers along the blade: (a) thrust coefficient (b) power coefficient, (c) propeller efficiency.

The "*Mod. BEM + Post Stall*" curve includes the post stall model described in Section 2.5.3.2. Since there are different post-stall models available, the selection of the adequate post-stall model was studied and the results are presented in Section 3.2.4. Figure 3.20 shows that the best performance prediction is obtained using the post-stall model together with 3D Equilibrium. Thus, the simulations throughout this thesis were performed using the post-stall model (Corrigan & Schillings, 1994) and 3D Equilibrium.

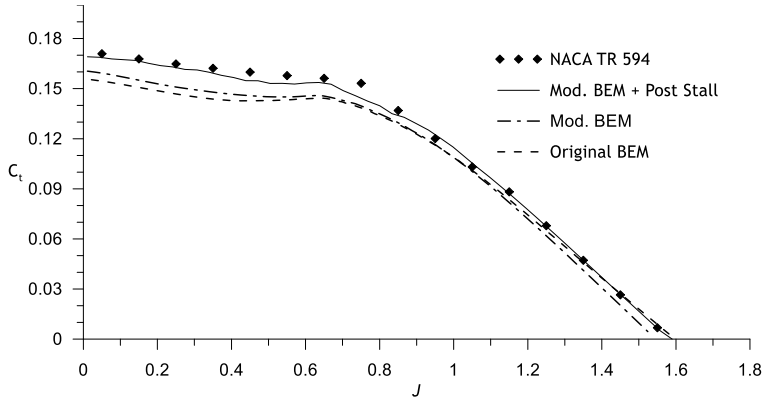

(a)

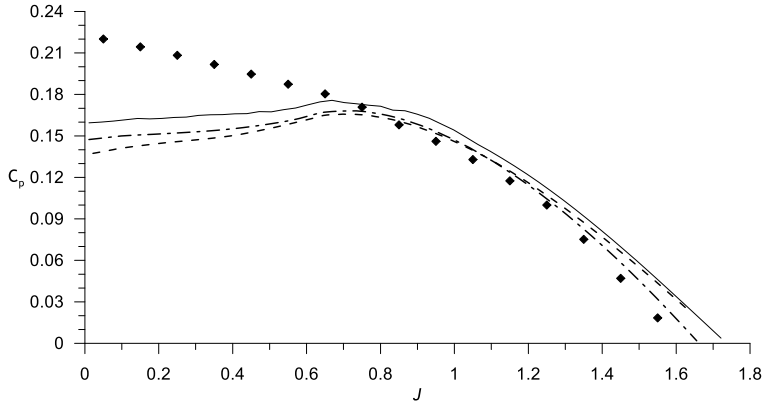

(b)

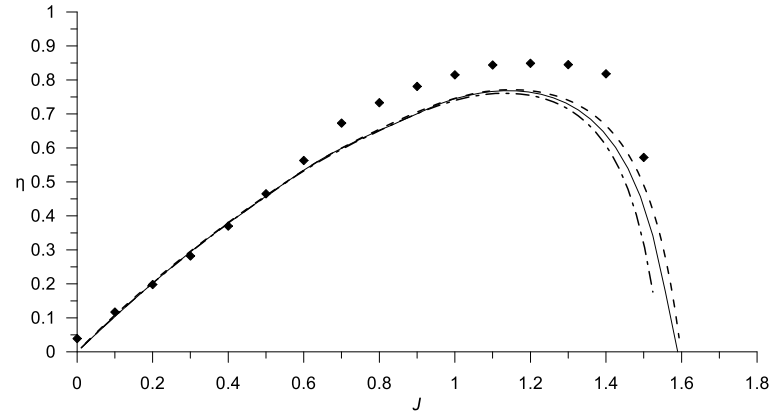

(c)

Figure 3.20 - Modelation influence on the simulated propeller performance: (a) thrust coefficient (b) power coefficient (c) propeller efficiency.

3.2.3 - Methods for Drag Coefficient at 90º Prediction Validation

A new method for predicting the drag coefficient at an AoA of 90º was described in Section 2.4.2.1. In order to evaluate the improvements in the propeller performance prediction of the new proposed method for the $C_{D_{90}}$ calculation, additional simulations of the propellers presented in Section 3.2.1.1 and Section 3.2.1.2 were performed. The results are presented and discussed below. Since both methodologies lead to close predictions for the drag coefficient at 90 degrees, the simulations were only performed with the method that correlates the airfoil's drag coefficient at 90 degrees with the airfoil's leading edge radius.

3.2.3.1 NACA Technical Report 594

The procedure described in Section 3.2.2 was applied in order to obtain the propellers' performance predictions. The curve "*JBLADE* $C_{D_{90}} = 1.4$*"* presented in Figure 3.21 represents the initial formulation as it was incorporated in QBLADE (Marten *et al.*, 2013) for wind turbines but extended here to simulate propellers. These curves were obtained with a constant value of drag coefficient as suggested by Montgomerie (1996) in his first method. According to this method, the value of, $C_{D_{90}} = 1.4$ was used for all airfoils from root to tip of the blades. Figure 3.21 (a) and Figure 3.21 (b) show that this methodology underpredicts the propeller's thrust and power coefficients, especially in the lower advance ratio region.

The curves "*JBLADE Improved Polar*" correspond to the modified polars extrapolation, as described in Section 2.4.2.1. These solid lines were obtained with the method in which the CD_{90} is correlated with the airfoil's leading edge radius. Observing Figure 3.21 (a) and (b) it is possible to conclude that this methodology represents the closest prediction of the propeller performance over all advance ratios range for the thrust coefficient. The power coefficient is still underpredicted, but an improvement is observed when compared to the *"JBLADE* CD_{90}*=1.4"*

The curves "*JBLADE* $C_{D_{90}} = 2.2$*"* follow the same procedure as presented for the curve "*JBLADE* $C_{D_{90}} = 1.4$*"* modifying only the value of the $C_{D_{90}}$ from 1.4 to 2.2. This value of $C_{D_{90}}$ lead to an over prediction of the thrust coefficient (see Figure 3.21(a)) in the lower advance ratio region. Regarding power coefficient (see Figure 3.21 (b)), its prediction becomes closer to the experimental data but still under predicted.

Since the proposed method modifies the value of drag coefficient at 90 degrees AoA to a more reasonable value, it changes the extrapolated 360º AoA airfoil drag coefficient polar and consequently improves the propeller performance prediction. It is seen that the CD_{90} and the complete 360º AoA range airfoil polars play an important role in the predicted performance with a visible improvement in the thrust and power coefficients, especially at low advance ratios region.

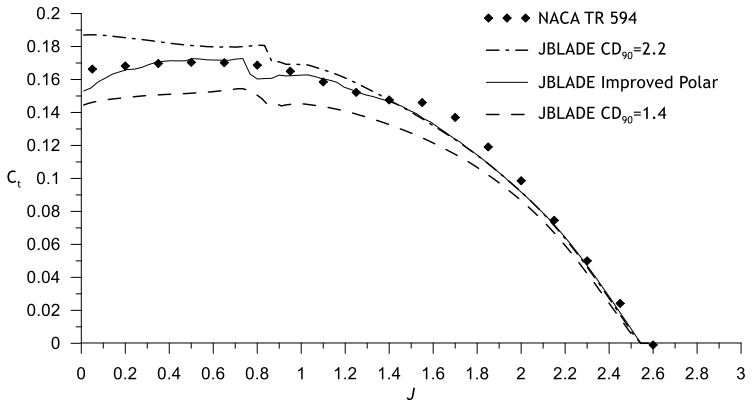

(a)

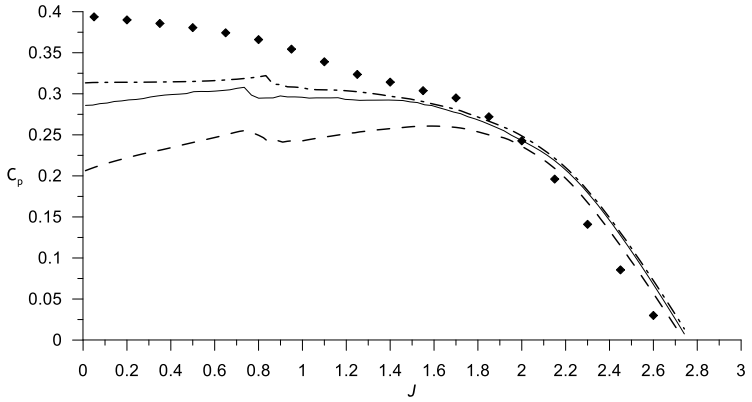

(b)

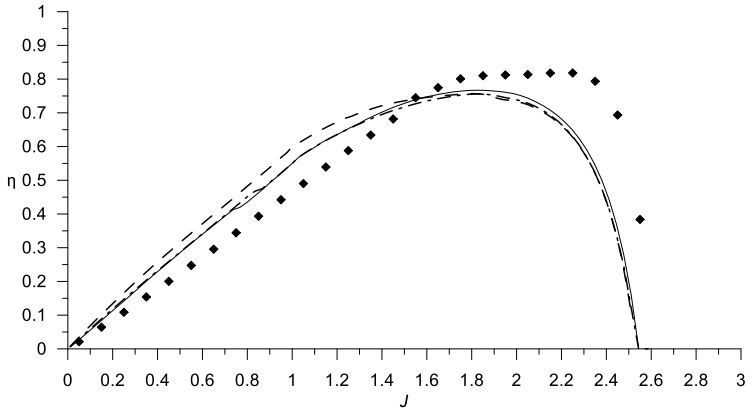

(c)

Figure 3.21 - Influence of the 360 polars extrapolation in the propeller performance and comparison with data from NACA TR 594 for $\theta_{75}=45°$: (a) thrust coefficient (b) power coefficient (c) propeller efficiency.

3.2.3.2 NACA Technical Report 530

Figure 3.22 shows the results for the reference propeller pitch angles of $\theta_{75} = 30°$. Observing the thrust coefficient results (see Figure 3.22 (a)) no significant differences are observed between the improved and previous CD90=1.4 models for this particular test case, and both seem to diverge from the experimental results as the advance ratio reduces to the lower limit.

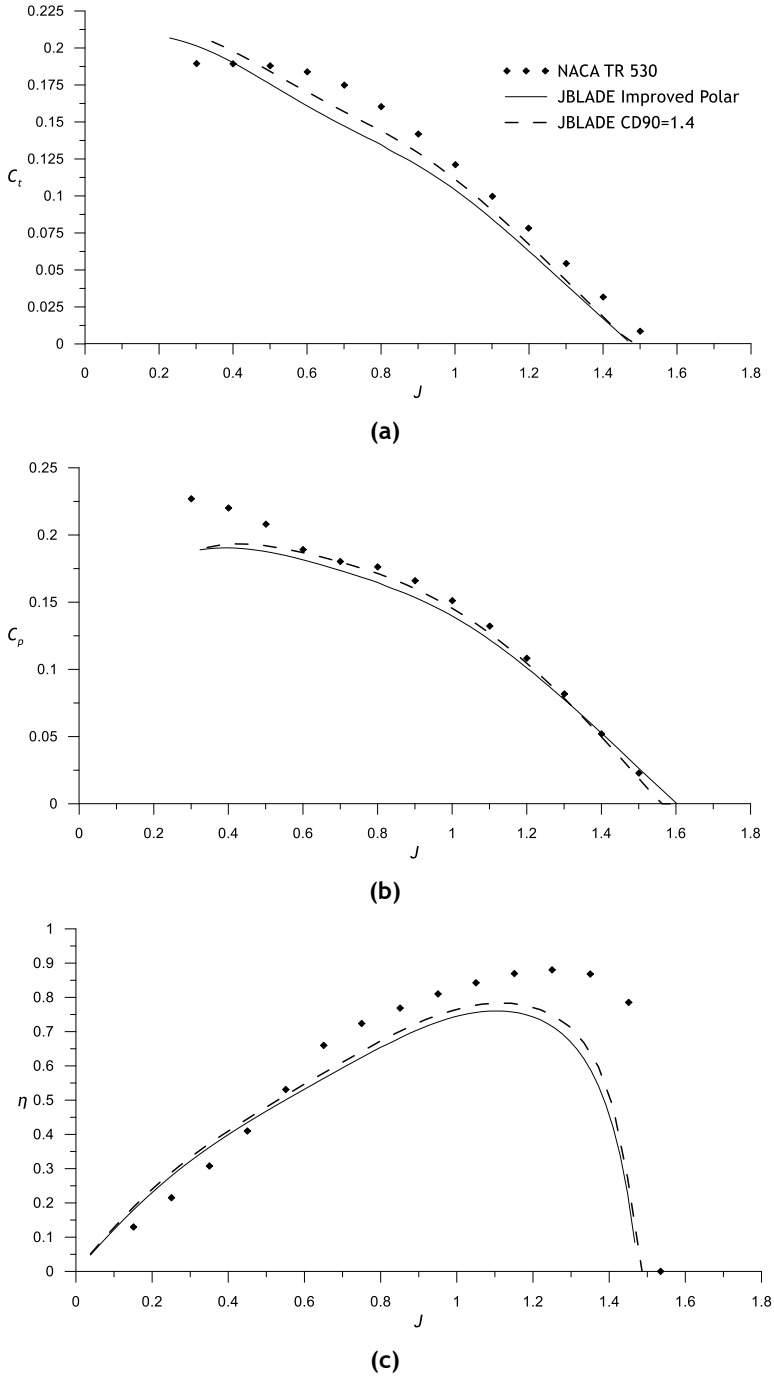

Figure 3.22 - Influence of the 360 polars extrapolation in the propeller performance and comparison with data from NACA TR 530 for θ_{75}=30°: (a) thrust coefficient (b) power coefficient (c) propeller efficiency.

Figure 3.23 presents the comparison between both methodologies for the propeller from NACA TR 530 but with $\theta_{75} = 40°$. Both thrust and power coefficients (see Figure 3.23 (a) and (b)) predicted using the method that correlates the airfoil leading edge with the CD_{90} are closer of the experimental data than the predictions obtained with the method of constant CD_{90}. The difference is more pronounced in the small advance ratios region and practically does not exist for advance ratios bigger than 0.8.

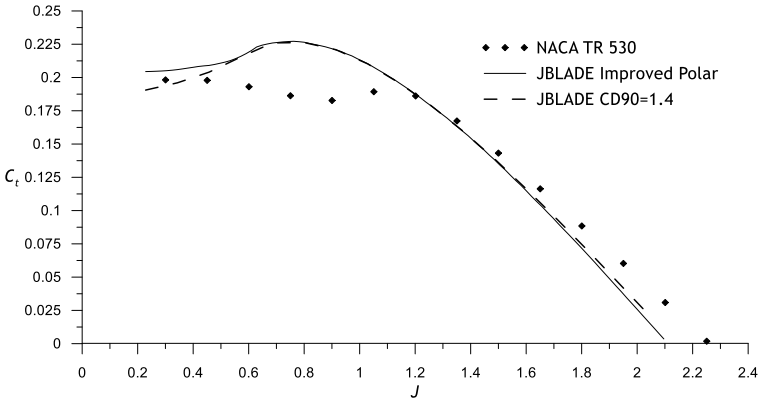

(a)

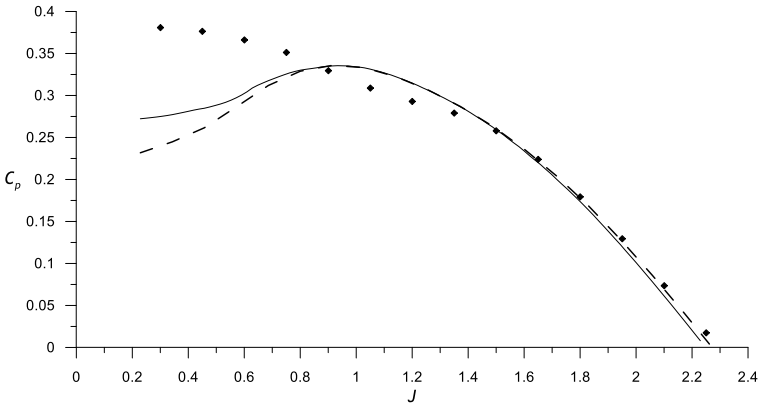

(b)

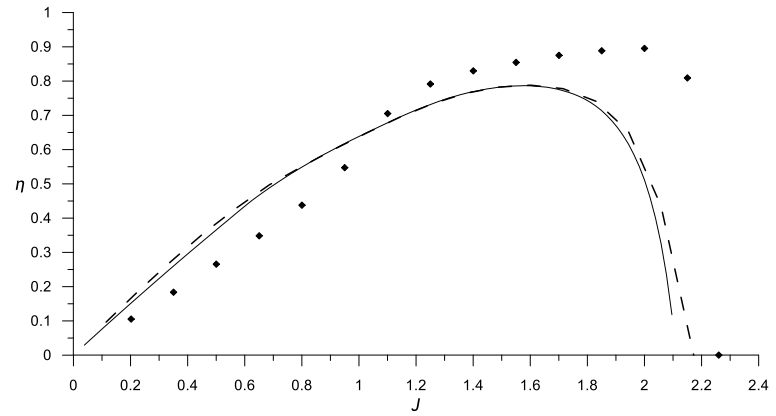

(c)

Figure 3.23 - Influence of the 360 polars extrapolation in the propeller performance and comparison with data from NACA TR 530 for θ_{75}=40° (a) thrust coefficient (b) power coefficient, (c) propeller efficiency.

However It should be noted that from TR530 it is clear that the abrupt reduction of the c_t and c_p values occurring at low advance ratio is then reversed as the advance ratio lowers even more. So, the apparent divergence may not really exist. On the other hand, for such a low pitch setting of 30º, both models underpredict the peak efficiency values, although the improved model behaves slightly worst than the previous model. The power coefficient (see Figure 3.22 (b)) also shows no significant differences between both methods and experimental data.

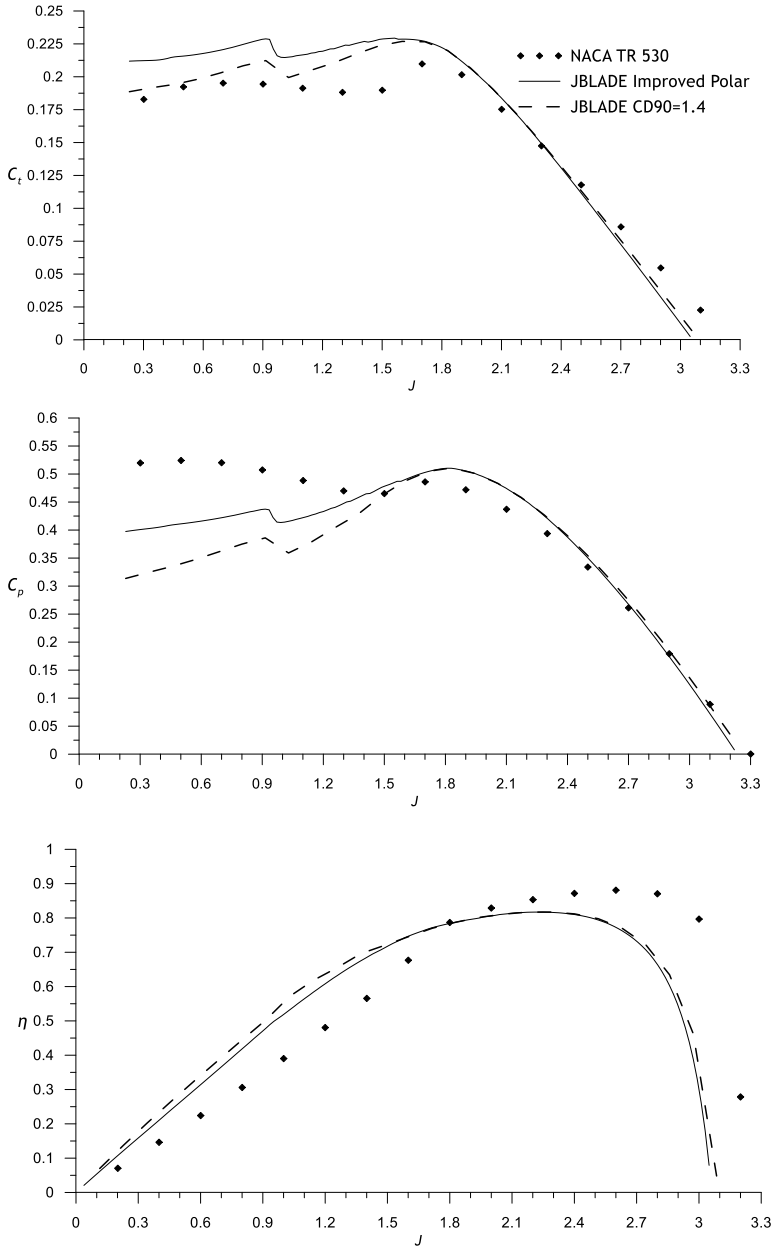

Figure 3.24 - Influence of the 360 polars extrapolation in the propeller performance and comparison with data from NACA TR 530 for $\theta_{75}=50°$ (a) thrust coefficient (b) power coefficient, (c) propeller efficiency.

Figure 3.24 presents the comparison between both methodologies for the propeller from NACA TR 530 but with $\theta_{75} = 50°$. Observing Figure 3.24 (a) it is possible to conclude that the method that correlates the airfoil leading edge with the CD_{90} is overestimating the thrust coefficient, with the method of constant CD_{90} is giving the best results for this specific case. Figure 3.24 (b) shows that the new proposed method improves the estimation of the power coefficient for this specific propeller, especially in the smaller advance ratios region.

3.2.4 - Post-Stall Models

The post-stall models described in Section 2.5.3.2 were implemented in JBLADE and the propellers from NACA Report No. 594 were also used to evaluate the post-stall models behaviour and improvements when compared to the original BEM formulation.

3.2.4.1 NACA Technical Report 594

Figure 3.25 (a) shows that all the implemented models improve the thrust coefficient prediction when compared with a simulation in which no post-stall was used ("Original BEM" curve). The models show small discrepancies between the experimental and predicted thrust coefficients. Figure 3.25 (b) shows the effect of the post-stall models in the power coefficient prediction.

Contrary to the thrust coefficients prediction, the power coefficient is significantly under predicted, even with the post-stall models correction. For both, thrust coefficient and power coefficient it is shown that the effect of the post-stall models is more pronounced on the low advance ratios regions. It was found that for this case the model developed by Corrigan & Schillings (1994) performs best over the range of conditions studied, but still exhibited some limitations, especially in power coefficient prediction as mentioned.

For the case of $\theta_{75} = 45°$ (see Figure 3.26 (a) to (c)), it was decided not to perform the simulations with the BEM Original theory, since the results will be worst, when compared with the results obtained using the post-stall models. Different models are predicting significantly different thrust coefficients which happens once each model changes the lift coefficient in a different way and as the higher the angle of attack, the higher are the differences on the lift coefficient at each blade's section.

Besides the Dumitrescu & Cardos (2007) and the Corrigan & Schillings (1994) models, the other post-stall models tend to overestimate the thrust coefficient (see Figure 3.26 (a)). The difference seen between the predictions and the real propeller performance at low advance region on Figure 3.25(b) and on Figure 3.26 (b) for all the post-stall model is interesting since, independently of the used post-stall model, there are no significant improvements in the predictions. It is clear that the analysed post-stall models fail to consistently improve the power coefficient prediction.

Globally, the model of Corrigan & Schillings (1994) perform better in bringing the predictions closer to the test data when compared with the other models. In general, the post-stall models have shown their ability to improve the performance prediction mostly in the thrust coefficient. The power coefficient is still significantly under predicted at low advance ratios. Further comparisons comprising forces distributions along the blade may help to better understand the lack of accuracy of these models and it will be the subject of future work.

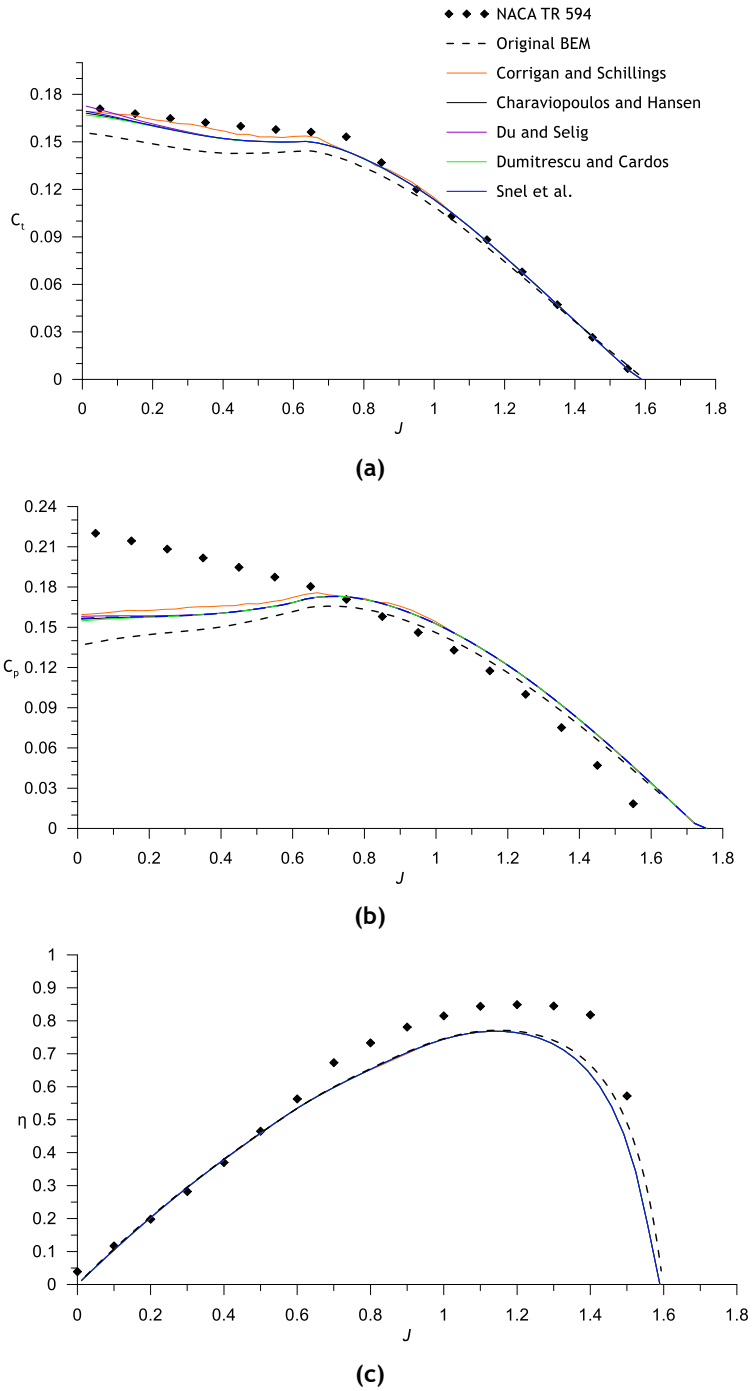

Figure 3.25 - Comparison between data predicted by JBLADE using different post-stall models and data from NACA TR No. 594 (Theodorsen *et al.*, 1937) for $\theta_{75}=30°$ (a) thrust coefficient (b) power coefficient (c) propeller efficiency.

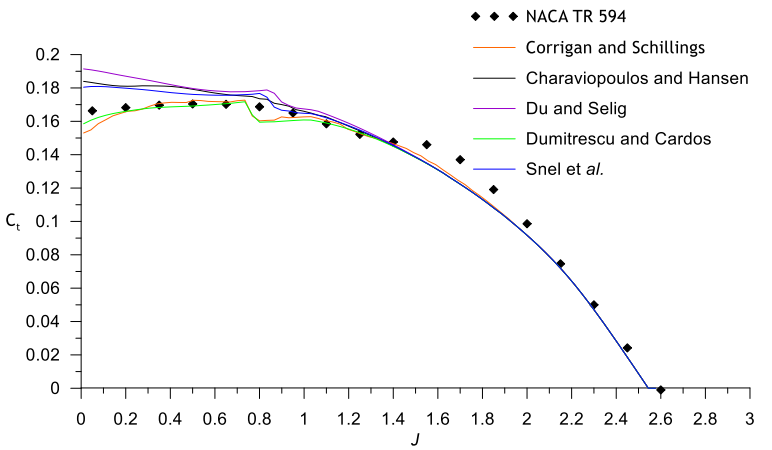

(a)

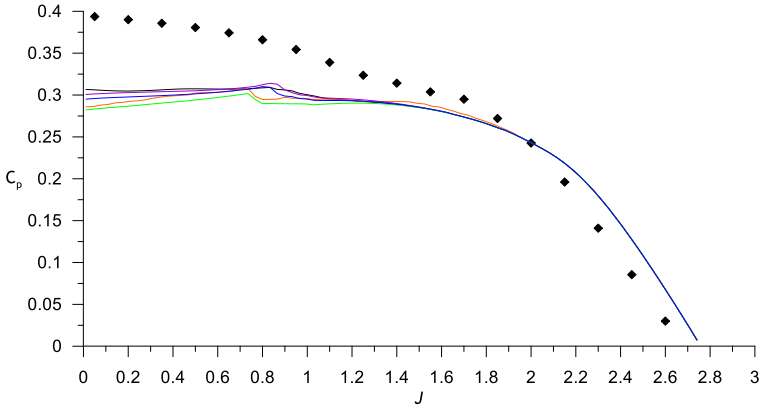

(b)

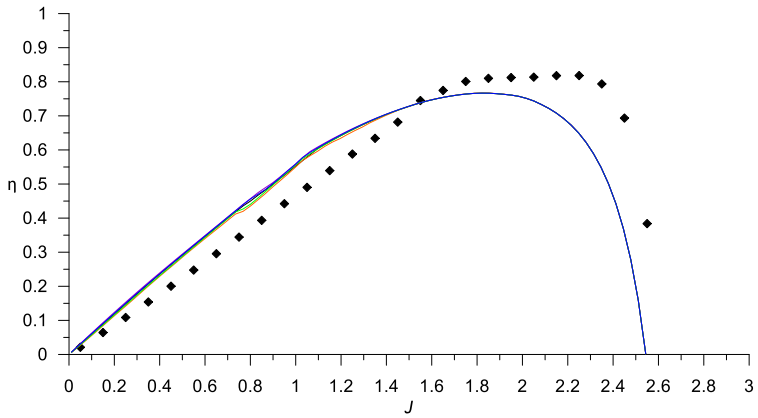

(c)

Figure 3.26 - Comparison between data predicted by JBLADE using different post-stall models and data from NACA TR No. 594 (Theodorsen *et al.*, 1937) for θ_{75}=45° (a) thrust coefficient (b) power coefficient (c) propeller efficiency.

3.2.5 - Inverse Design Methodology Validation

In order to validate the inverse design methodology implementation in JBLADE (see Section 2.5.5), the light aircraft propeller presented by Adkins & Liebeck (1994) was designed through the *Inverse Design sub-module*, presented in Section 3.1.3.1.

3.2.5.1 Adkins and Liebeck Propeller

The required data for propeller design are described in Table 3.1 and the resulting geometry is presented in Figure 3.27.

Table 3.1 – Input data for propeller inverse design.

Designation		Units
Power	52	kW
Rotation Speed	2400	RPM
Hub Diameter	0.30	m
Tip Diameter	1.75	m
Aircraft Velocity	49	m/s
Lift Coefficient	0.7	
No. of Blades	2	

Observing Figure 3.27 is possible to conclude that JBLADE is in good agreement with original implementation done by Adkins & Liebeck (1994).

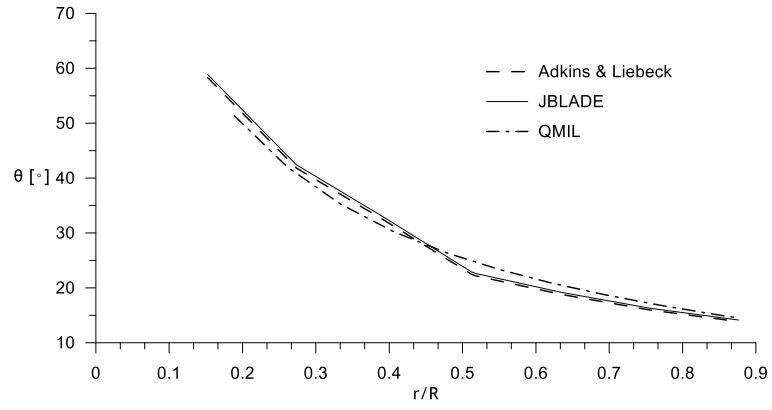

(a)

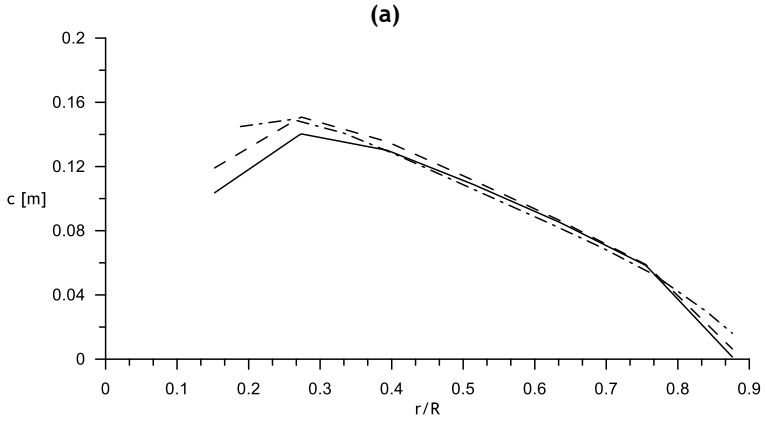

(b)

Figure 3.27 - Validation of the inverse design methodology. (a) blade incidence angle (b) chord

The implementation was checked also against QMIL (Drela, 2005b) since it uses a different approach for introducing the airfoil characteristics. The results have shown that similar geometries are obtained for the given propeller operating point.

3.2.6 - JBLADE *vs* Other BEM Codes

In order to verify the reliability of JBLADE to accurately calculate the propellers performance, geometries presented in Section 3.2.1 were simulated and the JBLADE predictions were compared with both experimental data and other existing BEM codes. The experimental data came from NACA TR 594 (Theodorsen *et al.*, 1937) and NACA TR 530 (Gray, 1941) while the existing BEM codes selected to the comparison with JBLADE were the well-known QPROP (Drela, 2006) and JAVAPROP (Hepperle, 2010).

3.2.6.1 NACA Technical Report 594

Observing Figure 3.28 (a), it is possible to conclude that JBLADE predicts a lower thrust coefficient in the smaller advance ratios region and closely match the experimental data in the higher advance ratio region. On the other hand, JAVAPROP (Hepperle, 2010) is correctly predicting the thrust coefficient for the smaller advance ratios and under predicting the thrust coefficient at bigger advance ratios region. The QPROP (Drela, 2006) is the code that performs worst for this situation, over estimating the thrust coefficient at smaller advance ratio and under predicting the thrust coefficient for the higher advance ratios.

Regarding power coefficient (see Figure 3.28 (b)), it is possible to observe that JBLADE is correctly predicting the power coefficient over all advance ratios. JAVAPROP is correctly predicting the propeller's power coefficient for the advance ratios between 0.2 and 0.4. Out of this advance ratio range, JAVAPROP is significantly under predicting the power coefficient. QPROP is over estimating the power coefficient values in the smaller advance ratios region and under estimating the values for the bigger advance ratios.

The propeller's efficiency results are shown in Figure 3.28 (c). Observing this figure, it is possible to conclude that both JAVAPROP and QPROP codes are correctly estimating the efficiency until an advance ratio about 0.5. However both codes estimate a smaller propeller efficiency at a smaller advance ratio. JBLADE, despite the fact that is slightly under estimating the efficiency (obtaining a maximum efficiency prediction close the other codes) is correctly predicting the advance ratio at which it occurs.

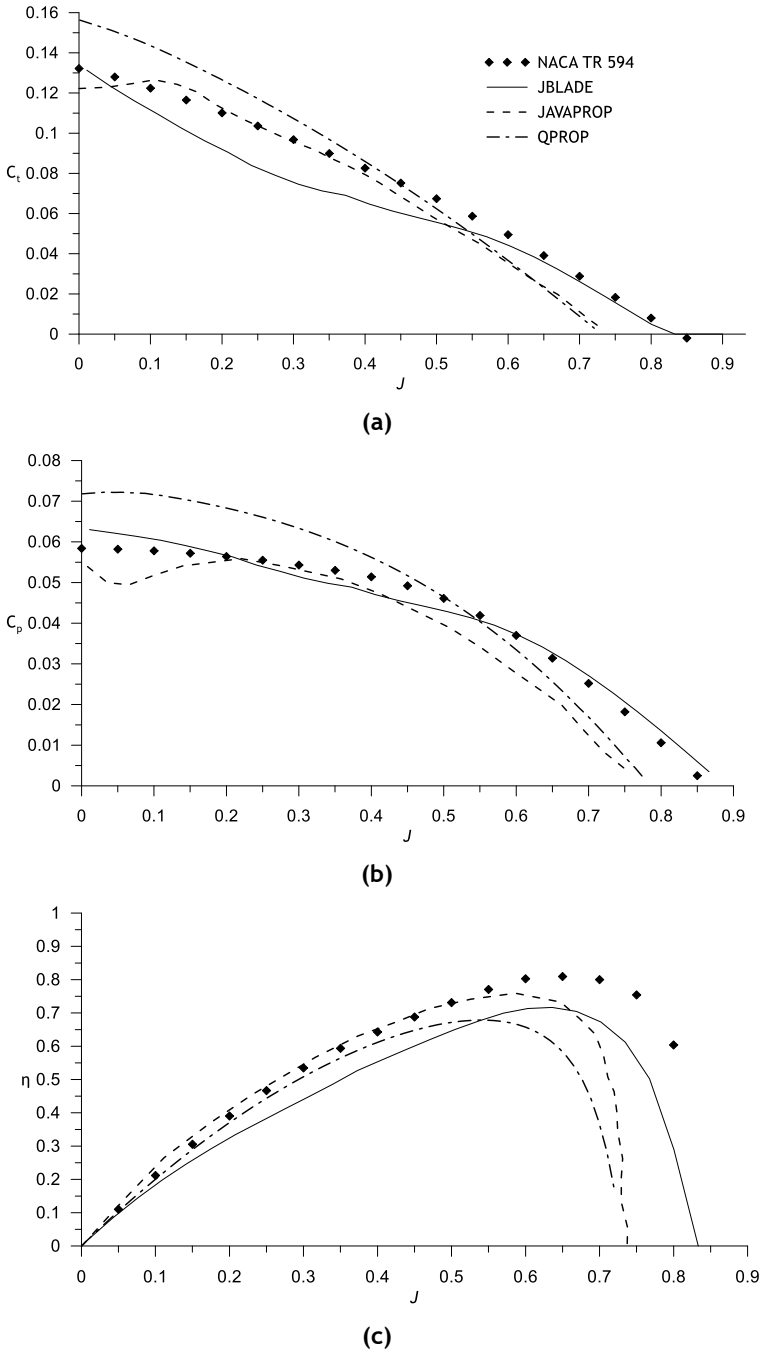

Figure 3.28 - Results of NACA TR 594 (Theodorsen *et al.*, 1937) for $\theta_{75}=15°$ (a) thrust coefficient (b) power coefficient (c) propeller efficiency.

Figure 3.29 (a) presents the thrust coefficient predictions of the JBLADE, JAVAPROP and QPROP codes. It shows that JBLADE is correctly predicting the thrust coefficient over all advance ratios, matching the experimental data. JAVAPROP is under predicting the thrust coefficient over the advance ratios while QPROP code is over estimating the thrust coefficient at smaller advance ratios but correctly predicting the thrust coefficient values for the zero thrust condition of the propeller.

Power coefficient results are shown in Figure 3.29 (b), showing that all the codes are significantly under estimating the power at low advance ratios. It was found that the cause may

be attributed to the airfoil's 360º angle of attack range airfoil polar misrepresentation just above the stall. Moreover, JBLADE and QPROP are slightly over estimating the power coefficient in the higher end while JAVAPROP is under predicting the power coefficient values.

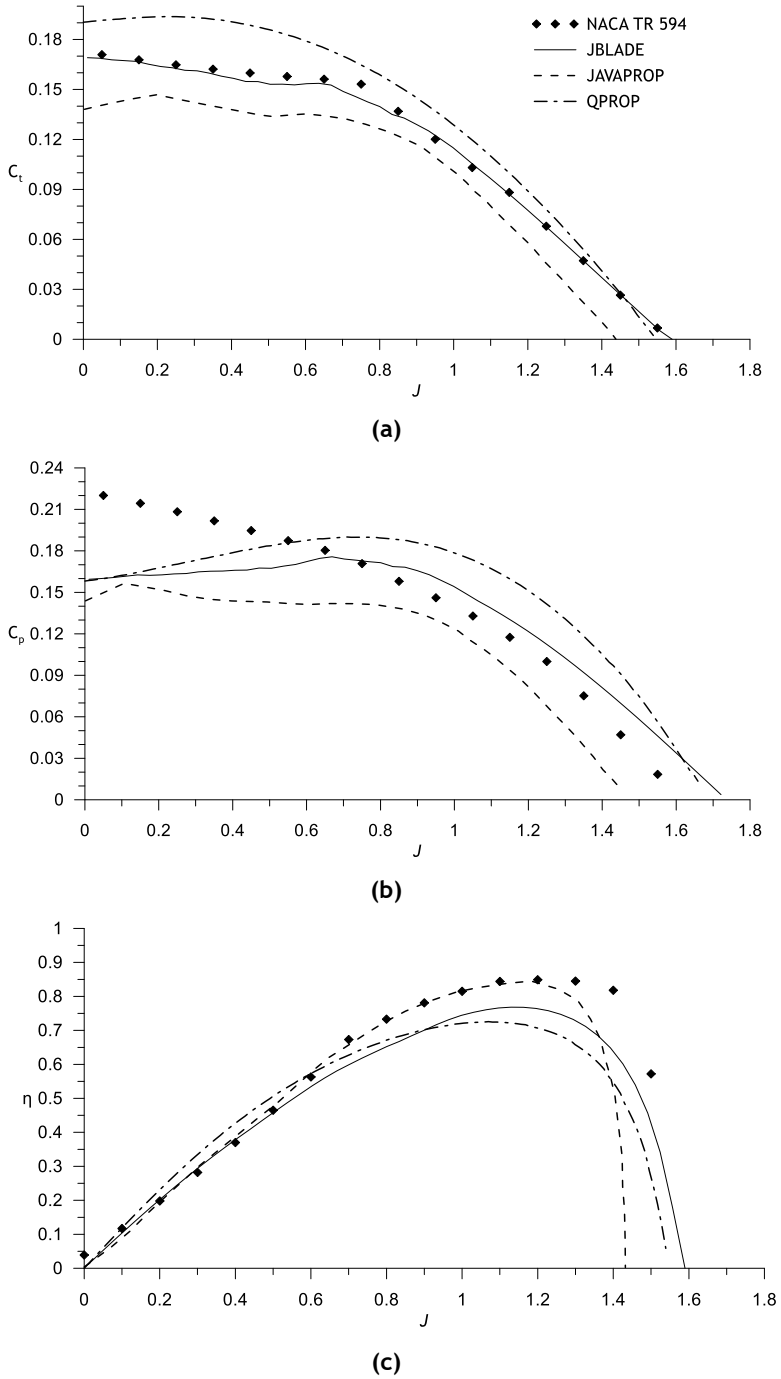

Figure 3.29 - Results of NACA TR 594 (Theodorsen *et al.*, 1937) for $\theta_{75}=30°$ (a) thrust coefficient (b) power coefficient (c) propeller efficiency.

Figure 3.29 (c) shows that JAVAPROP is under predicting the propeller efficiency and the advance ratio at which maximum efficiency occurs. The QPROP code is slightly over predicting the efficiency in the advance ratios range between 0.2 and 0.6 and under estimating the maximum efficiency values. However QPROP, together with JBLADE, are correctly predicting

the advance ratio at which maximum efficiency will occur. The JBLADE software is also under estimating the maximum efficiency value.

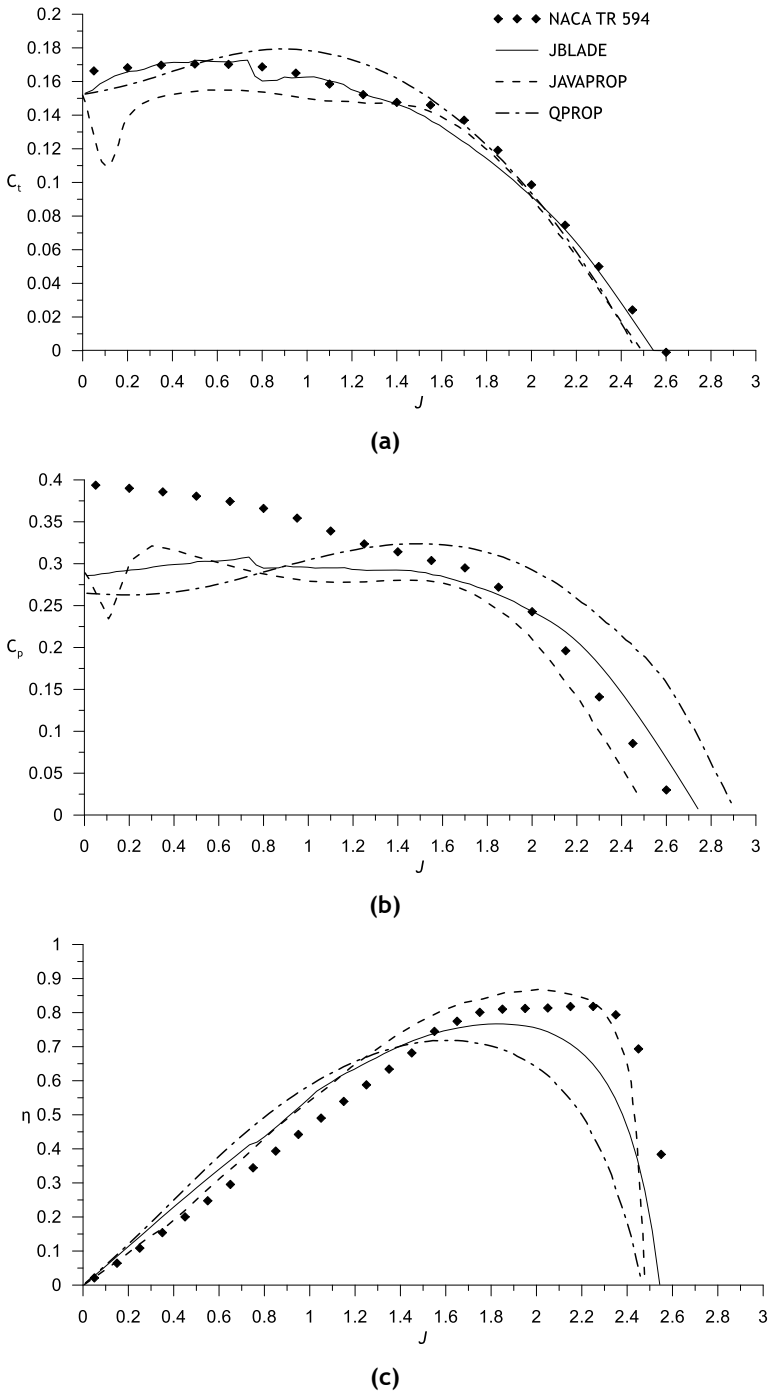

Figure 3.30 – Results of NACA TR 594 (Theodorsen *et al.*, 1937) for $\theta_{75}=45°$ (a) thrust coefficient (b) power coefficient (c) propeller efficiency.

Figure 3.30 (a) shows that JBLADE is correctly estimating the thrust coefficient. The JAVAPROP code is under estimating the thrust coefficient values in the smaller advance ratios region but correctly predicting the thrust for advance ratios bigger than 1.2. The QPROP code, despite the

over estimation of the thrust coefficient between 0.5 and 1.6 is also correctly predicting the thrust coefficient values for the bigger advance ratios.

Figure 3.30 (b) shows that all the BEM codes are under predicting the power coefficient in the smaller advance ratios region. The JBLADE is correctly predicting the power coefficient for bigger advance ratios while JAVAPROP and QPROP are, respectively, under predicting and over estimating the power coefficient values.

The propeller efficiency results (see Figure 3.30 (c)) shows that the propeller efficiency is over predicted in the advance ratios up to 1.5 by all the BEM codes. For bigger advance ratios JAVAPROP shows a slightly over estimation of the maximum efficiency value while JBLADE is estimating a maximum efficiency about 10% lower than the experiments. However, the advance ratio for the maximum efficiency closely matches the experimental values. This is related to the over prediction for power coefficients at high advance ratios.

Comparing JBLADE with the JAVAPROP (Hepperle, 2010) and QPROP (Drela, 2006) codes, it was shown that JBLADE gives the best overall results. The ability to correctly predict the thrust coefficient over the advance ratios, while predicts the power coefficient as good as the other existing BEM codes, makes JBLADE the most accurate BEM code to obtain the propeller performance predictions.

3.2.6.2 NACA Technical Report 530

Since the QPROP was the code that performed worst in the previously presented test cases, it was decided to compare the JBLADE predictions only with JAVAPROP estimations. The thrust coefficient results for the NACA TR No. 530 (Gray, 1941) propeller with $\theta_{75} = 30°$ are presented in Figure 3.31 (a). It shows that both JBLADE and JAVAPROP are correctly predicting the thrust coefficient with JBLADE performing slightly better in the bigger advance ratios region.

Figure 3.31 (b) confirms that the power coefficient obtained in JBLADE is under predicted at low advance ratios. However, contrary to what occurs in previous test case (see Figure 3.29 (b) and Figure 3.30 (b)), the power coefficient is much closely estimated in the higher advance ratios. JAVAPROP code presents even a bigger under estimation of the power coefficient at smaller advance ratios. Moreover, it also under predicts the power coefficient in the bigger advance ratios region.

Propeller efficiency results (see Figure 3.31 (c)) shows that JAVAPROP is overestimating the propeller performance in the advance ratio range between 0.1 and 0.6. The maximum efficiency values prediction of both codes are coincident and slightly under estimating. The value of the advance ratio at which the maximum efficiency occurs is quite well estimated by both JBLADE and JAVAPROP.

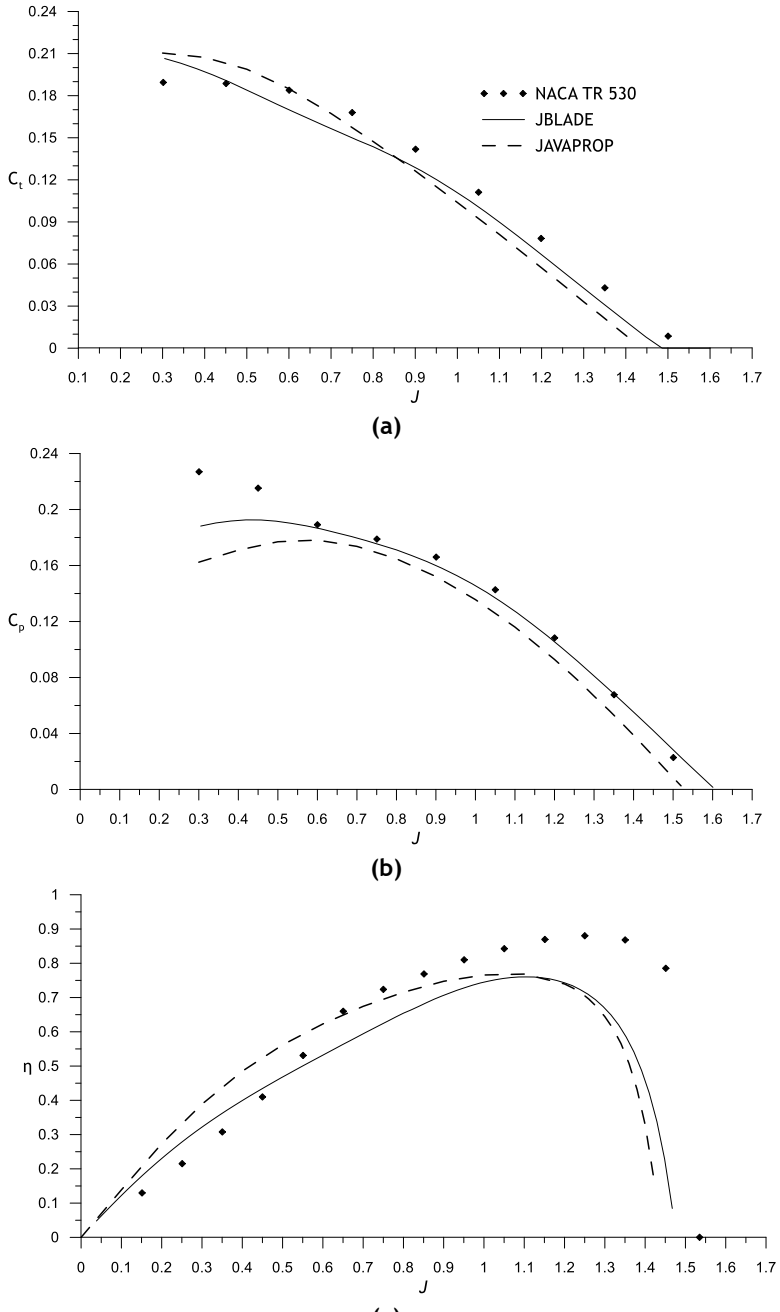

Figure 3.31 – Results of NACA TR 530 (Gray, 1941) for $\theta_{75}=30°$ (a) thrust coefficient (b) power coefficient (c) propeller efficiency.

The thrust coefficient (see Figure 3.32 (a)) is significantly over estimated by JBLADE for the advance ratios between 0.5 and 1.2. In addition, the thrust coefficient is slightly under predicted at bigger advance ratios but the JBLADE prediction is still closer to the experimental data than the JAVAPROP estimations obtained for this test case.

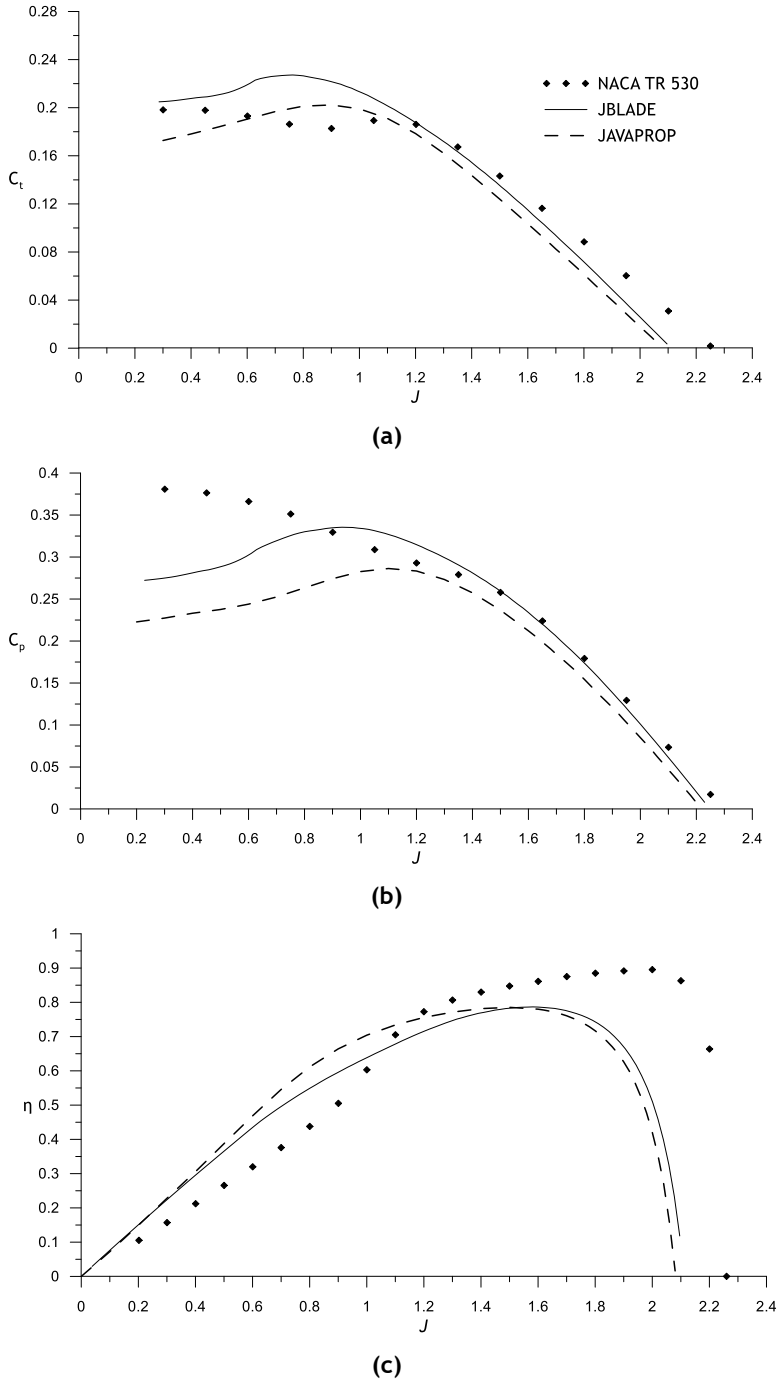

Figure 3.32 - Results of NACA TR 530 (Gray, 1941) for θ_{75}=40° (a) thrust coefficient (b) power coefficient (c) propeller efficiency.

Regarding power coefficient, presented in Figure 3.32 (b), it is observed that both JBLADE and JAVAPROP are under predicting the power coefficient in the smaller advance ratios region. However, the codes are giving better predictions in the bigger advance ratios region with a small advantage for the JBLADE software. Note that both experimental data and JBLADE prediction show a wave shape of the c_t and c_p curves at the lower end of the advance ratio. This behaviour is also observed in the experiments, although at a higher advance ratio.

Similarly to the previous test case, the advance ratio for the maximum propeller's efficiency (see Figure 3.32 (c)) the maximum efficiency is under estimated by both JBLADE and JAVAPROP codes. The maximum efficiency under prediction, in this test case, is related to the under prediction of the thrust coefficient at high advance ratios, since the power coefficient predicted closely match the experimental data for this advance ratio region. The codes' under prediction of the power coefficient in the smaller advance ratios region lead to an over estimation of the propeller efficiency observed in the advance ratios between 0.2 and 1.1.

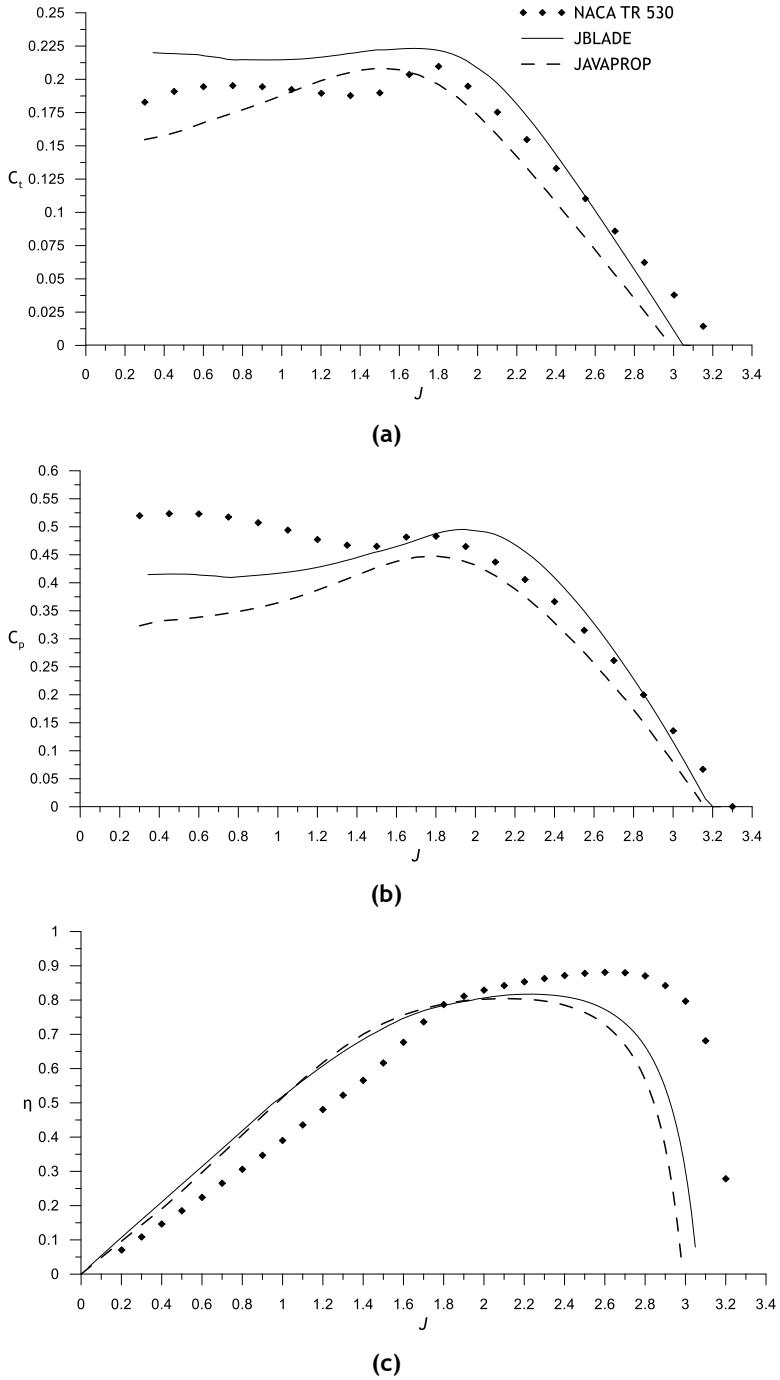

Figure 3.33 - Results of NACA TR 530 (Gray, 1941) for $\theta_{75}=50°$ (a) thrust coefficient (b) power coefficient (c) propeller efficiency.

The thrust coefficient data obtained for the propeller with $\theta_{75} = 50°$ (see Figure 3.33 (a)) show that JBLADE is slightly over estimating the thrust coefficient for the smaller advance ratios and under estimating it for the bigger values of the advance ratio. JAVAPROP is generally under predicting the thrust coefficient values over all the advance ratios, for this test case.

Figure 3.33 (b) presents the results for the power coefficient and it possible to observe that both codes are under predicting the values of the power coefficient at small advance ratios. The predictions of both JBLADE and JAVAPROP for bigger advance ratios is close to the experimental data.

The propeller efficiency data (see Figure 3.33 (c)) presents the same over estimation trend in the small advance ratios, due to the under prediction of the power coefficient in the smaller advance ratios. In addition, the maximum efficiency value is still under predicted by both JBLADE and JAVAPROP codes. The codes are also predicting a small advance ratio for the maximum efficiency value, when compared with experimental data.

The JBLADE software confirms the best overall results for these NACA Technical Report No. 530 test cases. The advantage of the JBLADE in these test cases comes from the better predictions of the power coefficient, since it estimates always higher power coefficient values for small advance ratios, when compared with JAVAPROP.

3.2.6.3 Adkins and Liebeck Propeller

The propeller presented by Adkins and Liebeck was also computed with JBLADE and the performance predictions were compared with the data found on the literature. The blade geometry (see Figure 3.15 (a)) was replicated inside JBLADE and it was herein analysed in the off-design condition.

The agreement between JBLADE and Adkins and Liebeck code as it is shown in Figure 3.34 is quite good. The differences between both codes in the low advance ratio region may come from the different approximations to the airfoil characteristics calculations done by different codes. However it was not possible to access the original code, and the results are compared only against the results published by Adkins & Liebeck (1994). The difference at Figure 3.34 (c) in the low advance region appears due to the different behaviour on the thrust coefficient results shown at Figure 3.34 (a).

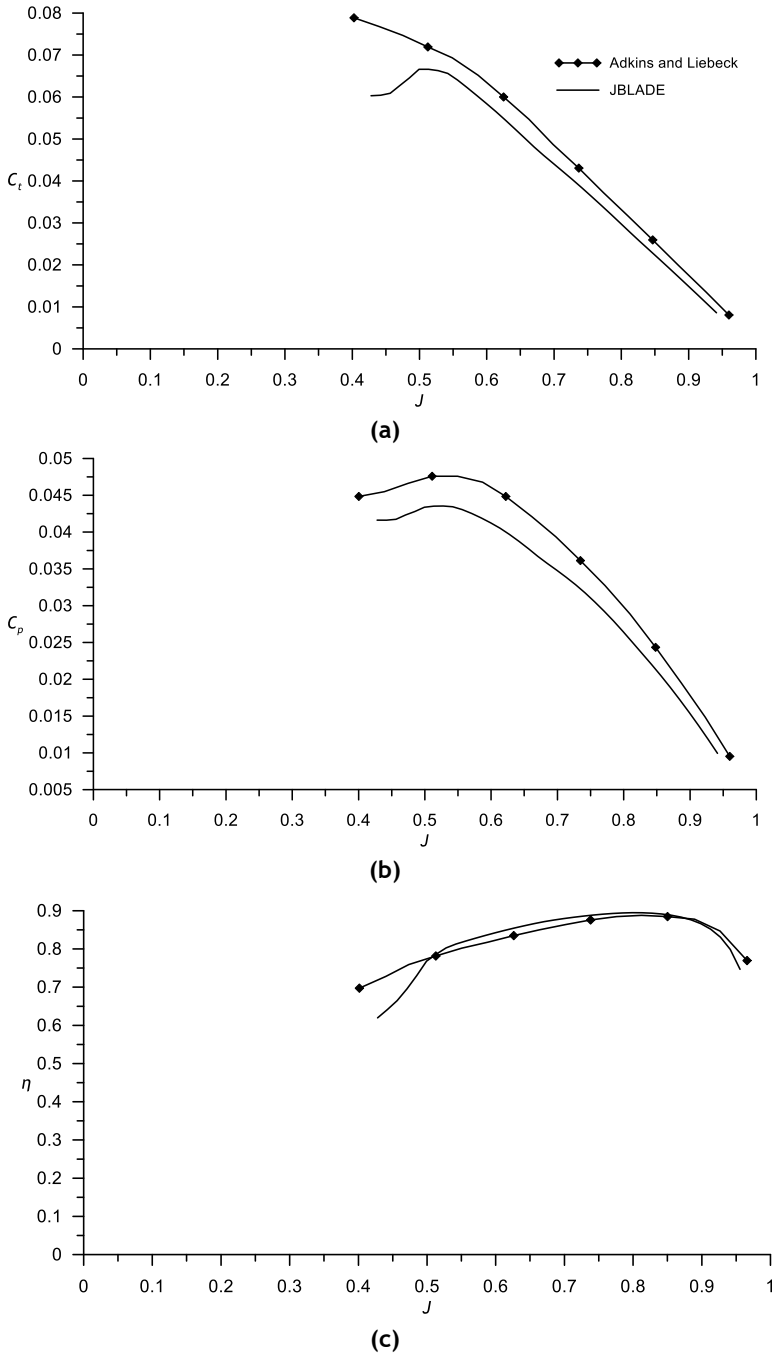

Figure 3.34 - Comparison between data predicted by JBLADE and data obtained from Adkins & Liebeck (1994). (a) thrust coefficient (b) power coefficient (c) propeller efficiency.

3.2.6.4 APC 11”x4.7” Propeller

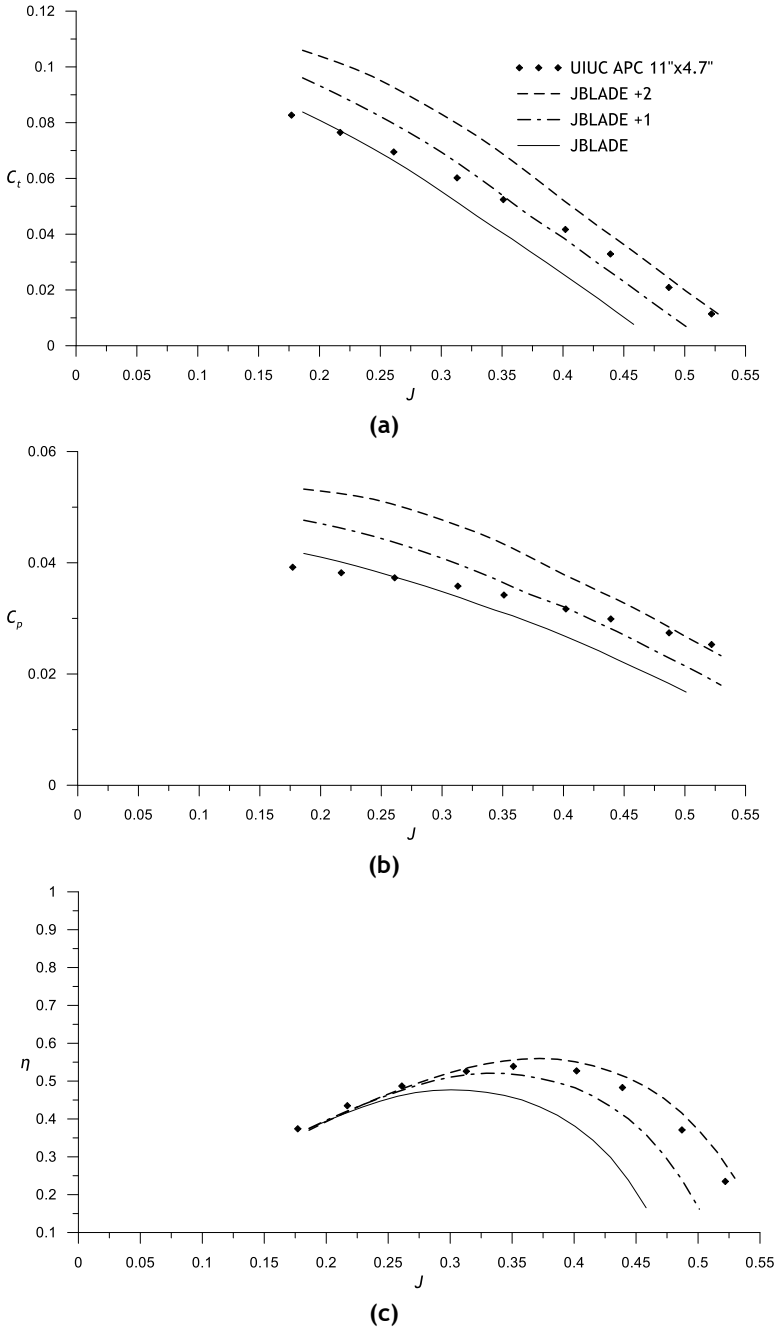

Figure 3.35 - Comparison between JBLADE predictions and data obtained from UIUC database for an APC 11”x4.7” for *3000* RPM (Brandt *et al.*, 2014). (a) thrust coefficient (b) power coefficient (c) propeller efficiency.

The comparison of the data predicted by JBLADE and experimental data obtained from UIUC Propeller Data Site (Brandt *et al.*, 2014) for the APC 11”x4.7” propeller at *3000* RPM is presented in Figure 3.35. Observing the thrust coefficient predictions (see Figure 3.35 (a)) it is possible to observe that JBLADE is in good agreement with experimental data for the smaller advance ratios region. However, for advance ratios bigger than 0.25 the JBLADE is predicting lower values of trust coefficient. Observing the Figure 3.35 (b) it is possible to observe the same behaviour, with JBLADE underpredicting the power coefficient for bigger advance ratios.

Since the advance ratio for the zero thrust condition as well as for the zero power condition are underpredicted, the advance ratio of the maximum efficiency is also underpredicted.

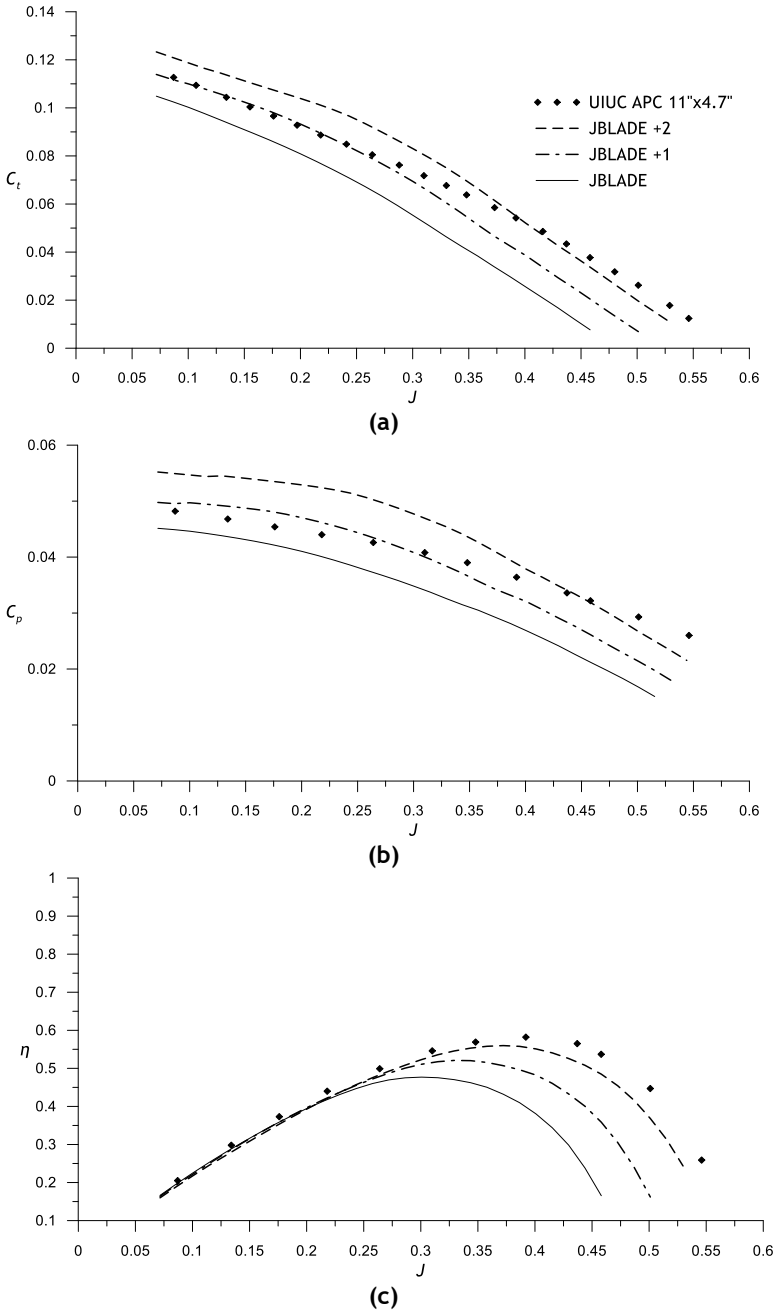

Figure 3.36 - Comparison between JBLADE predictions and data obtained from UIUC database for an APC 11"x4.7" for *6000* RPM (Brandt *et al.*, 2014). (a) thrust coefficient (b) power coefficient (c) propeller efficiency.

The data for the same propeller at *6000* RPM are presented at Figure 3.36 and also show that JBLADE is underpredicting both thrust coefficient (see Figure 3.36 (a)) and power coefficient (see Figure 3.36 (b)). Due to these underpredictions, the advance ratio for the maximum efficiency and the maximum efficiency (see Figure 3.36(c)) itself is underpredicted.

After a carefully analysis of the results and trying to understand what can be the origin of the difference between the simulations and the experimental data, the propeller performance coefficients obtained for different rotation speeds were found to grow when the rotational speed increases from *3000* RPM to *6000* RPM (see Figure 3.35 and Figure 3.36). This behaviour can be caused by the increase in the airfoil performance due to the Reynolds number increase. However, the XFOIL airfoil simulations did not show significant changes in the airfoil performance when the Reynolds number increases due to the increment in the rotation speed from *3000* RPM to *6000* RPM (see Figure 3.37).

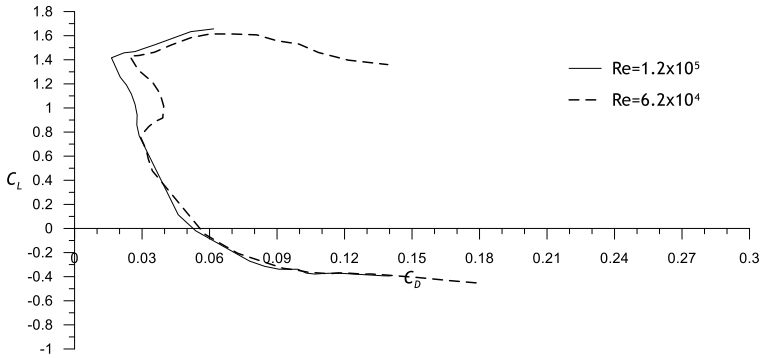

Figure 3.37 - Airfoil performance of the APC 11"x4.7" propeller obtained at *r/R=0.75* for *3000* RPM and *6000* RPM.

Other hypothesis was then formulated, based on the fact that propeller airfoil is very thin and the blades are susceptible to deform at higher rotational speed and thrust loadings, increasing its pitch angle. To verify this hypothesis, new simulations of the APC 11"x4.7" propeller were made in JBLADE considering a 1º and 2º increment on the blade's incidence angle. The results obtained with the new simulations seemed to be compatible with the hypothesis formulated, in which the blade was deformed to an increased pitch at *3000* RPM and even further at *6000* RPM, although more research needs to be done on this subject to measure the deformation. This blade deformation hypothesis lead to the implementation of a structural sub-module in the JBLADE in order to predict the deformation of the blades and allowing the user to perform an additional iteration loop to obtain the performance estimation of the deformed propeller. This *Structural sub-module* implementation and validation is described in detail in Section 3.2.7

3.2.7 - Structural Sub-Module Validation

The formulation presented in Section 2.6 was implemented inside JBLADE as a new sub-module, described in Section 3.1.6. In order to validate the implementation of the theory, the results obtained in JBLADE for different propellers' blades (see Table 3.2) were compared with simulations performed in the structural sub-module of CATIA V5®.

3.2.7.1 CATIA simulation validation

In order to validate the structural analysis inside CATIA a new structural simulation was defined. The blade was divided into 20 sections in order to apply the distributed force obtained in JBLADE as a group of discrete forces along the blade. The blade material was properly defined and the normal force previously calculated in the *Propeller Simulation sub-module* was then exported and inserted in CATIA for each respective section. An example of the results produced by a CATIA analysis is presented at Figure 3.38. The blade was considered as a cantilevered beam and the displacement of each section was exported in order to be compared with JBLADE data.

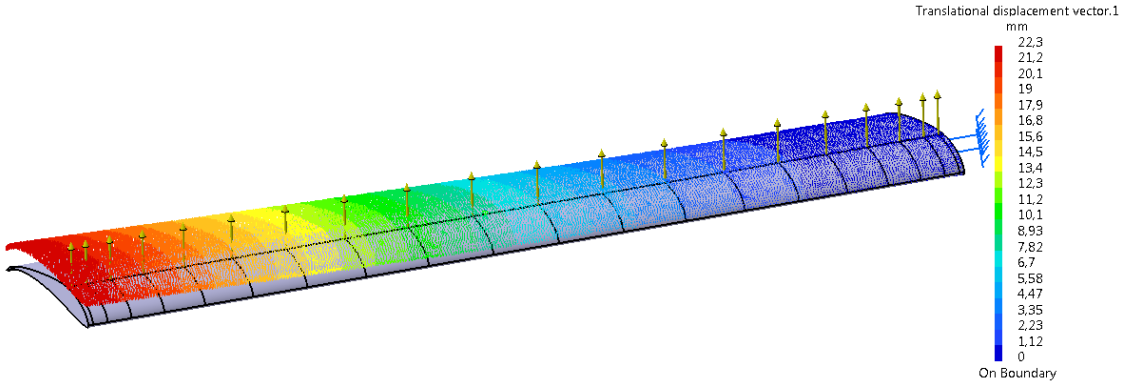

Figure 3.38 – Example of a bending Simulation in CATIA v5.

A mesh independency study was performed using Blade 5 (see Table 3.2), since it uses different airfoils, and it is a tapered blade, with non-uniform chord along the span, representing the more complex test case. Three meshes were defined and as it is possible to observe in Figure 3.39, the difference in the maximum displacement between the "Used Mesh" and the "Refined Mesh" is about 0.00046%. Thus, all the simulations in CATIA were performed with the intermediate mesh, saving some computational time.

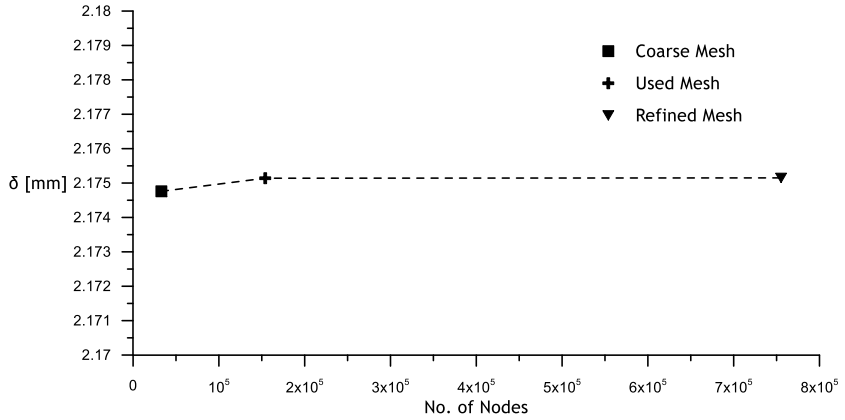

Figure 3.39 – Mesh independency study performed in CATIA for Blade 5.

3.2.7.2 Blade's geometrical properties validation

Concerning the blade's volume and mass calculations, five different blades were designed in JBLADE. The airfoils used (see Table 3.2) in the blades were exported from JBLADE and the blades were then built using the multi-section body tool in CATIA. Different structural concepts were used, as presented in Table 3.2: a completely solid blade (with different materials), a blade with a thin skin, and a blade with a skin and core material. Each blade was divided into 20 sections along which the properties were verified.

Table 3.2 – Blade Definition for Structural Sub-Module validation.

	Root Airfoil	Tip Airfoil	Root Chord, *m*	Tip Chord, *m*	Span, *m*	Structure Concept	Material
Blade 1	S1223	S1223	0.2	0.2	1.0	Solid	Aluminium
Blade 2	NACA 0012	NACA 0012	0.2	0.2	1.0	Solid	Pine Wood
Blade 3	NACA 0012	NACA 0012	0.2	0.2	1.0	*6* mm skin thickness	Aluminium
Blade 4	NACA 0012	NACA 0012	0.2	0.2	1.0	*6* mm skin + Core Material	Aluminium + Rohacell
Blade 5	NACA 4412	NACA 0012	0.3	0.1	1.0	Solid	Aluminium

The properties of the materials used in the blades are presented in Table 3.3.

Table 3.3 – Properties of the Materials used in the blades.

Material	Density, kg/m^3	Young Modulus, *GPa*	Shear Modulus, *GPa*
Aluminium	2710	70.0	26.0
Pine Wood	500	17.0	5.9
Rohacell 110 A	110	0.16	0.05

The results of volume and mass estimations obtained in JBLADE were compared with CATIA (see Table 3.4) and it is possible to conclude that the difference between both software is always less than 0.1%.

As expected, the worst result was performed for the blade 5, since it has different airfoils in the root and tip and different chords as well. The validation of the moment of inertia calculation (see Section 2.6.2) was also performed and the results are presented in Table 3.5 for the used airfoils.

Table 3.4 – Volume and Mass comparison using JBLADE and CATIA V5.

	JBLADE		CATIA		Error, %	
	Volume, dm^3	Mass, kg	Volume, dm^3	Mass kg	Volume	Mass
Blade 1	2.595	7.032	2.597	7.038	0.0848	0.0881
Blade 2	3.288	4.275	3.288	4.275	0.0079	0.0094
Blade 3	0.130	0.353	0.130	0.353	0.0154	0.028
Blade 4	3.288	4.622	3.288	4.622	0.0082	0.0092
Blade 5	3.5607	9.651	3.563	9.656	0.065	0.052

It is shown that the bigger difference between the JBLADE and CATIA occurs for the I_{xx} of S1223 airfoil. This may be attributed to the higher camber of the airfoil and its thin trailing edge. For all the NACA airfoils, the estimations obtained in JBLADE are in good agreement with the CATIA data.

Table 3.5 – 2D Airfoil properties comparison using JBLADE and CATIA.

		JBLADE	CATIA	Error, %
S1223	I_{xx}, m^4	6.12e-07	5.70e-07	6.818
	I_{yy}, m^4	2.70e-5	2.76e-05	2.211
	Xcentroid, mm	106.64	107.068	0.362
	$Y_{centroid}$, mm	20.508	20.476	0.401
	Area, cm^2	60.0696	60.287	0.362
NACA 0012	I_{xx}, m^4	1.09e-07	1.09e-07	0.071
	I_{yy}, m^4	7.26e-06	7.26e-06	0.009
	$X_{centroid}$, mm	84.091	84.087	0.005
	$Y_{centroid}$,mm	6.85e-19	0.000	0.000
	Area, cm^2	32.881	32.884	0.008
NACA 2312	I_{xx}, m^4	1.53e-07	1.52e-07	0.839
	I_{yy}, m^4	7.25e-06	7.26e-06	0.151
	$X_{centroid}$, mm	84.124	84.089	0.041
	$Y_{centroid}$, mm	12.548	12.545	0.027
	Area, cm^2	32.857	32.872	0.044
NACA 4412	I_{xx}, m^4	7.55e-09	7.55e-09	0.047
	I_{yy}, m^4	4.54e-07	4.54e-07	0.076
	$X_{centroid}$, mm	42.055	42.044	0.025
	$Y_{centroid}$, mm	3.086	3.086	0.012
	Area, cm^2	8.219	8.221	0.029

The results for the intermediate sections of Blade 5 are presented in Table 3.6, since the airfoils in the middle of the blade are intermediate shapes between the root and tip airfoils. Table 3.6 shows that JBLADE is correctly predicting the intermediate sections' properties. The bigger

difference between JBLADE data and CATIA data occurs for the I_{xx} of section 18. However even in this section the difference is small, below the 3.5%.

Table 3.6 – 2D properties comparison using JBLADE and CATIA for intermediate sections of Blade 5.

	JBLADE I_{xx}, m^4	CATIA I_{xx}, m^4	*Error* %	JBLADE I_{yy}, m^4	CATIA I_{yy}, m^4	*Error* %	JBLADE *Area*, mm^2	CATIA *Area*, mm^2	*Error* %
1	6.03E-07	6.02E-07	0.021	3.62E-05	3.62E-05	0.072	73.42	73.44	0.031
2	5.75E-07	5.75E-07	0.035	3.46E-05	3.46E-05	0.058	71.79	71.82	0.031
3	5.32E-07	5.33E-07	0.131	3.21E-05	3.21E-05	0.053	69.17	69.19	0.030
4	4.78E-07	4.79E-07	0.241	2.89E-05	2.90E-05	0.071	65.65	65.67	0.032
5	4.16E-07	4.18E-07	0.375	2.53E-05	2.53E-05	0.047	61.39	61.41	0.035
6	3.51E-07	3.53E-07	0.509	2.15E-05	2.15E-05	0.055	56.57	56.59	0.034
7	2.88E-07	2.90E-07	0.657	1.77E-05	1.77E-05	0.058	51.37	51.39	0.037
8	2.29E-07	2.31E-07	0.760	1.40E-05	1.42E-05	1.464	45.98	46.00	0.039
9	1.77E-07	1.79E-07	0.819	1.11E-05	1.11E-05	0.005	40.60	40.62	0.042
10	1.34E-07	1.35E-07	0.842	8.41E-06	8.41E-06	0.032	35.38	35.40	0.044
11	9.83E-08	9.90E-08	0.764	6.23E-06	6.24E-06	0.021	30.47	30.48	0.045
12	7.08E-08	7.13E-08	0.649	4.53E-06	4.53E-06	0.018	25.97	25.98	0.048
13	5.03E-08	5.50E-08	8.603	3.24E-06	3.24E-06	0.003	21.96	21.97	0.048
14	3.54E-08	3.55E-08	0.234	2.30E-06	2.30E-06	0.011	18.49	18.50	0.049
15	2.49E-08	2.50E-08	0.029	1.63E-06	1.63E-06	0.013	15.57	15.58	0.042
16	1.78E-08	1.77E-08	0.536	1.17E-06	1.17E-06	0.021	13.19	13.20	0.038
17	1.30E-08	1.30E-08	0.178	8.61E-07	8.61E-07	0.001	11.32	11.33	0.040
18	9.98E-09	9.65E-09	3.469	6.62E-07	6.62E-07	0.003	9.93	9.93	0.025
19	8.12E-09	8.11E-09	0.113	5.40E-07	5.40E-07	0.006	8.97	8.97	0.017
20	7.12E-09	7.12E-09	0.005	4.74E-07	4.74E-07	0.014	8.40	8.41	0.017

3.2.7.3 JBLADE bending validation

The blades presented in the Table 3.2 were simulated and the results for each blade are presented and they will be discussed below.

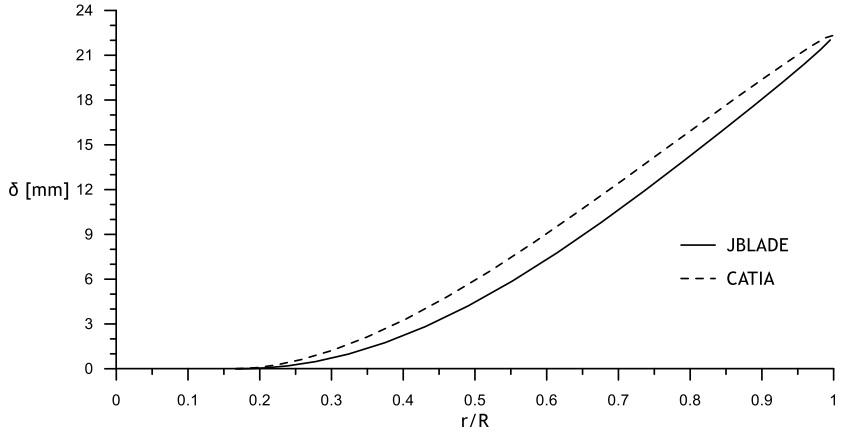

Figure 3.40 – Comparison of Bending calculated in JBLADE and CATIA for Blade 1.

Figure 3.40 presents the results for Blade 1 that uses the NACA 0012 airfoil from root to tip with a constant chord of 0.2m. The results show a good agreement between the vertical displacement predicted by JBLADE and CATIA. The difference between both curves may be due to the difference in the I_{xx} calculation (see Table 3.5). Since JBLADE predicts a higher I_{xx} for the blade's cross section, it results in a smaller bending of the blade, when compared with CATIA.

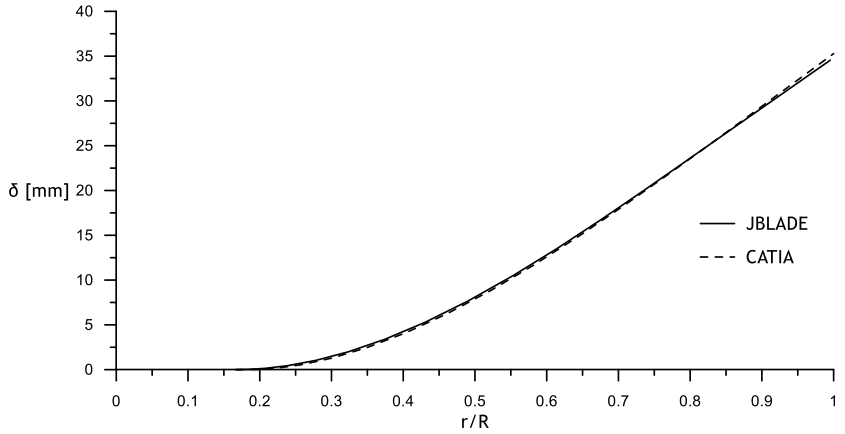

Figure 3.41 – Comparison of Bending calculated in JBLADE and CATIA for Blade 2.

The "Blade 2" is similar to the "Blade 1" but it is made from Pine Wood instead of Aluminium. The results are presented in Figure 3.41, and it is shown that JBLADE prediction of the blade's bending perfectly matches the CATIA simulation results. Since this blade uses a different material, it also shows that the JBLADE can correctly estimate the blade bending regardless the material selected for the blades.

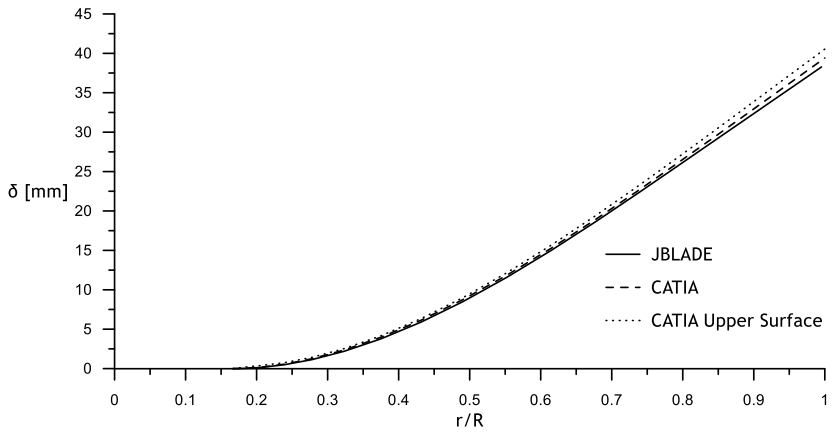

Figure 3.42 – Comparison of Bending calculated in JBLADE and CATIA for Blade 3.

Figure 3.42 presents the results of the "Blade 3". These results show that JBLADE is predicting less vertical displacement, and the difference increases towards the blade's tip. In all the simulations above, the vertical displacement was measured in the nodes of the upper surface of the blades. Since the "Blade 1" and "Blade 2" are completely solid, it was assumed that no internal deformation of the cross section occurred. However, for the case of the "Blade 3", since the blade is composed only by a thin skin of aluminium, the blade's cross section had suffered a small deformation (see Figure 3.43). Thus, the values of the displacement along the blade's leading edge were collected and also compared with JBLADE results in Figure 3.42. It was concluded that the difference in the vertical displacement between JBLADE and CATIA decreases, since the deformation on the blade's leading edge is smaller.

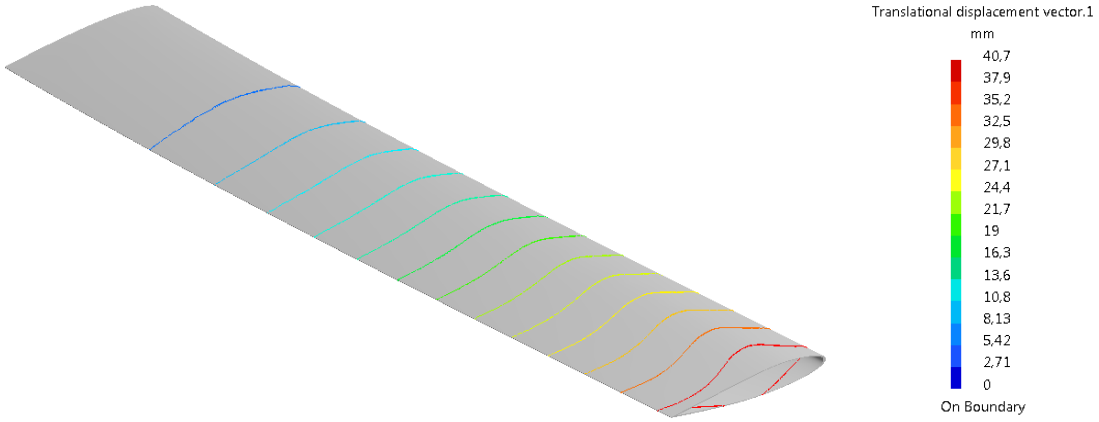

Figure 3.43 – Illustration of the skin deformation calculated in CATIA.

The "Blade 4" test case considers a constant section blade with a skin made by Aluminium and a Foam Core. The blade has a constant chord from root to tip, being similar to the "Blade 3" test case. Figure 3.44 shows that the vertical displacement estimated by JBLADE is in good agreement with CATIA data. This good agreement can be explained by the presence of the core material, which prevents the deformation of the blade's skin. At the same time these results

also confirm that the difference between JBLADE and CATIA in the "Blade 3" results came from the skin deformation of the blade.

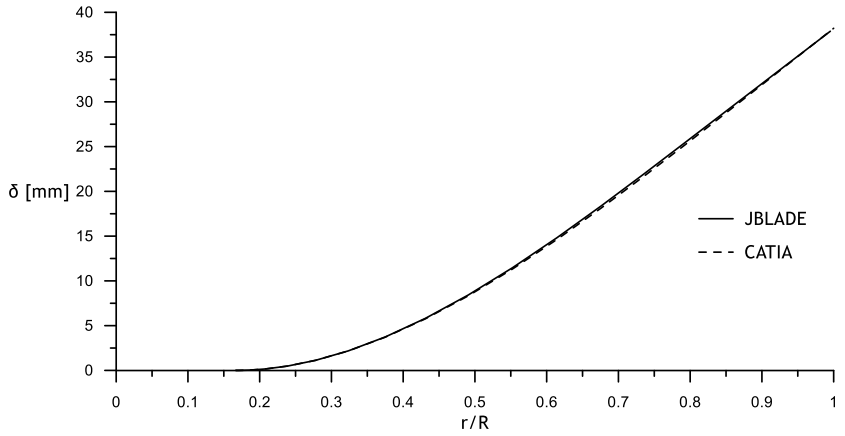

Figure 3.44 – Comparison of Bending calculated in JBLADE and CATIA for Blade 4.

Concerning the "Blade 5" test case (see Figure 3.45), the displacement estimated by JBLADE is also in a good agreement when compared with CATIA results. The small differences in the vertical displacement along the blade's span may arise from the fact that the blade was divided only in 20 stations. Since it has a more complex shape than the blades used in the previous tests cases may be necessary to increase the number of sections. In fact, there are small differences in the I_{xx} along the sections, as it is possible to observe in Table 3.6, which also contributes to the difference presented in Figure 3.45.

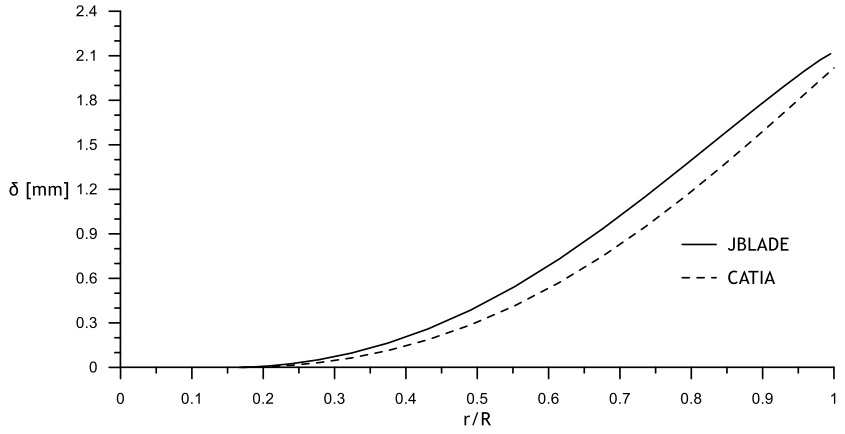

Figure 3.45 – Comparison of Bending calculated in JBLADE and CATIA for Blade 5.

The bending test cases presented above showed that JBLADE can be used to predict the blade's bending due to its produced thrust. This can help the user to design a more efficient propeller accounting with possible deformations (and the consequent losses of performance by the blade's airfoils) and helping the user to estimate the weight of the propeller, which can be crucial for the vehicles like MAAT cruiser airship.

3.2.7.4 JBLADE twist deformation validation

In order to validate the twist deformation calculation in JBLADE the formulation described in Section 2.6.3 was implemented in JBLADE and the propellers presented in Table 3.2 were validated through the comparison of JBLADE results with CATIA simulations.

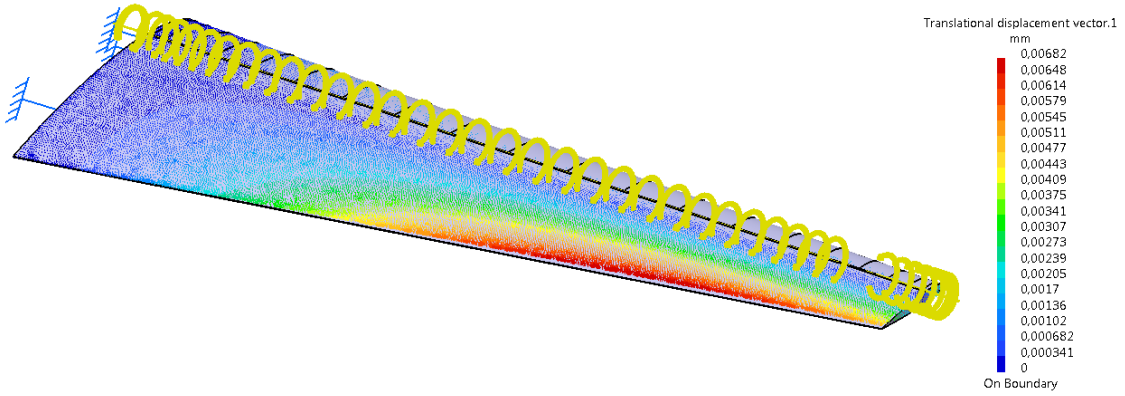

Figure 3.46 – Example of a Twist Deformation Simulation in CATIA V5.

A blade's twist simulation was defined in CATIA with respective twisting moments applied at 25% of the blade's chord. The moments were obtained in the JBLADE *Propeller Definition and Simulation sub-module* (see Section 3.1.5) and were then introduced in CATIA, as in Figure 3.46. The results were then exported from CATIA and compared with the JBLADE results. The vertical displacement of the trailing edge was used to address the blade's twist.

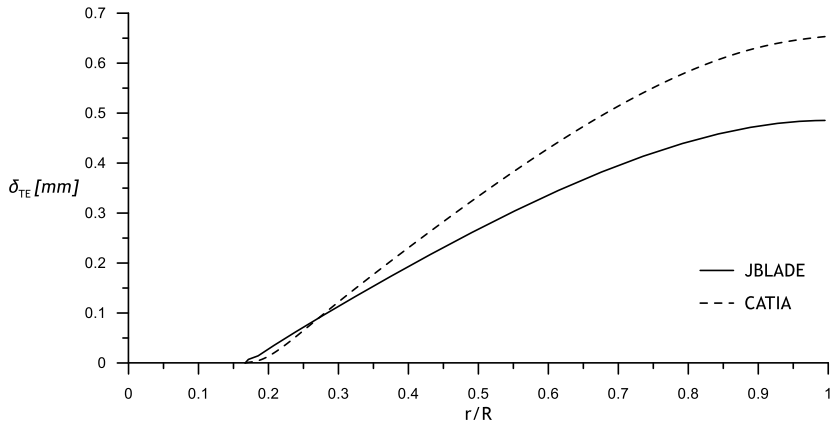

Figure 3.47 – Trailing Edge Displacement Comparison for Blade 1.

Figure 3.47 presents the comparison of JBLADE calculations and CATIA simulations for the "Blade 1 test case. The results show that JBLADE is under predicting the trailing edge displacement when compared with CATIA. The properties of the blades were estimated using the J_s (see Eq. 2.91), which may help to explain the difference between JBLADE and CATIA.

Since the JBLADE is predicting a bigger I_{xx} for the S1223 airfoil (see Table 3.5), it will result in a smaller twist deformation for the same load.

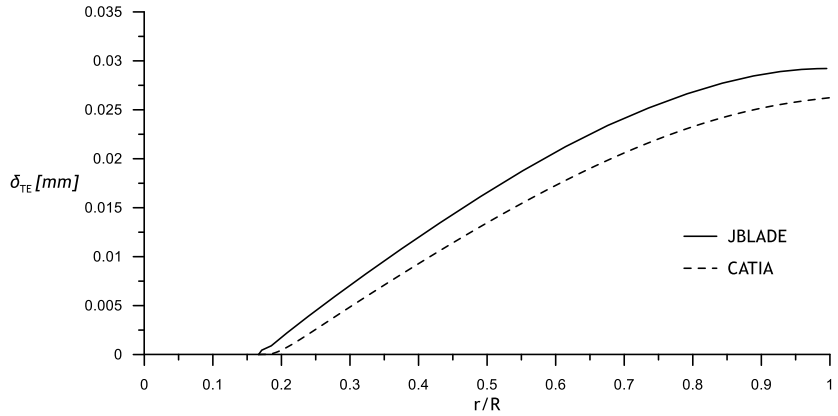

Figure 3.48 – Trailing Edge Displacement Comparison for Blade 2.

In Figure 3.48 it is possible to observe a JBLADE's good prediction of the trailing edge displacement along the blade's span for the "Blade 2" test case. The biggest discrepancy between JBLADE and CATIA occurs at the tip of the blade, where JBLADE is predicting the trailing edge displacement around 11% more than CATIA.

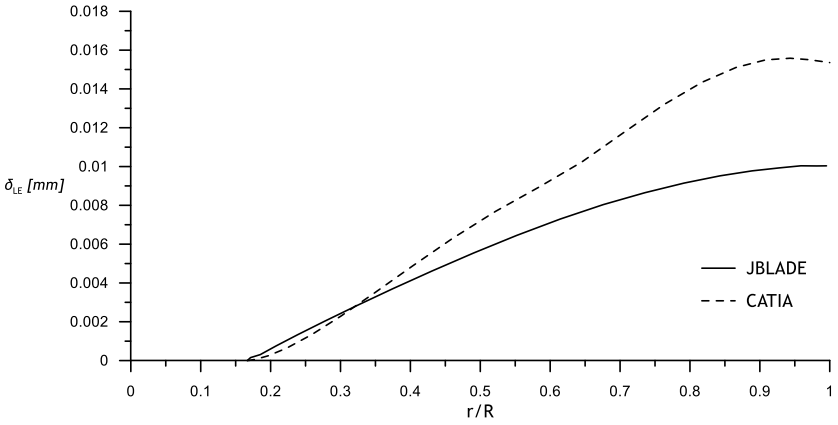

Figure 3.49 – Leading Edge Displacement Comparison for Blade 3.

The results of the "Blade 3" test case are presented in Figure 3.49. It can be seen that the agreement is not good. This can be attributed to the fact that this blade is made only with a 6 mm skin of aluminium. Therefore, CATIA shows large deformations of the skin (see Figure 3.43) that are included in the structural behaviour of the blade. On the other hand the skin deformation is not accounted in JBLADE. Another factor for the discrepancy may be that in JBLADE the bending deformation is accounted solely due to the thrust distribution along the blade while in fact there is some bending of the 25% chord line due to the actual torsion occurring around the elastic axis instead of the 25% chord line. JBLADE can be improved in the future, regarding this matter. For now it is not considered important regarding the propeller performance because this depends mostly on the torsion deformation distribution. In this

specific test case, the leading edge displacement was used as the comparison between JBLADE and CATIA, since the deformation is smaller on this region. The maximum difference occurs at the blade's tip with JBLADE predicting about 35% less leading edge displacement, since it does not account for any cross section deformation.

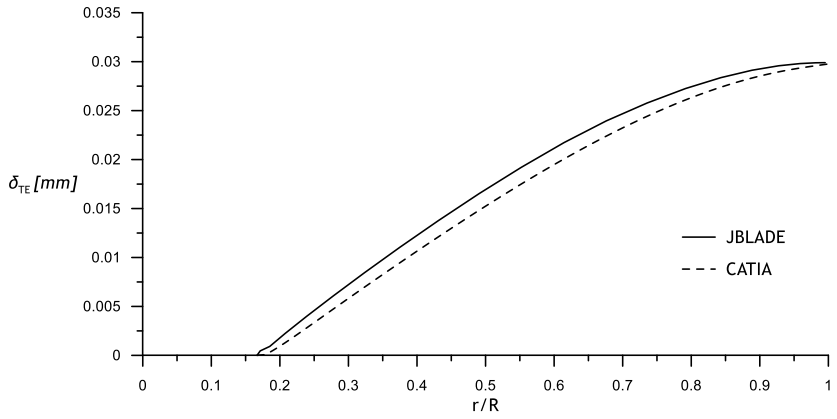

Figure 3.50 – Trailing Edge Displacement Comparison for Blade 4.

Figure 3.50 shows the trailing edge displacement comparison for "Blade 4" test case. Similarly to what was presented at Section 3.2.7.3, the JBLADE's predictions closely match the values obtained in CATIA simulations, since the core material present in this blade does not allow the cross section deformation. The small differences presented in Figure 3.50 may be attributed to the difference in the I_{yy} estimation, presented in Table 3.5 for the NACA 0012 airfoil.

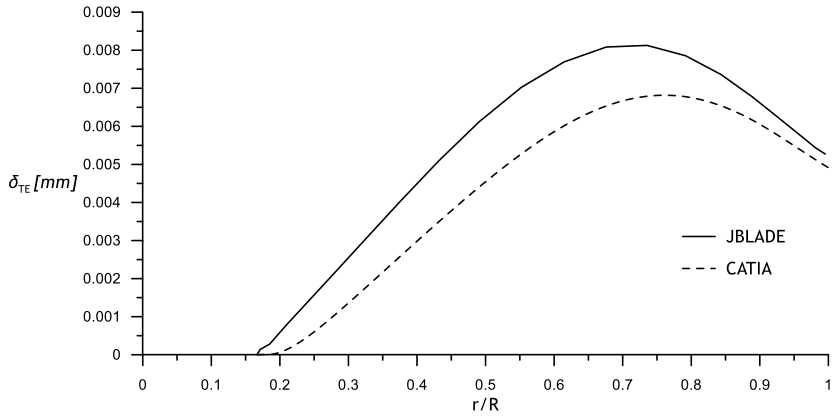

Figure 3.51 – Trailing Edge Displacement Comparison for Blade 5.

The results for the "Blade 5" test case are presented in Figure 3.51. Maximum difference for the trailing edge displacement occurs around 750 mm and the difference between JBLADE and CATIA is around 25%. JBLADE is correctly predicting the behaviour of the deformation, following the trend obtained in CATIA. The difference come from I_{xx} along the span as well as from the twisting constant J_s, since JBLADE uses only an approximation based in the cross section area, chord and section's I_{xx}.

The test cases presented above have shown that JBLADE is capable to correctly predict the blade's deformation, helping the user to avoid possible damages on the designed propellers. In addition, looking to the absolute values of the twist validation test cases it is possible to conclude that the values are small and even differences of about 10% are almost unnoticeable and they will not affect the propellers's performance in a significant way.

This page has been intentionally left blank
for double side copying

Chapter 4

Comparison between Computational Fluid Dynamics and XFOIL Predictions for High Lift Low Reynolds Number Airfoils

Blade Element Momentum theory is an extensively used technique for calculation of propeller aerodynamics performance. To use this method the airfoil data need to be as accurate as possible in order to allow the correct calculation of the loads and power using the BEM code. At the same time, Computational Fluid Dynamics methods are becoming increasingly popular in the design and optimization of devices that depend on aerodynamics. For fixed and rotary wings applications, the airfoil lift over drag coefficient is what most determines the device's performance such that selecting a suitable computational tool is crucial for the design engineer. In the case of airfoils operating at low Reynolds numbers ($60\,000<Re<500\,000$), an accurate prediction of the transition position along the chord is essential to correctly simulate their performance characteristics. It has been shown (Selig, 2003) that XFOIL code has this capability and is widely used for airfoil design and optimization. However, it is unclear if recent transition and turbulence models can produce better airfoil performance predictions. The XFOIL Code, the Shear Stress Transport k-ω turbulence model and a refurbished version of k-kl-ω transition model were used to predict the airfoil aerodynamic performance. These airfoil performance predictions are compared to evaluate if CFD could improve JBLADE propeller performance estimation.

4.1 - Theoretical Formulation

4.1.1 - *k-kl-ω* model

The work of Mayle & Schulz (1996), was responsible for setting the foundations for the laminar kinetic energy theory. The latter theory accounts for the kinetic energy of the velocity fluctuations that occur within the laminar boundary layer pre-transitional region. These velocity oscillations were measured for the first time in 1937 as a result of the pioneer experimental work of Dryden (1937).

It was concluded that the free-stream turbulence was responsible for the occurrence of such boundary layer perturbations. Taylor (1939) made an interesting observation regarding these pre-transitional laminar velocity fluctuations. It was acknowledged that these oscillations were related with thickening and thinning of the boundary layer. Later in 1971, the experimental work of Klebanoff (1971) explicitly identified these stream wise fluctuations, naming them as breathing modes. However, Kendall (1991) renamed these velocity oscillations as Klebanoff modes in honour of the original discoverer. Based on this new transition theory, many novel RANS transition models have been developed since then. In 2004, the numerical work of Walters & Leylek (2004) presented a locally formulated laminar fluctuation kinetic energy transition model. The turbulence transition closure was named $k-kl-\epsilon$, and it was implemented in the commercial software Ansys Fluent. Later in 2008, Walters & Cokljat (2008) presented an improved version of the original 2004 transition model, the $k-kl-\omega$. Besides the change in the turbulence length scale variable from ϵ to ω some model constants and functions were also modified. The *k-kl-ω* transition model can be resumed down to three transport equations. One for the laminar fluctuations kinetic energy, another for the turbulent kinetic energy and the last one for the specific turbulent kinetic energy dissipation rate. The incompressible transport equations are disclosed in Eq. 4.1 to Eq. 4.3:

$$\frac{\partial kl}{\partial t} = P_{kl} + R_{BP} - R_{NAT} - D_L + \frac{\partial}{\partial x_j}\left[\nu \frac{\partial kl}{\partial x_j}\right] \tag{4.1}$$

$$\frac{\partial k}{\partial t} = P_k + R_{BP} + R_{NAT} - \omega k - D_T + \frac{\partial}{\partial x_j}\left[\left(\nu + \frac{\alpha_t}{\sigma_k}\right)\frac{\partial k}{\partial x_j}\right] \tag{4.2}$$

$$\frac{\partial \omega}{\partial t} = C_{\omega_1}\frac{\omega}{k}P_{k_{t,s}} + \left(\frac{C_{\omega R}}{fw} - 1\right)\frac{\omega}{k}\left(R_{BP} + R_{NAT}\right) - C_{\omega_2}\omega^2 + C_{\omega_3}f_\omega \alpha_t f_W^2 \frac{\sqrt{k}}{y^3} + \frac{\partial}{\partial x_j}\left[\left(\nu + \frac{\alpha_t}{\sigma_\omega}\right)\frac{\partial \omega}{\partial x_j}\right] \tag{4.3}$$

The production terms in Eq. 4.1 and Eq. 4.2 are based on velocity strain rate defined in Eq. 4.4 and Eq. 4.5:

$$P_k = \nu_{T,s} S^2 \tag{4.4}$$

$$P_{kl} = \nu_{T,l} S^2 \quad 4.5$$

One of the most interesting features of this transition model is the turbulence scale division. Introduced in the work of Walters & Leylek (2004), this was also applied in the 2008 $k-kl-\omega$ transition model version (Walters & Cokljat, 2008). This concept has been shown to be present in fully turbulent boundary layers by Moss & Oldfield (1996) and Thole & Bogard (1996). The concept divides the turbulence in large and small scales. The large scale is related to the laminar fluctuation kinetic energy production through the "splat mechanism", as suggested by Volino (1998) and mentioned by Bradshaw (1994). The small scale is related to regular turbulence. The model assumes that far from wall surfaces the small scale turbulent kinetic energy is equal to the free-stream turbulent kinetic energy. The definition of the limiting length scale is obtained from Eq. 4.6, where λ_T is the length of the small scale turbulence defined in Eq. 4.7:

$$\lambda_{eff} = \min(C_{\lambda y}, \lambda_T) \quad 4.6$$

$$\lambda_T = \frac{\sqrt{k}}{\omega} \quad 4.7$$

The small scale turbulent kinematic viscosity is calculated in Eq. 4.8, making use of a collection of damping functions, which attempt to simulate various mechanisms, such as the shear-sheltering effect presented in Eq. 4.9, the turbulence intermittency (see Eq. 4.10) and the kinematic and viscous wall effect as presented in Eq. 4.11 and Eq. 4.12 respectively. The last damping function is based on effective turbulent Reynolds number (see Eq. 4.13) and in order to satisfy the realizability of C_μ, it is calculated according to Eq. 4.14. In the work of Walters & Cokljat (2008) and Walters & Leylek (2004), C_μ is a simplified version of its original form according to the work of Shih *et al.* (1994) and Shih *et al.* (1995).

$$\nu_{T,s} = f_v f_{INT} C_\mu \sqrt{k_{T,s}} \lambda_{eff} \quad 4.8$$

$$f_{SS} = e^{\wedge}\left[-\left(\frac{C_{ss}\nu\Omega_{\mathrm{v}}}{k}\right)^2\right] \quad 4.9$$

$$f_{INT} = \min\left(\frac{k_L}{C_{INT} k_{TOT}}, 1\right) \quad 4.10$$

$$f_W = \frac{\lambda_{eff}}{\lambda_T} \quad 4.11$$

$$f_v = 1.0 - e^{-\frac{\sqrt{Re_T}}{A_v}} \quad 4.12$$

$$Re_T = \frac{f_W^2 k}{\nu\omega} \quad 4.13$$

$$C_\mu = \frac{1}{A_0 + A_s\left(\frac{S}{\omega}\right)} \quad 4.14$$

The remaining *k-kl-ω* transition model description can be found in the work of Walters & Cokljat (2008). The described transition model was implemented in the open-source software OpenFoam (Greenshields, 2015). After a systematic analysis and testing of the transition model some modifications were proposed by Vizinho *et al.* (2013). Application of such modifications yielded improved results. One of the applied changes to the model was made to the turbulence intermittency damping function f_{INT} (see Eq. 4.10). This alteration avoids the fact that the original model predicts zero turbulent viscosity in the free-stream. This is so since k_L exists only near wall surfaces. Therefore the proposed term is then calculated as presented in Eq. 4.15:

$$f_{INT}^{new} = \min\left(\frac{k}{C_{INT}k_{TOT}}, 1\right) \qquad 4.15$$

Another relevant change in relation to the original model is the definition of turbulence Reynolds number, Re_T (see Eq. 4.13). The classical literature definition of turbulence Reynolds number as used by several turbulence models(Chang *et al.*, 1995; Craft *et al.*, 1997; Lardeau *et al.*, 2004) was applied also in the modified transition model. This will result in an improved asymptotic skin-friction coefficient behaviour along the fully turbulent region of the flow. The altered term is presented in Eq. 4.16.

$$Re_T^{new} = \frac{k}{\nu\omega} \qquad 4.16$$

The original model's turbulence specific dissipation rate destruction term is $-C_{\omega 2}\omega^2$. It was observed that the latter had an excessive effect near the wall. Also, in the work of Craft *et al.* (1996) the presented turbulence model has a set of equations resembling the presented turbulent kinetic energy, k, and the specific turbulent kinetic energy dissipation rate, ω, of the *k-kl-ω* transition model. In the present work, instead of ω, the transported quantity is the turbulent kinetic energy dissipation rate, $\tilde{\epsilon}$. The function of interest is $C_{\epsilon 2}$. This is multiplied by the term responsible for the destruction of the turbulent kinetic energy dissipation rate. Near the wall, its influence is reduced. The proposed hypothesis is then the imposition of a damping function, f_W, (see Eq. 4.11), multiplied to the $-C_{\omega 2}\omega^2$ term. The resulting term is given in the third element on the right side of Eq. 4.17.

$$\frac{D\omega}{Dt} = C_{\omega 1}\frac{\omega}{k}P_k + \left(\frac{C_{\omega R}}{f_W} - 1\right)\frac{\omega}{k}(R_{BP} + R_{NAT}) - C_{\omega 2}\omega^2 f_W + \\ + C_{\omega 3}f_\omega \alpha_T f_W^2 \frac{\sqrt{k}}{y^3} + \frac{\partial}{\partial x_j}\left[\left(\nu + \frac{\alpha_t}{\sigma_\omega}\right)\frac{\partial \omega}{\partial x_j}\right] \qquad 4.17$$

A more detailed description of the modified $k - kl - \omega$ turbulence transition model version is available in the work of Vizinho *et al.*(2013).

4.1.2 - Shear Stress Transport *k-ω* model

The Shear Stress Transport (SST) *k-ω* model (Menter, 1992, 1994) is a two-equation eddy-viscosity model. This Menter's *SST* formulation was developed to effectively blend the robust and accurate formulation of the *k-ω* model in the near wall region with the $k-\varepsilon$ model behaviour as the model switches to the latter away from the wall. The authors decided to choose the SST *k-ω* model due to its accuracy for a wide class of flows in which low Reynolds numbers airfoils are inserted as suggested in the literature (Bardina *et al.*, 1997). The SST *k-ω* model has a similar formulation to the Standard *k-ω* model. The transport equations are defined as presented in Eq. 4.18 and Eq. 4.19:

$$\frac{\partial}{\partial t}(\rho k)+\frac{\partial}{\partial x_i}(\rho k u_i)=\frac{\partial}{\partial x_j}\left(\Gamma_k\frac{\partial k}{\partial x_j}\right)+\tilde{G}_k-Y_k+S_k \tag{4.18}$$

and

$$\frac{\partial}{\partial t}(\rho \omega)+\frac{\partial}{\partial x_i}(\rho \omega u_i)=\frac{\partial}{\partial x_j}\left(\Gamma_\omega\frac{\partial \omega}{\partial x_j}\right)+G_\omega-Y_\omega+D_\omega+S_\omega \tag{4.19}$$

The $\tilde{G}_k$ represents the generation of turbulence kinetic energy due to the mean velocity gradients, calculated according to Eq. 4.20:

$$G_k=-\rho\overline{u_i'u_j'}\frac{\partial u_j}{\partial x_i} \tag{4.20}$$

The effective diffusivities for the $k-\omega$ model are given by Eq. 4.21:

$$\Gamma_k=\mu+\frac{\mu_t}{\sigma_k} \tag{4.21}$$

$$\Gamma_\omega=\mu+\frac{\mu_t}{\sigma_\omega} \tag{4.22}$$

Where σ_k and σ_ω are the turbulent Prandtl numbers for *k* and *ω* respectively and they are calculated as in Eq. 4.23 and Eq. 4.24:

$$\sigma_k=\frac{1}{\frac{F_1}{\sigma_{k,1}}+\frac{(1-F_1)}{\sigma_{k,2}}} \tag{4.23}$$

$$\sigma_\omega=\frac{1}{\frac{F_1}{\sigma_{\omega,1}}+\frac{(1-F_1)}{\sigma_{\omega,2}}} \tag{4.24}$$

The turbulent viscosity μ_t in Eq. 4.21 is computed as follows:

$$\mu_t = \frac{\rho k}{\omega} \frac{1}{\max\left[\frac{1}{\alpha^*}, \frac{SF_2}{a_1 \omega}\right]} \quad 4.25$$

where S represents the strain rate magnitude.

4.1.2.1 Low Reynolds Correction

The low Reynolds correction implemented in Ansys Fluent® modifies the α^* coefficient (see Eq. 4.25). This coefficient damps the turbulent viscosity and it is given by Eq.

$$\alpha^* = \alpha_\infty^* \left(\frac{\alpha_0^* + Re_t/Re_k}{1 + Re_t/Re_k}\right) \quad 4.26$$

where:

$$Re_t = \frac{\rho k}{\mu \omega} \quad 4.27$$

$$Re_k = 6 \quad 4.28$$

$$\alpha_0^* = \frac{\beta_i}{3} \quad 4.29$$

$$\beta_i = 0.072 \quad 4.30$$

Note that in the high Reynolds number form of the $k - \omega$ model $\alpha^* = \alpha_\infty^* = 1$.

4.1.3 - XFOIL

The XFOIL (Drela, 1989) code combines a potential flow panel method and an integral boundary layer formulation for the analysis of the flow around airfoils. The code was developed to rapidly predict the airfoil performance at low Reynolds numbers and its convergence is achieved through the iteration between the outer and inner flow solutions on the boundary-layer displacement thickness. Thus, the XFOIL code calculates the viscous pressure distribution and captures the influence of limited trailing-edge separation and laminar separation bubbles. The XFOIL uses an approximate e^N envelope method to calculate transition. With this method the code tracks only the most amplified frequency at a given point on the airfoil downstream from the point of instability to obtain the amplitude of that disturbance. Transition is assumed when this integrated amplitude reaches an empirically determined value. The appropriate amplification factor, *N*, to use into XFOIL calculations was calculated by Eq. 4.31, which was presented by van Ingen (2008):

$$N = -8.43 - 2.4\ln(Tu) \quad 4.31$$

Where Tu represents the absolute turbulent intensity. In the present work *N* was set to the default value of 9, which corresponds to a wing surface in an average windtunnel (Drela, 1989).

4.2 - Numerical Procedure

4.2.1 - Mesh Generation

In order to simulate the airfoils and compare the different Computational Fluid Dynamics (CFD) models, it was used a completely structured O-type mesh with the outer boundaries placed 30 chords away from the airfoil. The airfoil was defined with 250 points (see Section 3.2.2) and special attention was given to the regions near the wall in order to ensure $y^+<1$. The details of the final used mesh is shown in Figure 4.1.

4.2.2 - Boundary Conditions

To simulate the airfoil at the desired chord-based Reynolds number, corresponding to those of the available experimental results given by the literature ($Re = 2.0x10^5$) a density based solver was used. The far boundary was considered as a pressure farfield using the Mach number input to prescribe the flow speed. The desired angle of attack was obtained using the appropriate flow direction vector components. The airfoil top and bottom surfaces were defined as wall and the fluid inside the domain was defined as air with $\rho = 1.225$ kg/m^3 and $\mu = 1.79x10^{-5}$ Pa.s.

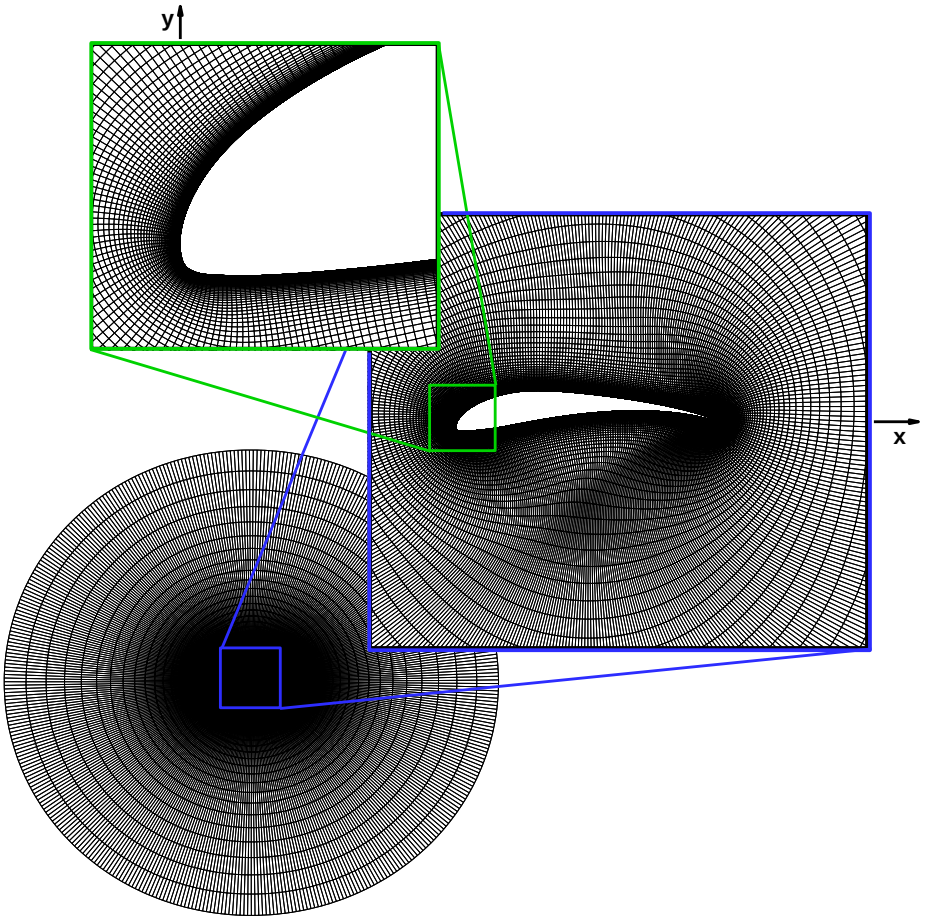

Figure 4.1 - Detail of the mesh around the airfoil used to obtain k-ω and k-kl-ω predictions.

These procedures give the advantage to simulate all angles of attack with only one mesh (Silva *et al.*, 2002). To correctly compute the lift and drag coefficients, the decomposition of the flow direction vector was used, according the Eq. 4.32 and Eq. 4.33.

$$L = L' \cos(\alpha) - D' \sin(\alpha) \quad 4.32$$

$$D = L' \sin(\alpha) + D' \cos(\alpha) \quad 4.33$$

where *L* and *D* are lift and drag, respectively, and *L´* and *D´* represent the components of the aerodynamic forces based on the original system of coordinates of Ansys Fluent.

4.3 - Results

4.3.1 - E387 Airfoil

The *E387* airfoil was designed during 1960s by Richard Eppler. Since it was specifically designed to use on model sailplanes this airfoil represented a significant improvement over the other airfoils available at that time. The airfoil performance predicted for $Re = 2.0\text{x}10^5$ by XFOIL, *k-kl-ω* transition model and *SST k-ω* turbulence model (with and without low Reynolds corrections) are compared to the University of Illinois Urbana-Campaign (UIUC) (Selig & Guglielmo, 1997) wind-tunnel measurements in Figure 4.2 (a) and (b).

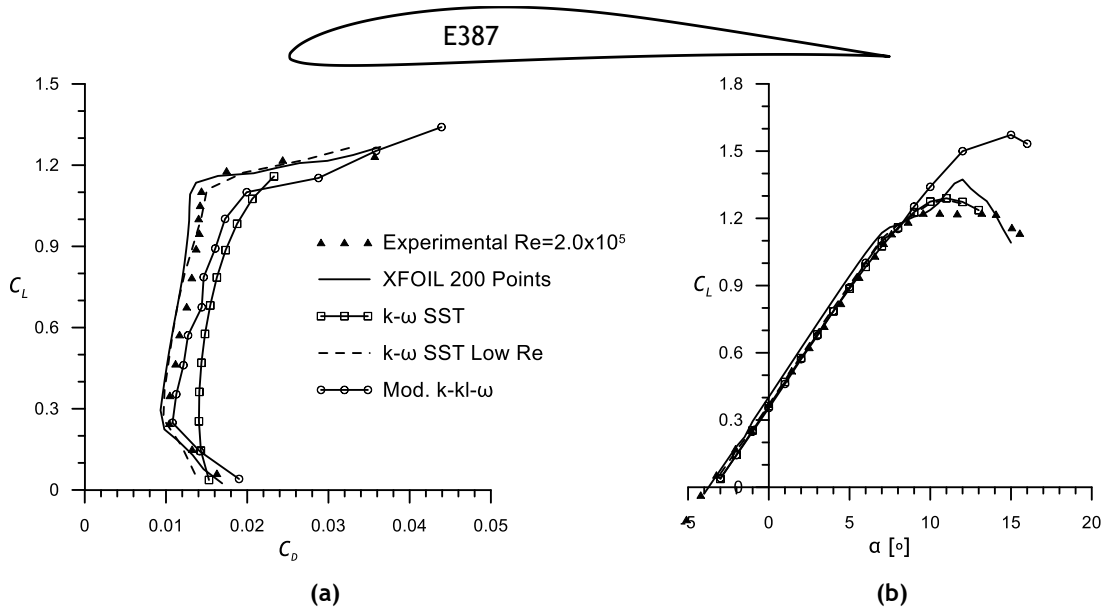

Figure 4.2 - Aerodynamic characteristics of the E 387 airfoil measured at Penn State UIUC wind tunnel (Sommers & Maughmer, 2003) compared with the numerical simulations results

The results presented in Figure 4.2 show that all the models are in good agreement with the experiments. The XFOIL and SST *k-ω* turbulence model with the Low Reynolds corrections (*k-ω SST Low Re*) are capable to accurately predict the corners of low drag region, although they

are predicting a slightly higher maximum lift coefficient. Regarding the SST *k-ω* without low Reynolds corrections, since it is unable to predict transition, it does not replicate the sharp corners, although the maximum lift coefficient is well predicted.

The refurbished version of *k-kl-ω* transition model presents better agreement with the experimental data than SST *k-ω* turbulence model without low Reynolds corrections. For the lower corner of low drag region this model can correctly predict the values of both lift and drag coefficients. In the direction of the top corner of the low drag region as the lift coefficient increases *k-kl-ω* transition model predicts a slightly higher drag coefficient for a given lift coefficient, making the curve appear a bit to the right when compared with the measurements.

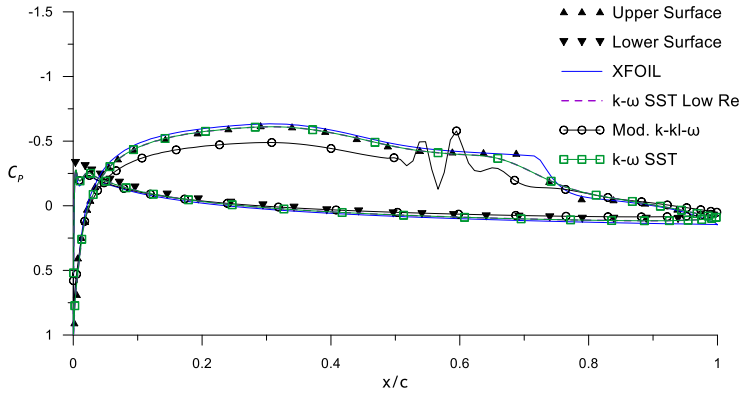

(a)

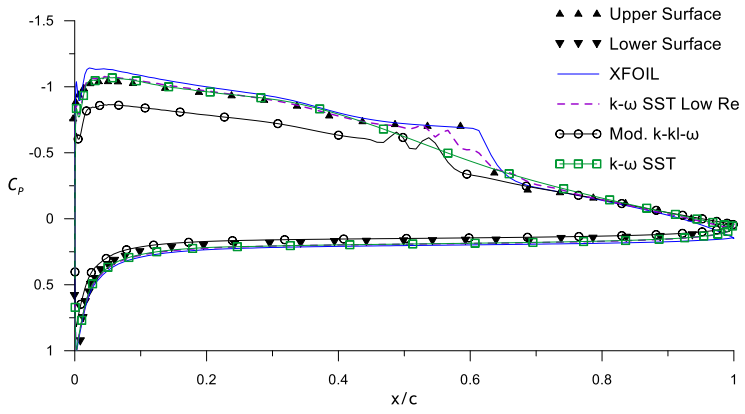

(b)

Figure 4.3 - Comparison of E387 airfoil pressure distributions measurements (McGee *et al.*, 1988) and results obtained with the CFD models and XFOIL, for *Re* = *2.0x10*^{5}. (a) *α=0º* (b) *α=4º*

Figure 4.3 (a) and (b) shows the pressure distribution for an angle of attack of 0 and 4 degrees, respectively. The results obtained from the above described numerical methods are compared with the measurements presented by McGee *et al.* (1988). At an AoA of 0º, XFOIL and SST *k-ω* turbulence model are in a perfect agreement with experiments, while the modified *k-kl-ω* transition model slightly under predicts the pressure coefficient in the upper surface of the

airfoil. At the angle of attack of 4º, the behaviour of different used methods remain the same, with a slightly under prediction in the *k-kl-ω* transition model until *x/c=0.6*

In Figure 4.4 (a) the transition position versus lift coefficient is plotted with airfoil's drag polar in order to observe the parallelism between the position of the transition and the laminar bucket limits. It is clear that the less steep part of the transition curves correspond to the limits of the laminar bucket of the drag polar as shown in Figure 4.4. In particular, one can note the lift coefficient of the transition ramps as the corners of the low drag bucket of the airfoil. The lower surface transition ramp at lift coefficient of about 0.3 as the lower corner and the upper surface transition ramp at lift coefficient of about 1.15 as the upper corner of the low drag bucket.

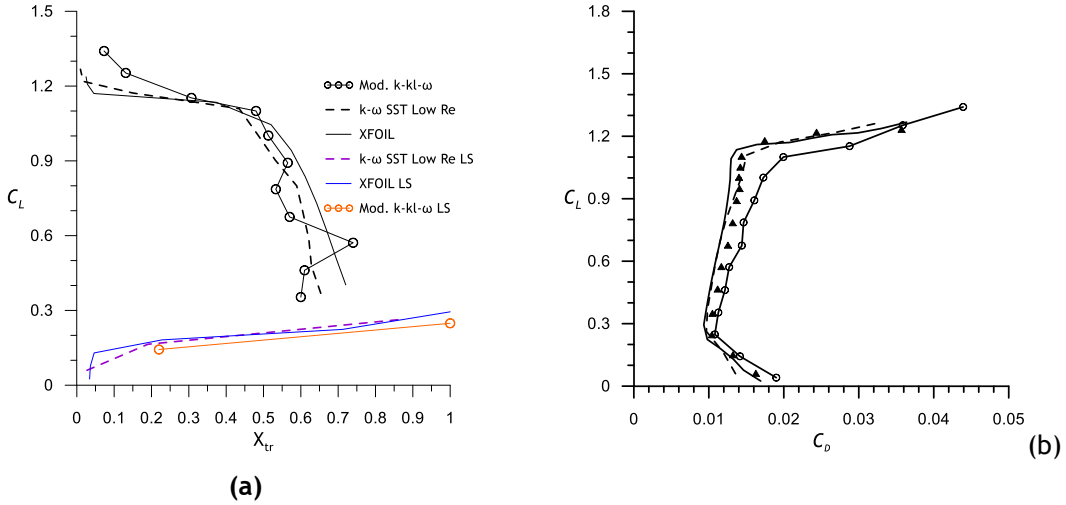

Figure 4.4 - (a) Transition position of the E387 airfoil upper and lower surfaces. (b) Drag polar of E387 for *Re= 2.0x10*^{5}.

The turbulence model SST *k-ω* with low Reynolds corrections and XFOIL give a close prediction but the later estimates the larger laminar flow extent at lower lift coefficients. The modified *k-kl-ω* transition model shows the same trend but only matches closely the other models around a lift coefficient of 1.18, overestimating the laminar flow extent at higher lift coefficients. The relation between transition position and the laminar bucket of the drag polar demonstrates the importance of a correct prediction of the transition position during the development of a new airfoil.

4.3.2 - S1223 Airfoil

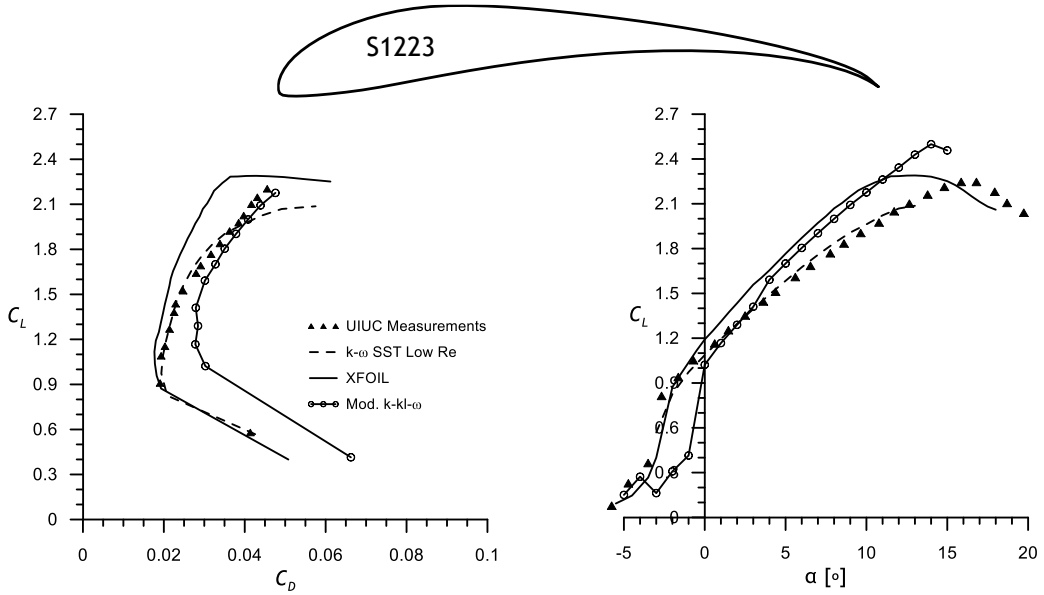

Figure 4.5 -Comparison between UIUC measurements (Selig & Guglielmo, 1997) and results obtained by CFD models and XFOIL for S1223 airfoil for *Re = 2.0x10^5*. (a) C_L *vs* C_D (b) C_L *vs* α.

The S1223 airfoil was designed by Selig & Guglielmo (1997) to achieve a Cl_{max} greater than 2 at $Re = 2.0\text{x}10^5$. The S1223 airfoil has $11.93\,\%$ thickness and camber of 8.67%. The UIUC experimental measurements (Selig & Guglielmo, 1997) showed a maximum lift coefficient of approximately 2.2 with moderate stall characteristics (see Figure 4.5 (b)).

Figure 4.5 shows the predictions for the S1223 airfoil polar. Since the turbulence model SST *k-ω* without low Reynolds corrections performed worst for the E387 airfoil (see Figure 4.2) it was decided not to use this model in the simulations done for the S1223 airfoil. For SST *k-ω* turbulence model with low Reynolds corrections, the agreement is good until the angle of attack of approximately 10º. Contrary to the predictions presented for the E387 airfoil, the *k-kl-ω* transition model does not predict the lower corner of low drag region accurately. However, the agreement for higher angles of attack is even better than the XFOIL predictions. For XFOIL, the maximum lift coefficient is well predicted, although it occurs in a lower angle of attack as it is possible to observe at Figure 4.5 (b). At higher angles of attack XFOIL tends to underestimate the drag coefficient.

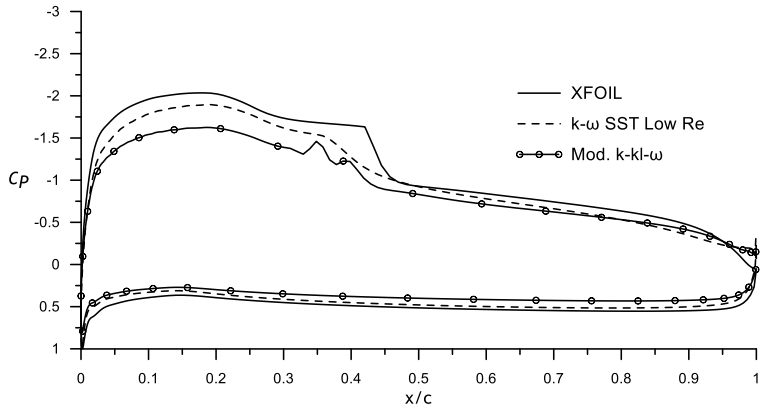

(a)

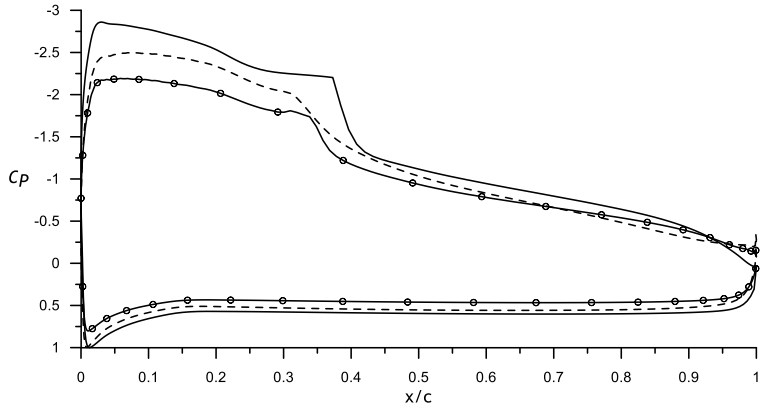

(b)

Figure 4.6 - Comparison of S1223 airfoil pressure distributions for *Re* = 2.0x10^5. (a) *a=4°* (b) *a=8°*

Figure 4.6 (a) shows the pressure distribution at $\alpha = 4°$ and it is possible to observe that all the models are presenting a similar behaviour.

Chapter 5

Propeller Design and Optimization for Application on the MAAT Cruiser Airship

In this chapter it will be presented the design and optimization of a propeller for application on the MAAT cruiser airship. The propeller's design process was initiated from with the inverse design method as described in Section 2.5.5. This allowed the determination of the blade geometric characteristics for the pre-determined cruise operating point. Different propellers were optimized with the inverse design method according to the chosen blade airfoil and airfoil operating point. The best design strategy can thus be found. These different propellers were then used in a parametric/sensitivity analysis in order to judge their relative merit in the overall flight envelope.

5.1 - High Altitude Propellers

Design and optimization of a high altitude propeller can be a challenging problem due to the extremely low air density and low temperature. This, in turn, causes a major drop in the blade operating Reynolds number and increase in the Mach number compared with the sea level operation. Even so, propellers have been and continue to be a choice for many of high altitude aircrafts: Egrett (1987), Condor (1988), Pathfinder (1993), Perseus A (1993), Perseus B (1994), Strato 2C (1995), Theseus (1996), Centurion (1998) and Helios (1999). Although there is only little information about these high altitude propellers, a brief description is presented below (see Table 5.1).

5.1.1 - Egrett

The Grob Egrett (*Egrett II*, 1990, 1991) is a high altitude reconnaissance platform developed for the German and U.S. Air Forces. The aircraft is a single engine propeller driven aircraft,

intended to fly at about *16000 m* and powered by a Garrett turboprop engine. It has a 4 bladed propeller with 3.04 meters in diameter that generates about 2773 N of thrust

5.1.2 - Condor

The Condor (Colozza, 1998) was a high altitude unmanned military demonstration aircraft used by U.S. army in high altitude (about *20500* m) reconnaissance missions. The propeller employed in the Condor aircraft was a 3 bladed variable pitch propeller with 4.90 meters in diameter, intended to provide 1129 N of thrust. However there is no experimental measurements of the propeller, since the Hartzell Company have never tested it due to the propeller's size and aircraft's proposed flight regime.

5.1.3 - Pathfinder

The Pathfinder (Colozza, 1998; Monk, 2010) aircraft was constructed by Aerovironment Inc. as a high altitude solar powered aircraft. It was able to fly at an altitude of *21800 m,* powered by 6 electric motors for propulsion which drive 6 fixed pitch propellers with 2.01 meters in diameter. The Pathfinder propellers have a 50.8° twist from the root to the tip.

5.1.4 - Perseus

Perseus (*Perseus B*, 1999) is a remotely piloted aircraft developed under NASA's Environmental Research Aircraft and Sensor Technology (ERAST) project. In its "B" version includes a propeller with 2 blades and 4.4 meters in diameter. The propeller was designed to absorb 50 kW of power at cruise altitude and it was designed using the XROTOR (Drela & Youngren, 2003), a propeller code developed at Massachusetts Institute of Technology. The propeller blades weigh about *7 kg* and an electric motor is used to change their pitch.

5.1.5 - Strato 2C

The Strato 2C (Schawe *et al.*, 2002) is a high altitude aircraft designed to perform its missions at altitudes up to 24 000 meters. It uses two variable pitch propellers with 5 blades and a diameter of 6 meters. The propellers work at *640* RPM during the cruiser and their pitch is controlled through a hydraulic actuator driven by the propeller gearbox. However, above *18500 m* their performance is severely affected by the flow separation decreasing their efficiency up to 66% at *24000 m*. One of the causes identified for the observed decrease in the propellers' efficiency may be the usage of not sufficiently carefully designed airfoils for the high Mach low Reynolds numbers conditions.

5.1.6 - Theseus

The Theseus (Merlin, 2013) was built by Aurora Flight Sciences, funded by NASA through the Mission To Planet Earth environmental observation program. It was a twin-engine, unpiloted vehicle, powered by two *59.66 kW* turbocharged piston engines that drove two propellers with *2.74 m* in diameter. Propellers were designed to generate *409 N* of thrust each one.

Table 5.1- High-altitude propeller data.

Year	Aircraft Name	Propeller Thrust, *N*	Propeller Diameter, *m*	T/A, N/m^2	Altitude, *m*
1987	Egrett (*Egrett II*, 1990, *Egrett II*, 1991)	2773	3.04	305.42	16329
1988	Condor (Colozza, 1998)	1129	4.90	59.87	20500
1993	Pathfinder (Colozza, 1998; Monk, 2010)	23	2.01	7.25	21802
1994	Perseus (*Perseus B*, 1999)	388	4.40	102.07	18373
1995	Strato 2C (Schawe *et al.*, 2002)	2500	6.00	88.42	24000
1996	Theseus (Merlin, 2013)	409	2.74	69.36	18288

5.2 - MAAT Cruiser Requirements

To design a new propeller for application on the MAAT cruiser airship it was necessary to identify the airship's power requirements. Thus, the total thrust needed for the MAAT airship, provided by the MAAT consortium partners in charge with the cruiser aerodynamics, is presented at Table 5.2. The propeller's disk loading was initially selected based on the analysis of Table 5.1. After selecting the disk loading an initial study on the number of propellers needed to reach the total thrust was performed.

Table 5.2- Initial Considerations for the study of number of propellers.

Designation		Units
Total thrust	339650	N
Disk loading	300	N/m^2
Total area of actuator disk	1132.17	m^2

The implemented parametric study (see Figure 5.1) shows that if 50 propellers are selected, each one needs to provide $6.8\ kN$ of thrust. After some iteration on the inverse design method, it was decided to increase the maximum diameter from 5.3 *m* to 6 *m*, reducing the disk loading to around $240\ N/m^2$. The rotation rate was calculated using a fixed Mach number of 0.6 at the

blade's tip that resulted in *550* RPM. The airship's propulsive properties are presented in Table 5.3.

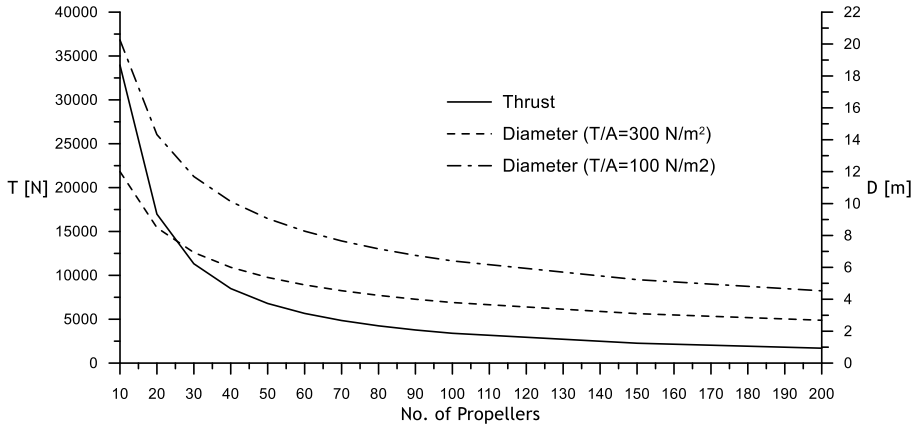

Figure 5.1 – Parametric study of the thrust for each propeller and their respective diameter.

Table 5.3- MAAT cruiser propulsive system properties.

Designation		Units
No. of Propellers	50	
Thrust	6.79×10^3	N
Rotation Speed	550	RPM
Propeller Diameter	6	m
Disk Loading	240.15	N/m^2

5.3 - Propeller Design and Optimization

The main goal of any propeller is to transfer the shaft power provided by the engine to the air stream as efficiently as possible. Propellers operating at high altitudes experience a number of unique design issues such as the aforementioned changes in the atmospheric conditions that must be addressed. These changes of atmospheric conditions with altitude are herein assumed to correspond to the International Standard Atmosphere (ISA) ('U.S. Standard Atmosphere', 1976). The main properties of the atmosphere at 16km altitude, in which the propeller will operate, according to ISA model, are summarized in Table 5.4.

Table 5.4- Atmosphere Conditions for an altitude of 16 km.

Designation		Units
Air Density	0.165	kg/m^3
Absolute Viscosity	1.44×10^{-5}	$kg/(m.s)$
Speed of Sound	295.07	m/s

5.3.1 - Airfoil Development

Since the blade airfoils' *L/D* ratios are required as inputs into the inverse design methodology, different airfoils were analysed with the *XFOIL module* (see Figure 5.2) at the operating Reynolds and Mach numbers enabling an initial look at the airfoil characteristics. The *L/D* ratio has a small but noticeable effect on the final blade needed chord and twist. These ratios also have a significant effect on the propeller performance.

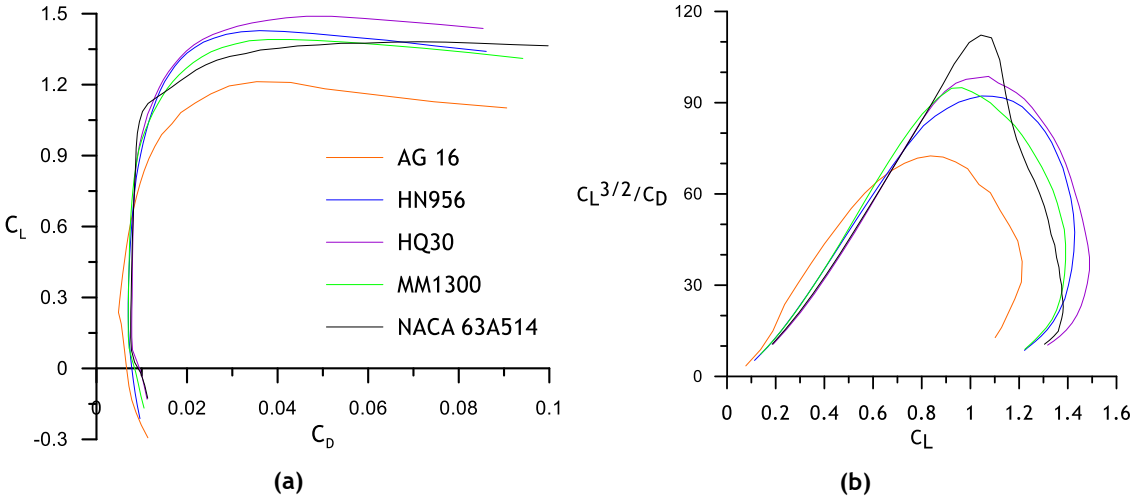

Figure 5.2 - Airfoils comparison performed in JBLADE's XFOIL sub-module for Re=5.00x10^5 and M=0.1 (a) C_L vs C_D (b) $C_L^{3/2}/C_D$ vs C_L

The airfoil with highest $L^{3/2}/D$ from those that were initially considered, the NACA 63A514, was then set as a base airfoil and improved (Gamboa & Silvestre, 2013) in order to increase its *L/D* within a useful angle of attack range to reduce the power required by the propeller for the previously selected disk loading and thrust. Since the propeller was designed to operate at high altitudes, the blade chord calculated through the inverse design methodology tends to be big leading to propellers with high solidity.

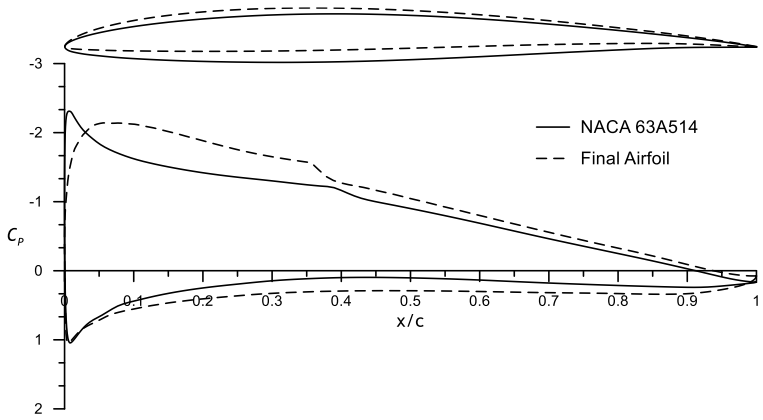

Figure 5.3 -Base and final airfoils shapes comparison and their pressure coefficient distribution for Re=5.70x10^5 and α=6.0º

The comparison between the base and the improved airfoils shape and pressure coefficient distribution along the chord is presented in Figure 5.3. Their polars are presented in Figure 5.4 and it is possible to observe that the improved airfoil presents higher $L^{3/2}/D$ and L/D ratios.

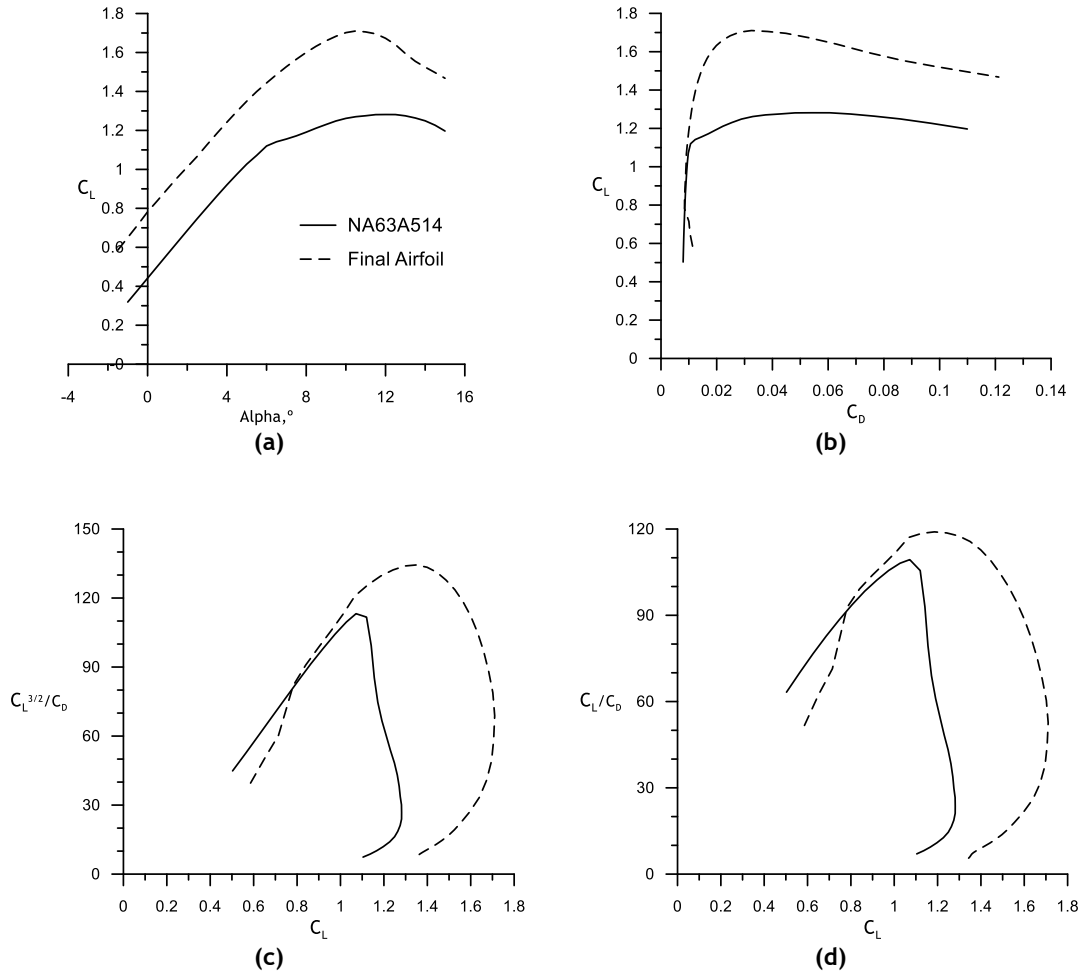

Figure 5.4 - Comparison between NACA 63A514 and improved airfoil for Re= 5.70x10^5. (a) C_L vs α (b) C_L vs C_D (c) L/D vs C_L (d) $L^{3/2}/D$ vs C_L.

These maxima ratios occur for higher lift coefficients, leading to a reduction of the blade chord needed to generate a given thrust. The final airfoil polars were obtained for the relevant Blade and Mach number range in the JBLADE *XFOIL module*. These airfoil polars were then extrapolated such that the lift and drag coefficients became available for 360º airfoil angle of attack range (Morgado et al., 2013).

5.4 - A New High Altitude Propeller Geometry Design Concept

The propeller design point consists on the airship's velocity, the thrust that the propeller needs to produce, the propeller hub and tip radius, the position of each intermediate section and the air density at the desired altitude. The Reynolds number at r/R=0.75 was then estimated for the selected operating point and used to calculate the airfoil aerodynamic characteristics. After

the extrapolation, the airfoil data were used in the *Inverse Design sub-module*, allowing the calculation of an initial blade geometry.

High altitude propellers tend to have a high solidity factor due to the limitation in the blade tip speed for a given tip Mach number and the high altitude very low air density that limit the dynamic pressure acting on the blades. This problem leads to propellers with a high number of low aspect ratio blades. As an alternative to the traditional way of designing a propeller, in which the lift coefficient is prescribed along the blades' span, JBLADE Software allows the usage of the airfoil's best $L^{3/2}/D$ or L/D. The use of the airfoil best $L^{3/2}/D$ as a blade design concept leads to a minimization of the needed chord along the blade, since the airfoil is operating at a higher lift coefficient than the typically used best airfoil L/D condition. To maximize the airfoils' efficiency they can be individually optimized for the Reynolds number at their respective radial position, allowing even further blade chord reduction, maximizing the propeller's efficiency. According to some cases presented in the literature (Colozza, 1998; Koch, 1998) the same airfoil was used along all blade span.

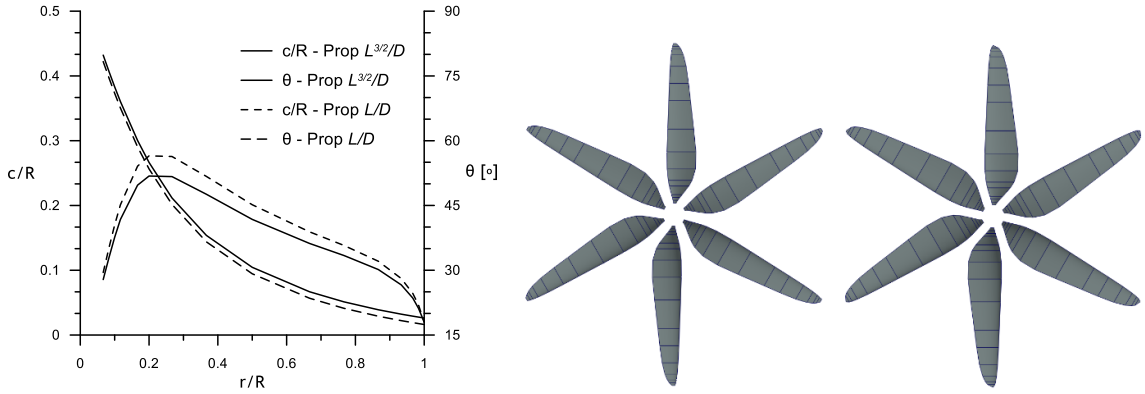

Figure 5.5 - (a) Comparison of propellers geometries (b) $L^{3/2}/D$ Propeller (c) L/D Propeller

After obtaining the initial geometry, the propeller performance was computed and the Reynolds and Mach numbers distributions along the blade radius (see Figure 5.6) were determined. The airfoil polars along the blade were updated for the actual distributions and the inverse design methodology was applied again. This procedure was repeated until no modifications were observed in the blade's chord and twist.

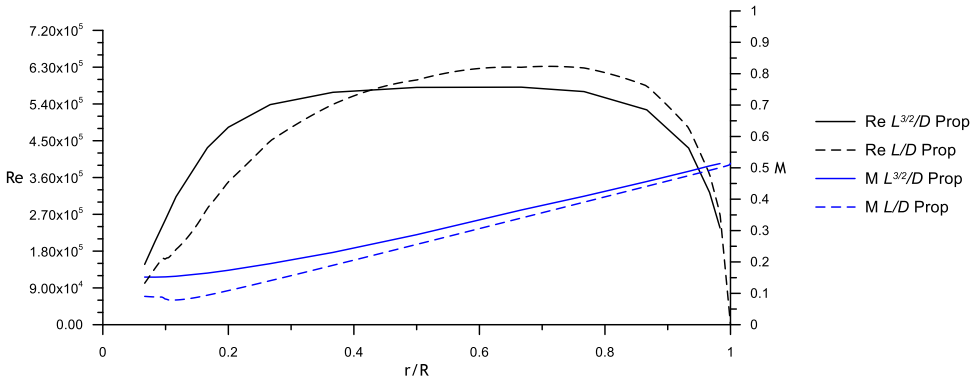

Figure 5.6 - Final Reynolds and Mach numbers distribution along blade radius for *V = 28m/s* at *r/R=0.75*

Two different propellers (see Figure 5.5) were produced following the above mentioned design methodology: one using the airfoil best L/D and the other with airfoil's best $L^{3/2}/D$. For both designs, the hub radius was fixed at 0.2 meters and the tip radius was set to 3 m, according to the conditions defined in Table 5.3. The improved airfoil, presented in Section 5.3.1, was used along all the blades' sections for both propellers. The results obtained for both propellers were compared with conventional CFD results obtained for the same geometries and they are presented in Section 6.2.2. One of the objectives of this study was also to understand which concept (the $L^{3/2}/D$ or L/D) along the blade span will produce more efficient propellers.

Chapter 6

3D Propeller CFD Simulations

In this chapter the Computational Fluid Dynamics simulations, performed for different propellers, will be presented. An APC 10”x7” SF propeller was simulated and the results were used to validate the new 3D Flow Equilibrium model, presented in Section 2.4.1. The two propellers designed for application in the MAAT cruiser airship, presented in Section 5.4, were also simulated along their operational envelope. The propellers’ performance was then compared with JBLADE Software results, since there is no experimental data for these particular propellers’ geometries.

6.1 - APC 10”x7” SF Propeller

An APC 10”x7” SF propeller was used to validate JBLADE for low Reynolds number predictions. The airfoil of the APC 10”x7” SF propeller was obtained by Carvalho (2013) and introduced in JBLADE. The airfoil was then simulated for the proper Reynolds and Mach numbers distributions along the blade and the propeller was replicated using the geometry presented in Figure 6.1 in JBLADE and the propeller performance was computed for comparison with the CFD results.

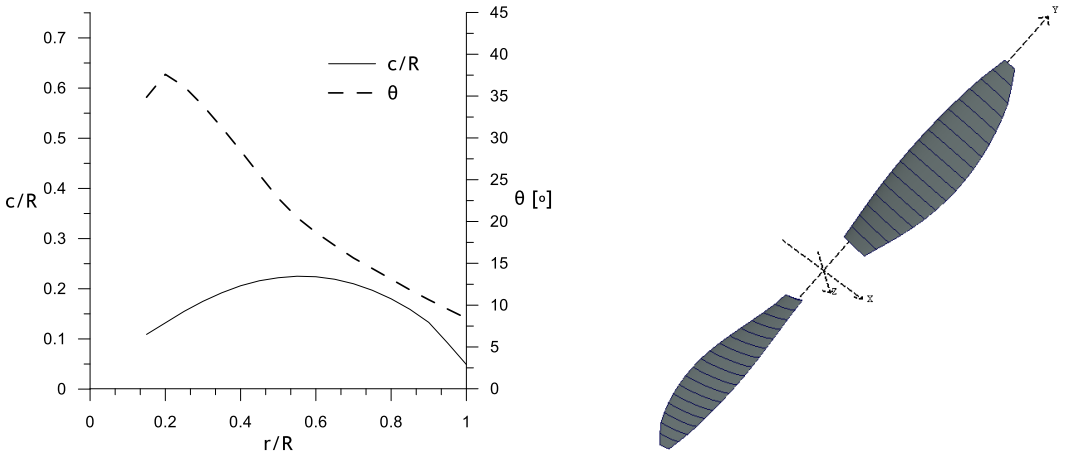

Figure 6.1 - APC 10"x7" SF propeller geometry (Brandt *et al.*, 2014) and its shape after introduced in JBLADE.

6.1.1 - CFD procedure

A CFD simulation of the propeller was performed in order to validate the new 3D Equilibrium formulation, presented in Section 2.4.1. A commercial package of Ansys Fluent® (*ANSYS FLUENT Theory Guide*, 2010) with the SST *k-ω* turbulence model (Menter, 1994; Menter *et al.*, 2003) was used. The hybrid mesh (see Figure 6.2 and Figure 6.3) contains *2.89* million points and it was chosen to use an implicit integration of the incompressible Reynolds Averaged Navier-Stokes equations coupled with turbulent transport equations. Furthermore, the SIMPLE algorithm was used for pressure-velocity coupling. In order to consider the rotation of the propeller a Multiple Reference Frame (MRF) approach was adopted. Thus, the computational domain is divided in two regions: the internal domain which covers the propeller and it was rotating at *3000* RPM and the external domain which was considered to be stationary.

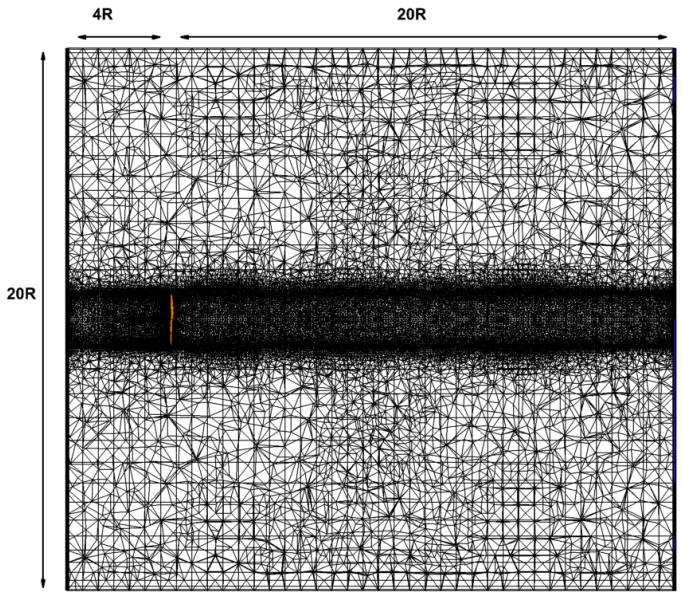

Figure 6.2 – Domain dimensions used to simulate the APC 10"x7" SF propeller.

The second order upwind scheme was used for the convection terms while the diffusion terms were discretized using the central scheme. The convergence of the numerical solution was controlled by assigning suitable under relaxation of the transport equations and observed that the relative numerical error of the solution dropped below 10^{-8}. The blade surfaces of the used mesh (see Figure 6.4) were defined by 300 nodes in the span wise and 100 nodes in the chord direction.

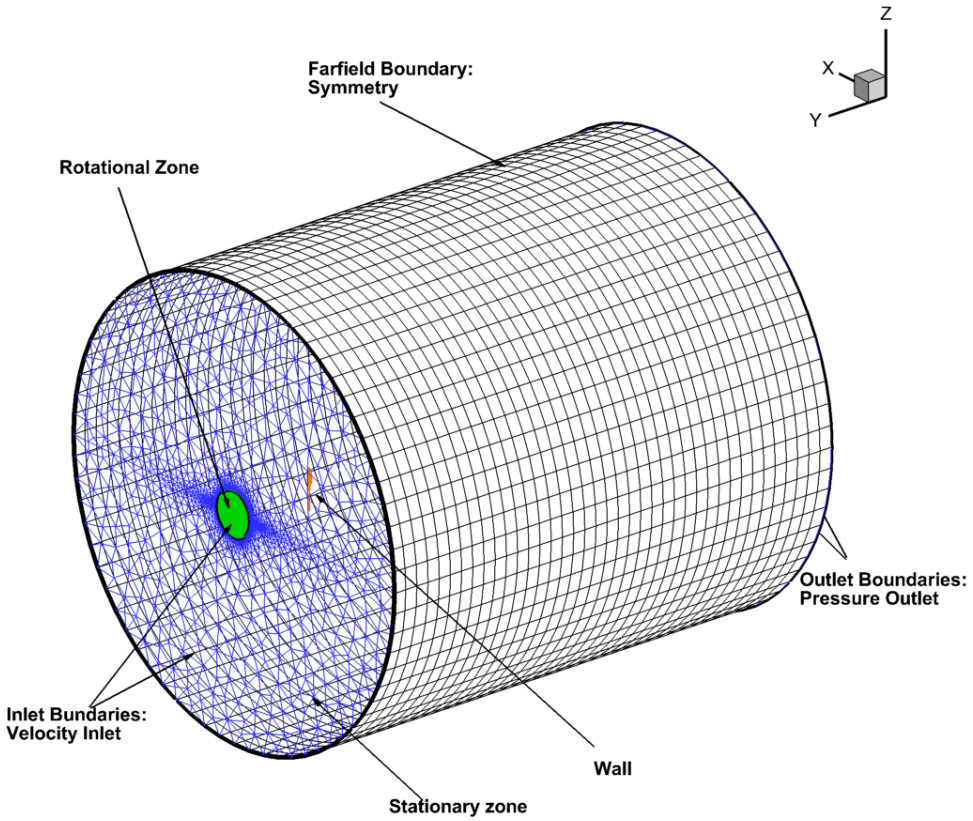

Figure 6.3 – Domain and boundary conditions used to simulate the APC 10”x7”SF propeller.

Mesh independency tests were accomplished to ensure that the obtained results were not dependent of the selected mesh. As presented in Figure 6.5, three different meshes were used to ensure the independency of the results. The coarse mesh (see Table 6.1) was composed by 1.72 million cells, the used mesh was prepared with 2.89 million and the refined mesh consisted in 6.45 million cells.

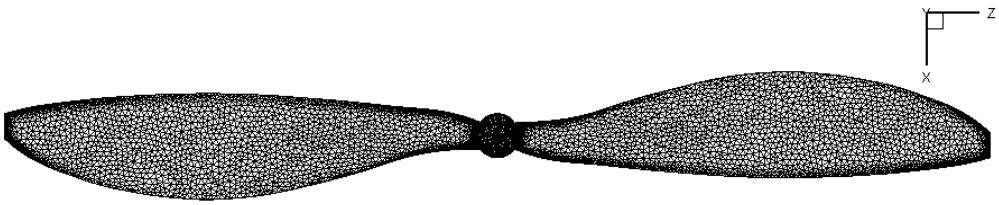

Figure 6.4- Distribution of the cells on the blade surface.

The mesh independence study was performed for an operating condition of *3000* RPM and a freestream speed of 5 m/s, corresponding to an advance ratio of about 0.39. The air density was *1.225* kg/m^3 and the air dynamic viscosity was set to 1.78x10^{-5} Pa.s. Regarding the thrust coefficient, the difference between the used mesh and the refined mesh was 0.92% while the power coefficient presented a difference of 0.24%. Concerning the propeller efficiency, the difference between refined mesh and used mesh was about 0.32%. Thus, since the result is not affected and in order to save time, the mesh with 2.89 million was used in the remaining calculations.

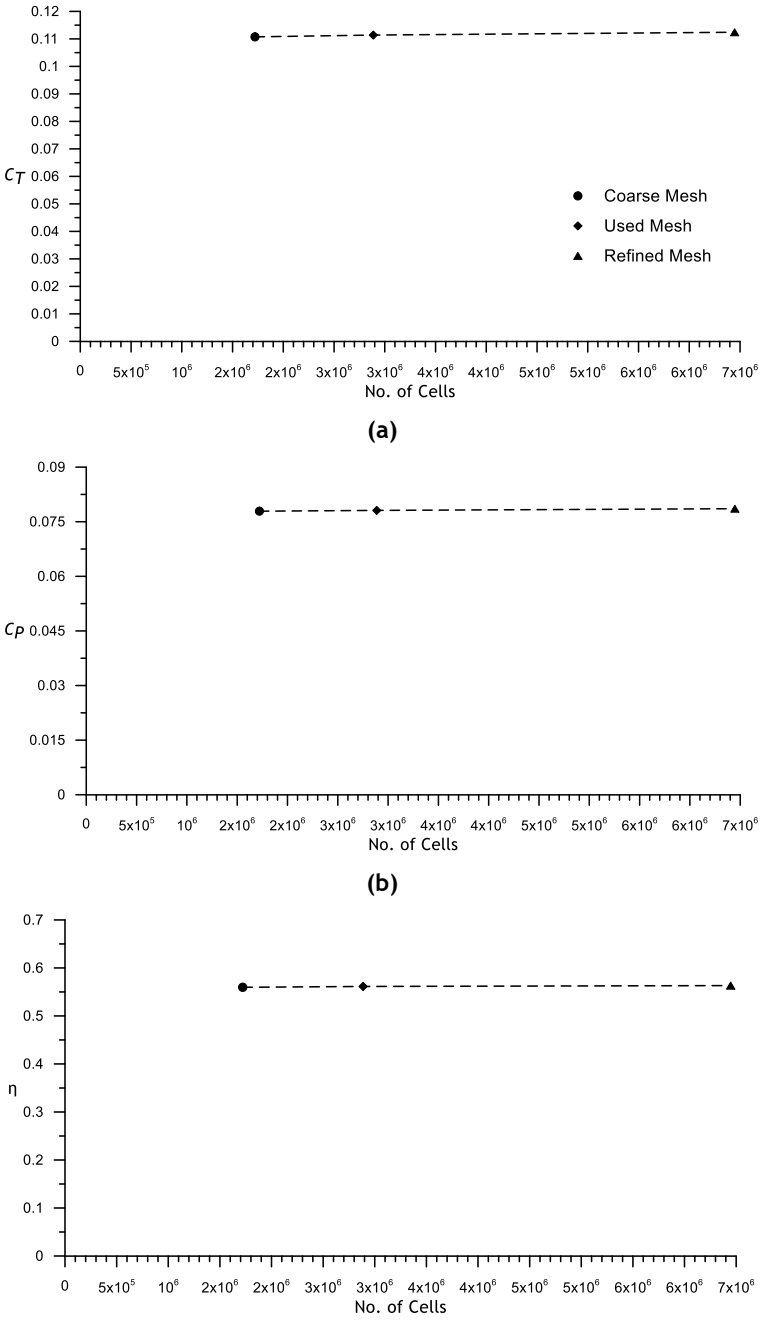

Figure 6.5 – CFD Simulations mesh independency tests performed for APC 10"x7" SF propeller for *3000* RPM and 5 *m/s*. (a) thrust coefficient (b) power coefficient, (c) propeller efficiency.

Table 6.1- Number of cells of different meshes used in the mesh independency tests.

Designation	No. of Cells
Coarse Mesh	$1.72x10^6$
Used Mesh	$2.89x10^6$
Refined Mesh	$6.45x10^6$

6.1.2 - 3D Flow equilibrium validation

The tangential velocity along an APC 10"x7" Slow Flyer radius was plotted together with CFD data and original BEM formulation in order to validate the new proposed model for 3D flow equilibrium (see Section 2.4.1).

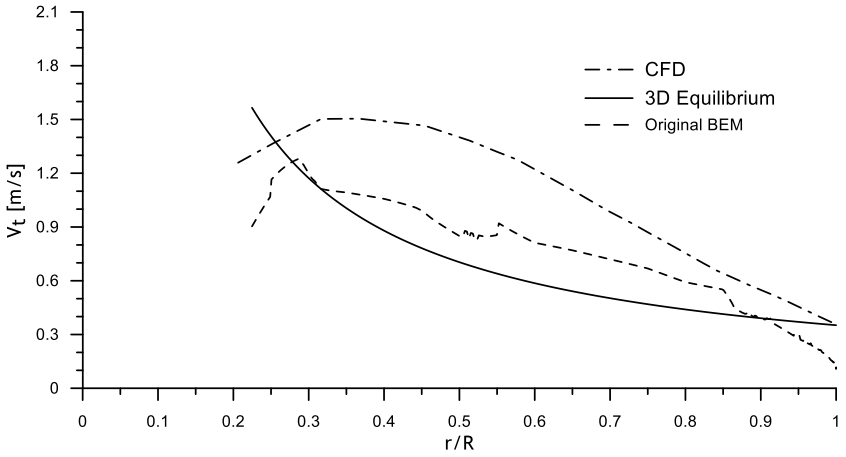

Figure 6.6 - Tangential velocity distribution along an APC 10x7"SF propeller (Brandt *et al.*, 2014) **blade radius, at 1 m behind the propeller plane, for CFD, original BEM formulation and new proposed 3D Flow Equilibrium model.**

It is seen in Figure 6.6 that the 3D Equilibrium hypothesis is a fair approximation with reality considering that the CFD results show the real trend. It is also clear the weakness of BEM in respect to the tangential induction since each annular element of the disk has no relation to its neighbour elements allowing discontinuities in the tangential induction profile. The under prediction of tangential velocity in the BEM simulation is related to the lower power coefficient that results from its formulation in this static thrust condition. The simulations were performed for static condition at *3000* RPM. The air was defined with a density of *1.225* kg/m^3 and a dynamic viscosity of $1.78x10^{-5}$ Pa.s.

6.1.3 - Performance prediction

Figure 6.7 shows that both JBLADE and CFD simulations predictions follow the experimentally measured thrust coefficient. In the lower advance ratios region, the JBLADE predicted thrust coefficient values are over predicted while the CFD thrust coefficient is slightly over predicted,

compared with the experimental measurements along all advance ratios. Considering the whole advance ratio interval, JBLADE predictions are closer to UIUC experimental data for the thrust coefficient than the CFD results. Regarding the power coefficient calculations, JBLADE and CFD simulations agree with the measurements. The difference between JBLADE and UIUC experiments increases moderately with the increase in the advance ratio. The difference between CFD simulations and experimental values is constant, with a slight over prediction from CFD calculations.

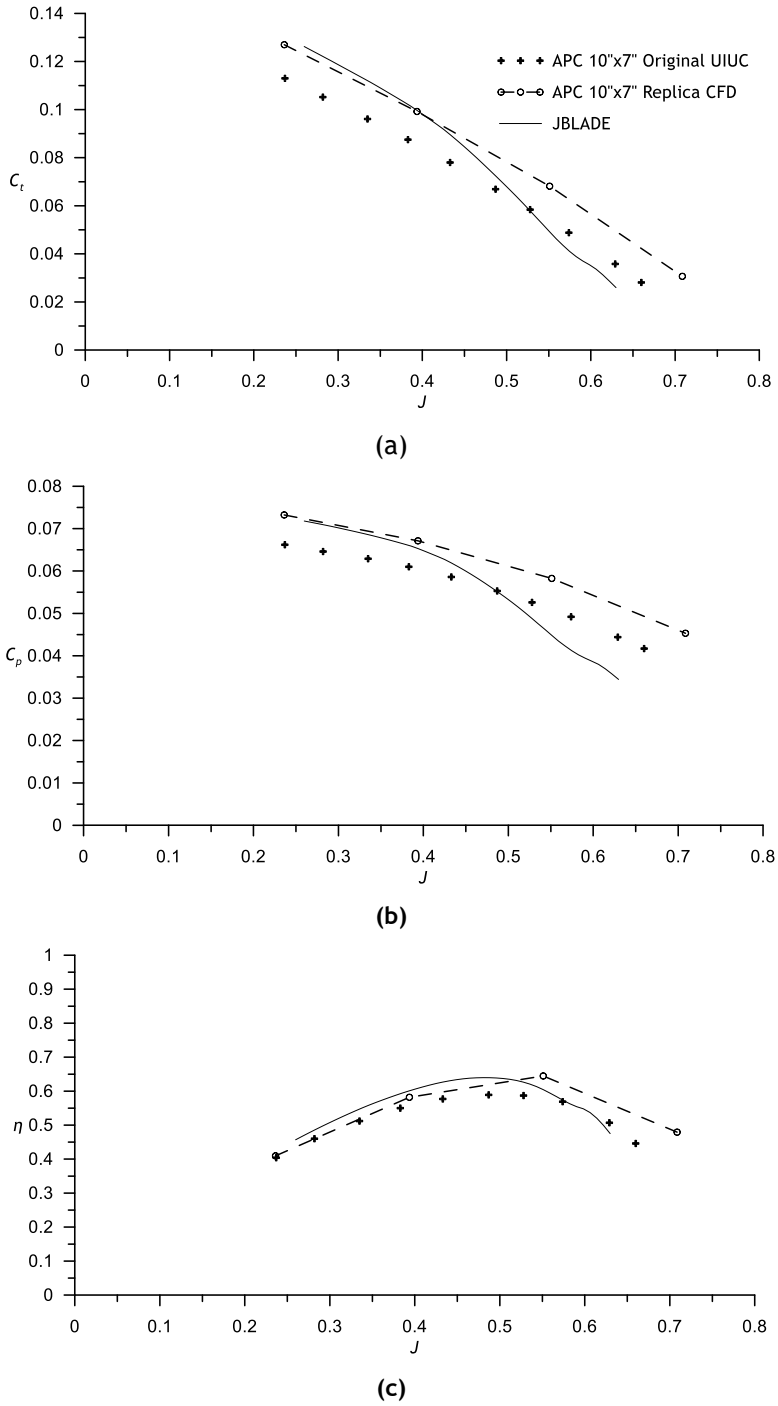

Figure 6.7 – Performance prediction comparison for APC 10"x7" SF propeller (a) thrust coefficient (b) power coefficient (c) propeller efficiency.

The JBLADE prediction is higher at low advance ratios and drops to under predicted values for high advance ratios. Nevertheless, the difference in JBLADE to the experimental data remains smaller than that of the CFD results. JBLADE and CFD simulations correctly predict the maximum efficiency of the propeller as well as the advance ratio value for its maximum. However, while JBLADE predicts the zero efficiency limit at an advance ratio lower than the experiments, CFD predicts that zero efficiency for a higher advance ratio.

Overall the JBLADE predictions are closer to the experimental data than the CFD results for the low Reynolds APC 10"x7" SF propeller. Figure 6.8 shows the distribution of the pressure on the blades' surfaces and iso-surfaces of the velocity magnitude in the flow field.

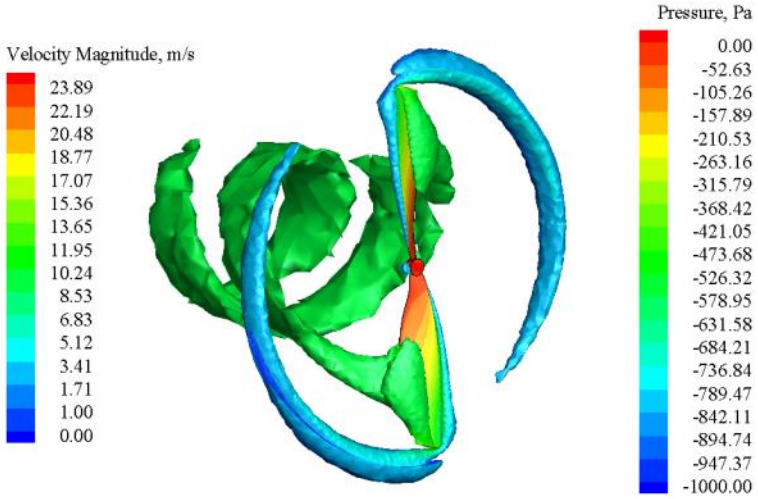

Figure 6.8 - Pressure distribution on blade surface and velocity magnitude distribution on the iso-surfaces for V_∞=*1 m/s* and *3000* RPM.

6.2 - MAAT Cruiser Propeller

6.2.1 - CFD procedure

The computational fluid dynamics simulations were performed for the possibility to study the features of the flow structure and to obtain more detailed information, in order to identify the parameters that affect the flow and the efficiency of the propeller. Since there is no experimental data for the designed cruiser propeller, the numerical simulations were done and used to compare with JBLADE software results.

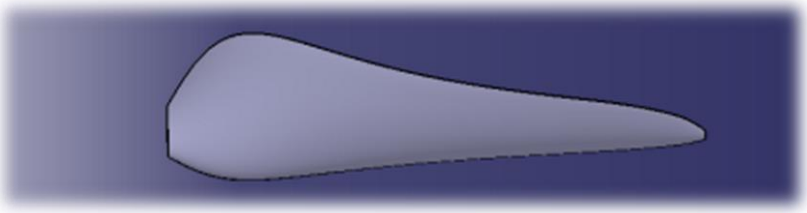

Figure 6.9 - Example of the blade geometry transformed into a CAD part for meshing purposes.

The airfoils used in the CFD simulation were exported from JBLADE and imported into the CATIA V5 CAD software. Each section was translated making the *xx* axis coincident with the 25% of the chord.

The airfoils were then rotated according to Figure 5.5 (a) and a multi-section body was generated (see Figure 6.9). The mesh was generated and the computational domain was composed of about 2 million of tetrahedral cells clustered around the blade surface as it is presented in Figure 6.10. The boundaries of the domain representing the free stream conditions were set at 3 radius to the inlet and 10 radius to the outlet.

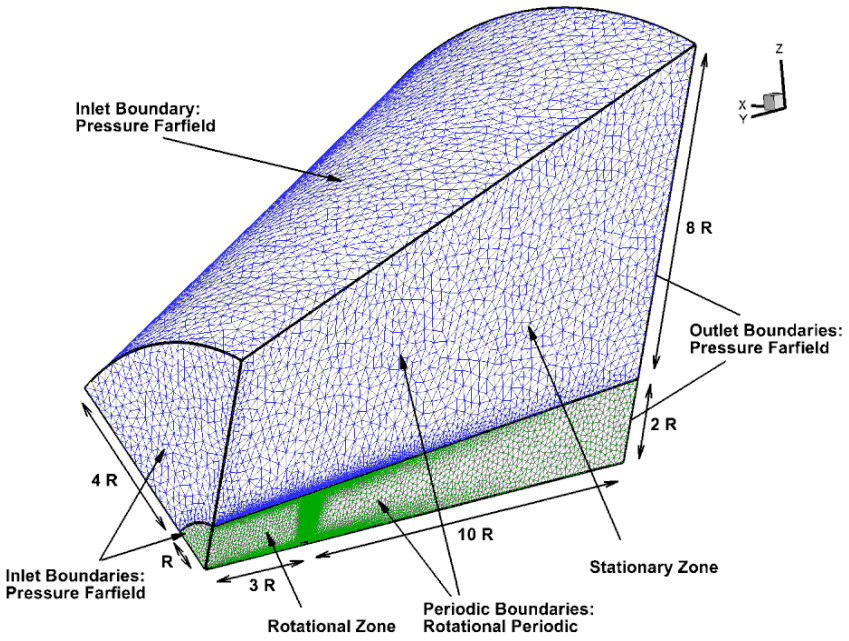

Figure 6.10 - Representation of the computational domain and its boundary conditions

The blade surfaces walls (see Figure 6.11) were defined by 300 nodes in the span wise and 200 nodes on the chord direction.

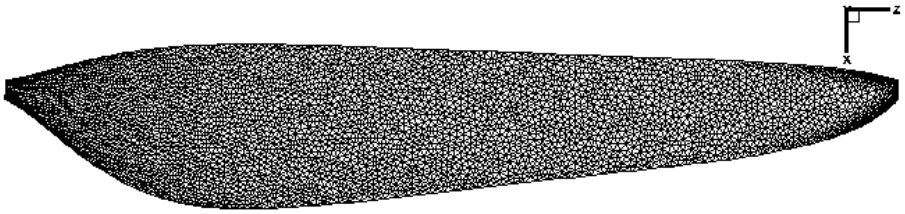

Figure 6.11 - Distribution of the cells on the blade surface.

Mesh independency tests were performed to an operating condition of *550* RPM and a freestream speed of *30 m/s*, corresponding to an advance ratio of about 0.55. The air density was *0.165* kg/m^3 and the air dynamic viscosity was set to *1.44x10*$^{-5}$ Pa.s ensure that the obtained results are not dependent of the used mesh. As presented in Figure 6.12, three different grids

were used to ensure the results mesh independency. The coarse mesh (see Table 6.2) was composed by *1.65* million cells, the used mesh had *2.7* million and the refined mesh consisted in *4.18* million cells. The maximum discrepancy between the used mesh and the refined mesh was *3.9%* for thrust coefficient and *4.2%* for the power coefficient. Thus, since the results were not significantly affected by the mesh and in order to save computational time the mesh with *2.7* million cells was used in the remaining calculations.

Table 6.2- Number of cells of different meshes used in the mesh independency tests.

Designation	No. of Cells
Coarse Mesh	$1.65x10^6$
Used Mesh	$2.7x10^6$
Refined Mesh	$4.18x10^6$

Furthermore, in order to reduce the computation time and facilitate the meshing process, periodic boundary conditions were used. The y^+ was controlled by the external refinement of the mesh near the blade, through the creation of prismatic cells around the surface of the blade such that the first point above the blade surface had a value $y^+<1$. As presented in Figure 6.10, the inlet, the outlet and the far domain were stated as a pressure far field boundaries. At the inlet the flow speed and direction is prescribed by inputting the value of the Mach number and the direction of the flow along the domain, together with the values of static pressure and temperature. The value of turbulent intensity and viscosity assigned to these boundaries were 0.1 % and 10 respectively. The value of the pressure and temperature were changed according to ISA models to correspond to an altitude of 16000 meters above sea level. The blade surface was defined as wall with no slip because the blade was considered stationary wall in respect to the adjacent rotating zone.

Numerical simulations of steady compressible Reynolds-Averaged Navier-Stokes (RANS) equations and the turbulent mode with absolute velocity formulation were accomplished by discretizing each governing equation within the Finite Volume Method (FVM) using a cell centred collocated arrangement of primitive variables. Moreover, the k-ω SST turbulence model (Menter, 1994) was used to deal with the time-averaging of the closure equations and for simulating the turbulence.

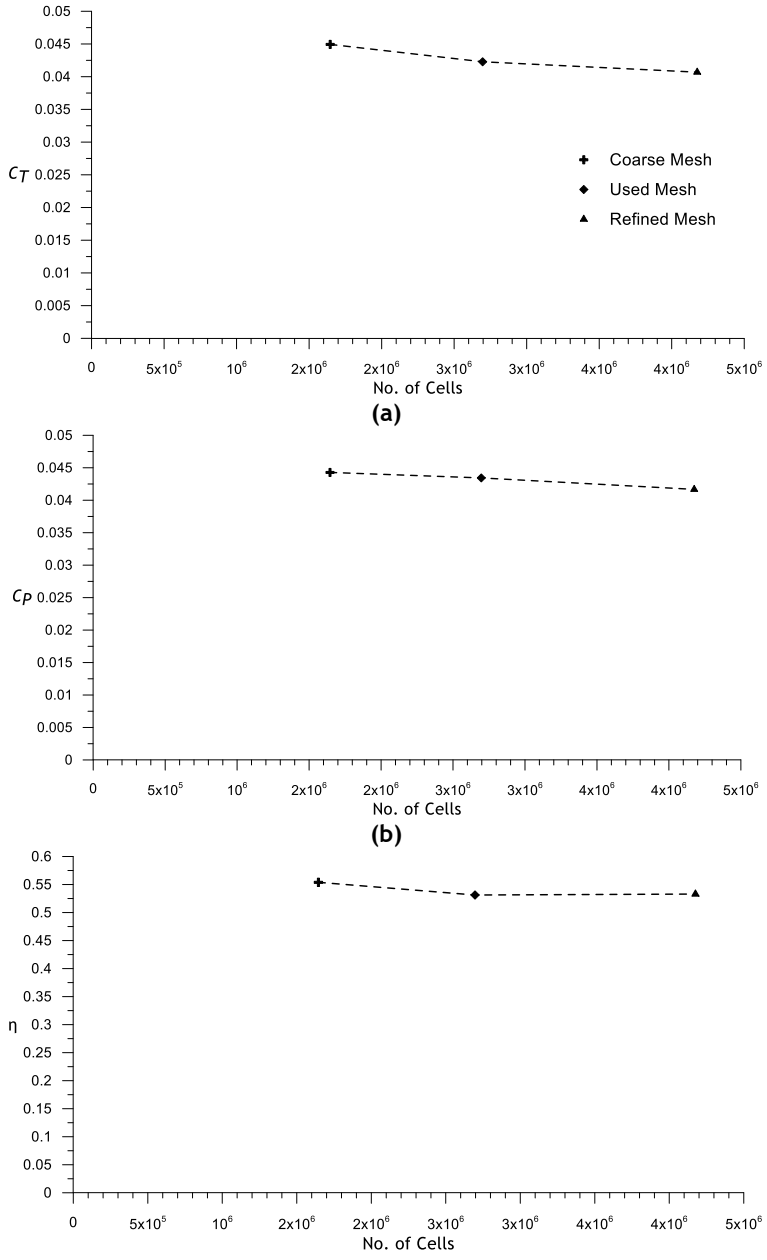

Figure 6.12 - Mesh independency study made for $L^{3/2}/D$ propeller at $V=30$ m/s. (a) thrust coefficient (b) power coefficient, (c) propeller efficiency.

The domain was divided in two regions: the rotating and stationary zones as presented in Figure 6.10. The Multiple Reference Frame (MRF) method was chosen to consider the blade rotation, preventing the need to perform transient calculations by solving the governing equations in a rotational reference frame, by considering the centripetal and Coriolis acceleration. This method is more suitable for steady state simulations where the unsteadiness of the problem can be ignored. Also the implicit coupled density based solver available in Ansys Fluent® was selected for the coupling of the momentum and continuity equations. Spatial discretization of the flow convective fluxes and turbulence variables were performed by the higher order advection upstream splitting method (AUSM) schemes and second order upwind scheme respectively. Moreover, least square cell based method was used for all gradients.

The rotational speed of *550* RPM was considered for the rotating domain. For improving the convergence of the solution, the rotational speed was increased gradually from *100* RPM to the final rotational speed of *550* RPM. The convergence of the numerical solution was controlled by assigning 1 to the courant number for the iterative solution and considering suitable under relaxation factors for the turbulent variables. The convergence of the solution was also guaranteed by monitoring the relative numerical error of the solution to drop below 10^{-8}. In order to compare the results of the numerical simulation with the obtained results from the JBLADE software, the propellers were tested over a range of free stream velocity between *10 m/s* and *65 m/s*.

6.2.2 - Performance prediction

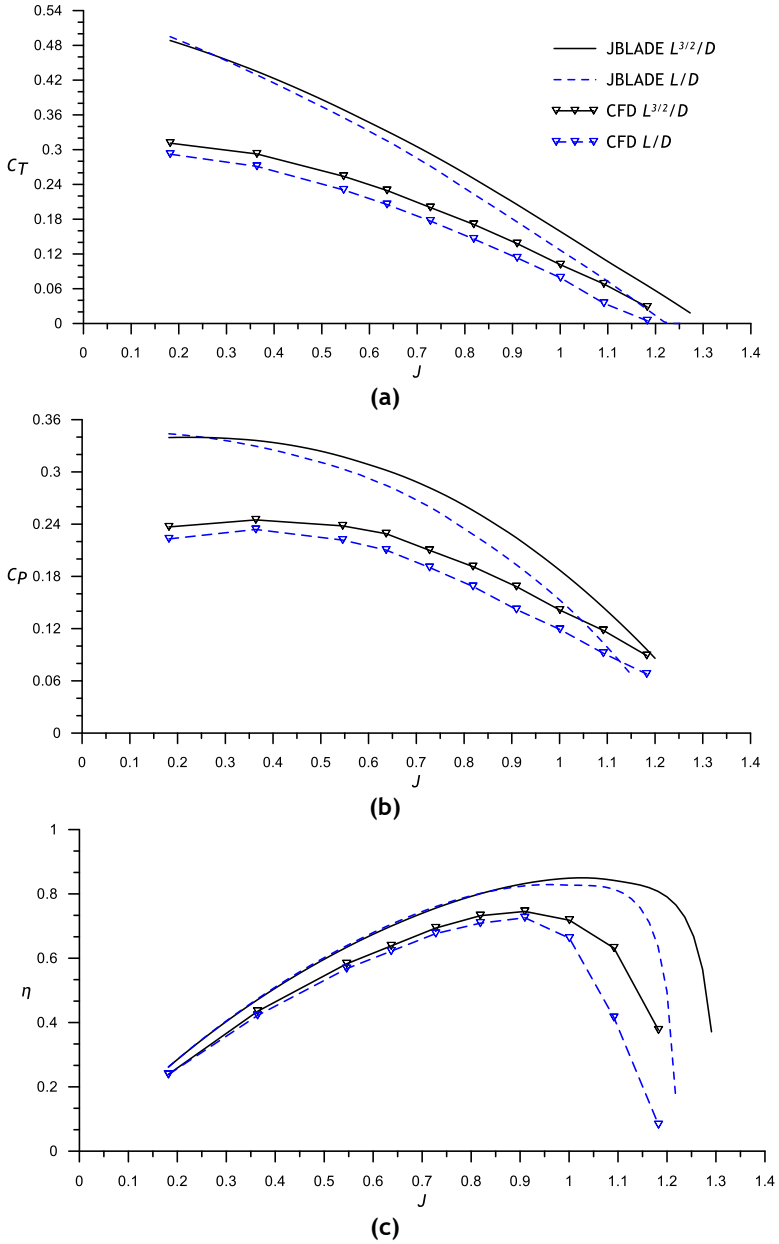

Figure 6.13 - Comparison between data predicted by JBLADE and CFD for the designed propellers: (a) thrust coefficient (b) power coefficient, (c) propeller efficiency.

Contrary to the methods used in which the airfoil lift coefficient is prescribed along the blade span, in these designed propellers, the airfoil's best $L^{3/2}/D$ and the airfoils' best L/D were used to obtain 2 different propellers (see Section 5.4). The performance of the propellers is presented in Figure 6.13. Observing Figure 6.13 it is possible to observe that JBLADE predicts a bigger thrust coefficient than CFD in the lower advance ratio region. This over estimation drops as the advance ratio increases. At the higher advance ratios, JBLADE and the CFD data tend to agree. The results also show that the power coefficient is also over estimated by JBLADE at low advance ratios when compared with the CFD simulations. Due to the differences presented in thrust and power coefficient, the propeller efficiency is over predicted by JBLADE when compared with the CFD results.

The advance ratio for the maximum efficiency is 1.05 for JBLADE against 0.9 obtained with CFD but the maximum efficiency is estimated to be 10% higher than the CFD simulations values. This is related to the JBLADE's over prediction of the thrust coefficient at high advance ratios. More than comparing JBLADE results with the CFD simulations, Figure 6.13 also shows that JBLADE correctly predicts the difference between the two different design concepts. Notably, the proposed new concept of optimizing the operating $L^{3/2}/D$ of the blade's airfoil results in a more efficient propeller. The difference also appeared in CFD simulations and it is possible to conclude that JBLADE can be successfully used to produce different propeller geometries and select the relative best one to proceed to the next design phase.

In order to further understand the merit of designing the blade for optima $L^{3/2}/D$ on the performance, the distribution of the skin friction on the two distinct blades are compared in Figure 6.14 and Figure 6.15 for the same operating point with a freestream speed of $50\ m/s$, and at 550 RPM, corresponding to an advance ratio of about 0.91.

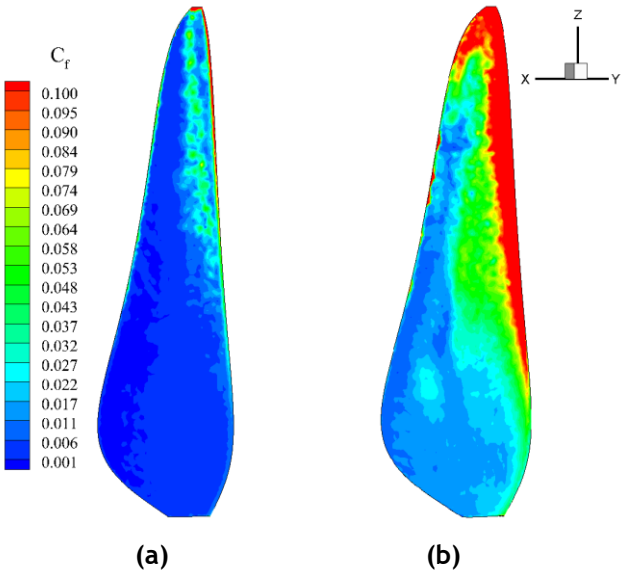

Figure 6.14 - Skin friction coefficient distribution on upper surface for an advance ratio of 0.91. (a) $L^{3/2}/D$ Propeller (b) L/D Propeller.

Figure 6.14 and Figure 6.15 clearly show that the skin friction coefficient of the blade designed using concept of maximizing L/D is higher than the skin friction coefficient on the blade designed using the airfoil's best $L^{3/2}/D$. This is not beneficial for the performance of the blade, since the input power will be partly used to overcome the extra drag caused by the blade shape. Most of these losses are occurring near the leading edge of the airfoil and mostly in the tip region of the blade. This clearly relates to the higher efficiency of the best $L^{3/2}/D$ blade propeller seen in Figure 6.13.

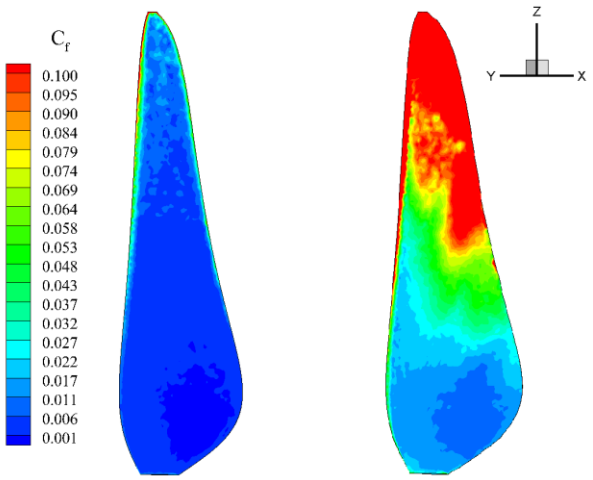

(a) **(b)**

Figure 6.15 - Skin friction coefficient distribution on lower surface for an advance ratio of 0.91. (a) $L^{3/2}/D$ Propeller (b) L/D Propeller.

Another parameter that could be used for analysing the blade design is the pressure coefficient (see Figure 6.16 and Figure 6.17). The main component of the thrust is originating from pressures forces. The blade's thrust generation capability increases with the increase in the difference of the pressure between upper and lower sides of the propeller's blade.

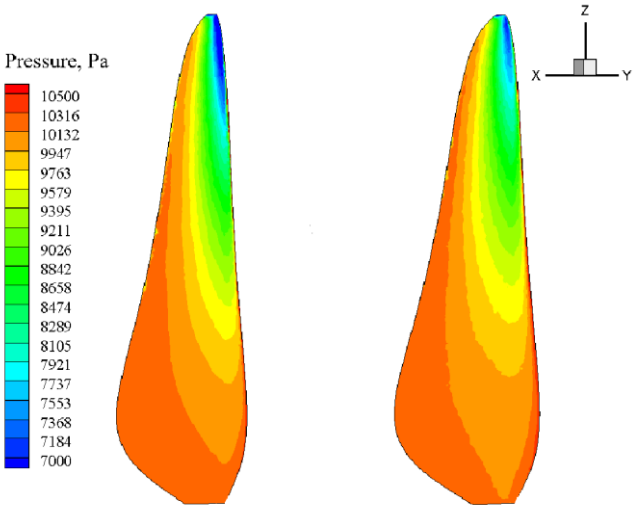

(a) **(b)**

Figure 6.16 - Pressure distribution on upper surface for an advance ratio of 0.91 (a) $L^{3/2}/D$ Propeller (b) L/D Propeller.

When the blade is rotating, the lower pressure appears on blade's upper side and the higher pressure appears on the blade lower side. The biggest difference of pressure distributions appears on the blade's tip while at blade root the difference is smaller.

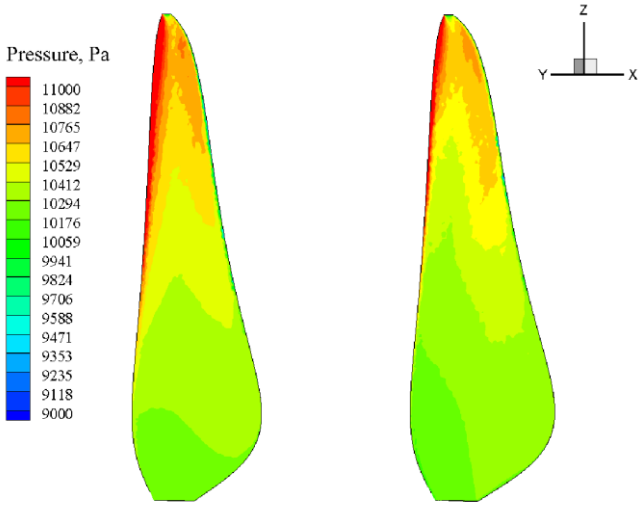

(a) **(b)**

Figure 6.17 - Pressure distribution on upper surface for an advance ratio of 0.91. (a) $L^{3/2}/D$ Propeller (b) L/D Propeller.

The comparison of the two distinct design concept blades reveals that the propeller designed with maximum $L^{3/2}/D$ concept provides higher pressure differences all over the blade surface, which means that the propeller produces higher thrust when compared with the propeller designed with airfoil's best L/D concept.

Chapter 7

Wind Tunnel Low Reynolds Propeller Testing

This chapter presents the development of the experimental setup for low Reynolds propeller testing. The data obtained with the developed experimental setup were compared against reference experimental data to validate the installation.

7.1 - Experimental Setup

7.1.1 - Wind tunnel

The tests were performed in the subsonic wind tunnel of the Aerospace Sciences Department at University of Beira Interior, presented in Figure 7.1.

Figure 7.1 – Wind tunnel of Aerospace Sciences Department.

The wind tunnel is an open-return type with a *6.25:1* contraction ratio. The test section is nominally *0.8 m x 0.8 m* in cross section, with *1.5 m* length. The maximum speed available at the test section is about *33 m/s*, obtained through a 15 *kW* alternated current motor, connected to a six-bladed fan. In addition, the wind-tunnel settling chamber contains a honeycomb and two anti-turbulence screens allowing a good flow quality in the test section.

7.1.2 - Thrust Balance Concept

In order to measure the performance of the propellers it was necessary to develop a new test rig. The design selected for the thrust balance, shown in Figure 7.2, is similar to the T-shaped pendulum structure originally built in UIUC (Brandt & Selig, 2011). An effort was made to reduce the complexity of the assembly inside the wind tunnel test section, in order to ensure minimal flow and measurements disturbances. The position of the load cell can be modified according to the propeller's expected thrust, in order to use the full scale of the load cell for different propellers, reducing the measurements errors and uncertainties. Flexural pivots were chosen over the standard bearings since they greatly reduce the adverse tendencies that affect the standard bearings, when used in static applications, namely friction and stiction.

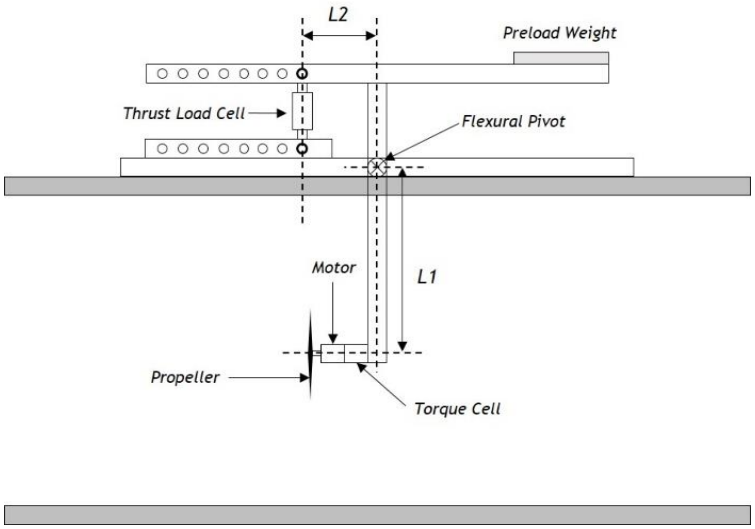

Figure 7.2 – Thrust Balance Concept (Alves, 2014).

The pendulum was designed in order that the propeller, and consequently the thrust vector, were located at the centre of the test section. Additionally, a preload weight, as presented in Figure 7.2, was added to the balance, maintaining the load cell in tension throughout the complete advance ratio range. This pre-load weight ensures that the load cell does not reach the negative thrust conditions. The detailed development of the thrust balance can be found at Alves (2014).

7.1.3 - Thrust and Torque Measurements

A *FN3148 Load Cell* (2012) (see Figure 7.3 (a)), manufactured by FGP Sensors & Instrumentation, was used to measure the propellers' thrust. This load cell has a maximum capacity of *100 N* for both tension and compression. Regarding the torque measurements, it was used a reaction torque sensor, model RTS-100 (see Figure 7.3 (b)), produced by Transducer Techniques (*RTS-100*, 2014). Both sensors are connected to a shielded connector block (*SCB-68*, 2009), produced by National Instruments.

Thrust Load Cell (FN 3148)	Reaction Torque Sensor (RTS-100)
	
(a)	**(b)**
• Full Scale: 100*N* • Tension and Compression • Accuracy: 0.05% of Full Scale • Integrated Mechanical Stops • High Level Outup Model with Integrated Amplifier	• Rated Output 1.5mv/V nominal • Capacity: 100 in-oz • Clock Wise/Counter Clock Wise • Non Repetability : 0.05% of Rated Output

Shielded Connector Block (SCB-68)

(c)
• Shielded I/O connector block for use with 68-pin X, M, E, B, S, and R Series DAQ devices • Screw terminals for easy I/O connections or for use with the CA-1000 • 2 general-purpose breadboard areas

Figure 7.3 - Sensors specifications (a) Thrust load cell (b) Torque Reaction Sensor (c) Shielded Connector Block.

7.1.4 - Propeller rotation speed measurement

A Fairchild Semiconductor *QDR 1114* (2013) photo reflective object sensor was used to measure the propeller rotational speed. This sensor is used to count the number of revolutions that the shaft makes in a fixed time interval, resulting on an accuracy of *±0.5 Rev/0.75 s*. The sensor circuit, comprising an infrared emitting diode, a phototransistor and a photo reflector circuit (see Figure 7.4), was developed by Santos, (2012) to make the output signal independent of the distance from the reflecting surface. With this circuit the sensor can be placed up to *2* mm from the reflective surface. The output voltage switches between *0.27* V when the sensor is pointed to a white surface and *4.61* V when the sensor is pointed to a black surface. The circuit has a response time of around *50* µsec. Since the rotational speed of the tested propeller had never exceeded *7000 RPM*, the output voltages and response time of the circuit proved to be sufficient for accurate rotation speed measurements.

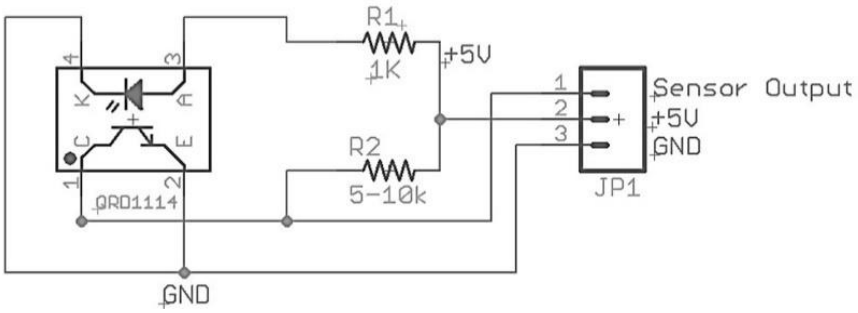

Figure 7.4 - Photoreflector circuit's schematics (Santos, 2012)

7.1.5 - Free stream flow speed measurement

The freestream velocity is measured with a differential pressure transducer, an absolute pressure transducer and a thermocouple. The measuring mechanism uses two static pressure ports, one at the tunnel settling chamber and another at the entrance of the test section as presented in Figure 7.5.

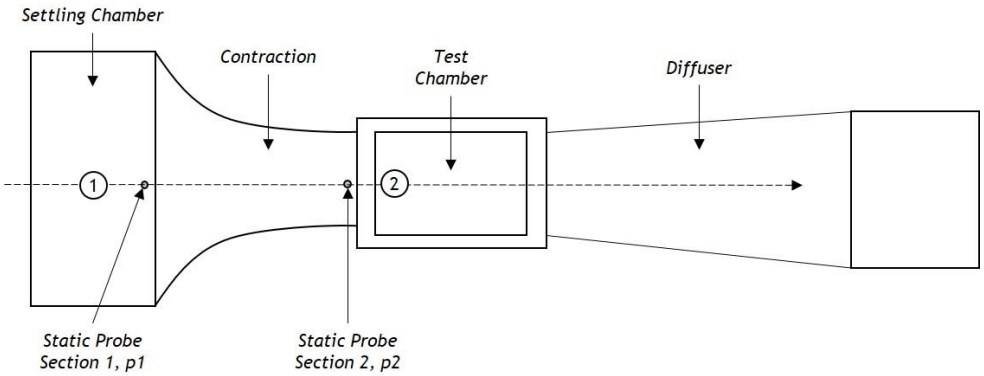

Figure 7.5 – Wind tunnel Schematics with representation of the static pressure ports location.

The contraction section causes an increase in velocity and consequently, a decrease in the pressure at the test section. The pressure difference between the wind tunnel settling chamber and the test section is a measure of the flow rate through the tunnel. Thus, the velocity can be determined through Bernoulli's equation:

$$\frac{p_1}{\rho}+\frac{1}{2}V_1^2+gz_1=\frac{p_2}{\rho}+\frac{1}{2}V_2^2+gz_2 \tag{7.1}$$

Considering that the tunnel is horizontal, $z_1 = z_2$, then:

$$V_2^2-V_1^2=\frac{2(p_1-p_2)}{\rho} \tag{7.2}$$

Relating the velocities from the 1D incompressible continuity relation:

$$A_1V_1=A_2V_2 \tag{7.3}$$

or

$$V_2=\frac{A_1}{A_2}V_1 \tag{7.4}$$

Combining Eq. 7.12, Eq. 7.3 and Eq. 7.4, the flow velocity in the test section is calculated by:

$$V_2=\sqrt{\frac{2(p_1-p_2)}{\rho\left[1-\left(\frac{A_2}{A_1}\right)^2\right]}} \tag{7.5}$$

The atmospheric pressure outside of the tunnel is measured with an absolute pressure transducer made by Freescale Semiconductor model *MPXA4115A* (2009). The temperature is measured with a National Instruments *LM335* (1999) thermocouple located at the inlet of the wind tunnel.

7.1.6 - Balance Calibration

Before using the rig for any tests, each measuring instrument was calibrated. For the torque sensor calibration (see Figure 7.6 (a)), calibrated weights were used with a known length to create a calibration torque, and by adding and removing weights, a linear relationship between the torque and voltage was calculated. Regarding the thrust calibration, it was made *in situ* using calibrated weights and a low-friction pulley system to create an axial load simulating the propeller thrust on the load cell (see Figure 7.6 (b)). By increasing and decreasing a known force on the load cell, a linear relationship between the thrust and voltage was determined. These calibration procedures need to be regularly performed to ensure consistent results.

Calibration was later verified using check-loads. Pure and combined check-loads were repeatedly applied to verify the balance calibration.

(a) (b)

Figure 7.6 – Illustration of calibrations procedure (Alves, 2014). (a) Torque sensor (b) Thrust load cell.

7.1.7 - Test Methodology

To perform the static performance tests, the propeller thrust and torque were measured along with the local atmospheric pressure and temperature at different RPM. Regarding the dynamic performance tests, with freestream speed, the propeller rotational speed was set to the desired value and the wind tunnel's freestream velocity was increased from 4 m/s to 28 m/s by 1 m/s increments. At freestream velocities smaller than 4 m/s, it was difficult to obtain the needed freestream velocity stability to proceed with the measurements, due to the interference between the propeller wake and the wind tunnel's fan. At each measured freestream velocity, the propeller thrust and torque were measured along with the ambient pressure and temperature. If the torque value became too close to zero, the test was finished because the propeller was entering the windmill brake state.

The collecting data procedure (see Figure 7.7) begins with the execution of a LabView® data acquisition and reduction routine. The control software powers up the motor to the first pre-defined RPM setting and data for each freestream velocity step is collected. This procedure is repeated for all RPMs. Once the data is collected, the data reduction sub-routine is executed. The collected data was systematically reduced, recorded and stored.

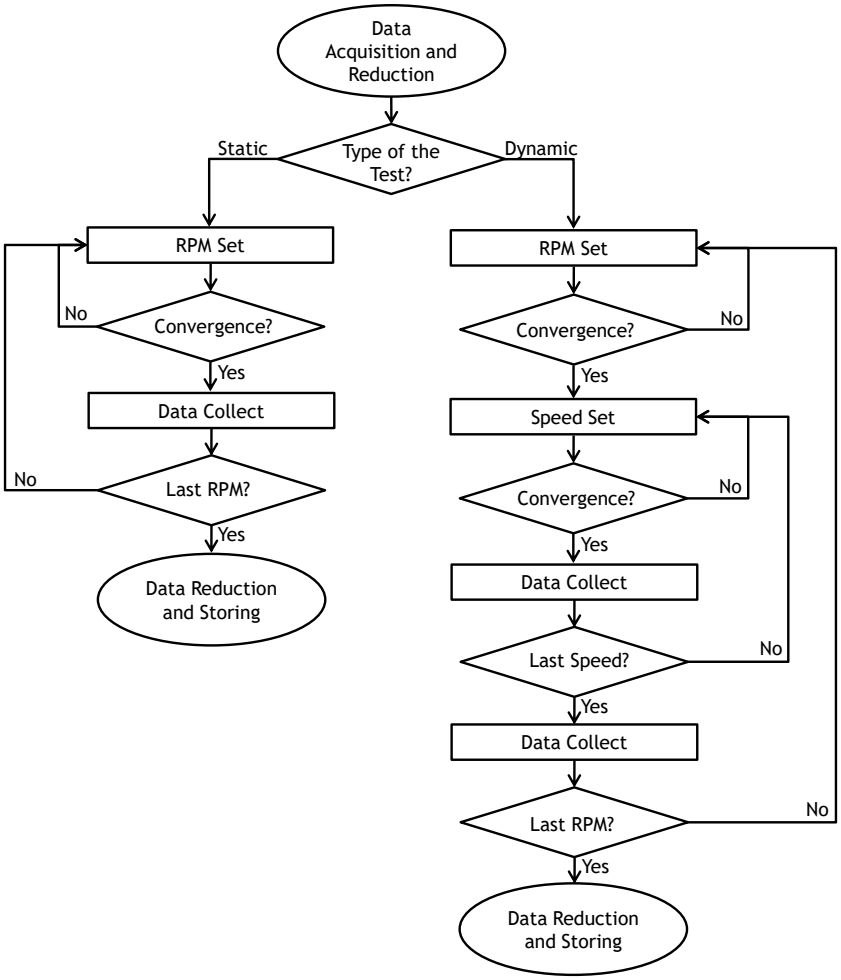

Figure 7.7 – Flowchart of the test methodology.

The procedure of collecting data in each freestream velocity was preceded by a data convergence check period, ensuring that the steady state was reached before start recording data. To do so, freestream and propeller rotational speed convergence criteria were implemented (see Table 7.1).

Table 7.1- Convergence criteria to achieve wind tunnel steady state.

Criteria	Minimum time, s
$\left\|RPM - RPM_{target}\right\| < 10\ rpm$	50.0
$\left\|V_\infty - V_{\infty_{target}}\right\| < 0.06\ m/s$	50.0

When both convergence criteria are verified, the data start to be recorded over a pre-defined period of time. Figure 7.8 shows a typical behaviour of the torque and thrust outputs during the collecting data phase, transition for the next freestream speed, convergence and, at the right, the collection of the data in the second pre-defined velocity.

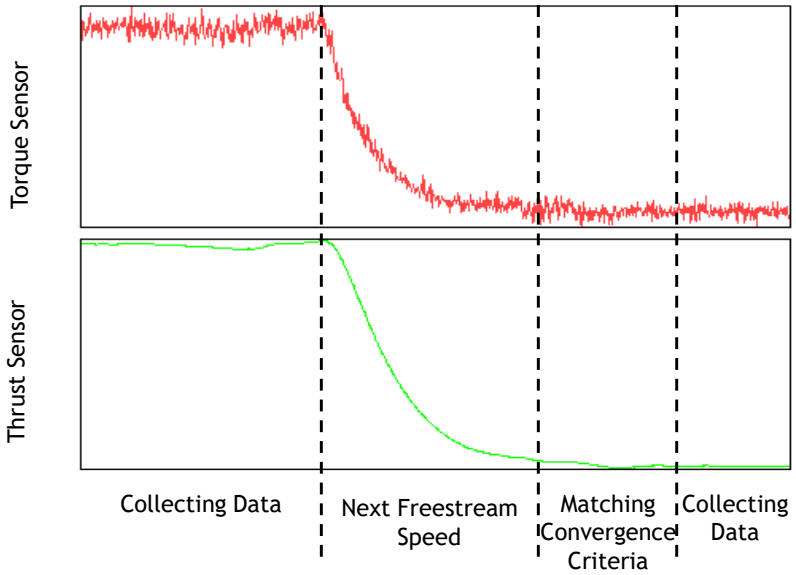

Figure 7.8 - Torque and Thrust outputs during the convergence and data collection phases.

7.2 - Wind Tunnel Corrections

7.2.1 - Boundary corrections for propellers

The interference experienced by a propeller in a closed test section of a wind tunnel was object of study by Glauert (1933). A propeller, when producing a positive thrust, creates a wake or slipstream of increased velocity as presented in Figure 7.9. Considering that the flow is confined within the test section solid walls, the condition of flow continuity leads to reduced velocity and increased pressure of the fluid surrounding the wake. These modified conditions behind the propeller change the relationship between the thrust and the freestream velocity of the wind tunnel propeller for a given rotational speed. Such that, in confined conditions, the thrust developed by the propeller is greater than would be developed in an unconstrained flow of the same freestream velocity with the same propeller rotation rate and blade pitch. Alternatively, it can also be said that the thrust developed would be equal to that which would be expected at a lower value V' in the unconstrained freestream velocity.

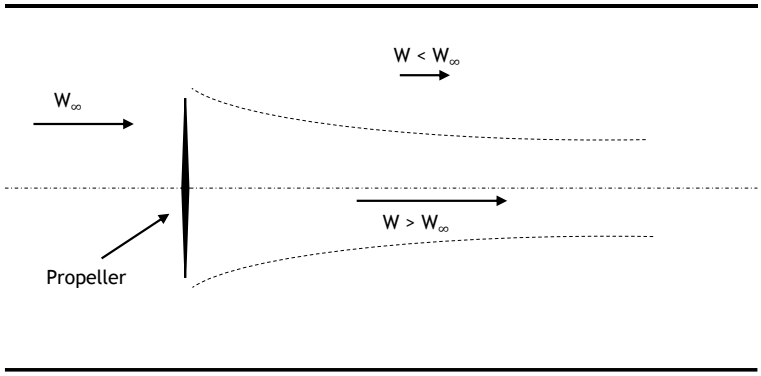

Figure 7.9 - Effect of the propeller in a closed test section.

The correction allows the calculation of the equivalent unconstrained freestream speed at which the propeller would produce the same thrust as it is producing inside the test section.

$$\frac{V_\infty}{V'} = 1 - \frac{\tau_4 \alpha_1}{2\sqrt{1+2\tau_4}} \tag{7.6}$$

where:

$$\tau_4 = \frac{T}{\rho A V'^2} \tag{7.7}$$

and

$$\alpha_1 = \frac{A}{C} \tag{7.8}$$

where A represents the propeller disk area, C represents the jet cross sectional area and T the propeller thrust.

7.2.2 - Motor fixture drag correction

Due to the presence of the torque transducer and the motor fixture, the measured thrust is actually $T\text{-}D_{fixture}$. To obtain the actual values of thrust, an assembly's drag model was implemented in order to correct the measured thrust values for different freestream velocities. The total force is given by:

$$T = \rho n^2 D^4 C_T + D_{fixture} \tag{7.9}$$

The assembly's drag was estimated according to:

$$D_{fixture} = qSC_D \tag{7.10}$$

where:

$$q = \frac{1}{2}\rho V_{drag}^2 \tag{7.11}$$

Considering that the fixture is located in the propeller slipstream, a fixture drag velocity was used as the corrected freestream velocity given by Glauert's method plus the slipstream induced velocity at the propeller disk given by the Actuator Disk Theory:

$$V_{drag} = -\frac{V_\infty}{2} + \sqrt{\left(\frac{V_\infty}{2}\right)^2 + \frac{T}{2\rho A}} + V_\infty \tag{7.12}$$

Based on the characterization of drag coefficient of various 3D bodies, and according with the literature (Selig & Ananda, 2011), an approximate C_D value of 1 proved to be adequate. The frontal area, was obtained from the 3D CAD model.

7.3 - Validation of the Test Rig

As it was previously mentioned, the experimental setup was designed to allow the testing of a wide range of low Reynolds propellers. However, before performing any tests to new and uncatalogued propellers, the test rig measurements were validated. This validation included a sample independence test which ensures that the results are not affected by the number of samples recorded at each test point. Furthermore, the same propeller test was run in 3 different days to ensure the repeatability of the test results. To finish the validation process, the obtained data for 2 different APC propellers were compared with data obtained by UIUC (Brandt, 2005) and data collected by the propellers manufacturer APC ('APC Propeller Performance Data', 2014).

7.3.1 - Sampling time independence

The stored value of any measured variable is itself the mean of *N* values collected at a sampling rate of *8Hz*. Although a higher number of samples at each point represents a more accurate result, it also represents a higher time for data acquisition at each point. In order to find the number of samples high enough that does not affect the results without spending too much time at each test point, five different number of samples (and consequently five different times) were considered to compare the results as shown in Table 7.2. The corresponding thrust coefficient results, presented at Figure 7.10 (a), show small discrepancies between 50 samples and the remaining numbers of samples used. This discrepancy appears at an advance ratio of 0.3. For the power coefficient results (see Figure 7.10 (b)), the difference between the 2 smaller samples number (50 and 100 samples) and the remaining numbers of samples is also presented. Since the results show no significant improvements when more than 200 samples are used, it was decided to use 400 samples at each point, as a compromise between sampling number and sampling time, since with this setting each test point take less than one minute.

Table 7.2- Convergence criteria to achieve wind tunnel steady state.

Sampling number	Sampling Time, *s*
50	6.25
100	12.5
200	25
400	50
800	100

7.3.2 - Measurements repeatability

To ensure that the measurements are not dependent on the weather conditions on a specific day, the measurements for a specific propeller were performed on 3 distinct days in terms of weather conditions. Furthermore, the measurements repeatability quality is an indicator of the integrity of the measurement system.

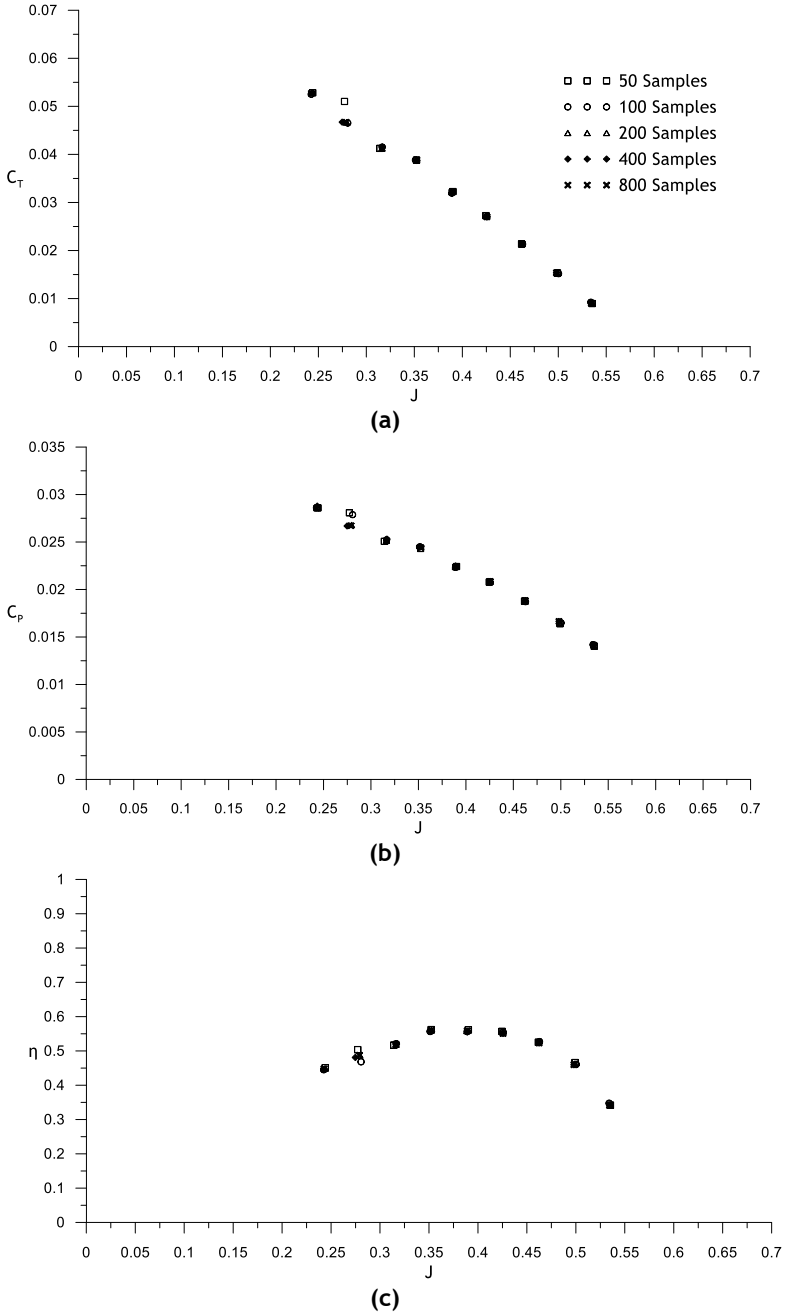

Figure 7.10 – Number of samples independence test. (a) thrust coefficient (b) power coefficient (c) propeller efficiency.

If a measurement system cannot produce consistent and repeatable measurements, a verification of the measurements accuracy cannot be performed. The test rig was submitted to

repeatability tests with the same propeller and the same test procedure. Furthermore, the same measuring instruments, with the same calibration were used. Figure 7.11 shows comparisons of the APC 11”x5.5” Thin Electric performance data collected in different days.

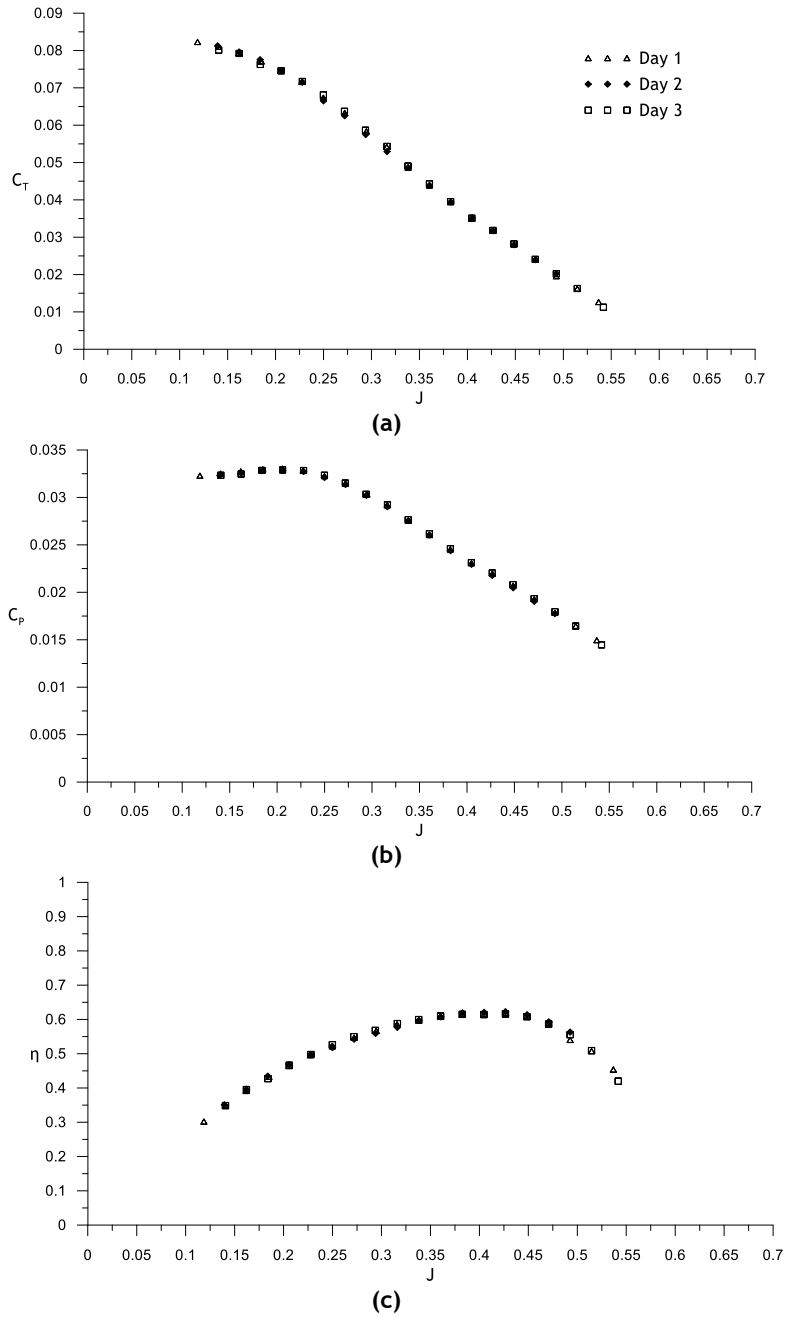

Figure 7.11 – Three days testing. (a) thrust coefficient (b) power coefficient (c) propeller efficiency.

Although the tests were performed during the summer, the weather conditions were quite different in the three days of testing, with sun on the first day moving to wind and rain on the remaining two days. As it is possible to observe in Figure 7.11, the plotted results show an exceptional repeatability for both thrust coefficient and power coefficient. In addition, since the propeller efficiency is calculated using the thrust and power coefficient it also shows good repeatability over the different days measurements.

7.3.3 - Propeller performance data comparison

To finish the validation of the test rig, the performance of two different APC commercial propellers was measured and compared with results available on the literature. The used propellers were the APC 10”x4.7” Slow Flyer and the APC 11”x5.5” Thin Electric. Their performance data were compared with UIUC measurements (Brandt *et al.*, 2014) and with the propellers’ manufacturer data (‘APC Propeller Performance Data’, 2014). The UIUC data were downloaded from the UIUC Propeller Datasite and they were corrected according to instructions provided by Selig & Ananda (2011). The APC propeller data were obtained from the APC website (‘APC Propeller Performance Data’, 2014).

7.3.3.1 APC 10”x4.7” Slow Flyer

The APC 10”x4.7” Slow Flyer propeller (see Figure 7.12) is an injection moulded propeller. It is made from long fibre composite developed by APC (‘APC Propeller Materials’, 2014).

Figure 7.12 – APC 10”x4.7” Slow Flyer Propeller.

The results of the propeller performance data for *4000* RPM are presented in Figure 7.13. It is possible to observe that the UBI measured thrust coefficient values (see Figure 7.13 (a)) are slightly lower when compared to the UIUC thrust coefficient values. The values presented by the propeller’s manufacturer (‘APC Propeller Performance Data’, 2014) shows a smaller thrust coefficient for the lowest advance ratio. In addition, the zero thrust condition occurs for higher advance ratio when compared to UBI and UIUC. Regarding the power coefficient (see Figure 7.13 (b)), the measured values show good agreement with the values presented by UIUC. The APC power coefficient values show better comparison than the thrust coefficient, although in the lower advance ratios the discrepancy tends to increase. Since the APC measurements show the zero thrust occurring at higher advance ratio, the maximum efficiency occurs at a higher advance ratio. However, the value of efficiency itself is slightly lower than the value measured by UBI and UIUC.

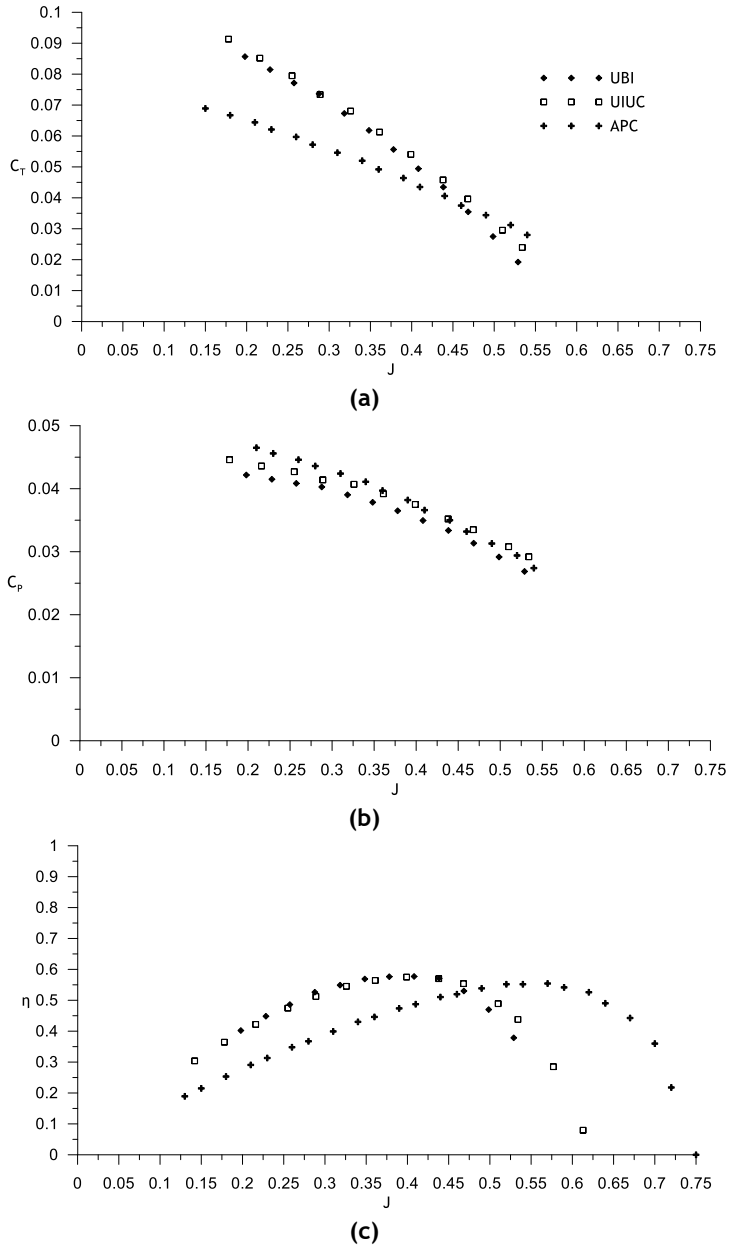

Figure 7.13 – APC 10"x4.7" Slow Flyer performance comparison for *4000* RPM. (a) thrust coefficient (b) power coefficient (c) propeller efficiency.

Regarding the *5000* RPM results, presented in Figure 7.14, it is possible to observe that the UBI measured thrust coefficient shows good agreement with the UIUC values. The APC thrust coefficient still shows lower values for the lower advance ratios and a different slope, leading that the zero thrust condition occurs at a higher advance ratio. Regarding the power coefficient, the UBI measured values still show some offset from the UIUC values. This discrepancy is almost constant at about 6%. The APC values rapidly increase for different advance ratios lower than 0.15, maintaining a correct trend for higher advance ratios. The efficiency obtained by UBI closely matches the UIUC efficiency value and the advance ratio of its maximum. The APC efficiency is again slightly under predicted and its maximum occurs for higher advance ratios, due to the slope of the thrust coefficient values.

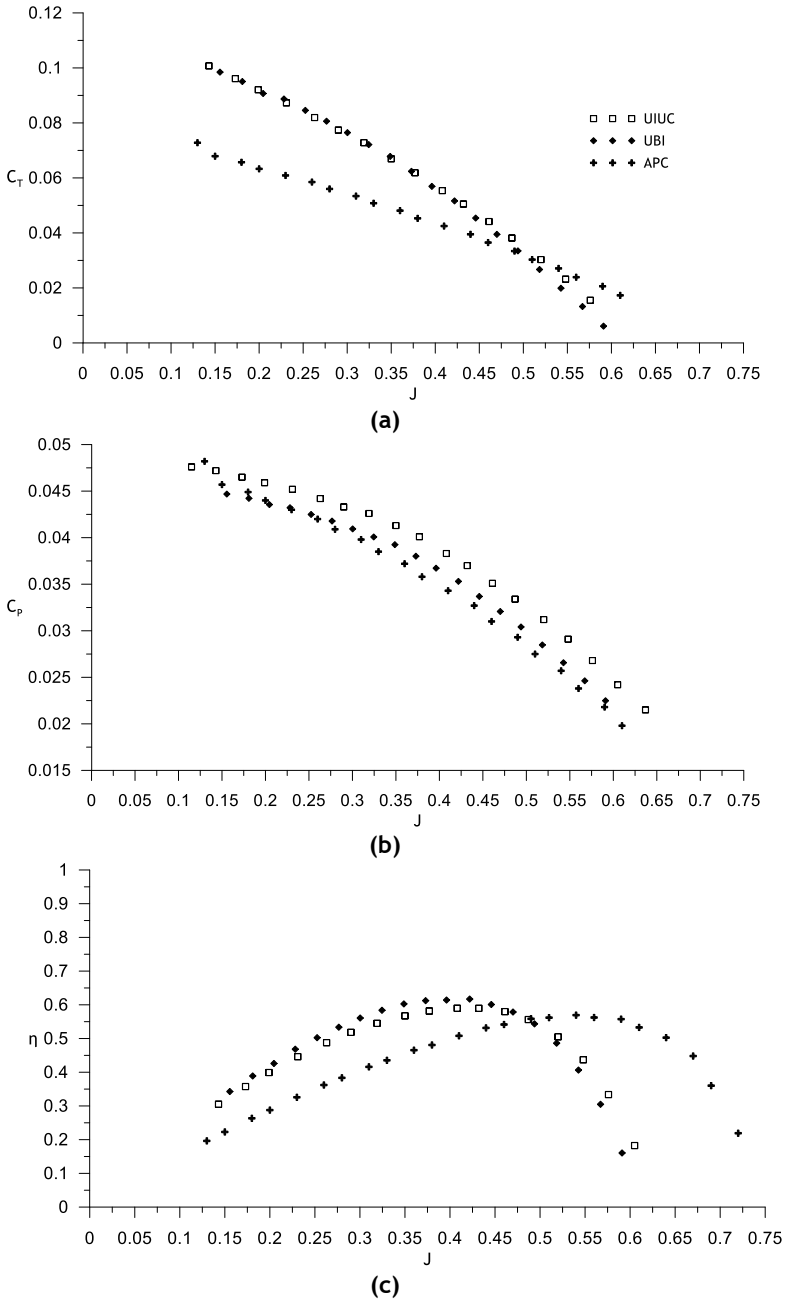

Figure 7.14 – APC 10x4.7" Slow Flyer performance comparison for *5000* RPM. (a) thrust coefficient (b) power coefficient (c) propeller efficiency.

7.3.3.2 APC 11"x5.5" Thin Electric

The APC 11"x5.5" Thin Electric propeller (see Figure 7.15) is also an injection moulded propeller using the long fibre composite as material. The performance data obtained for the APC 11"x5.5" Thin Electric propeller for 3000 RPM, 4000 RPM and 5000 RPM are presented, respectively, in Figure 7.16, Figure 7.17 and Figure 7.18.

Figure 7.15 – APC 11”.5.5” Thin Electric Propeller.

For the 3000 RPM (see Figure 7.16), the thrust coefficient measured by UBI closely matches the value obtained by UIUC. The APC data keep the different behaviour presented in the APC 10”x4.7” results from the UBI and UIUC, proving that those differences are not related with the propeller shape. Concerning the power coefficient, UBI and UIUC values are in good agreement, while APC is presenting slightly higher values over the advance ratio range. As previously mentioned, the maximum efficiency, obtained by APC, occurs at a higher advance ratio due to the difference presented in the thrust coefficient measurements.

Regarding the 4000 RPM (see Figure 7.17) UBI’s measured thrust coefficient values are slightly higher than the values measured by UIUC, especially at lower advance ratios. The power coefficient measurements obtained by UBI are in good agreement with the measurements from UIUC. The APC measurements show a correct trend, although the values are slightly higher than those measured by UBI and UIUC. Due to the difference presented on the thrust coefficient measurements, the efficiency obtained by UBI is slightly higher than the efficiency presented by UIUC.

For the *5000* RPM (see Figure 7.18) the thrust coefficient measured at UBI shows an offset when compared to the UIUC. This offset is bigger at intermediate advance ratios and tends to disappear at higher advance ratios. The APC data still presents the different behaviour previously mentioned, with lower thrust coefficient at lower advance ratios and showing the zero thrust condition at a higher advance ratio. The UBI’s power coefficient values show a negative offset at lower advance ratios and a small positive offset at intermediate advance ratios. Since the differences on the thrust coefficient are bigger than the differences on power coefficient the propeller’s efficiency is higher than the efficiency obtained by UIUC.

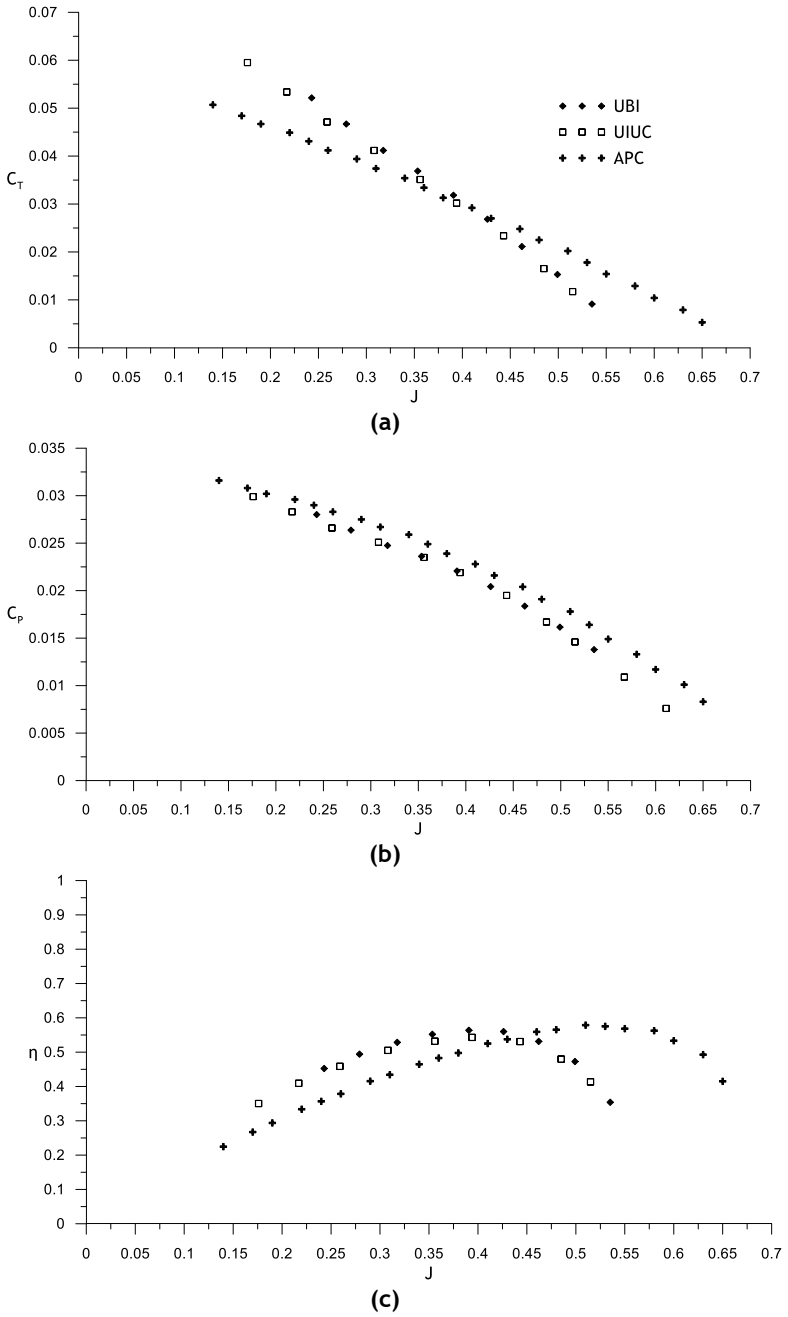

Figure 7.16 - APC 11”x5.5” Thin Electric performance comparison for *3000* RPM. (a) thrust coefficient (b) power coefficient (c) propeller efficiency.

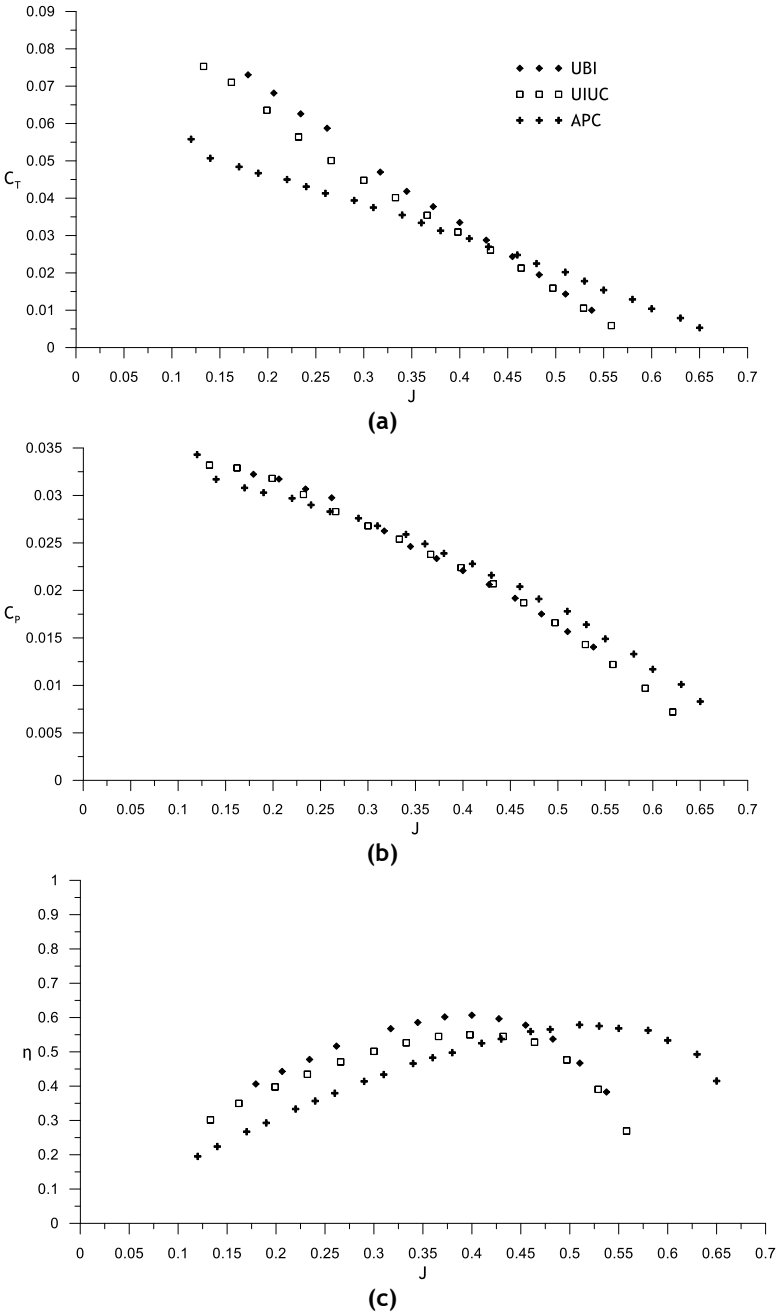

Figure 7.17 - APC 11”x5.5” Thin Electric performance comparison for *4000* RPM. (a) thrust coefficient (b) power coefficient (c) propeller efficiency.

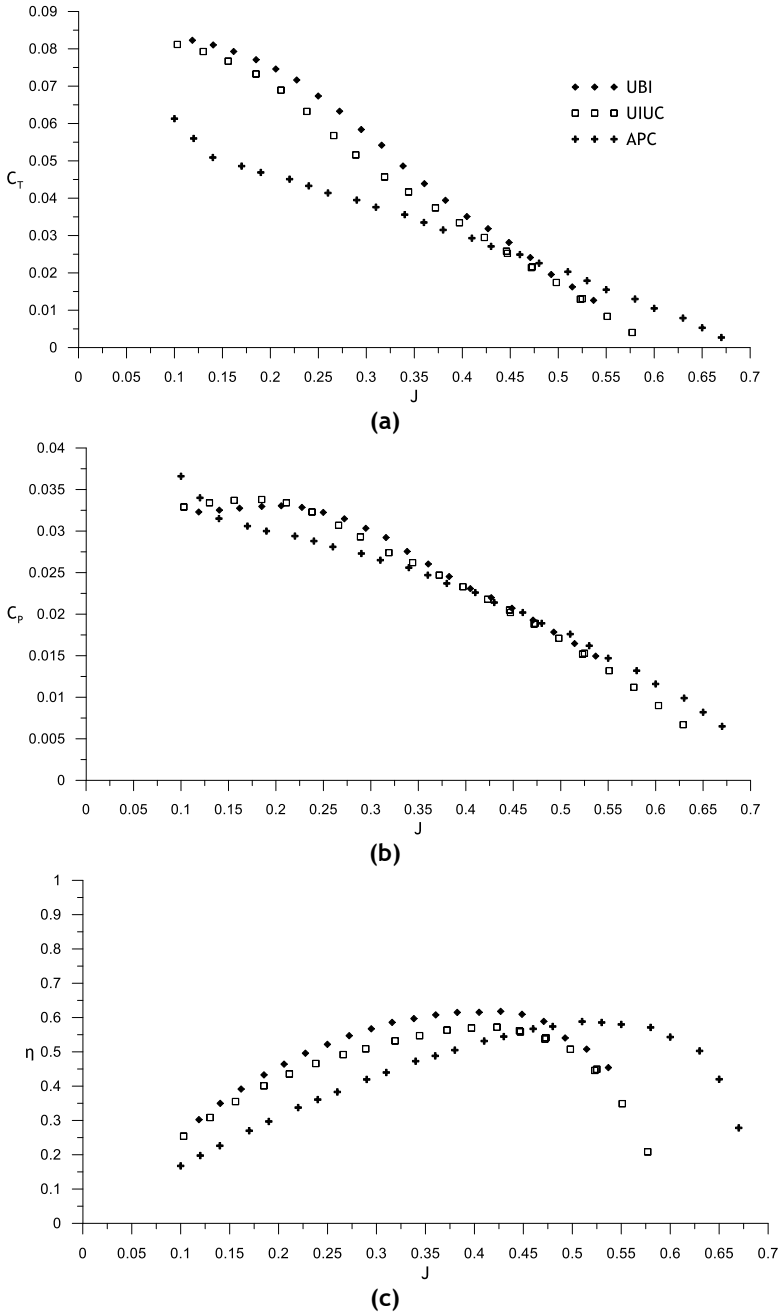

Figure 7.18 - APC 11"x5.5" Thin Electric performance comparison for *5000* RPM. (a) thrust coefficient (b) power coefficient (c) propeller efficiency.

Observing all the rotational speeds, it is possible to conclude that the thrust coefficient increases with the increase in the propeller rotational speed for the same advance ratio. The increase in the rotational speed leads to an increment in the Reynolds number at which the airfoil is operating. Since these low Reynolds propellers operate around their airfoil's critical Reynolds numbers, this increase of the rotational speed consequently leads to an increment in the airfoils maximum lift coefficient, causing an increment in the thrust coefficient. In addition, the lift-to-drag ratio also increases with the Reynolds number increment leading to higher efficiencies at higher rotational speeds.

7.3.4 - Uncertainty Analysis

To calculate the level of precision of the obtained results an uncertainty analysis was performed. The error propagation begins with the primary measured quantities including thrust, torque, atmospheric pressure, flow's temperature and flow differential pressure. During this analysis it was assumed that there is no error on the conversion from the sensor's voltages to the physical quantities. In addition it was considered that the propeller's diameter was exact as specified by the manufacturer. To start the analysis each sensor uncertainty was considered as presented at Table 7.3.

Table 7.3- Convergence criteria to achieve wind tunnel steady state.

Measurement	Sensor	Uncertainty
Thrust	FGP FN3148	± 0.05 N
Torque	Transducer Techniques RTS-100	± 0.000339 N.m
Atmospheric Temperature	National Instruments LM335	± 1.0 K
Atmospheric Pressure	Freescale Semiconductor MPXA4115A	±30 Pa
Propeller RPM	Fairchild Semiconductor QRD1114	± 5 RPM
Differential Pressure	MKS 226A Differential Pressure Manometer	± (0.3 x Reading) Pa

The error on the freestream velocity is given by:

$$\sigma_V = \sqrt{\left[\frac{\partial V}{\partial(p_1 - p_2)}\delta(p_1 - p_2)\right]^2 + \left[\frac{\partial V}{\partial T_{atm}}\delta T_{atm}\right]^2 + \left[\frac{\partial V}{\partial P_{atm}}\delta P_{atm}\right]^2} \quad 7.13$$

The error on advance ratio can be expressed by:

$$\sigma_J = \sqrt{\left[\frac{\partial J}{\partial(p_1 - p_2)}\delta(p_1 - p_2)\right]^2 + \left[\frac{\partial J}{\partial T_{atm}}\delta T_{atm}\right]^2 + \left[\frac{\partial J}{\partial P_{atm}}\delta P_{atm}\right]^2 + \left[\frac{\partial J}{\partial n}\delta n\right]^2} \quad 7.14$$

The error on C_T is given by:

$$\sigma_{C_T} = \sqrt{\left[\frac{\partial C_T}{\partial T}\delta T\right]^2 + \left[\frac{\partial C_T}{\partial T_{atm}}\delta T_{atm}\right]^2 + \left[\frac{\partial C_T}{\partial P_{atm}}\delta P_{atm}\right]^2 + \left[\frac{\partial C_T}{\partial n}\delta n\right]^2} \quad 7.15$$

The error on C_P is given by:

$$\sigma_{C_P} = \sqrt{\left[\frac{\partial C_P}{\partial Q}\delta Q\right]^2 + \left[\frac{\partial C_P}{\partial T_{atm}}\delta T_{atm}\right]^2 + \left[\frac{\partial C_P}{\partial P_{atm}}\delta P_{atm}\right]^2 + \left[\frac{\partial C_P}{\partial n}\delta n\right]^2} \quad 7.16$$

And finally the error on efficiency is as follow:

$$\sigma_\eta = \sqrt{\left[\frac{\partial \eta}{\partial T}\delta T\right]^2 + \left[\frac{\partial \eta}{\partial Q}\delta Q\right]^2 + \left[\frac{\partial \eta}{\partial T_{atm}}\delta T_{atm}\right]^2 + \left[\frac{\partial \eta}{\partial P_{atm}}\delta P_{atm}\right]^2 + \left[\frac{\partial \eta}{\partial n}\delta n\right]^2 + \left[\frac{\partial V}{\partial (p_1 - p_2)}\delta (p_1 - p_2)\right]^2} \quad 7.17$$

A summary of the uncertainty analysis relative to the APC 10"x7" Slow Flyer propeller (see Section 7.4) at *5000* RPM test is presented at Figure 7.3.

Table 7.4- APC 10"x7" Slow Flyer propeller uncertainty for *4000* RPM.

	Uncertainty				
V'	V, %	J, %	C_t, %	C_p, %	η, %
4	2.834	0.186	0.193	0.463	2.874
5	3.833	0.178	0.173	0.446	3.859
6	2.533	1.744	3.363	3.376	3.126
7	1.480	0.176	0.267	0.502	1.576
8	0.817	0.170	0.245	0.477	0.964
9	0.891	0.166	0.181	0.450	1.003
10	0.551	0.177	0.222	0.520	0.758
11	0.617	0.167	0.236	0.468	0.791
12	0.420	0.163	0.203	0.493	0.660
13	0.334	0.166	0.235	0.540	0.654
14	0.380	0.173	0.332	0.606	0.755
15	0.309	0.171	0.332	0.654	0.765
16	0.376	0.173	0.539	1.407	1.553
17	0.273	0.171	0.926	0.854	1.267
18	0.237	0.172	1.290	1.001	1.268

It can be noted that for freestream velocities around *5-6 m/s* interval there is an increased uncertainty in the results. By analysing the raw data, this appears to be a result of higher fluctuations on the measurements around this velocity interval. Observing the Table 7.4 it is possible to conclude that for freestream velocities above *7 m/s*, the uncertainty in this parameter is less than 1%. The uncertainty in C_t is typically less than 0.3% while the uncertainty in $C_P$is typically less than 0.6%. Additionally, the uncertainty in η is typically less than 1%.

The observed uncertainties proved to be small and, as expected, they increase as the predominant primary measurement decreases such as the uncertainty in freestream velocity which increases as P_{diff}measurements decrease. This increased uncertainty can be found at the 5-6 *m/s* freestream velocity interval for all the tests.

7.4 - APC 10”x7” SF Propeller Inverse Design

7.4.1 - Propeller CAD inverse design

An APC 10”x7”SF original propeller was cutted and digitized as presented by Carvalho (2013), following the indiactions given in Drela (2005a). The resulting airfoil was imported in the CAD Software and the propeller was designed and manufactured in order to be tested in the UBI’s wind tunnel and compared with the original APC 10”x7” SF propeller.

The coordinates of the airfoils were exported from JBLADE and imported into CATIA V5 using a Microsoft Excel macro. The airfoils were radially positioned using their leading edge as the origin (see Figure 7.19 (a)). Subsequently, the airfoils were translated in the chord wise direction up to their quarter chord positions became coincident with the radial axis (see Figure 7.19 (b)). This represents the geometry as it is considered inside JBLADE, since the JBLADE software does not account any sweep in the blades. The airfoils were then independently rotated about their quarter chord point, according to the blade incidence distribution in the geometry data obtained in the literature (Brandt *et al.*, 2014).

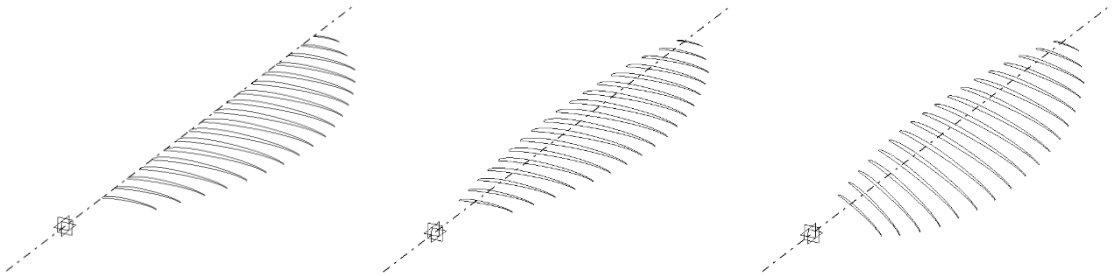

(a) **(b)** **(c)**

Figure 7.19 –Propeller CAD design steps (a) airfoils import and leading edge alignment (b) airfoils translation to their quarter chord point (c) airfoils pitch setting.

The leading and trailing edges guidelines were built passing on each airfoil section and the CATIA multi-section solid tool was used to obtain the propeller blade. The hub region was then designed and attached to the blades, resulting in the propeller presented in Figure 7.20.

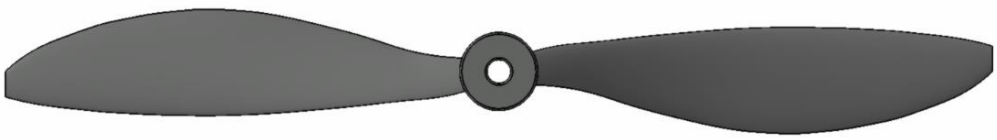

Figure 7.20 - Top view of final blade geometry.

7.4.2 - Moulds manufacture

In order to perfectly replicate the geometry, it was decided to use CNC machined moulds. To design the moulds, the top and bottom surfaces of the blade were extracted and 2 different solid parts were obtained in CATIA (see Figure 7.21). After obtaining the two mould halves, four holes were added to ensure the correct alignment during the mould filling. Each mould geometry was then exported and imported in the milling CAM software, allowing the generation of the three axis CNC Router cutter paths.

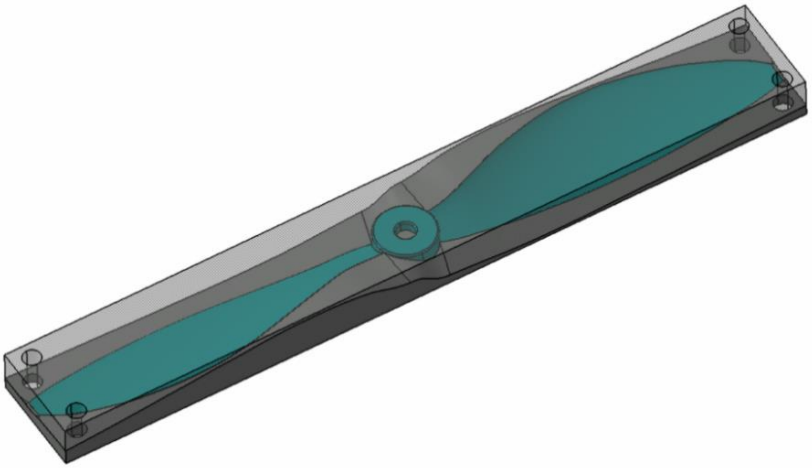

Figure 7.21 – View of the blade within the mould, showing the mould halves matching.

The PowerMill® CAM software was used to generate the necessary G code. After importing the geometry into the software the dimensions of the raw material block were defined. The next step was the definition of different tools used along the machining process.

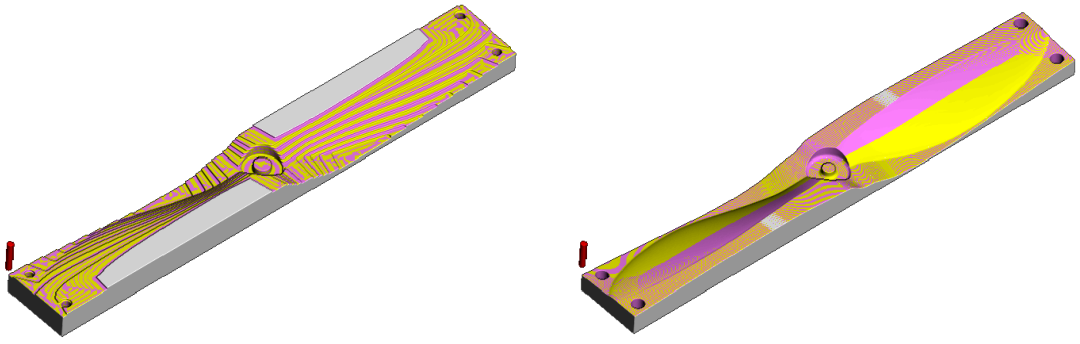

(a) **(b)**

Figure 7.22 – (a) Illustration of the mould after the roughing path. (b))Illustration of the mould after the finishing path.

The 8 mm drill was firstly used to remove the bigger part of the material (see Figure 7.22 (a)) while the 3 mm drill was used to finish the surface of the mould (see Figure 7.22 (b)). The final obtained mould is presented in Figure 7.23.

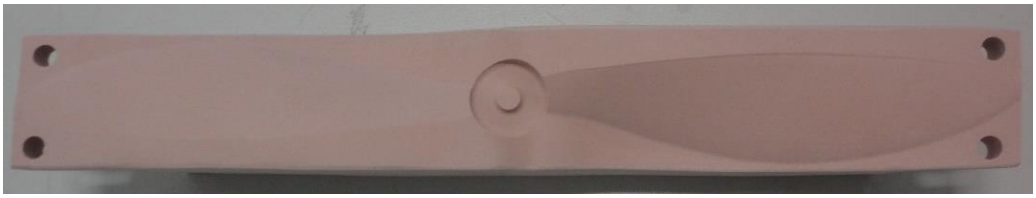

Figure 7.23 – Final obtained mould.

While being machined, the moulds were supported at various locations with two face adhesive tape to prevent any movement of the block due to the cutting forces applied by CNC machine.

7.4.3 - Propeller manufacture

The material used to manufacture the propeller was epoxy resin reinforced with carbon fibre. The different layers of carbon fibre were previously cutted to correctly fit inside the mould. Four layers were used to give the necessary thickness to the propeller blades, with some extra reinforcements in the root region as presented in Figure 7.24.

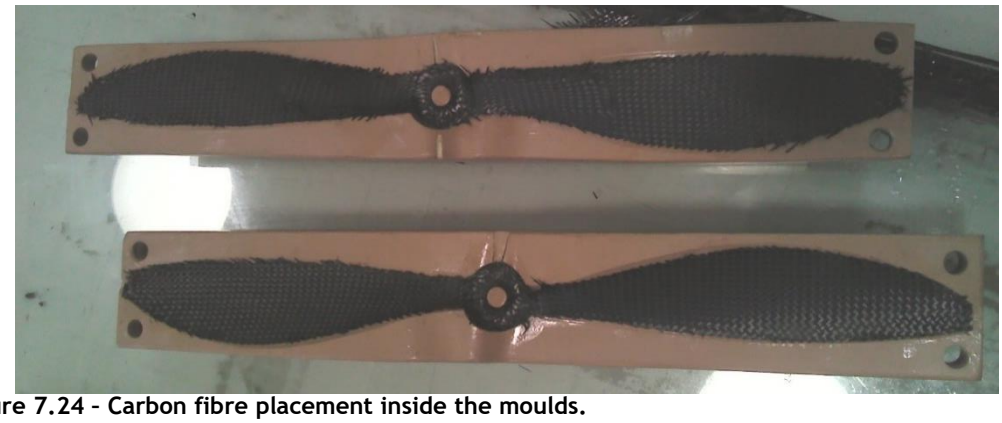

Figure 7.24 – Carbon fibre placement inside the moulds.

The carbon fibre was then impregnated with epoxy resin and fitted within the moulds. After inserting the impregnated carbon fibre cloth layers, the moulds were closed and filled with epoxy in order to fill any air bubbles and give the correct blade shape to the propeller's blades (see Figure 7.25).

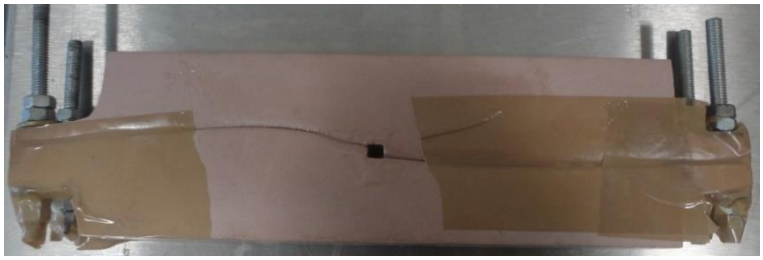

Figure 7.25 – Closed moulds with carbon fibre inside and with a hole to allow the moulds fill with epoxy resin.

After the epoxy curing process the moulds were opened and the blades were finally hand-finished to achieve a smooth surface. The final produced propeller is presented in Figure 7.26.

Figure 7.26 – Final manufactured propeller, representing the APC 10”x7” SF propeller in JBLADE Software.

The manufactured propeller was then mounted in the experimental test rig presented in Section 7.1 and it was tested. Its performance is presented in Section 7.5.

7.5 - Results and Discussion

The replica of APC 10”x7” Slow Flyer was tested in the wind tunnel and the data was compared with JBLADE predictions. Figure 7.27 presents the static thrust and torque obtained in UBI’s wind tunnel for the original APC 10”x7” SF and for the built propeller replica.

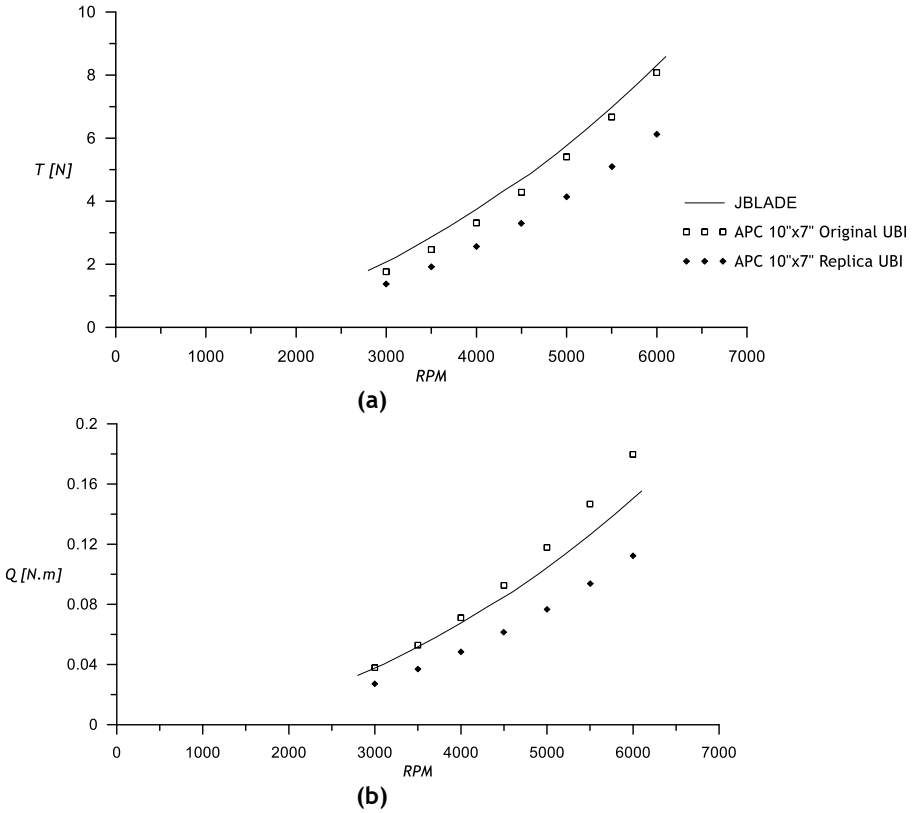

Figure 7.27 - APC 10”x7” Slow Flyer static performance comparison with JBLADE predictions. (a) propeller thrust (b) propeller torque

Observing Figure 7.27 (a) it is possible to observe that the JBLADE predictions are overestimating the thrust coefficient, when compared to the APC 10”x7” SF replica but are close to the original propeller performance. Regarding the torque (see Figure 7.27 (b)) the JBLADE is also overestimating the torque when compared with replicated propeller. However,

the predictions for higher rotational speeds tend to approach the replicated propeller data. Again, the predictions are quite close to the original propeller data although deteriorate towards higher advance ratios.

Figure 7.28 presents the propeller wind tunnel measurements and JBLADE predictions for *3000* RPM. It is possible to observe that the thrust coefficient (see Figure 7.28 (a)) of the original propeller is higher than the replica built at UBI and also higher than JBLADE predictions. It is also possible to observe a slightly bigger thrust coefficient predicted by JBLADE when compared to the UIUC data. For bigger advance ratios, when the Reynolds numbers become bigger (but still in the 10^5 range), the predictions of the JBLADE match the replicated propeller experimental data.

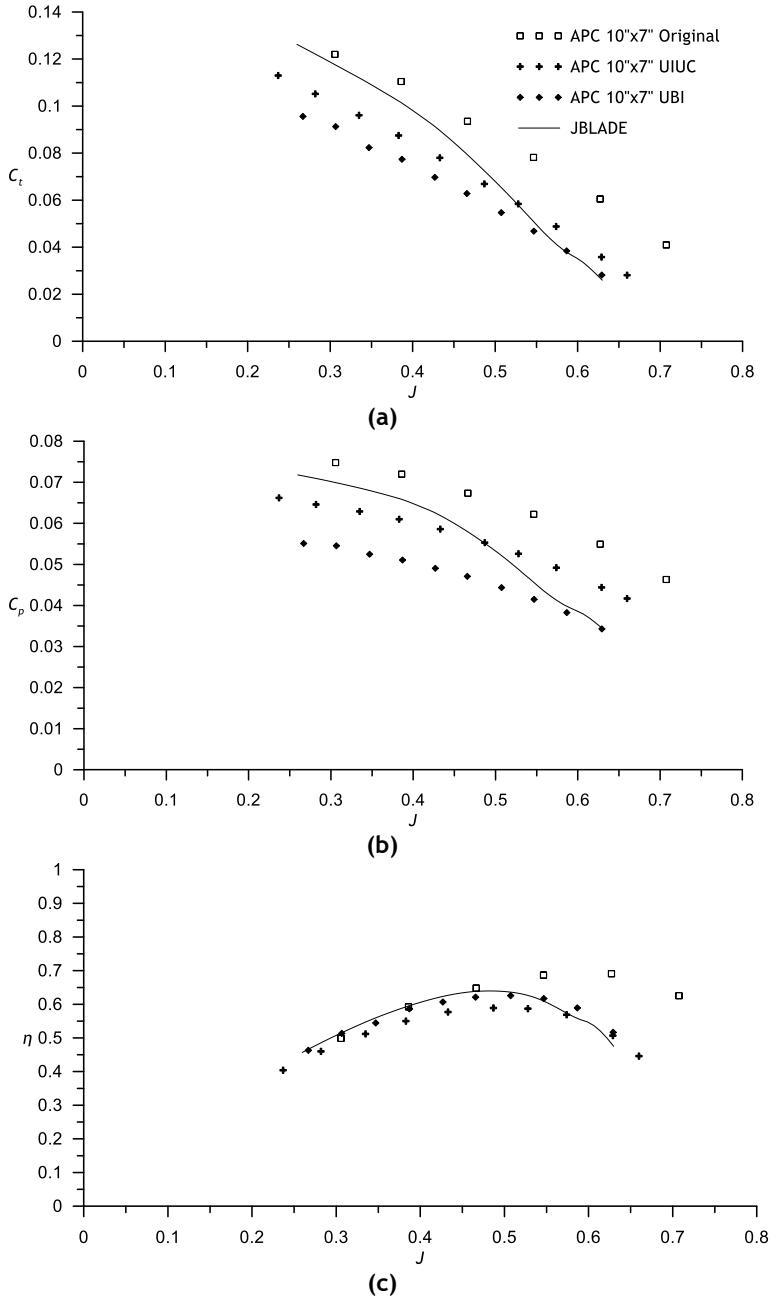

Figure 7.28 - APC 10"x7" Slow Flyer performance comparison with JBLADE Predictions for *3000* RPM (a) thrust coefficient (b) power coefficient (c) propeller efficiency.

Observing the power coefficient (see Figure 7.28 (b)) it is possible to conclude that the power coefficient of the original propeller obtained in UBI's wind tunnel is bigger than that of the UIUC data. The power coefficient obtained for the APC 10"x7" SF replicated at UBI is also smaller, following the thrust coefficient results. JBLADE power coefficient predictions also match the replicated propeller measurements at bigger advance ratios.

Since the propeller efficiency is directly dependent on the thrust and power coefficient, the measurements obtained at UBI's wind tunnel indicate higher maximum efficiency, occurring at bigger advance ratio for the original APC 10"x7" SF propeller. Regarding the replicated propeller measurements, UIUC measurements and JBLADE predictions, they indicate similar maximum efficiency value, occurring for an advance ratio of about 0.5.

The propellers measurements for *6000* RPM are presented in Figure 7.29. Observing the thrust coefficient measurements (see Figure 7.29 (a)) it is possible to observe the same trend that was presented in the *3000* RPM measurements, with the original propeller presenting bigger thrust coefficient. JBLADE is still overestimating the propeller thrust coefficient for smaller advance ratios but as the Reynolds numbers increase, the prediction gets closer to the measurements.

Regarding power coefficient (see Figure 7.29 (b)), the original propeller data obtained in the UBI's wind tunnel is also presenting higher power coefficient when compared with UIUC measurements and with the replicated propeller. JBLADE is still overestimating the power coefficient for small advance ratios. However, contrary to the *3000* RPM results, for *6000* RPM is underestimating the power coefficient at bigger advance ratios.

Observing the propeller efficiency (see Figure 7.29 (c)) it is possible to conclude that JBLADE is predicting a similar maximum efficiency value as the replicated propeller. However, JBLADE is predicting the maximum efficiency for bigger advance ratio than the experimental measurements. Following what was presented for the *3000* RPM, the original propeller measurements at UBI are indicating a bigger maximum efficiency value, occurring at bigger advance ratio, when compared to the UIUC and replicated propeller measurements.

Generally, the results presented in Figure 7.27, Figure 7.28 and Figure 7.29 show good agreement between JBLADE and measurements. Thus, it was shown that JBLADE can be used to accurately predict the propeller performance.

From the general comparison of the original propeller and its replica it can be concluded that large discrepancies exist between them. This can be due to the method suggested by Drela, (2005a) for obtaining the airfoils' geometry and blade pitch and chord distributions. A 3D scan for obtaining the replica would probably result in a closer replica. On the other hand, the significant discrepancies between the replica experimental data and the JBLADE predictions

suggest that the structural analysis sub-module should interact with the aerodynamic simulation sub-module to account the fluid-structure interaction on the propeller performance predictions. For now, the JBLADE structure sub-module can only be used in the perspective of correcting the working propeller geometry due to loads on the fabrication of the blades as the literature sometimes mentions as “hot” *vs* “cold” propeller shapes.

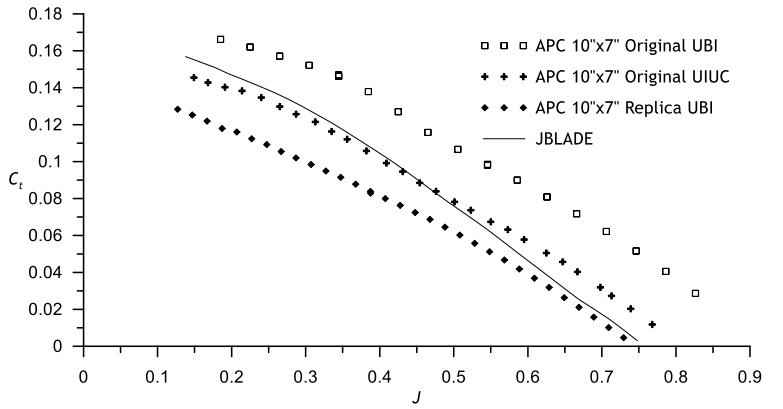

(a)

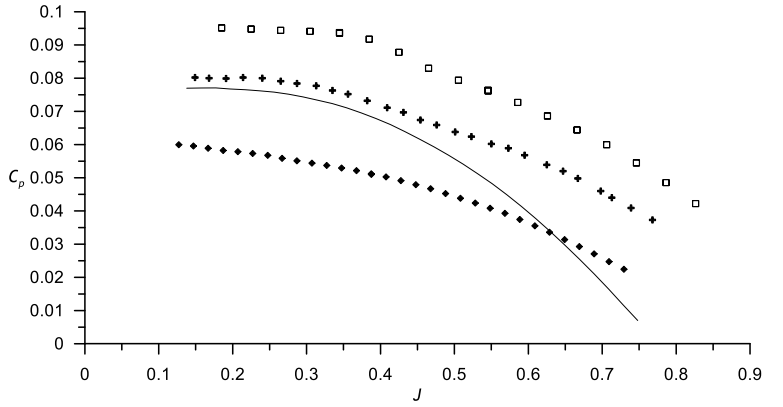

(b)

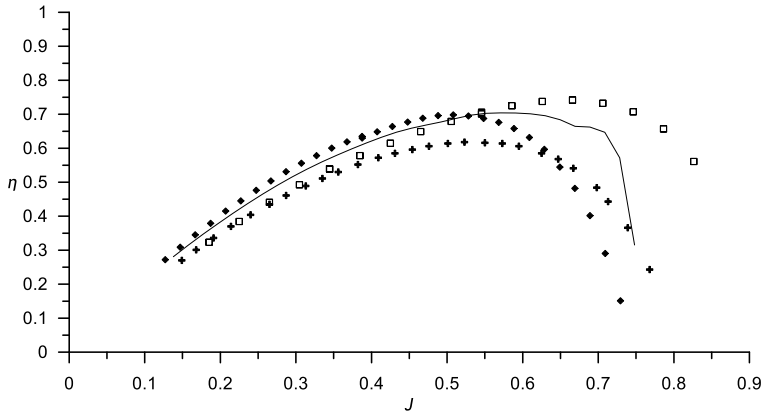

(c)

Figure 7.29 - APC 10”x7” Slow Flyer performance comparison with propeller built for a rotational speed of *6000* RPM (a) thrust coefficient (b) power coefficient (c) propeller efficiency.

Chapter 8

Conclusions

8.1 - Summary and conclusions

The JBLADE software was developed and validated through the comparison of different propellers' performance data from RANS CFD and experiments. It was found that the correct modelling of the post-stall airfoil characteristics play a major role, especially in the low advance-ratio performance predictions. A new 3D equilibrium model was developed and validated against conventional RANS CFD simulations. A new correlation for predicting the drag coefficient at 90º angle of attack was developed allowing an improved modelling of the airfoil post stall characteristics that proved to be reliable and improves the performance predictions. The fitting of the correlation originally suggested by Timmer (2010) was also improved and implemented. Different post-stall models originally developed for wind turbines were extended to propeller performance predictions showing that they can improve the predictions over other available codes. The *Inverse Design sub-module* was integrated in the JBLADE software and validated against reference data. A basic *Structural sub-module* was also implemented and validated against FEM Software data. The results have shown that both the tip displacement and the torsion along the blade predicted by JBLADE are in good agreement with the more complex CATIA V5 FEM simulations. In addition, this sub-module allows the prediction of propeller's deflections due to the thrust generation for a given operation point leading to an extra optimization loop, in which the user can re-design the propeller to achieve its maximum efficiency when operating, instead of optimize only the "cold" geometry. It should be mentioned that although throughout the validation significant discrepancies were observed between JBLADE and the experimental data, those propellers geometries always corresponded to the "cold" geometry while the experimental performance data occurs in the "hot" geometry. So, one could not expect excellent fits. For now, the JBLADE structure sub-module can only be used in the perspective of correcting the working propeller geometry due to loads on the fabrication of the blades as the literature sometimes mentions as "hot" *vs* "cold" propeller

shapes. It was shown that the XFOIL remains an excellent airfoil design and analysis tool with predictions being comparable to those of RANS CFD with the most suited turbulence and transition closure models. A new airfoil to use in the MAAT cruiser airship propeller was developed. It was shown that a new concept of using the $L^{3/2}/D$ optimization in the blade leads to more efficient propellers. The APC 10"x7" SF propeller experimental data was used to validate JBLADE for low Reynolds number simulations. A new low Reynolds propellers wind tunnel test rig was developed and validated through the comparison of the performance with reference data available in the literature for some commercially available propellers. The new test rig proved to be suitable to test a wide range of low Reynolds number propellers up to a diameter of about 14". Furthermore, a replica of APC 10"x7" SF was built to test a prototype construction technique and its performance was characterized in the wind tunnel.

Considering the work presented in this thesis, the major conclusions are:

- A new software suitable for low Reynolds propeller design was developed and validated against numerical and experimental data.
- An inverse design methodology together with a simple structural sub-module were implemented in the JBLADE and validated.
- A new 3D Equilibrium model was developed and validated.
- A new method to calculate the drag coefficient of the airfoils at 90 degrees, based on the airfoil's leading edge shape was developed.
- The post stall models were extended to propeller performance prediction and they were implemented and validated in the JBLADE Software.
- An efficient airfoil to use at high altitudes in low Reynolds propellers was developed.
- Two propellers, for application on the MAAT cruiser airship were designed, proving that a new concept of using the airfoil best $L^{3/2}/D$ produces more efficient propellers.
- An original experimental test rig was developed and validated against reference data.
- A replica of an APC 10"x7" SF propeller was built and tested.

8.2 - Future Works

Regarding future works, it is proposed to develop a more complete 3D equilibrium model that will not be dependent of the constant axial induction assumption on the propeller's disk. In the future, the JBLADE propeller structure sub-module can be used to interact with the aerodynamic simulation sub-module to account the fluid-structure interaction on the propeller performance predictions. Some additional sub-modules can be implemented in JBLADE such as an electrical motor model, to couple with the existing aerodynamic module, in order to estimate the efficiency of the complete powerplant, instead of the propeller performance alone. It can also be implemented the possibility to account for the blade sweep of the propellers. Other propeller blades structure concepts can be implemented in the structural module and the formulation itself can be improved.

This page has been intentionally left blank
for double side copying

Bibliography

AC65-12A. (1976). *Mechanics Powerplant Handbook*, 1st Editio. Washington D.C.: Department of Transportation - FAA.

Adkins, C. N. & Liebeck, R. H. (1994). Design of optimum propellers. *Journal of Propulsion and Power* Vol.10, (5), pp. 676–682. doi: 10.2514/3.23779.

Alves, P. (2014). *Low Reynolds Number Propeller Performance Measurement in Wind Tunnel Test Rig*.

Azuma, A. & Kawachi, K. (1979). Local Momentum Theory and Its Application to the Rotary Wing. *Journal of Aircraft* Vol.16, (1), pp. 6–14. doi: 10.2514/3.58476.

Banks, W. H. H. & Gadd, G. E. (1963). Delaying Effect of Rotation on Laminar Separation. *AIAA Journal* Vol.1, (4), pp. 941–941. doi: 10.2514/3.1687.

Bardina, J., Huang, P., Coakley, T., Bardina, J., Huang, P. & Coakley, T. (1997). Turbulence modeling validation. In *28th Fluid Dynamics Conference*. Reston, Virigina: American Institute of Aeronautics and Astronautics. doi: 10.2514/6.1997-2121.

Benini, E. (2004). Significance of blade element theory in performance prediction of marine propellers. *Ocean Engineering* Vol.31, (8-9), pp. 957–974. doi: 10.1016/j.oceaneng.2003.12.001.

Betz, A. & Prandtl, L. (1919). Schraubenpropeller mit Geringstem Energieverlust. *Nachrichten von der Gesellschaft der Wissenschaften zu Göttingen, Mathematisch-Physikalische Klasse* pp. 193–217.

Biermann, D. (1936). Compromises in Propeller Design. *Journal of the Aeronautical Sciences* Vol.3, (4), pp. 142–144. doi: 10.2514/8.162.

Black, S. D. (1997). *Integrated lifting-surface/Navier-Stokes design and analysis methods for marine propulsors*.

Bouatem, A. & Mers, A. Al. (2013). Validation of Chaviaro Poulos and Hansen Stall Delay Model in the Case of Horizontal Axis Wind Turbine Operating in Yaw Conditions. *Energy and Power Engineering* Vol.05, (01), pp. 18–25. doi: 10.4236/epe.2013.51003.

Bradshaw, P. (1994). Turbulence: the chief outstanding difficulty of our subject. *Experiments in Fluids* Vol.16, (3-4), pp. 203–216. doi: 10.1007/BF00206540.

Brandt, J. B., Deters, R. W., Ananda, G. K. & Selig, M. S. (2014). UIUC Propeller Data Site. *UIUC Propeller Database - University of Illinois at Urbana-Champaign*. (accessed 10/07/2014) [Available at: http://m-selig.ae.illinois.edu/props/propDB.html].

Brandt, J. & Selig, M. (2011). Propeller Performance Data at Low Reynolds Numbers. In *49th AIAA Aerospace Sciences Meeting including the New Horizons Forum and Aerospace Exposition*, pp. 1–18. Reston, Virigina: American Institute of Aeronautics and Astronautics. doi: 10.2514/6.2011-1255.

Brandt, J. B. (2005). *Small-Scale Propeller Performance at Low Speeds*.

Caldwell, F. W. (1937). Propellers for Aircraft Engines of High Power Output. *Journal of the Aeronautical Sciences* Vol.5, (2), pp. 37–52. doi: 10.2514/8.510.

Carvalho, I. D. (2013). *Low Reynolds Propellers for Increased Quadcopters Endurance*.

Chang, K. C., Hsieh, W. D. & Chen, C. S. (1995). A Modified Low-Reynolds-Number Turbulence Model Applicable to Recirculating Flow in Pipe Expansion. *Journal of Fluids Engineering* Vol.117, (3), pp. 417–423. doi: 10.1115/1.2817278.

Chaviaropoulos, P. K. & Hansen, M. O. L. (2000). Investigating Three-Dimensional and Rotational Effects on Wind Turbine Blades by Means of a Quasi-3D Navier-Stokes Solver. *Journal of Fluids Engineering* Vol.122, (2), pp. 330–336. doi: 10.1115/1.483261.

Colozza, A. (1998). *High Altitude Propeller Design*. Cleveland.

Corrigan, J. & Schillings, J. (1994). Empirical Model for Blade Stall Delay Due to Rotation. In *American Helicopter Society Aeromechanics Specialists*. San Francisco.

Craft, T. J., Launder, B. E. & Suga, K. (1996). Development and application of a cubic eddy-viscosity model of turbulence. *International Journal of Heat and Fluid Flow* Vol.17, (2), pp. 108–115.

Craft, T. J., Launder, B. E. & Suga, K. (1997). Prediction of turbulent transitional phenomena with a nonlinear eddy-viscosity model. *International Journal of Heat and Fluid Flow* Vol.18, (1), pp. 15–28. doi: 10.1016/S0142-727X(96)00145-2.

Curtiss-Wright. (1944). *Propeller Theory*, 1st Editio. Caldwell: Curtiss-Wright Corporation Propeller Division.

Deperrois, A. (2011). *Analysis of Foils and Wings Operating at Low Reynolds Numbers - Guidelines for XFLR5 v6.03*.

Digia. (2014). Qt Project. (accessed 18/02/2014) [Available at: http://qt-project.org/].

Dreier, M. E. (2007). Aerodynamics of Propellers. In *Introduction to Helicopter and Tiltrotor Flight Simulation*, pp. 149–168. doi: 10.2514/5.9781600862083.0149.0168.

Drela, M. (2005a). *Propeller Characterization for QPROP*.

Drela, M. (1988). Low-Reynolds-number airfoil design for the M.I.T. Daedalus prototype - A case study. *Journal of Aircraft* Vol.25, (8), pp. 724–732. doi: 10.2514/3.45650.

Drela, M. (1989). XFOIL - An Analysis and Design System for Low Reynolds Number Airfoils.pdf. In *Low Reynolds Number Aerodynamics*, pp. 1–12. Edited by T. J. Mueller. Berlin: Springer-Velag.

Drela, M. (2005b). *QMIL User Guide*.

Drela, M. (2006). *QPROP Formulation*.

Drela, M. & Youngren, H. (2003). *XROTOR User Guide*.

Dryden, H. (1937). *Air Flow in the Boundary Layer Near a Plate - NACA Report 562*.

Drzewiecki, S. (1892). *Bulletin de L'Association Maritime. Bulletin de L'Association Technique Maritime*. Paris.

Du, Z. & Selig, M. (1998). A 3-D stall-delay model for horizontal axis wind turbine performance prediction. In *1998 ASME Wind Energy Symposium*. Reston, Virigina: American Institute of Aeronautics and Astronautics. doi: 10.2514/6.1998-21.

Dumas, A., Trancossi, M., Madonia, M. & Giuliani, I. (2011). Multibody Advanced Airship for Transport. In *SAE Technical Paper 2011-01-2786*. doi: 10.4271/2011-01-2786.

Dumitrescu, H. & Cardos, V. (2007). A stall-delay model for rotating blades. *PAMM* Vol.7, (1), pp. 4100003–4100004. doi: 10.1002/pamm.200700178.

Van Eaton, E. H. (1991). *Airships and the Modern Military. Distribution*. Carlisle Barracks.

Eppler, R. & Hepperle, M. (1984). A Procedure for Propeller Design by Inverse Methods. In *International Conference on Inverse Design Concepts in Engineering Sciences*, pp. 445–460. Austin: G. S. Dulikravich.

Fanoe, O. (1974). Optimum Propeller in Viscous Flow. *Journal of Aircraft* Vol.11, (4), pp. 241–242. doi: 10.2514/3.59227.

Favier, D., Maresca, C. & Ettaouil, A. (1989). Numerical and experimental investigation of isolated propeller wakesin axial flight. *Journal of Aircraft* Vol.26, (9), pp. 837–846. doi: 10.2514/3.45849.

Feng, J., Wang, L., Ahuja, V., Lee, Y. T. & Merkle, C. L. (1998). CFD modeling of tip vortex for open marine propellers. In *Proceedings of the 1998 ASME Fluid Engineering Division Summer Meeting*. Washington D.C.: ASME.

Froude, W. (1920). *On the Elementary Relation Between Pitch, Slip and Propulsive Efficiency*.

Gamboa, P. V & Silvestre, M. A. R. (2013). AIRFOIL OPTIMIZATION WITH TRANSITION CURVE AS OBJECTIVE FUNCTION. In *VI International Conference on Adaptive Modeling and Simulation ADMOS 2013*, pp. 1–12.

Gault, D. (1957). *A correlation of low speed airfoil section stalling characteristics with reynolds number and airfoil geometry - Technical Note 3963*.

Glauert, H. (1933). *Wind Tunnel Interference on Wings, Bodies, and Airscrews*.

Glauert, H. (1935). Airplane propellers. In *Aerodynamic theory*. Edited by Durand WF.

Goldstein, S. (1929). On the Vortex Theory of Screw Propellers. *Proceedings of the Royal Society A: Mathematical, Physical and Engineering Sciences* Vol.123, (792), pp. 440–465. doi: 10.1098/rspa.1929.0078.

Gray, W. (1941). *Wind-Tunnel Tests of Two Hamilton Standard Propellers Embodying Clark Y and Naca 16-Series Blade Sections - Technical Report No. 530*. Washington.

Greenshields, C. J. (2015). *OpenFOAM - User Guide*.

Hall, G. F. (1969). A method of analysis for propellers at extreme angles-of-attack. *Journal of Aircraft* Vol.6, (1), pp. 52–58. doi: 10.2514/3.44001.

Hepperle, M. (2010). *JavaProp - Design and Analysis of Propellers*.

Hernandez & Crespo. (1987). Aerodynamic Calculation of the Performance of Horizontal Axis Wind Turbines and Comparison with Experimental Results. *Wind Engineering,*.

Hsiao, C. T. & L., P. L. (1998). Numerical computation of tip vortex flow generated by a marine propeller. In *Proceedings of the 1998 ASME Fluid Engineering Division Summer Meeting*. Washington D.C.: ASME.

Van Ingen, J. (2008). The eN Method for Transition Prediction. Historical Review of Work at TU Delft. In *38th Fluid Dynamics Conference and Exhibit*. Reston, Virigina: American Institute of Aeronautics and Astronautics. doi: 10.2514/6.2008-3830.

Johnson, W. (1986). Recent developments in rotary-wing aerodynamic theory. *AIAA Journal* Vol.24, (8), pp. 1219–1244. doi: 10.2514/3.9425.

Kendall, J. (1991). Studies on laminar boundary layer receptivity to freestream turbulence near a leading edge. In *Boundary layer stability and transition to turbulence; Proceedings of the Symposium, ASME and JSME Joint Fluids Engineering Conference*.

Klebanoff, P. (1971). Effects of free-stream turbulence on a laminar boundary layer. *Bulletin of American Physics Society* Vol.16, pp. 1323.

Koch, L. D. (1998). *Design and Performance Calculations of a Propeller for Very High Altitude Flight*.

Lardeau, S., Leschziner, M. a. & Li, N. (2004). Modelling Bypass Transition with Low-Reynolds-Number Nonlinear Eddy-Viscosity Closure. *Flow, Turbulence and Combustion formerly `Applied Scientific Research'* Vol.73, (1), pp. 49–76. doi: 10.1023/B:APPL.0000044367.24861.b7.

Larrabee, E. E. (1979). Practical Design of Minimum Induced Loss Propellers. In *SAE Technical Paper 790585*. doi: 10.4271/790585.

Liao, L. & Pasternak, I. (2009). A review of airship structural research and development. *Progress in Aerospace Sciences* Vol.45, (4-5), pp. 83–96. doi: 10.1016/j.paerosci.2009.03.001.

Lindenburg, C. (2000). Aerodynamic airfoil coefficients at large angeles of attrak. In *Annual IEA Symposyum on the Aerodynamics of Wind Turbines*, pp. 1–18. Golden.

Marten, D., Wendler, J., Pechlivanoglou, G., Nayeri, C. N. & Paschereit, C. O. (2013). QBLADE : An Open Source Tool for Design and Simulation of Horizontal and Vertical Axis Wind Turbines. *International Journal of Emerging Technology and Advanced Engineering* Vol.3, (3), pp. 264–269.

Marten, D. & Wendler, J. (2013). *QBlade Guidelines v0.6*. Berlin.

Massini, G., Rossi, E. & D'Angelo, S. (1988). Wind Tunnel Measurements of Aerodynamics Coefficients of Asymmetrical Airfoil Sections for Wind Turbines Blades Extended to High Angles of Attack. In *European Wind Energy Conference*, pp. 241–255. Herning: H.S. Stephens and Associates.

Mayle, R. E. & Schulz, A. (1996). The Path to Predicting Bypass Transition. In *Volume 1: Turbomachinery*, pp. 405–411. ASME. doi: 10.1115/96-GT-199.

Mccormickf, B. W. (1955). The Effect of a Finite Hub on the Optimum Propeller. *Journal of the Aeronautical Sciences (Institute of the Aeronautical Sciences)* Vol.22, (9), pp. 645–650. doi: 10.2514/8.3419.

McCoy, H. M. (1939). A Discussion of Propeller Efficiency. *Journal of the Aeronautical Sciences* Vol.6, (6), pp. 227–234. doi: 10.2514/8.833.

McCoy, H. M. (1944). Propeller Design Requirements. *Journal of the Aeronautical Sciences (Institute of the Aeronautical Sciences)* Vol.11, (3), pp. 261–271. doi: 10.2514/8.11142.

McGee, R., Walker, B. & Millard, B. (1988). *Experimental Results for the Eppler 387 Airfoil at Low Reynolds Numbers in the Langley Low-Turbulence Pressure Tunnel*. Hampton, Virginia.

Menter, F. R. (1992). Influence of freestream values on k-omega turbulence model predictions. *AIAA Journal* Vol.30, (6), pp. 1657–1659. doi: 10.2514/3.11115.

Menter, F. R. (1994). Two-equation eddy-viscosity turbulence models for engineering applications. *AIAA Journal* Vol.32, (8), pp. 1598–1605. doi: 10.2514/3.12149.

Menter, F., Ferreira, J. C., Esch, T. & Konno, B. (2003). The SST Turbulence Model with Improved Wall Treatment for Heat Transfer Predictions in Gas Turbines. In *Proceedings of the International Gas Turbine Congress*, pp. 1–7. Tokyo.

Merlin, P. W. (2013). *Crash Course - Lessons Learned form Accidents Involving Remotely Piloted and Autnomous Aircraft*. National Aeronautics and Space Administration.

Miley, S. (1982). *A Catalog of Low Reynolds Number Airfoil Data for Wind Turbine Applications*. College Stations Texas.

Miley, S. J., Ash, R. L., Hyde, K. W., Landman, D. & Sparks, A. K. (2002). Propeller Performance Tests of Wright Brothers' 'Bent-End' Propellers. *Journal of Aircraft* Vol.39, (2), pp. 234–241. doi: 10.2514/2.2944.

Monk, J. S. (2010). *A Propeller Design and Analisys Capability Evaluation for High Altitude Propellers*.

Montgomerie, B. (1996). *Drag Coefficient Distribution on a Wing at 90 Degrees to the Wind*. Petten.

Montgomerie, B. (2004). *Methods for Root Effects, Tip Effects and Extending the Angle of Attack Range to +-180º, with Application to Aerodynamics for Blades on Wind Turbines and Propellers*. Stockholm.

Morgado, J., Silvestre, M. Â. R. & Páscoa, J. C. (2015). Validation of New Formulations for Propeller Analysis. *Journal of Propulsion and Power*. doi: 10.2514/1.B35240.

Morgado, J., Silvestre, M. Â. R. & Páscoa, J. C. (2012). Parametric Study of a High Altitude Airship According to the Multi-Body Concept for Advanced Airship Transport - MAAT. In *IV Conferência Nacional em Mecânica dos Fluidos, Termodinâmica e Energia*. Lisbon.

Morgado, J. P., Silvestre, M. A. & Pascoa, J. (2013). Full Range Airfoil Polars for Propeller Blade Element Momentum Analysis. In *2013 International Powered Lift Conference*. Reston, Virginia: American Institute of Aeronautics and Astronautics. doi: 10.2514/6.2013-4379.

Moss, R. & Oldfield, M. (1996). Effect of free-stream turbulence on flat-plate heat flux signals: spectra and eddy transport velocities. *Journal of Turbomachinery* Vol.118, pp. 461–467.

Ostowari, C. & Naik, D. (1984). Post Stall Studies of Untwisted Varying Aspect Ratio Blades With a NACA 4415 Series Airfoil Sections - Part I. *Wind Engineering* Vol.8, (3), pp. 176–194.

Phillips, W. F. (2002). Propeller Momentum Theory with Slipstream Rotation. *Journal of Aircraft* Vol.39, (1), pp. 184–187. doi: 10.2514/2.2914.

Prouty, R. W. (2003). *Helicopter Performance, Stability, and Control*, 3rd Editio. Malabar: Krieger Publishing Company, Inc.

Rankine, W. M. J. & Froude, R. E. (1889). *On the Mechanical Principles of the Action of the Propellers*. Transactions of the Institute of Naval Architects.

Ribner, H. S. & Foster, S. P. (1990). Ideal efficiency of propellers - Theodorsen revisited. *Journal of Aircraft* Vol.27, (9), pp. 810–819. doi: 10.2514/3.45941.

Rizk, M. & Jou, W.-H. (1986a). Propeller design by optimization. In *24th Aerospace Sciences Meeting*. Reston, Virigina: American Institute of Aeronautics and Astronautics. doi: 10.2514/6.1986-81.

Rizk, M. H. (1985). Application of the single-cycle optimization approach to aerodynamicdesign. *Journal of Aircraft* Vol.22, (6), pp. 509–515. doi: 10.2514/3.45157.

Rizk, M. H. & Jou, W.-H. (1986b). Propeller design by optimization. *AIAA Journal* Vol.24, (9), pp. 1554–1556. doi: 10.2514/3.9479.

Rizk, M. H. (1983). The Single-Cycle Scheme: A New Approach to Numerical Optimization. *AIAA Journal* Vol.21, (12), pp. 1640–1647. doi: 10.2514/3.60164.

Rwigema, M. K. (2010). Propeller blade element momentum theory with vortex wake deflection. In *27th Congress of the International Council of the Aeronautical Sciences*, pp. 1–9. Nice.

Santos, P. (2012). *Pesornal Notes*. Covilhã.

Saravanamuttoo, H., Rogers, G. & Cohen, H. (1996). *Gas Turbine Theory*, 4th Editio. London: LonSman Group Limited.

Schawe, D., Rohardt, C. & Wichmann, G. (2002). Aerodynamic design assessment of Strato 2C and its potential for unmanned high altitude airborne platforms. *Aerospace Science and Technology* Vol.6, (1), pp. 43–51. doi: 10.1016/S1270-9638(01)01127-0.

Selig, M. S. (2003). *Low Reynolds Number Airfoil Design Lecture Notes*.

Selig, M. S. & Ananda, G. (2011). *Low Reynolds Number Propeller Perfomance Data : Wind Tunnel Corrections for Motor Fixture Drag*.

Selig, M. S. & Guglielmo, J. J. (1997). High-Lift Low Reynolds Number Airfoil Design. *Journal of Aircraft* Vol.34, (1), pp. 72–79. doi: 10.2514/2.2137.

Shih, T., Zhu, J. & Lumley, J. (1994). *A New Reynolds Stress Algebraic Equation Model - NASA TM 106644*. Ohio.

Shih, T.-H., Liou, W. W., Shabbir, A., Yang, Z. & Zhu, J. (1995). A new k-ϵ eddy viscosity model for high reynolds number turbulent flows. *Computers & Fluids* Vol.24, (3), pp. 227–238. doi: 10.1016/0045-7930(94)00032-T.

Silva, D., Avelino, M. & De-Lemos, M. (2002). Numerical study of the airflow around the airfoil S1223. In *II Congresso Nacional de Engenharia Mecânica*. João Pessoa.

Snel, H., Houwink, R. & Bosschers, J. (1994). *Sectional Prediction of Lift Coefficients on Rotating Wind Turbine Blades in Stall*. Petten.

Sommers, D. & Maughmer, M. (2003). *Theoretical Aerodynamic Analyses of Six Airfoils for Use on Small Wind Turbines*. Golden.

Strash, D., Lednicer, D. & Rubin, T. (1998). Analysis of propeller-induced aerodynamic effects. In *16th AIAA Applied Aerodynamics Conference*. doi: 10.2514/6.1998-2414.

Taylor, G. (1939). Some recent developments in the study of turbulence. In *Fifth International Congress for Applied Mechanics*. Cambridge, Massachusetts.

Theodorsen, T. (1948). *Theory of Propellers*. New York: McGraw-Hill Book Company.

Theodorsen, T., Stickle, G. W. & Brevoort, M. J. (1937). *Caracteristics of Six Propellers Including the High-Speed Range - NACA TR No. 594*. Langley.

Thole, K. & Bogard, D. (1996). High freestream turbulence effects on turbulent boundary layers. *Journal of Fluids Engineering* Vol.118, pp. 276–284.

Timmer, W. A. (2010). Aerodynamic characteristics of wind turbine blade airfoils at high angles-of-attack. In *TORQUE 2010: The Science of Making Torque from Wind*, pp. 71–78. Creete.

Viterna, L. A. & Janetzke, D. C. (1982). *Theoretical and experimental power from large horizontal-axis wind turbines*. Washington, DC (United States). doi: 10.2172/6763041.

Viterna, L. & Corrigan, R. (1982). *Fixed Pitch Rotor Performance of Large Horizontal Axis Wind Turbines*. Cleveland.

Vizinho, R., Pascoa, J. C. & Silvestre, M. (2013). High Altitude Transitional Flow Computation for a Propulsion System Nacelle of MAAT Airship. *SAE International Journal of Aerospace* Vol.6, (2), pp. 2013–01–2268. doi: 10.4271/2013-01-2268.

Volino, R. J. (1998). A New Model for Free-Stream Turbulence Effects on Boundary Layers. *Journal of Turbomachinery* Vol.120, pp. 613–620.

Wald, Q. R. (2006). The aerodynamics of propellers. *Progress in Aerospace Sciences* Vol.42, (2), pp. 85–128. doi: 10.1016/j.paerosci.2006.04.001.

Walters, D. K. & Cokljat, D. (2008). A Three-Equation Eddy-Viscosity Model for Reynolds-Averaged Navier–Stokes Simulations of Transitional Flow. *Journal of Fluids Engineering* Vol.130, (12), pp. 121401. doi: 10.1115/1.2979230.

Walters, D. K. & Leylek, J. H. (2004). A New Model for Boundary Layer Transition Using a Single-Point RANS Approach. *Journal of Turbomachinery* Vol.126, (1), pp. 193. doi: 10.1115/1.1622709.

Wang, X., Ma, Y. & Shan, X. (2009). Modeling of Stratosphere Airship. In *Advances in Theoretical and Applied Mechanics*, pp. 123–142.

Welty, G. D. (1935). Light Alloy Propeller Blades. *Journal of the Aeronautical Sciences* Vol.2, (1), pp. 35–38. doi: 10.2514/8.66.

Wilson, J. R. (2004). A new era for airships. *Aerospace America* (May), pp. 27–31.

Worasinchai, S., Ingram, G. & Dominy, R. (2011). A low-Reynolds-number, high-angle-of-attack investigation of wind turbine aerofoils. *Proceedings of the Institution of Mechanical Engineers, Part A: Journal of Power and Energy* Vol.225, (6), pp. 748–763. doi: 10.1177/0957650911405411.

De Young, J. (1965). Propeller at high incidence. *Journal of Aircraft* Vol.2, (3), pp. 241–250. doi: 10.2514/3.43646.

U.S. Standard Atmosphere. (1976). .

***Egrett II*. (1990).** . Greenville: GROB Company.

***Egrett II*. (1991).** . Mattsies: Grob Company.

***Perseus B*. (1999).** . Edwards.

***LM335*. (1999).** .

***SCB-68*. (2009).** . Austin, Texas.

***MPXA4115A*. (2009).** *Datasheet*.

***ANSYS FLUENT Theory Guide*. (2010).** . Ansys Inc.

***FN3148 Load Cell*. (2012).** . Measurements Specialties.

***QDR 1114*. (2013).** .

***RTS-100*. (2014).** .

APC Propeller Performance Data. (2014). *Advanced Propellers Precision Composites*. (accessed 12/08/2014) [Available at: http://www.apcprop.com/v/downloads/PERFILES_WEB/datalist.asp].

APC Propeller Materials. (2014). *Advanced Propellers Precision Composites*. (accessed 12/08/2014) [Available at: http://www.apcprop.com/v/Research/research.html#materials].

Appendix A

Partial Derivatives for Error Estimation

This page has been intentionally left blank
for double side copying

A.1 – Freestream Velocity

$$\frac{\partial W}{\partial (p_1 - p_2)} = \frac{625\ R\ T_{atm}}{609\ P_{atm}\sqrt{\frac{1250(p_1 - p_2)RT_{atm}}{609\ P_{atm}}}} \quad \text{A.1}$$

$$\frac{\partial W}{\partial T_{atm}} = \frac{625\ R\ (p_1 - p_2)}{609\ P_{atm}\sqrt{\frac{1250(p_1 - p_2)RT_{atm}}{609\ P_{atm}}}} \quad \text{A.2}$$

$$\frac{\partial W}{\partial P_{atm}} = \frac{625(p_1 - p_2)\ R\ T_{atm}}{609\ P_{atm}^2\sqrt{\frac{1250(p_1 - p_2)RT_{atm}}{609\ P_{atm}}}} \quad \text{A.3}$$

A.2 – Advance Ratio

$$\frac{\partial J}{\partial (p_1 - p_2)} = \frac{625\ R\ T_{atm}}{609D\ P_{atm}n\sqrt{\frac{1250(p_1 - p_2)RT_{atm}}{609\ P_{atm}}}} \quad \text{A.4}$$

$$\frac{\partial J}{\partial T_{atm}} = \frac{625\ R\ (p_1 - p_2)}{609\ P_{atm}\sqrt{\frac{1250(p_1 - p_2)RT_{atm}}{609\ P_{atm}}}} \quad \text{A.5}$$

$$\frac{\partial J}{\partial P_{atm}} = \frac{625(p_1 - p_2)\ R\ T_{atm}}{609\ DP_{atm}^2n\sqrt{\frac{1250(p_1 - p_2)RT_{atm}}{609\ P_{atm}}}} \quad \text{A.6}$$

$$\frac{\partial J}{\partial n} = \frac{\sqrt{\frac{1250(p_1 - p_2)RT_{atm}}{609\ P_{atm}}}}{Dn^2} \quad \text{A.7}$$

A.3 – Thrust Coefficient

$$\frac{\partial C_t}{\partial T} = \frac{R\ T_{atm}}{D^4P_{atm}n^2} \quad \text{A.8}$$

$$\frac{\partial C_t}{\partial T_{atm}} = \frac{R\ T}{D^4P_{atm}n^2} \quad \text{A.9}$$

$$\frac{\partial C_t}{\partial P_{atm}} = \frac{R\ T_{atm}T}{D^4P_{atm}^2n^2} \quad \text{A.10}$$

$$\frac{\partial C_t}{\partial n} = \frac{2R\ T_{atm}T}{D^4P_{atm}n^3} \quad \text{A.11}$$

A.4 - Power Coefficient

$$\frac{\partial C_p}{\partial Q} = \frac{2\pi R T_{atm}}{D^5 P_{atm} n^2} \quad \text{A.12}$$

$$\frac{\partial C_p}{\partial T_{atm}} = \frac{2\pi R Q}{D^5 P_{atm} n^2} \quad \text{A.13}$$

$$\frac{\partial C_p}{\partial P_{atm}} = \frac{2\pi R T_{atm} Q}{D^5 P_{atm}^2 n^2} \quad \text{A.14}$$

$$\frac{\partial C_p}{\partial n} = \frac{4\pi R T_{atm} Q}{D^5 P_{atm} n^3} \quad \text{A.15}$$

A.5 - Propeller Efficiency

$$\frac{\partial \eta}{\partial T} = \frac{\sqrt{\frac{1250(p_1 - p_2) R T_{atm}}{609\ P_{atm}}}}{2\pi Q n} \quad \text{A.16}$$

$$\frac{\partial \eta}{\partial Q} = -\frac{T\sqrt{\frac{1250(p_1 - p_2) R T_{atm}}{609\ P_{atm}}}}{2\pi Q^2 n} \quad \text{A.17}$$

$$\frac{\partial \eta}{\partial (p_1 - p_2)} = \frac{625\ R\ T_{atm} T}{1218\pi P_{atm} Q n \sqrt{\frac{1250(p_1 - p_2) R T_{atm}}{609\ P_{atm}}}} \quad \text{A.18}$$

$$\frac{\partial \eta}{\partial T_{atm}} = \frac{625\ R(p_1 - p_2) T}{1218\pi P_{atm} Q n \sqrt{\frac{1250(p_1 - p_2) R T_{atm}}{609\ P_{atm}}}} \quad \text{A.19}$$

$$\frac{\partial \eta}{\partial P_{atm}} = -\frac{625\ R P_{atm}(p_1 - p_2) T}{1218\pi P_{atm}^2 Q n \sqrt{\frac{1250(p_1 - p_2) R T_{atm}}{609\ P_{atm}}}} \quad \text{A.20}$$

$$\frac{\partial \eta}{\partial n} = -\frac{T\sqrt{\frac{1250(p_1 - p_2) R T_{atm}}{609\ P_{atm}}}}{2\pi Q n^2} \quad \text{A.21}$$

Appendix B

Publications

This page has been intentionally left blank
for double side copying

List of Publications

Peer Reviewed Journal Papers

I. Validations of New Formulations for Propeller Analysis
Morgado, J., Silvestre, M. A. R. and Páscoa, J. C.
Journal of Propulsion and Power, Vol 31 (2015) pp. 467-477.
http://arc.aiaa.org/doi/abs/10.2514/1.B35240

II. Propeller Performance Measurements at Low Reynolds Numbers
Silvestre, M. A. R., Morgado, J., Alves, P., Santos, P., Gamboa, P. and Páscoa, J. C.
International Journal of Mechanics Vol. 9 (2015) pp. 154-166 ISSN: 1998-4448
http://www.naun.org/main/NAUN/mechanics/2015/a372003-136.pdf

III. A Comparison of Post-Stall Models Extended for Propeller Performance Prediction
Morgado, J., Silvestre, M. A. R. and Páscoa, J. C.
Accepted for Publication, Aircraft Engineering and Aerospace Technology, 2015
DOI: 10.1108/AEAT-07-2014-0119.R1.

IV. High Propeller Design and Analysis
Morgado, J.,Abdollahzadeh, M., Silvestre, M. A. R. and Páscoa, J. C.
Aerospace Science and Technology, Vol. 45 (2015) pp. 398-407
http://dx.doi.org/10.1016/j.ast.2015.06.011

V. Comparison between CFD and XFOIL Predictions for High Lift, Low Reynolds Number Airfoils
Morgado, J., Vizinho, R., Silvestre, M. A. R. and Páscoa, J. C.
Aerospace Science and Technology, Vol. 52 (2016) pp. 207-214
http://dx.doi.org/10.1016/j.ast.2016.02.031

Peer Reviewed International Conferences

I. Full Range Airfoil Polars for Propeller Blade Element Momentum Analysis
Morgado, J., Silvestre, M. A. R. and Páscoa, J. C.
Proc. of 2013 International Powered Lift Conference, AIAA, Los Angeles, USA, August 2013. http://arc.aiaa.org/doi/abs/10.2514/6.2013-4379

II. JBLADE: a Propeller Design and Analysis Code
Silvestre, M. A. R., Morgado, J. and Páscoa, J. C.
Proc. of 2013 International Powered Lift Conference, AIAA, Los Angeles, USA, August 2014. http://arc.aiaa.org/doi/abs/10.2514/6.2013-4220

III. A new Software for Propeller Design and Analysis
Morgado, J., Silvestre, M. A. R. and Páscoa, J. C.
6th AFCEA Students Conference, AFCEA, Bucharest, Romania, March 2014.

IV. Comparison between CFD and XFOIL Predictions for High Lift, Low Reynolds Number Airfoils
Morgado, J., Vizinho, R., Silvestre, M. A. R. and Páscoa, J. C.
ESCO 2014, 4th European Seminar on Computing, Pilsen, Czech Republic, June, 2014
http://www.esco2014.femhub.com/docs/ESCO2014_Book_of_Abstracts.pdf#page=199

V. Low Reynolds Propeller Performance Testing
Silvestre, M. A. R., Morgado, J., Alves, P., Santos, P., Gamboa, P. and Páscoa, J. C.
5th International Conference on FLuid Mechanics and Heat & Mass Transfer, WSEAS, Lisbon, Portugal, October 2014. http://www.wseas.us/e-library/conferences/2014/

Peer Reviewed National Conferences

I. Parametric Study of a High Altitude Airship According to the Multi-Body Concept for Advanced Airship Transport - MAAT
Morgado, J., Silvestre, M. A. R. and Páscoa, J. C.
Proc. of IV Conferência Nacional Em Mecânica Dos Fluidos, Termodinâmica e Energia, LNEC, Lisbon, Portugal, May 2012

JOURNAL OF PROPULSION AND POWER

PREPRINT

Validation of New Formulations for Propeller Analysis

J. Morgado,* M. Â. R. Silvestre,† and J. C. Páscoa‡
University of Beira Interior, 6200-001 Covilhã, Portugal

DOI: 10.2514/1.B35240

This paper reports the development of a new propeller design and analysis tool. JBLADE uses an improved version of blade element momentum that embeds a new model for the three-dimensional flow equilibrium. In addition, a new method for the prediction of the airfoil drag coefficient at a 90 deg angle of attack for a better poststall modeling is also presented. The software is developed as an open-source tool for the simulation of propellers and has the capability to estimate the performance of a given propeller geometry in design and offdesign operating conditions. The software allows the introduction of the blade geometry as an arbitrary number of sections. To validate the code, the propellers from NACA Technical Report 530 by Gray ("Wind-Tunnel Tests of Two Hamilton Standard Propellers Embodying Clark Y and NACA 16-Series Blade Sections," 1941) and NACA Technical Report 594 by Theodorsen et al. ("Characteristics of Six Propellers Including the High-Speed Range," 1937) were simulated and the results were checked against the experimental data and against those of other available codes. Although current development work is focused in the design of airship propellers, the long-term goal of the JBLADE development is to provide a user-friendly, accurate, and validated open-source code that can be used to design and optimize propellers for distinct applications.

Nomenclature

a_a	=	axial induction factor
a_t	=	tangential induction factor
B	=	number of blades
C_a	=	axial force coefficient
C_D	=	airfoil drag coefficient
C_L	=	airfoil lift coefficient
C_t	=	tangential force coefficient
c	=	blade local chord, m
c_p	=	power coefficient
c_t	=	thrust coefficient
D	=	propeller diameter, m
F	=	Prandtl's correction factor
L	=	lift force, N
P	=	power, W
Q	=	torque, N · m
R_{LE}	=	airfoil leading-edge radius
r	=	radius of blade element position, m
T	=	thrust, N
t	=	airfoil thickness
W	=	element relative velocity, m/s
W_a	=	element axial velocity, m/s
W_t	=	element tangential velocity, m/s
x/c	=	nondimensional x position
$(y/c)_{0.0125}$	=	nondimensional y position at x/c equal to 0.0125
α	=	angle of attack, deg
θ	=	incidence angle, deg
ρ	=	air density, kg/m^3
σ_r	=	local solidity ratio
ϕ	=	inflow angle, deg
Ω	=	rotation speed, rad/s

I. Introduction

THE problems caused by growth in the transportation sector, e.g., the rise of fuel consumption and cost, as well as pollution and consequent climate change led to a reconsideration of the transportation systems by the most economically advanced nations [1]. Nowadays, despite all technologic developments, as we proceed into the 21st century, we may be about to witness the return of slower air transport as a means of increasing energy efficiency and business profitability.

Slowing down aircraft can take us toward the airship. After an initial development until the 1930s, the airships were only considered as a mere curiosity. At their peak, in the late 1930s, airships were unrivaled in transoceanic transportation. Nowadays, they can be used effectively as platforms for different purposes [2–5], especially activities that require long endurance or hovering for a long time.

In Europe, the development of the new airships is also being supported by the European Union through the Multibody Concept for Advanced Airship for Transport (MAAT [6]) project. This collaborative project aims to develop a heavy lift cruiser–feeder airship system in order to provide middle- and long-range transport for passengers and goods. The MAAT system is composed of the cruiser and the feeder modules. The feeder is a vertical takeoff and landing system that ensures the connection between the ground and the cruiser. It can go up and down by control of the buoyancy force and displace horizontally to join to the cruiser. The cruiser is conceived to move mostly in a horizontal way at high altitude. Since the MAAT project has the objective of operating an airship at stratospheric altitudes, propellers are a valid option for the airships' propulsion [7].

An airship propeller must be efficient in thrust per unit of power in the hovering flight condition, and it needs to have a high propulsive efficiency in cruise flight. The design of a propeller for an altitude of about 15 km can itself be difficult [8], but it is crucial to develop a numerical tool that allows the design and optimization of MAAT airship propellers over the broad operating conditions in which these will operate. To maximize the propeller performance over the intended extreme flight envelope, it is required to optimize the shape and structure of the propeller as well as the coupling with its respective motor sets. The optimization process is based on the analysis and comparison of numerous designs and their relative merits. This can only be achieved in a practical way with low-computational-cost numerical tools.

The first developments related to the theory of propellers occurred in the 19th century with Rankine [9] and Froude [10] through a work focused on marine propellers. Later, Drzewiecki [11] presented the blade element theory. However, he did not take into account the effect

of the propeller-induced velocity on each element. In 1919, Betz and Prandtl [12] stated that the load distribution for lightly loaded propellers with minimum energy loss is such that the shed vorticity forms regular helicoidal vortex sheets moving backward, undeformed behind the propeller. Thus, the induced losses of the propellers will be minimized if the propeller slipstream has a constant axial velocity and if each cross section of the slipstream rotates around the propeller axis like a rigid disk [13].

Prandtl (as cited by Glauert [14]) found an approximation to the flow around helicoidal vortex sheets, which is good if the advance ratio is small and improves as the number of blades increases. The approximation presented by Prandtl is still applied in simple mathematical codes. Later, Goldstein [15] found a solution for the potential field and the distribution of circulation for propellers with small advance ratios. Theodorsen [16], through his study on the vortex system in the far field of the propeller, concluded that Goldstein's solution [15] for the field of a helicoidal vortex sheet remains valid, even for moderate/highly loaded propellers. In 1980, Larrabee [17] analyzed the steady air loads on the propeller and presented a practical design theory for minimum induced loss propellers. This method is a combination between momentum theory, blade element theory, and vortex theory. Later on, Adkins and Liebeck [18] presented improvements with small-angle approximations and light-load approximations, overcoming the restrictions in the method developed by Larrabee [17].

Presently, there are several codes to design propellers and predict their performance. These codes typically use the blade element momentum (BEM) theory together with two-dimensional airfoil data. However, they are somewhat inconsistent in accurately predicting the propeller thrust and power [19] over a significant portion of the propeller's speed envelope. Part of the inaccuracy comes from the classical BEM assumption that the velocity induced by one element has no effect on its neighboring blade elements [20]. This is dealt with in the present work by modifying the classical BEM theory with the introduction of a new three-dimensional (3-D) flow equilibrium formulation that redistributes the tangential induced velocity. Another part of the failure to accurately compute the propeller performance results from the deep-stall angles of attack that the blade elements can achieve during their normal operation, since the experimental data from wind-tunnel measurements are only available over a limited interval of angles of attack [21,22], commonly between -5 to $+20$ deg, and the airfoil performance prediction codes do not work in this full range of high angles of attack.

Although some analytical and experimental studies [23–27] have tried to fully understand the effect of the complex 3-D flow physics of rotary wings on the blade airfoils' aerodynamics, there is still a need to extend the common available airfoil data to the full interval of angles of attack involved in blade operations in order to obtain a closer prediction of airfoil performance.

II. Methodology

A. Classical Blade Element Momentum Theory

To model the propeller, the blade is divided into a set of blade elements. Each blade element is a discrete rotating wing (see Fig. 1) [28]. The blade element relative velocity and respective inflow angle are computed through the axial and tangential velocity components. The axial velocity results from the sum of the propeller airspeed to the induced axial velocity at the propeller disk. The tangential velocity results from the sum of the velocity of the element due to the propeller rotation, with the induced tangential velocity. The induced velocity components are determined from the momentum theory, for the annulus swept by the rotating blade element, and used to calculate the angle of attack as the difference between ϕ and θ. With α, the element's lift and drag coefficients can be determined. With these coefficients, the axial and tangential force coefficients are obtained according to the local θ:

$$C_a = C_L \cos\phi - C_D \sin\phi \tag{1}$$

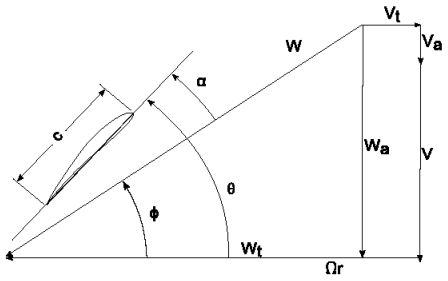

Fig. 1 Blade geometry and velocity triangle at an arbitrary radius blade position [28].

$$C_t = C_L \sin\phi + C_D \cos\phi \tag{2}$$

To describe the overall propeller performance, the forces are obtained from the force coefficients according to

$$F_x = \frac{1}{2}\rho W^2 c C_x \tag{3}$$

The total thrust and torque of the propeller are calculated from

$$T = B\int_{R_{\text{root}}}^{R_{\text{tip}}} F_a \,\mathrm{d}r \tag{4}$$

$$Q = B\int_{R_{\text{root}}}^{R_{\text{tip}}} F_t r \,\mathrm{d}r \tag{5}$$

With the total torque from Eq. (5), the necessary shaft power is obtained:

$$P = \Omega Q \tag{6}$$

and dimensionless thrust and power coefficients are calculated from their definitions:

$$c_t = \frac{T}{\rho n^2 D^4} \tag{7}$$

$$c_p = \frac{P}{\rho n^3 D^5} \tag{8}$$

When the advance ratio is defined as presented in Eq. (9), the propeller efficiency is computed through Eq. (10):

$$J = \frac{v}{nD} \tag{9}$$

$$\eta = \frac{c_t}{c_p} J \tag{10}$$

The iteration variables of the classical BEM method are the axial and tangential induction factors, defined from the induced velocity components as

$$a_a = \frac{W_a - V}{V} \tag{11}$$

$$a_t = \frac{\Omega r - W_t}{\Omega r} \tag{12}$$

and by including results from momentum theory

$$a_a = \left(\frac{4F\sin^2\phi}{\sigma C_a} - 1\right)^{-1} \tag{13}$$

$$a_t = \left(\frac{4F\sin\phi\cos\phi}{\sigma C_t} + 1\right)^{-1} \tag{14}$$

where σ_r is the ratio of the blade element area to the annulus sweep by the element in its rotation, and it is defined by Eq. (15):

$$\sigma_r = \frac{cB}{2\pi r} \tag{15}$$

In Eqs. (13) and (14), F compensates for the amount of work that can actually be performed by the element according to its proximity to the blade's root or tip. If the element is at the blade tip, its contribution will be zero. F is estimated according to Eq. (16) in the 3-D corrections model.

To compute ϕ, the induction factors a_a and a_t must be known. An arbitrary value is assigned for both axial and tangential induction factors for the first iteration. The iteration is repeated for all blade elements. Thus, with lift and drag coefficients for the angle of attack, the induction factors are updated and compared to the ones from the previous iteration. As soon as the difference is below the convergence criteria defined by the user, the iteration stops and the next blade element is computed.

B. Three-Dimensional Corrections Model

During each iteration, the code also takes into account the losses caused by tip and root vortices. These corrections, previously described by Prandtl [14], are modeled by

$$F = \frac{2}{\pi}a\cos(e^{-f}) \tag{16}$$

where

$$f_{\text{root}} = \frac{B}{2}\left(1 + \frac{R_{\text{root}}}{r}\right)\frac{1}{g} \tag{17}$$

$$g_{\text{root}} = \frac{R_{\text{root}}}{r}\tan\phi \tag{18}$$

or

$$f_{\text{tip}} = \frac{B}{2}\left(1 - \frac{r}{R_{\text{tip}}}\right)\frac{1}{g} \tag{19}$$

$$g_{\text{tip}} = \frac{r}{R_{\text{tip}}}\tan\phi \tag{20}$$

C. New Three-Dimensional Flow Equilibrium Model

The theoretical formulation presented in Secs. II.A. and II.B. assumes that the flow in the propeller annulus is two-dimensional, meaning that radial movement of the flow is neglected. But for such a condition, tridimensional equilibrium [29] must exist. Furthermore, the classical BEM formulation assumes that neighboring blade-element-induced velocities are independent, which lacks physical reasoning [20]. In JBLADE, this issue is addressed by a new model based on 3-D flow equilibrium:

$$W_a\frac{\partial W_a}{\partial r} + W_t\frac{\partial W_t}{\partial r} + \frac{W_t^2}{r} = 0 \tag{21}$$

The case where W_a is maintained constant across the propeller annulus reduces Eq. (21) to

$$\frac{\mathrm{d}W_t}{\mathrm{d}r} = -\frac{W_t}{r} \Leftrightarrow W_t r = \text{const.} \tag{22}$$

In this case, the whirl varies inversely with the radius, which is best known as the free vortex condition. Although this differs substantially from the ordinary BEM approach, where the momentum theory applied to the tangential velocity induction totally disregards the neighbor elements to determine the element's V_t, it makes sense when one considers that, from far upstream down to the propeller disk, the flow should be isentropic or close to irrotational, thus respecting the free vortex condition. To implement this equilibrium condition, in the first iteration, the force coefficients are computed assuming no tangential induction factor, which means that $a_t = 0$. The mass flow rate at annulus element i is calculated as

$$\dot{m}_i = 2\rho W_a \pi r\,\mathrm{d}r \tag{23}$$

and

$$\dot{m}_{\text{total}} = \int_{r_{\text{root}}}^{r_{\text{tip}}} \dot{m}_i \tag{24}$$

To satisfy the momentum conservation, the total propeller torque will be the result of a free vortex-induced tangential velocity profile with an average axial velocity $\bar{W}_a$ across the propeller disk. A reference value of tangential induced velocity is used that corresponds to that at 75% of the blade radius position, $V_{t_{75}}$. The average axial velocity is

$$\bar{W}_a = \frac{\dot{m}_{\text{total}}}{\pi\rho R^2} \tag{25}$$

According to Eq. (26), at a given element, V_t is

$$V_t = \frac{0.75RV_{t_{75}}}{r} \tag{26}$$

$$Q = \int 4\pi\rho\bar{W}_a V_t r\,\mathrm{d}r \tag{27}$$

Thus, replacing Eqs. (25) and (26) in Eq. (27) and solving for $V_{t_{75}}$,

$$V_{t_{75}} = \frac{2}{3}\frac{Q}{\pi\rho\bar{W}_a R(R_{\text{tip}}^2 - R_{\text{root}}^2)} \tag{28}$$

The tangential induction factor can be updated, and the coefficients will be calculated again with the updated tangential induction factor:

$$a_t = \frac{V_t}{\Omega r} \tag{29}$$

The tangential velocity along an APC 10×7 in. slow flyer blade radius was plotted together with computational fluid dynamics (CFD) data and original BEM formulation in order to validate the new proposed model.

It is seen in Fig. 2 that the 3-D equilibrium hypothesis is a fair approximation with reality, considering that the CFD results show the real trend. The weakness of the BEM is also clear with respect to the tangential induction, since each annular element of the disk has no relation to its neighbor elements, allowing discontinuities in the tangential induction profile. The underprediction of tangential velocity in the BEM simulation is related to the lower power coefficient that results from its formulation in this static thrust condition.

To check the validity of the 3-D equilibrium hypothesis, a CFD simulation of the actual 3-D rotating propeller was performed. The propeller geometry details can be found in the University of Illinois Urbana–Champaign propeller data site [30]. Regarding the CFD simulation of the propeller, the commercial package Fluent® [31] is used with the k-w shear-stress transport turbulence model [32].

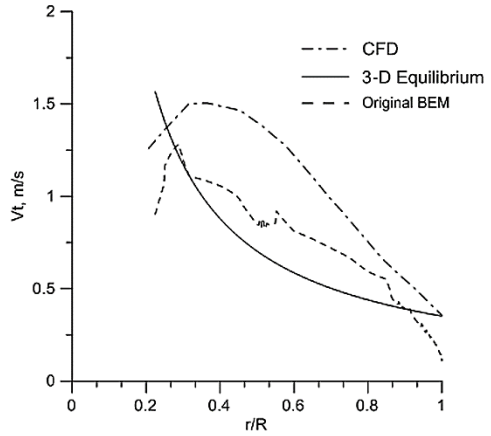

Fig. 2 Tangential velocity distribution along an APC 10 × 7 in. [30] blade radius at 1 m behind the propeller plane for CFD, original BEM formulation, and new proposed 3-D flow equilibrium model.

The hybrid mesh contains 2.5×10^6 points, and it is used as an implicit integration of the incompressible Navier–Stokes equation coupled with turbulent transport equations. Furthermore, the SIMPLE algorithm is used for pressure–velocity coupling. To consider the rotation of the propeller, a multiple reference frame approach is adopted. Thus, the computational domain is divided into two regions: the internal domain, which covers the propeller and is rotating at 3000 rpm; and the external domain, which is considered to be stationary. The second-order upwind scheme is used for the convection terms, whereas the diffusion terms are discretized using a central scheme. The convergence of the numerical solution is controlled and observed by assigning suitable underrelaxation of the transport equations so that the relative numerical error of the solution drops below 1.0^{-7}.

D. New Method for C_{D90} Prediction

During the extrapolation process, one of the aspects with major weight, as referred to by Montgomerie [21], is the airfoil drag coefficient at an angle of attack of 90 deg. The developments to predict the drag coefficient at 90 deg began with Gault [33], who presented the low-speed stalling characteristics of airfoils and correlated them with a single specific upper thickness coordinate at $x/c = 0.0125$. The results presented by Gault are restricted to airfoils without high-lift devices and to airfoils with aerodynamically smooth surfaces, and he considered the Reynolds number influence on airfoil stalling characteristics. Later, in 1995, Montgmorie [21] presented two different methods to predict the value of the drag coefficient and its distribution along a wind turbine blade. The first method considers a constant drag coefficient distribution along the entire blade and represents the most widely used method by manufacturers. The second method consists of a curvilinear distribution of the drag coefficient at 90 deg.

Initially, the method described by Montgmorie [34] was used in JBLADE, but the authors found that different extrapolated 360 deg polars will lead to significant differences in final predicted power and thrust forces for the same propeller.

In this new proposed method, C_{D90} is correlated with the airfoil leading-edge radius. The leading-edge radius of an arbitrary airfoil is calculated using an approximation by the least-square method on its set of contour coordinates. For a NACA four-digit-series airfoil, it is possible to calculate the leading-edge radius through Eq. (30) [35]:

$$R_{\mathrm{LE}} = 1.109t^2 \tag{30}$$

The leading-edge radius was calculated for different NACA airfoils, and the results are presented in Table 1.

The greatest difference occurs for an airfoil with 9% thickness, and it is 3.75%, which is a reasonably low value. The leading-edge radius of specific airfoils was then calculated and plotted against their experimentally measured values of drag coefficient at 90 deg, as presented in Fig. 3.

The linear correlation that was found to fit the data is shown in Eq. (31):

$$C_{D_{90}} = 2.0772 - 3.978\mathrm{LE}_{\mathrm{Radius}} \tag{31}$$

In addition, an improvement to the fitting previously presented by Timmer [36] was implemented. The airfoil y coordinate at $x/c = 0.0125$ for more airfoils (see Table 2 [22,36–39]) was calculated, and airfoils were added to the originally considered database.

The comparison between new and original correlations can be observed in Fig. 4. This new correlation was also implemented in the JBLADE [40] software, providing a second option for the calculation of C_{D90}, and consequently for airfoil polar extrapolation.

The new fit obtained with the y coordinate at $x/c = 0.0125$ is given by

$$C_{D_{90}} = 2.086 - 4.6313(y/c)_{0.0125} \tag{32}$$

E. Poststall Model

The rotational motion of the blade affects the element's boundary layer such that the airfoil stall shifts to higher angles of attack. So, a correction for the mentioned problem is also implemented in JBLADE. The correction is based on the work of Corrigan and Schillings [41] and is presented in Eq. (33). This model is based on the local solidity ratio and relates the stall delay to the ratio of the local blade chord to radial position:

$$c_{\mathrm{rot}(\alpha+\Delta\alpha)} = c_{\mathrm{non\text{-}rot}}\left(\frac{\mathrm{d}c_l}{\mathrm{d}\alpha}\Delta\alpha\right) \tag{33}$$

where

$$\Delta\alpha = \left[\left(\frac{K(\frac{c}{r})}{0.136}\right)^n - 1\right](\alpha_{C_{l_{\max}}} - \alpha_{C_{l_0}})$$

The separation point is related with the velocity gradient K through Eq. (34):

$$\left(\frac{c}{r}\right) = 0.1517\ \mathrm{K}^{-1.084} \tag{34}$$

F. JBLADE Software

To implement and verify the improvements presented in this paper, the proposed models were implemented in JBLADE software. JBLADE [40] is being developed by the authors as a numerical open-source propeller design and analysis code written in C++/QML programming language [42]. The code is based on QBLADE [43,44]

Table 1 Leading-edge (LE) radius calculations and errors due to least-square method approximation

Airfoil name	LE radius with Eq. (30)	LE radius with least-square method	Error, %
NACA 0012	0.01597	0.01596	0.06
NACA 0015	0.02495	0.02472	0.93
NACA 0018	0.03593	0.03525	1.93
NACA 4409	0.00898	0.00933	3.75
NACA 4412	0.01597	0.01629	1.96
NACA 4415	0.02495	0.02511	0.64
NACA 4418	0.03593	0.03597	0.11

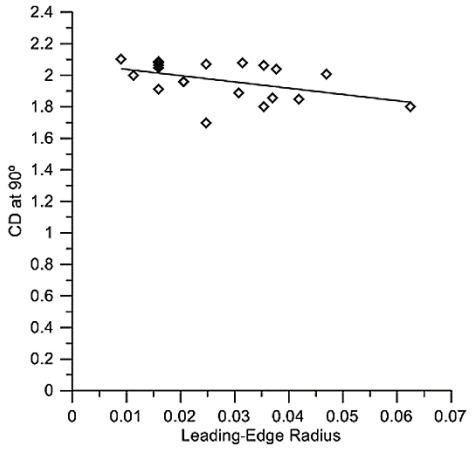

Fig. 3 Measured airfoil drag coefficient at 90 deg angle of attack vs airfoil leading-edge radius.

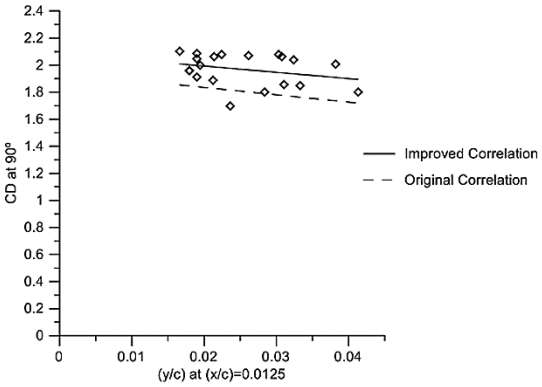

Fig. 4 Comparison between original and improved correlations based on method described by Timmer [36].

and XFLR5 [45] codes. It uses the classical blade element momentum theory, modified to account for three-dimensional flow equilibrium. Its methodology and theoretical formulation for propeller analysis are presented herein. The code can estimate the performance curves of a given design for offdesign analysis. The software has a graphical user interface, making easier to build and analyze the propeller simulations. The long-term goal of the JBLADE is to provide a user-friendly, accurate, and validated open-source code that can be used to design and optimize a variety of propellers.

The airfoil performance figures needed for the blades simulation come from QBLADE's coupling with the open-source code XFOIL [46]. This integration, which is also being improved, allows the fast design of custom airfoils and computation of their lift and drag polars. In addition, it is possible to import extrapolated, wind-tunnel, or CFD airfoil polars in the propeller simulation.

III. Results and Discussion

A. Test Cases

To validate JBLADE code and verify the reliability of the new developed models, the propellers described in NACA Technical Reports 594 [47] and 530 [48] were simulated.

The propellers have the Clark Y airfoil, with variable thickness along the blade span sections. Details of the propeller geometries and data for the different blade pitch angles can be seen in Figs. 5 and 6.

The propeller presented in Fig. 5 corresponds to the configuration named "nose 6–propeller c" from NACA Technical Report 594 [47], whereas the geometry in Fig. 6 corresponds to propeller 6267A-18 from NACA Technical Report 530 [48].

The airfoil polars were obtained with the XFOIL module. Each section of the blade has specific Reynolds and Mach numbers for which the airfoils were previously simulated. These polars were extrapolated such that the lift and drag coefficients became available for higher angles of attack. The geometries presented on the left sides of Figs. 5 and 6 were replicated in JBLADE, and the corresponding airfoil for each blade section was used, obtaining the propeller represented on the right sides of Figs. 5 and 6. The blade pitch angle was adjusted to the given angle at 75% of the radius, and the propeller performance was computed.

To correctly replicate the geometries previously presented, the authors have researched how the pitch angle was measured in the NACA reports [47,48]. However, the NACA reports do not give a clear indication about how the blade angle was measured at each radial position. Analyzing the two common reference lines (see Fig. 7), it was concluded that NACA tests refer to the lower surface of the blade, which was the usual practice at that time. Analyzing the difference on a Clark Y airfoil having 12% thickness, it becomes

$$\theta_{\text{Axis}} - \theta_{\text{LowerSurface}} = 2 \text{ deg} \tag{35}$$

Table 2 Maximum drag coefficient measured and calculated by two methods for a set of airfoils

Airfoil name	Reference	Measured C_{D90}	Calculated C_{D90} with $\text{LE}_{\text{Radius}}$	Calculated C_{D90} with $y/c_{(x/c=0.0125)}$
DU 91-W2-250	Timmer [36]	1.859	1.9302	1.9424
DU-97-W-300	Timmer [36]	1.845	1.9107	1.9319
FX 84-W-127	Massini et al. [37]	2.000	2.0325	1.9959
FX 84-W-218	Massini et al. [37]	2.040	1.9274	1.9359
LS-417	Timmer [36]	1.887	1.9545	1.9874
LS-421-MOD	Massini et al. [37]	2.010	1.8903	1.9088
NACA 0012	Lindenburg [22]	2.090	2.0141	1.9983
NACA 0012	Massini et al. [37]	2.050	2.0141	1.9983
NACA 0012	Timmer [36]	1.914	2.0141	1.9983
NACA 0015	Miley [38]	1.700	1.9779	1.9766
NACA 0018	Timmer [36]	1.800	1.9368	1.9544
NACA 4409	Ostowari and Naik [39]	2.100	2.0411	2.0089
NACA 4412	Ostowari and Naik [39]	2.060	2.0140	1.9868
NACA 4415	Ostowari and Naik [39]	2.068	1.9792	1.9652
NACA 4418	Ostowari and Naik [39]	2.060	1.9367	1.9433
NACA 23012	Massini et al. [37]	2.082	2.0140	1.9820
NACA 23017	Massini et al. [37]	2.078	1.9517	1.9453
NACA 23024	Lindenburg [22]	1.798	1.8283	1.8948
NACA 63-215	Lindenburg [22]	1.959	1.9954	2.0030

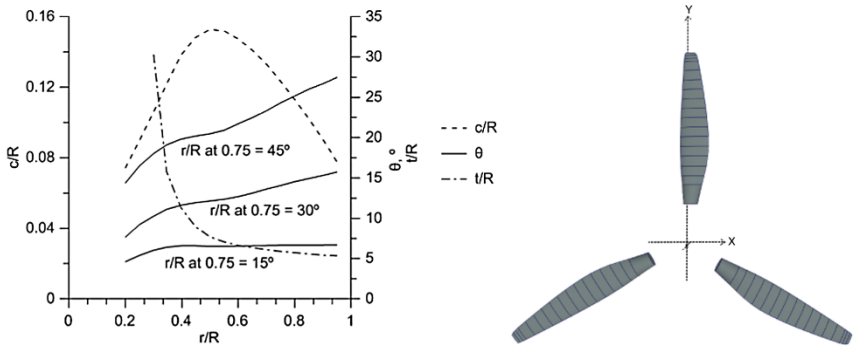

Fig. 5 Propeller geometry presented in NACA technical report 594 [47] and its shape after introduced in JBLADE. The propeller has three blades and a diameter of 3.054 m.

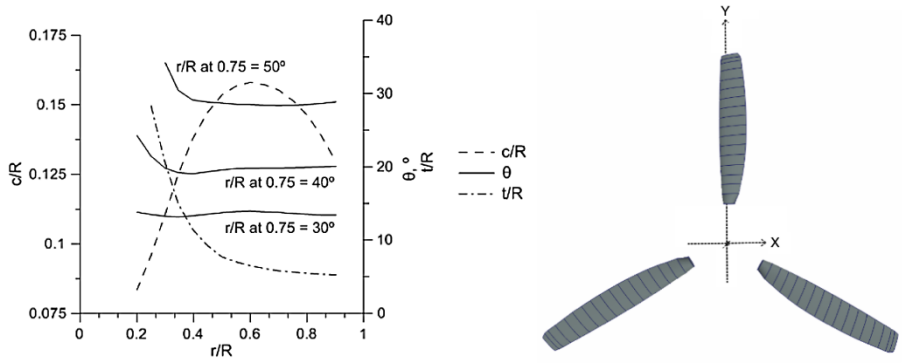

Fig. 6 Propeller geometry presented in NACA technical report 530 [48] and its shape after introduced in JBLADE. The propeller has three blades and a diameter of 3.073 m.

Since JBLADE uses the axis of the airfoil as the reference for the angle measurements, those 2 deg were added to the geometries found in the NACA reports [47,48].

B. Propeller Simulation

To simulate the propeller in JBLADE, the number of points required to define the airfoil coordinates in order to optimize XFOIL numerical accuracy was first studied. In Fig. 8 are presented the different polars obtained with different numbers of points in the airfoil definition. It was concluded that, for more than 200 points, XFOIL does not show a significant difference in the airfoil polars. So, each airfoil should be redefined in order to have 200 points.

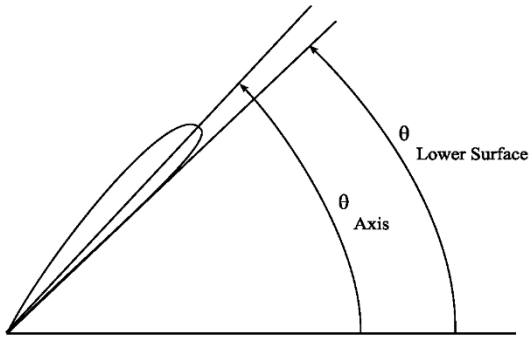

Fig. 7 Two possible references for blade pitch angle.

To validate the computations for a wide range of advance ratios, independent simulations for small and large advance ratios were computed and compared with the previously calculated curve using an average distribution of Reynolds and Mach numbers along the blade (see Fig. 9). For each of the blade's defining sections, the average Reynolds and Mach numbers were set as the mean values corresponding to half the advance ratio that corresponded to the propeller operating conditions used to collect the experimental data. The "VMIN" points were obtained with the distribution of Reynolds and Mach numbers for a low-airspeed operating condition. The propeller rotational speed was constant at 1800 rpm. The airfoil polars were calculated using those Reynolds and Mach numbers, and the propeller performance was only analyzed for that specified speed. The "VMAX" points were obtained with same procedure but for an airspeed close to the highest-advance-ratio zero thrust condition. The "COMPUTED" curves were calculated with the Reynolds and Mach number distributions collected for the intermediate velocities close to the maximum efficiency ("VMED" points). These averaged Reynolds and Mach number distributions (VMED) correspond to the intermediate advance ratio corresponding to that particular pitch setting, and they allow a close approximation for the full range of advance ratios, simplifying the simulation.

The history of the improvements on the theoretical formulation of JBLADE can be seen in Fig. 10 [49] and Fig. 11. "JBLADE$C_{D9} = 1.4$" was the initial formulation, as it was incorporated in QBLADE for wind turbines but extended here to simulate propellers. The dashed lines were obtained with a constant value of drag coefficient as suggested by Montgomorie [21] in his first method. According to this method, the value of $C_{D90} = 1.4$ was used for all airfoils from root to tip. "BEM–improved 360 polar"

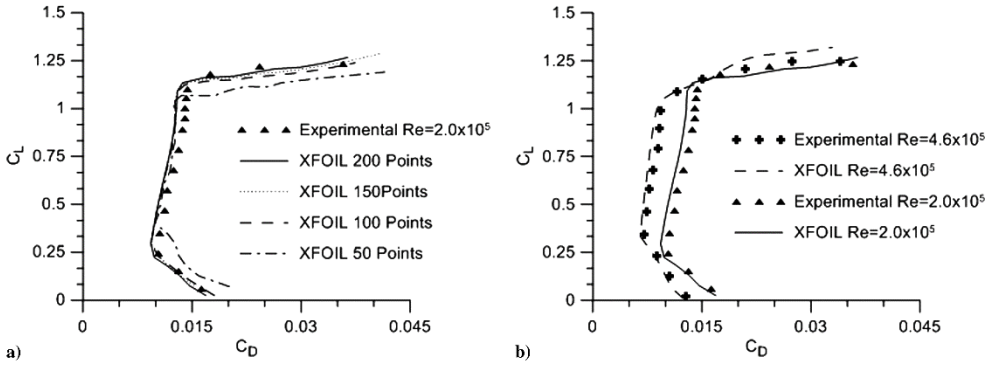

Fig. 8 Representations of a) validation of polar calculation using different number of points to define an airfoil in XFOIL; and b) comparison between XFOIL and experimental studies [49] for E387 airfoil and different Reynolds numbers.

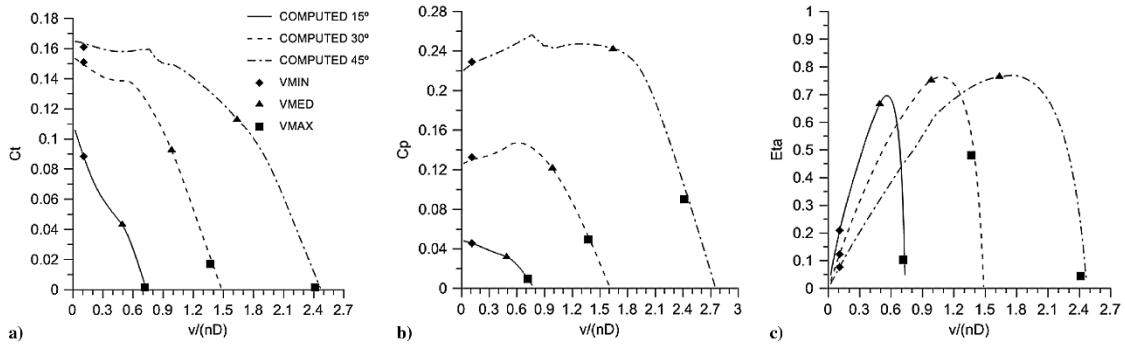

Fig. 9 Validation of calculations using a distribution of averaged Reynolds and Mach numbers along the blade: a) thrust coefficient, b) power coefficient, and c) propeller efficiency.

corresponds to the modified 360 deg range of angle-of-attack polar model improvement described in Sec. II.D. The solid lines were obtained with the presently proposed methods, where C_{D90} is correlated with the leading-edge radius. This method modifies the value of drag coefficient at 90 deg to a more reasonable value, and consequently changes the extrapolated 360 deg angle-of-attack airfoil drag coefficient polar. "JBLADE$C_{D9} = 2.2$" also represents a constant C_{D90} along the blade. It is seen that the C_{D90} and the complete 360 deg angle-of-attack range airfoil polars play an important role in the predicted performance, with a visible improvement in the thrust and power coefficients at low advance ratios and a slight underprediction at high advance ratios for the thrust coefficient.

The "mod. BEM" curve in Fig. 11 corresponds to the modification of the classical BEM with the 3-D equilibrium described in Sec. II.C, resulting in significant improvements throughout the complete advance ratio range. "Mod. BEM + poststall" includes the poststall model described in Sec. II.E and corresponds to the final formulation used in the simulations thereafter.

C. Results

Figure 12 shows that JBLADE closely predicts the thrust coefficient; however, the power coefficient is significantly underpredicted at low advance ratios and slightly overestimated in the higher end. It was found in the first case that the cause may be attributed to the airfoil's 360 deg angle-of-attack range airfoil polar misrepresentation just above the stall since that, at the lower advance ratios together with high pitch angles, a significant portion of the blade root is well into deep-stall angles of attack and the airfoil performance is obtained from XFOIL predictions that are not accurate for poststall regimes. The propeller efficiency is thus overpredicted in this region. The advance ratio for the maximum efficiency closely matches the experimental values, but the maximum

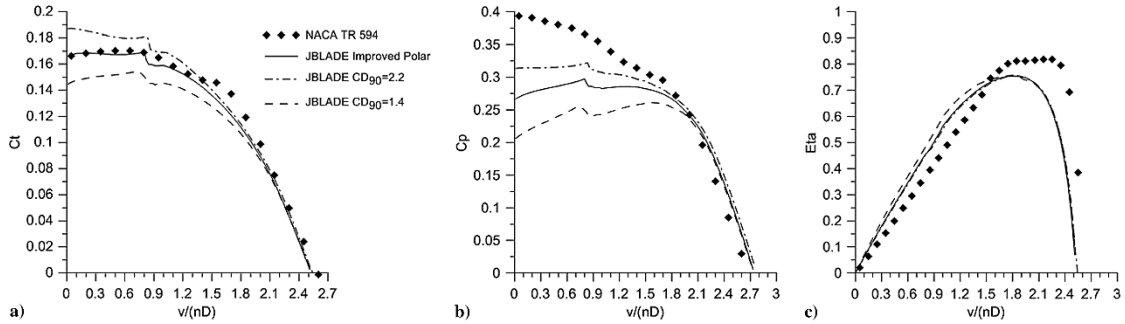

Fig. 10 Influence of the 360 polars extrapolation in the propeller performance.

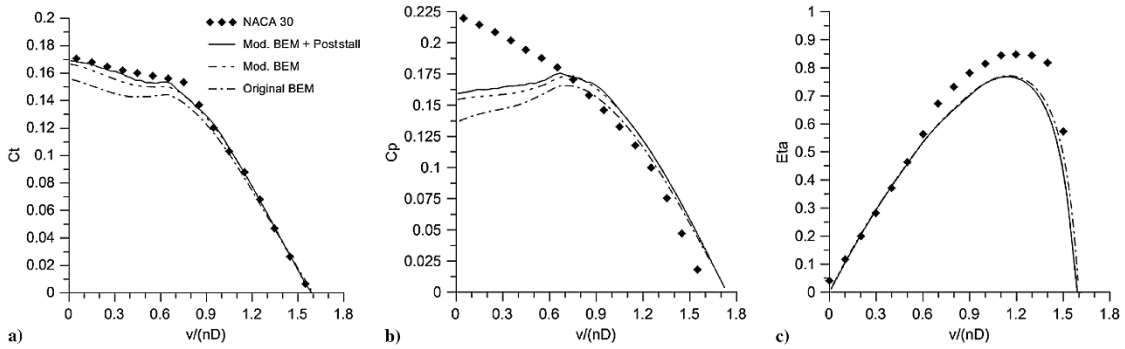

Fig. 11 Different formulations influence on the simulated propeller performance: a) thrust coefficient, b) power coefficient, and c) propeller efficiency.

efficiency is estimated at about a 10% lower value than the experiments. This is related to the overprediction for power coefficients at high advance ratios. One possible cause may be that the 3-D equilibrium condition still depends on the assumption of constant axial-induced velocity across the propeller disk. Comparing with JAVAPROP [50] and QPROP [28], JBLADE gives the best overall results.

Figure 13 shows the results of for the test case of NACA technical report 530 [48] for the reference propeller pitch angles of 30 deg (top), 40 deg (middle), and 50 deg (bottom) at 75% of the blade radius. Since

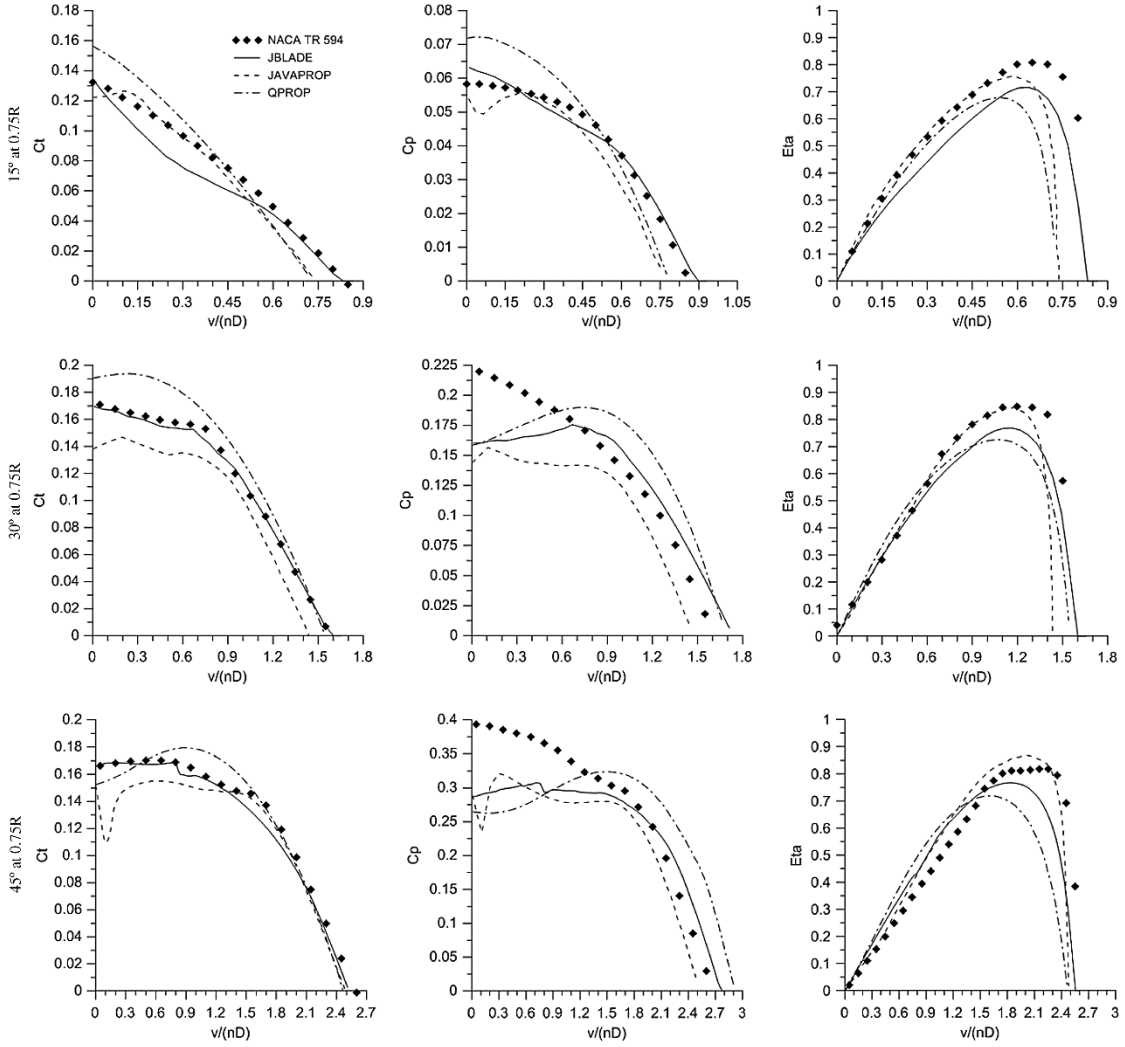

Fig. 12 Comparison between data predicted by JBLADE, QPROP [28], JAVAPROP [50], and data obtained from NACA Technical Report 594 [47].

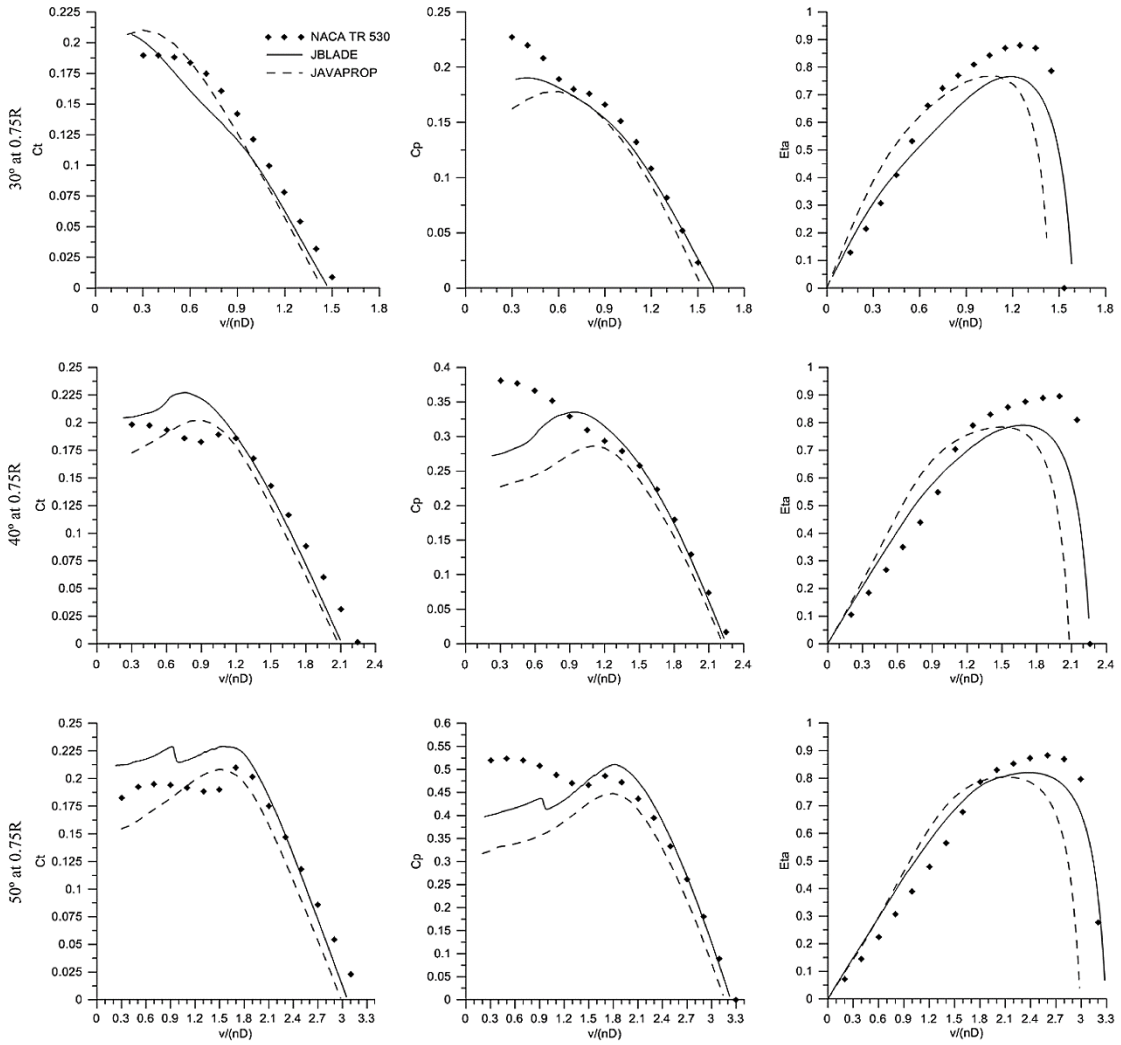

Fig. 13 Comparison between data predicted by JBLADE, JAVAPROP [50], and data obtained from NACA Technical Report 530 [48].

QPROP performed the worst in the first test case, only JAVAPROP was used for comparison with JBLADE in this second test case.

These results confirm that the power coefficient is underpredicted at low advance ratios, but contrary to what occurs in the previous test case, it is more closely estimated in the higher advance ratios. The thrust coefficient is significantly overestimated in the low-advance-ratios region, and it is slightly underpredicted in the higher-advance-ratios region, but the prediction is clearly closer to the experiments than that of JAVAPROP. Similar to the previous test case, the advance ratio for the maximum efficiency is correctly predicted, but the maximum efficiency is underestimated. Also, in this case, the advance ratio where the maximum efficiency occurs is correctly predicted. In this test case, this is related to the underprediction for thrust coefficients at high advance ratios. When compared with JAVAPROP, JBLADE confirms the best overall results.

IV. Conclusions

The JBLADE software proves to be useful for comparison of different propellers designs. The improvement of the classical BEM formulation with a 3-D flow equilibrium condition significantly improves the predictions for lower advance ratios with respect to other BEM codes. The correct modeling of the poststall airfoil characteristics was also found to play a major role in these low-advance-ratio performance predictions. This was achieved by studying a set of airfoil poststall characteristics in order to obtain a new correlation between the airfoil drag coefficient at 90 degr and the airfoil leading-edge radius. The proposed correlation proved to be reliable and can be used for all types of airfoils: both symmetric and asymmetric. The improvements in the method to extrapolate the drag coefficient polar, besides reducing the errors introduced by the user for not knowing what C_{D90} value to use, lead to significant improvements in the prediction of the propeller performance coefficients. The fitting of the correlation suggested by Timmer [36] was also improved and implemented, providing different options to extrapolate the drag coefficient for the full 360 deg of angle of attack. The new proposed models, after their implementation in JBLADE code, provided significant improvements on the prediction of the propeller performance.

Further improvement for the performance prediction at the low advance ratios might be achieved with high-fidelity CFD

simulations, given the suitability of turbulence models to obtain closer-to-real poststall airfoil characteristics. Nevertheless, computational fluid dynamics is more expensive and JBLADE allows a fast selection of the promising propeller geometry during an optimization procedure.

Acknowledgments

The present work was performed as part of Project Multibody Concept for Advanced Airship for Transport (reference no. 285602), supported by the European Union through the 7th Framework Programme. Part of the work was also supported by both the Center for Mechanical and Aerospace Sciences and Technologies and the Portuguese Foundation for Science and Technology (research unit no. 151).

References

[1] Wilson, J. R., "A New Era for Airships," *Aerospace America*, Vol. 42, No. 5, May 2004, pp. 27–31.

[2] Wang, X., Ma, Y., and Shan, X., "Modeling of Stratosphere Airship," *Advances in Theoretical and Applied Mechanics*, Vol. 2, No. 3, 2009, pp. 123–142.

[3] van Eaton, E. H., "Airships and the Modern Military," U.S. Army War College, Carlisle Barracks, Carlisle, PA, 1991, pp. 1–36.

[4] Liao, L., and Pasternak, I., "A Review of Airship Structural Research and Development," *Progress in Aerospace Sciences*, Vol. 45, Nos. 4–5, May–July 2009, pp. 83–96. doi:10.1016/j.paerosci.2009.03.001

[5] Morgado, J., Silvestre, M. Â. R., and Páscoa, J. C., "Parametric Study of a High Altitude Airship According to the Multi-Body Concept for Advanced Airship Transport—MAAT," *Proceedings of IV Conferência Nacional em Mecânica dos Fluidos, Termodinâmica e Energia*, Paper 90, LNEC, Lisboa, 2012.

[6] Dumas, A., Trancossi, M., Madonia, M., and Giuliani, I., "Multibody Advanced Airship for Transport," Soc. of Automotive Engineers TP-2011-01-2786, Warrendale, PA, 2011.

[7] Ilieva, G., Páscoa, J. C., Dumas, A., and Trancossi, M., "A Critical Review of Propulsion Concepts for Modern Airships," *Central European Journal of Engineering*, Vol. 2, No. 2, April 2012, pp. 189–200. doi:10.2478/s13531-011-0070-1

[8] Monk, J. S., "The Aerodynamic Design of an Optimised Propeller for a High Altitude Long Endurance UAV," *Proceedings of 23rd Congress of International Council of the Aeronautical Sciences*, ICAS Paper 2002-5.10.4, Pretoria, 2002.

[9] Rankine, W. M. J., "On the Mechanical Principles of the Action of the Propellers," *Transactions of the Institute of Naval Architects*, Vol. 6, No. 13, 1865, pp. 30–390.

[10] Froude, W., "On the Elementary Relation Between Pitch, Slip and Propulsive Efficiency," NASA TR-NASA-TM-X-61726, 1920.

[11] Drzewiecki, S., "Méthode Pour la Détermination des éléments Mécaniques des Propulseurs Hélicoïdaux," *Bulletin de L'Association Technique Maritime*, Vol. 3, No. 3, 1892, pp. 11–31.

[12] Betz, A., and Prandtl, L., "Schraubenpropeller mit Geringstem Energieverlust," *Göttinger Nachrichten*, Vol. 1919, 1919, pp. 193–217.

[13] Eppler, R., and Hepperle, M., "A Procedure for Propeller Design by Inverse Methods," *Proceedings of International Conference on Inverse Design Concepts in Engineering Sciences*, G.S. Dulikravich, Austin, TX, Oct. 1984, pp. 445–460.

[14] Glauert, H., "Airplane Propellers," *Aerodynamic Theory*, Dover, New York, 1963, pp. 251–268.

[15] Goldstein, S., "On the Vortex Theory of Screw Propellers," *Proceedings of the Royal Society of London, Series A: Mathematical, Physical and Engineering Sciences*, Vol. 123, No. 792, April 1929, pp. 440–465. doi:10.1098/rspa.1929.0078

[16] Theodorsen, T., *Theory of Propellers*, McGraw–Hill, New York, 1948, pp. 1–168.

[17] Larrabee, E. E., "Practical Design of Minimum Induced Loss Propellers," Soc. of Automotive Engineers TP-790585, Warrendale, PA, 1979.

[18] Adkins, C. N., and Liebeck, R. H., "Design of Optimum Propellers," *Journal of Propulsion and Power*, Vol. 10, No. 5, 1994, pp. 676–682. doi:10.2514/3.23779

[19] Tangler, J. L., and Ostowari, C., "Horizontal Axis Wind Turbine Post Stall Airfoil Characteristics Synthesization," *DOE/NASA Wind Turbine Technology Workshop*, Paper DE91002198, 1984.

[20] Wald, Q., "The Aerodynamics of Propellers," *Progress in Aerospace Sciences*, Vol. 42, No. 2, 2006, pp. 85–128. doi:10.1016/j.paerosci.2006.04.001

[21] Montgomerie, B., "Drag Coefficient Distribution on a Wing at 90 Degrees to the Wind," The Energy Research Center of the Netherlands (ECN) ECN-95-061, Amesterdam, 1996.

[22] Lindenburg, C., "Aerodynamic Airfoil Coefficients at Large Angeles of Attrak," *Proceedings of Annual IEA Symposyum on the Aerodynamics of Wind Turbines*, Paper ECN-RX-01-004, Golden, CO, Dec. 2000.

[23] Ostowari, C., and Naik, D., "Post Stall Studies of Untwisted Varying Aspect Ratio Blades with a NACA 44XX Series Airfoil Sections—Part II," *Wind Engineering*, Vol. 9, No. 3, 1985, pp. 149–164.

[24] Snel, H., Houwink, R., and Bosschers, J., "Sectional Prediction of Lift Coefficients on Rotating Wind Turbine Blades in Stall," The Energy Research Center of the Netherlands (ECN) ECN-C-93-052, Amesterdam, 1994.

[25] Hand, M. M., Simms, D. A., Fingersh, L. J., Jager, D. W., Cotrell, J. R., Schreck, S., and Larwood, S. M., "Unsteady Aerodynamics Experiment Phase VI: Wind Tunnel Test Configurations and Available Data Campaigns," National Renewable Energy Lab. TR-500-29955, Golden, CO, 2001.

[26] Lindenburg, C., "Investigation into Rotor Blade Aerodynamics Analysis of the Stationary Measurements on the UAE Phase-VI Rotor in the NASA-Ames Wind Tunnel," The Energy Research Center of the Netherlands (ECN) ECN-C-03-025, Amesterdam, 2003.

[27] Tangler, J. L., "The Nebulous Art of Using Wind-Tunnel Airfoil Data for Predicting Rotor Performance: Preprint," *Proceddings of ASME 2002 Wind Energy Symposium*, American Soc. of Mechanical Engineers, Fairfield, NJ, 2002, pp. 190–196. doi:10.1115/WIND2002-40

[28] Drela, M., "QPROP Formulation," 2006, http://web.mit.edu/drela/Public/web/qprop/qprop_theory.pdf [retrieved 25 Oct. 2013].

[29] Saravanamuttoo, H., Rogers, G., and Cohen, H., *Gas Turbine Theory*, 4th ed., Longman Group Ltd., London, 1996, pp. 169–179.

[30] Ananda, G., *UIUC Propeller Database* [database], Aerospace Engineering, Univ. of Illinois Champaign, IL, http://aerospace.illinois.edu/m-selig/props/propDB.html [retrieved 25 Feb. 2014].

[31] *ANSYS FLUENT Theory Guide*, Ansys. Inc., Ann Arbor, MI, 2010.

[32] Menter, F., Ferreira, J. C., Esch, T., and Konno, B., "The SST Turbulence Model with Improved Wall Treatment for Heat Transfer Predictions in Gas Turbines," *Proceedings of the International Gas Turbine Congress*, Paper IGTC2003-TS-059, Tokyo, 2003, pp. 2–7.

[33] Gault, D., "A Correlation of Low Speed Airfoil Section Stalling Characteristics with Reynolds Number and Airfoil Geometry," NACA TN-3963, March 1957.

[34] Montgomerie, B., "Methods for Root Effects, Tip Effects and Extending the Angle of Attack Range to ±180 deg, with Application to Aerodynamics for Blades on Wind Turbines and Propellers," Swedish Defence Research Agency FOI-R-1305-SE, Stockholm, June 2004.

[35] Abbott, I., von Doenhoff, A., and Stivers, L., "Summary of Airfoil Data," NACA TR-824, 1945.

[36] Timmer, W. A., "Aerodynamic Characteristics of Wind Turbine Blade Airfoils at High Angles-of-Attack," *Proceedings of TORQUE 2010: The Science of Making Torque from Wind*, Crete, 2010, pp. 71–78.

[37] Massini, G., Rossi, E., and D'Angelo, S., "Wind Tunnel Measurements of Aerodynamics Coefficients of Asymmetrical Airfoil Sections for Wind Turbines Blades Extended to High Angles of Attack," *Proceedings of European Wind Energy Conference*, Paper EN3W/0018/I-JB, H.S. Stephens & Associates, Herning, 1988, pp. 241–245.

[38] Miley, S., *A Catalog of Low Reynolds Number Airfoil Data for Wind Turbine Applications*, Dept. of Aerospace Engineering Texas A&M Univ., College Station, TX, 1982, pp. 1–48.

[39] Ostowari, C., and Naik, D., "Post Stall Studies of Untwisted Varying Aspect Ratio Blades with a NACA 4415 Series Airfoil Sections—Part I," *Wind Engineering*, Vol. 8, No. 3, 1984, pp. 176–194.

[40] Silvestre, M. A., Morgado, J. P., and Pascoa, J., "JBLADE: A Propeller Design and Analysis Code," *2013 International Powered Lift Conference*, AIAA Paper 2013-4220, 2013. doi:10.2514/6.2013-4220

[41] Corrigan, J., and Schillings, J., "Empirical Model for Blade Stall Delay Due to Rotation," *Proceedings of the American Helicopter Society Aeromechanics Specialists*, Paper 8.4, San Francisco, 1994, pp. 1–15.

[42] "Qt Project," Software Version: Qt Creator 2.4.1, Digia PLC, Helsinki, 2013, http://qt-project.org/ [retrieved 18 Feb. 2014].

[43] Marten, D., Wendler, J., Pechlivanoglou, G., Nayeri, C. N., and Paschereit, C. O., "QBLADE: An Open Source Tool for Design and Simulation of Horizontal and Vertical Axis Wind Turbines," *International Journal of Emerging Technologies and Advanced Engineering*, Vol. 3, No. 3, Feb. 2013, pp. 264–269.

[44] Marten, D., and Wendler, J., "QBlade Guidelines v0.6," Technical Univ. of Berlin, Berlin, 2013.

[45] Deperrois, A., *Analysis of Foils and Wings Operating at Low Reynolds Numbers — Guidelines for XFLR5 v6.03*, 2011, http://www.xflr5.com/xflr5.htm [retrieved 3 Nov. 2013].

[46] Drela, M., "XFOIL—An Analysis and Design System for Low Reynolds Number Airfoils," *Low Reynolds Number Aerodynamics Lecture Notes in Engineering*, Vol. 54, Springer, Berlin, 1989, pp. 1–12.

[47] Theodorsen, T., Stickle, G. W., and Brevoort, M. J., "Characteristics of Six Propellers Including the High-Speed Range," NACA TR-594, 1937.

[48] Gray, W., "Wind-Tunnel Tests of Two Hamilton Standard Propellers Embodying Clark Y and Naca 16-Series Blade Sections," NACA TR-530, 1941.

[49] Selig, M. S., and Guglielmo, J. J., "High-Lift Low Reynolds Number Airfoil Design," *Journal of Aircraft*, Vol. 34, No. 1, Jan. 1997, pp. 72–79. doi:10.2514/2.2137

[50] Hepperle, M., "JavaProp—Design and Analysis of Propellers—User's Guide," 2010, http://www.mh-aerotools.de/airfoils/javaprop.htm [retrieved 4 Nov. 2013].

This page has been intentionally left blank
for double side copying

B.II – Propeller Performance Measurements at Low Reynolds Numbers

INTERNATIONAL JOURNAL OF MECHANICS Volume 9, 2015

Propeller Performance Measurements at Low Reynolds Numbers

Silvestre, M.A.R., Morgado, J., Alves, P., Santos, P., Gamboa, P., and Páscoa, J.C.

***Abstract*—** Propellers are being used as propulsive devices since the early days of aviation. However, if they are not properly designed, they can have poor efficiency, especially at low Reynolds numbers environments such as the case of the high altitude airships envisioned in the MAAT project. Experimental data those operating conditions are crucial to effectively improve and validate new numerical design tools. This work presents the development of an experimental setup for low Reynolds propeller testing. The experimental data were successfully compared against reference data to validate the test rig. In addition, the performance data for commercially available propellers that were not characterized in the existing literature is also presented.

***Keywords*—** Airships, Low Reynolds Propellers, MAAT Project, Wind Tunnel Experiments.

I. Introduction

IN the last years, high-altitude airships have been considered as a platform for different purposes [1]. Particularly, for application as telecommunication platforms, surveillance, monitoring and for transportation of people and goods [2-8]. In Europe, the Multibody Concept for Advanced Airship for Transport (MAAT [9]) airships are being developed as an alternative medium and long range transportation system. The project involves 12 different institutions and aims to develop a heavy lift cruiser–feeder airship system. Since the cruiser will operate at stratospheric altitudes, propellers are a valid option for propulsion [6,10-16].

Due to the high altitudes the MAAT airship propellers will operate in a Low Reynolds Number (LRN) flow environment. LRN effects can decrease the performance of propellers and the ability of the available numerical methods to predict that performance. To deal with this, JBLADE [17] software is being developed, as an open-source propeller design code, using a modified [18] Blade Element Momentum (BEM) theory which accounts for three dimensional flow equilibrium. The software is coupled with XFOIL [19, 20]for its suitability in predicting LRN airfoil performance [21] JBLADE will be used to design different propellers as well as to estimate their off-design performance.

To improve the prediction capability of JBLADE, accurate LRN propeller performance data is needed.

Experimental work on propeller performance was abundant before WWII [22, 23] and a sound database of propeller performance characteristics got established. That was the golden age of propeller driven aircraft. After WWII, the widespread of jet propulsion [24] limited the use of propellers to light aircraft. However, in recent times, the small Unmanned Aerial Vehicles (UAV) advent has triggered the interest in the LRN wing and propeller aerodynamics. UIUC Applied Aerodynamics Group is a world leading institution, very active in the study of LRN aerofoils and propellers, with several publications describing experimental studies on propeller performance [25-28].

This paper describes the development of a test rig for measuring propeller performance and the experimental tests procedure simulating the LRN environment found at high altitudes. A number of wind tunnel tests performed on different small propellers is reported. In addition, the validation of the experiments is described in detail and performance data not found in the literature is presented for a couple of well-known commercial propellers.

II. Methodology

A. Experimental Setup

The design chosen for the propeller thrust balance closely resembles the T-shaped pendulum concept implemented by UIUC [25]. A sketch of the design is shown in Fig. 1. An effort was made to reduce the complexity of the assembly inside the wind tunnel, in order to ensure minimal flow and measuring disturbances. The T-shaped pendulum is pivoted about two flexural pivots while being constrained by a load cell outside of the tunnel in an area above the test volume, where plenty of room is available. The flexural pivots are frictionless, stiction-free bearings with negligible hysteresis that are suited for applications with limited angular travel. The pivots are made with flat, crossed flat springs that support rotating sleeves. These flexural pivots were chosen over the standard bearings since they greatly reduce the adverse tendencies that bearings are prone to, when used in static applications, namely stiction and hysteresis.

M. A. R. Silvestre is with the Aerospace Sciences Department of University of Beira Interior, Edifício II das Engenharias, Calçada Fonte do Lameiro, n.° 1, 6201-001 Covilhã, Portugal (corresponding author, phone: +351 275 329 732 e-mail: mars@ubi.pt).

J. Morgado is with the Aerospace Sciences Department of University of Beira Interior, Covilhã, Portugal.

P. Alves is with the Aerospace Sciences Department of University of Beira Interior, Covilhã, Portugal.

P. Santos is with the Aerospace Sciences Department of University of Beira Interior, Covilhã, Portugal.

P. Gamboa is with the Aerospace Sciences Department of University of Beira Interior, Covilhã, Portugal.

J. C. Páscoa is with Electromechanics Department of University of Beira Interior, Covilhã, Portugal.

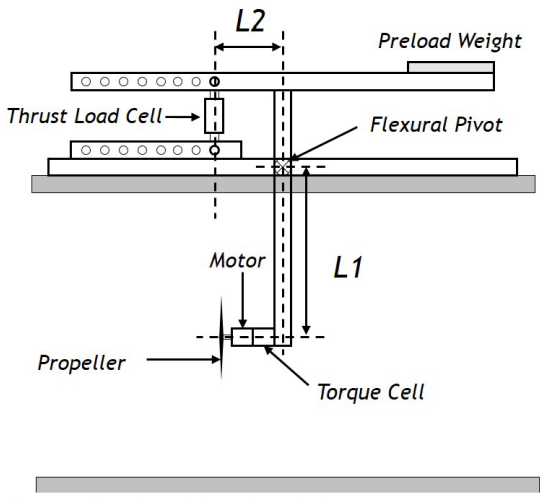

Fig. 1 T-shaped pendulum thrust balance concept.

The pendulum was designed in order to have the thrust vector located at the center of the test section. Another design concern was to ensure that there would be enough space for assembling the load cell and its accessories above the wind tunnel upper wall. Due to the 0.8mX0.8m dimensions of the test cross-section, it was decided to limit the maximum diameter of the propellers that can be tested to 14". Using the data available at the propeller performance database provided by UIUC [28], it was concluded that for 14" propellers, in static conditions, the worst case scenario, the maximum measured thrust is close to 15N.

A preload weight was added to the balance on the opposite side to the load cell (see Fig. 2). This preload weight keeps the load cell in tension throughout propeller testing to make sure the load cell does not slip during negative thrust conditions.

Load Cell Variable Positioning

One of the key concepts for the assembly's sensitivity is the possibility to adjust the position of the load cell along the upper arm of the pendulum. Thus, it becomes possible to use the full range of the load cell for different intervals of propeller's produced thrust. Fig. 2 shows the system sketch, such that the distance $L2$ can be adjusted between $80mm$ and $350mm$ in 10 increments of $30mm$ each.

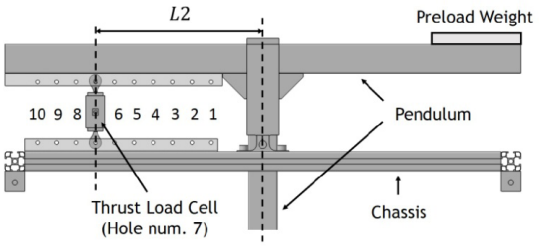

Fig. 2 Illustration of different load cell positions.

Thrust and Torq ue Measurement

The thrust load cell used is the FN3148 manufactured by FGP Sensors & Instrumentation having a maximum capacity of 100N. The torque produced by the propeller is measured using the RTS-100 and RTS-200 reaction torque transducers made by Transducer Techniques according to the torque level of the propeller being tested. Both thrust and torque load cells are connected to a high-precision strain gauge converter from mantracourt, model SCB-68 that converts a strain gauge sensor input to a digital serial output.

Propeller Speed Measurement

To measure the propeller rotation speed, a Fairchild Semiconductor QRD1114 photo-reflector was used to count the number of revolutions the output shaft makes in a fixed time interval ($0.75s$), resulting on an accuracy of $\pm 0.5Rev/0.75s$. This sensor is constituted by two distinct parts: an infrared emitting diode and a phototransistor. A simple circuit composed by a limiting resistor, a bias resistor and a *Schmitt trigger* is used. The former is used, as the name suggests, to limit the current to the infrared diode. The bias resistor is used to produce an output on the phototransistor side. The output of the phototransistor is further cleaned and digitized using a *Schmitt trigger*. The latter component is essential in order to make the output relatively independent of the distance from the reflecting surface.

Using this circuit, the sensor can be placed up to $2mm$ away from the reflective surface. The output voltage is near $0.27V$ when aimed at a white surface and about $4.61V$ when pointed at a black surface. The circuit has a response time of around $50\mu s$. The output voltages and response time of the circuit proved to be more than sufficient for measuring the rotational speed of the propellers, which never exceeded 7000 *RPM* as shown in *Section III*.

Freestream Velocity Measurement

The freestream velocity is measured with a differential pressure transducer, an absolute pressure transducer, and a thermocouple. The measuring mechanism uses two static pressure ports, one at the tunnel settling section and another at the entrance of the test volume, as it presented in Fig. 3.

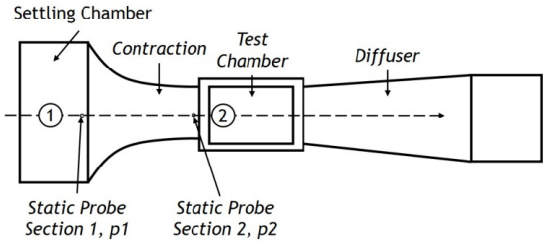

Fig. 3 Location of the static pressure ports.

The contraction section makes the velocity increase and the pressure decrease at the test chamber. This pressure

difference is a measure of the tunnel flow rate. Thus, the velocity can be determined from Bernoulli's equation:

$$\frac{p_1}{\rho}+\frac{1}{2}V_1^2+gz_1=\frac{p_2}{\rho}+\frac{1}{2}V_2^2+gz_2 \quad (1)$$

Considering that the tunnel is horizontal, $z_1 = z_2$, then:

$$V_2^2-V_1^2=\frac{2(p_1-p_2)}{\rho} \quad (2)$$

The incompressible continuity relationship:

$$A_1V_1=A_2V_2 \quad (3)$$

or

$$V_1=\frac{A_2}{A_1}V_2 \quad (4)$$

Combining (2) and (4), allows the determination of the flow velocity in the test section:

$$V_2=\sqrt{\frac{2(p_1-p_2)}{\rho\left[1-\left(\frac{A_2}{A_1}\right)^2\right]}} \quad (5)$$

The atmospheric pressure outside of the tunnel is measured with the absolute pressure transducer model MPXA4115A made by Freescale Semiconductor. The temperature is measured with a National Instruments LM335 thermocouple located at the inlet of the wind tunnel. This measuring method is also independent of possible inaccurate installations regarding the correct direction of the pitot probe as it uses the factory pre-installed wind tunnel static pressure ports.

B. Balance Calibration

Before using the rig for any tests, each measuring instrument was calibrated. The thrust calibration was made *in situ* using calibrated weights and a low-friction pulley system to create an axial load simulating the propeller thrust on the load cell (see Fig. 4 (b)). By increasing and decreasing a known force on the load cell, a linear relationship between the thrust and voltage was determined. Regarding torque sensor calibration (see Fig. 4 (a)), the calibrated weights are used with a moment arm to create a known torque, and by adding and removing weights, a linear relationship between the torque and voltage was also calculated. These calibration procedures need to be regularly performed to ensure consistent results. Calibration was later verified using check-loads. Pure and combined check-loads were repeatedly applied to verify the balance calibration.

(a) (b)

Fig. 4 Pictures of the thrust balance calibration procedure: (a) torque sensor (b) thrust load cell

C. Propeller Performance Parameters

Variables can be divided into two categories, namely measured and calculated variables. The measured variables are directly obtained from the measurement instruments. Physical measurements of thrust, torque, rotational speed, static pressures, atmospheric pressure, and temperature are gathered. From these quantities, propeller power and air density are calculated, respectively, according to:

$$P = 2\pi nQ \quad (6)$$

$$\rho=\frac{P_{abs}}{RT_{atm}} \quad (7)$$

The above measured and derived quantities are non-dimensionalized in order to obtain the propeller performance characteristics. These quantities include the thrust coefficient C_T, power coefficient, C_P, and propeller efficiency, η. In the static case, since the advance ratio is zero, C_T and C_P are plotted against the propeller rotational speed. For the non-static case, the coefficients and the efficiency are plotted against the advance ratio. The definitions for the advance ratio, thrust and power coefficients, and propeller efficiency are, respectively, given by:

$$J=\frac{V}{nD} \quad (8)$$

$$C_T=\frac{T}{\rho n^2D^4} \quad (9)$$

$$C_P=\frac{P}{\rho n^3D^5} \quad (10)$$

$$\eta=J\frac{C_T}{C_P} \quad (11)$$

where, V is the freestream velocity; D is the propeller diameter; T is the propeller thrust; P is the propeller power and n is the propeller rotational speed expressed in *rot/s*.

D. Wind Tunnel Corrections

Boundary Corrections for Propellers

The interference experienced by a propeller in a wind tunnel was object of study by Glauert [29]. A propeller, when producing a positive thrust, creates a wake or slipstream of increased velocity. Considering that in a closed wind tunnel the flow is confined between solid walls, the condition of flow continuity leads to reduced velocity and increased pressure of the fluid surrounding the wake.

These modified conditions behind the propeller change the relationship between the thrust and the freestream velocity of the wind tunnel propeller for a given rotational speed. Such that, in confined conditions, the thrust developed by the propeller is greater than would be developed in an unrestricted flow of the same freestream velocity with the same propeller rotation rate and blade pitch. Or, it can also be said that the thrust developed would be equal to that which would be expected at a lower V' in freestream velocity [30]. The correction for this effect is:

$$\frac{V'}{V} = 1 - \frac{\tau_4 \alpha_1}{2\sqrt{1+2\tau_4}} \quad (12)$$

where

$$\tau_4 = \frac{T}{\rho A V^2} \quad (13)$$

and

$$\alpha_1 = \frac{A}{C} \quad (14)$$

where A is the propeller disk area and C is the jet cross-sectional area, and T is thrust.

Motor Fixture Drag

Due to the presence of the torque transducer and the motor fixture, the measured thrust is actually given by (T-$D_{fixture}$). To obtain the actual values of thrust, an assembly's drag model was implemented in order to correct the measured thrust values for different freestream velocities. The propeller thrust is, thus, given by:

$$T = \rho n^2 D^4 C_T + D_{fixture} \quad (15)$$

The assembly's drag is estimated using:

$$T = \rho n^2 D^4 C_T + D_{fixture} \quad (16)$$

with

$$q = \frac{1}{2}\rho V_{drag}^2 \quad (17)$$

Considering that the fixture is located in the propeller slipstream, a fixture drag velocity was used as the corrected freestream velocity given by Glauert's method 2.14 plus the slipstream induced velocity, at the propeller disk, given by the Actuator Disk Theory.

$$V_{drag} = -\frac{V'}{2} + \sqrt{\left(\frac{V'}{2}\right)^2 + \frac{T}{2\rho A}} + V' \quad (18)$$

E. Test Methodology

For static performance tests, the propeller thrust and torque were measured along with the local atmospheric pressure and temperature at different *RPM*. For the performance tests with freestream speed, the propeller rotational speed was set to a desired value and the wind tunnel's freestream velocity was increased from 4 *m/s* to 28 *m/s* by 1 *m/s* increments. At freestream velocities smaller than 4 *m/s*, it was difficult to obtain the needed freestream velocity stability to proceed with the measurements, due to the interference between the propeller wake and the wind tunnel's fan. At each measured freestream velocity, the propeller thrust and torque were measured along with the ambient pressure and temperature. If the torque value became too close to zero, the test was finished because the propeller was entering the windmill brake state.

The collecting data procedure (see Fig. 5) begins with the execution of the LabView® data acquisition and reduction software. This is followed by putting the program to run test condition. The control software powers up the motor to the first pre-defined ***RPM*** setting and data for each freestream velocity step is collected. This procedure was repeated for all ***RPMs***. Once the data was collected, the data reduction sub-routine is executed. The collected data is systematically reduced, recorded and stored. Due to the complete automation of the process, the overall time for an entire run is just the physical tunnel run time. The procedure of collecting data in each freestream velocity is preceded by a "data convergence period" of 50s within a minimum error margin from the intended defined ***RPM*** and freetream velocity values to achieve the steady state.

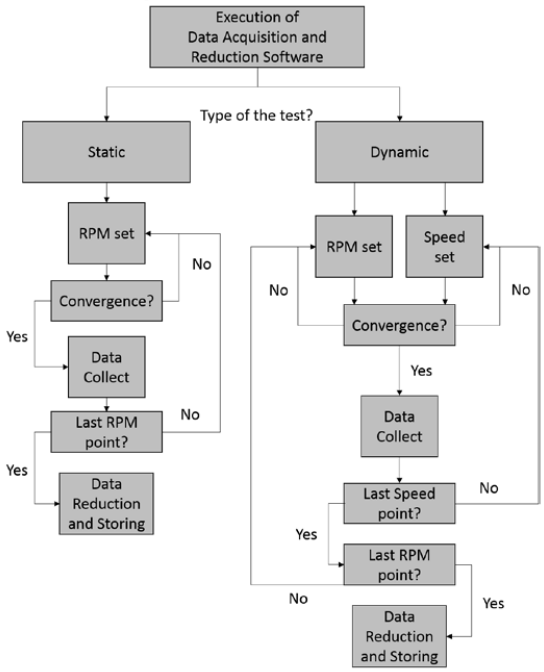

Fig. 5 Flowchart of the test methodology.

Convergence Criteria

The procedure of collecting data in each freestream velocity is preceded by a "data convergence period" to achieve the

steady state. Two similar convergence criteria are implemented, one for the freestream velocity set and the other for the propeller's RPM. Both convergence criteria are presented in Table 1:

Table 1 – Convergence criteria for *U* and *RPM*.

Criteria	Min. Time [s]
$\lvert RPM - RPM_{target} \rvert \leq 10\ RPM$	40.0
$\lvert U - U_{target} \rvert \leq 6\ m/s$	40.0

When both convergence criteria are verified, the data samples are recorded over a pre-defined period of time. In Fig. 6 an example is presented of the torque and thrust outputs during the convergence and data collect phases.

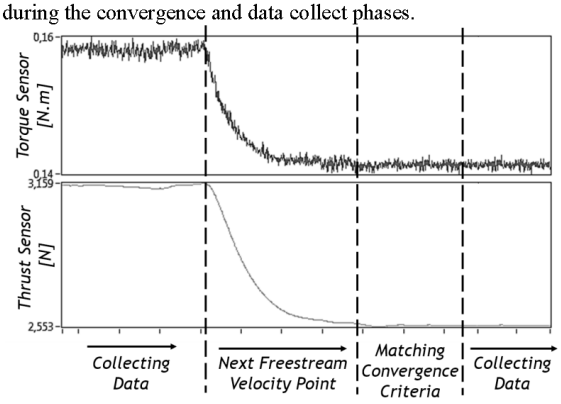

Fig. 6 Torque and Thrust outputs during the convergence and data collection phases.

III. Validation of the Test Rig

Before performing tests for new and uncatalogued propellers, the test rig was submitted to a complete validation study. The validation included a sample independence test in order to ensure that the results are not affected by the number of samples used to collect each point. The same propeller test was run with five different sampling settings as presented in Section 3.1. In addition, to ensure the repeatability of the measurements, the same propeller was tested in 3 different days, as shown in Section 3.2. Furthermore, the propeller performance obtained in UBI's wind tunnel was compared with the data obtained by UIUC[31].

A. Sampling Independence

The recorded output value of any measured or calculated variable is a mean of *N* values recorded at a sample rate of 8*Hz*. Since this frequency is constant, when the sample number, $\boldsymbol{N}$, increases, the sampling time also increases and the test runtime becomes higher. This validation test was performed in order to find an acceptable samples number that does not affect the final result. The APC 11"x5.5" Thin Electric propeller was used.

Table 2 No. of samples vs sampling time.

Number of Samples, $\boldsymbol{N}$	Sampling Time, $\boldsymbol{s}$
50	6.25
100	12.5
200	25.0
400	50.0
800	100.0

The results presented in Fig. 7 show some discrepancies for an advance ratio around 0.3 for the lower number of samples used to collect the data (50 and 100 samples) but converge for *N*>200. To ensure a correct data collection, 400 samples setting was used in all the tests presented herein. That with the 8 *Hz* sampling rate made each point collecting phase takes less than one minute.

B. Measurements Repeatability

To ensure that the measurements are not dependent on the weather conditions on a specific day, the measurements for a specific propeller were performed on 3 distinct days. Furthermore, the measurements repeatability quality is an indicator of the integrity of the measurement system. If a measurement system cannot produce consistent and repeatable measurements, a verification of the measurements accuracy cannot be performed. The test rig was submitted to repeatability tests fulfilling the following conditions:

- The same propeller and the same measurement procedure;
- The same measuring instruments, used under the same conditions;
- The same instrument calibration;
- Repetition over 3 consecutive days.

Fig. 8 shows comparisons of the APC 11"x5.5" Thin Electric performance data collected for the repeatability tests. Although the tests were performed during the summer, the weather conditions were quite different in the three days of testing, with sun on the first day moving to wind and rain on the remaining two days. However, the plotted results show an exceptional repeatability for all the performance parameters.

C. Performance Data Comparison

Two different APC commercial propellers were chosen to this step of validation, the 10x4.7" Slow Flyer and the 11x5.5" Thin Electric. Its performance data was compared with data available in the literature. The data for comparison was downloaded from the UIUC Propeller Data Site [28] and corrected according to Ref. [32].

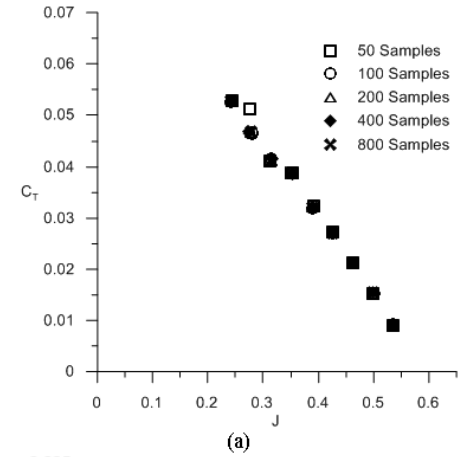

(a)

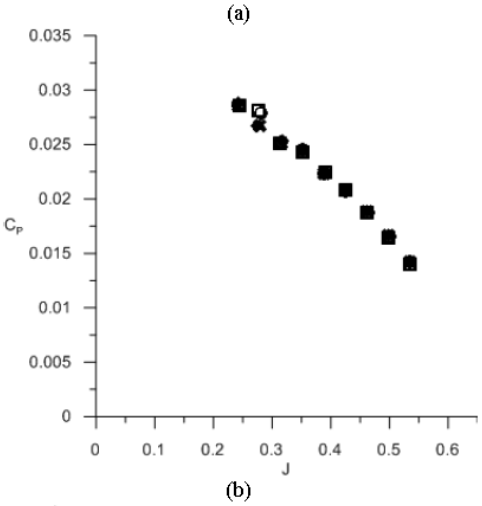

(b)

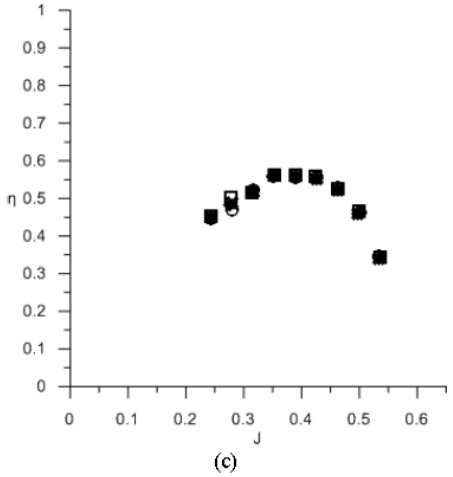

(c)

Fig. 7 Comparison using different number of samples for an APC 11"x5.5". (a) thrust coefficient (b) power coefficient (c) propeller efficiency.

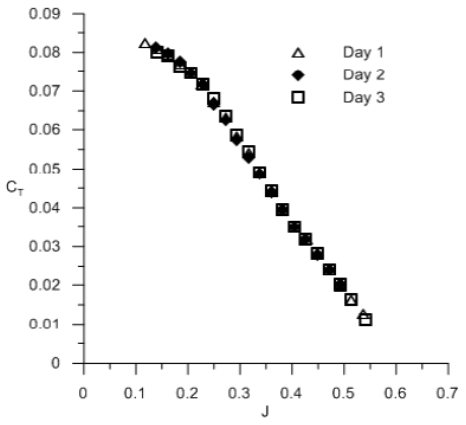

(a)

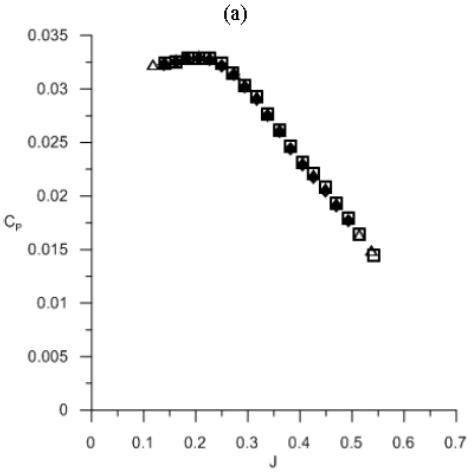

(b)

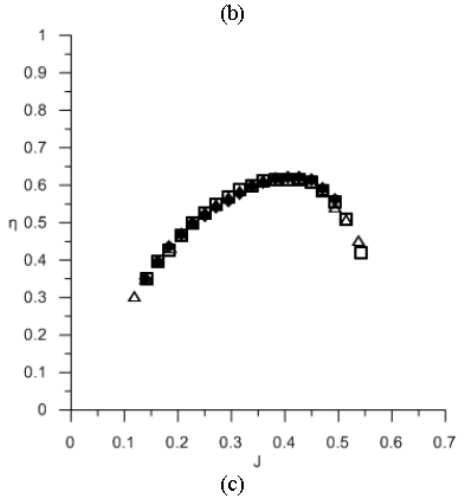

(c)

Fig. 8 Comparison of measurements performed in 3 different days. (a) thrust coefficient (b) power coefficient (c) propeller efficiency.

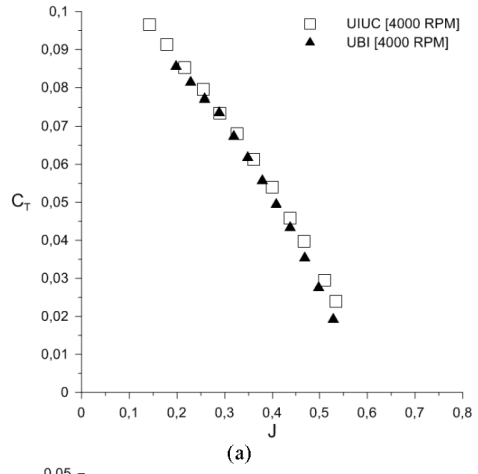

(a)

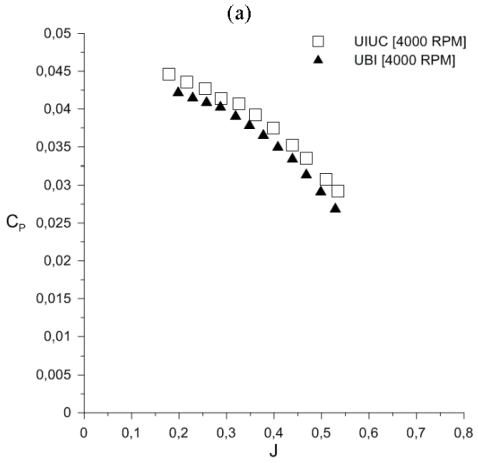

(b)

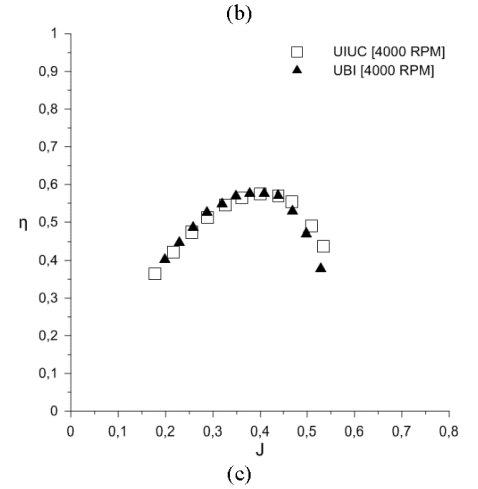

(c)

Fig. 9 APC 10"x4.7" Propeller data for 4000 *RPM* (a) thrust coefficient (b) power coefficient (c) propeller efficiency.

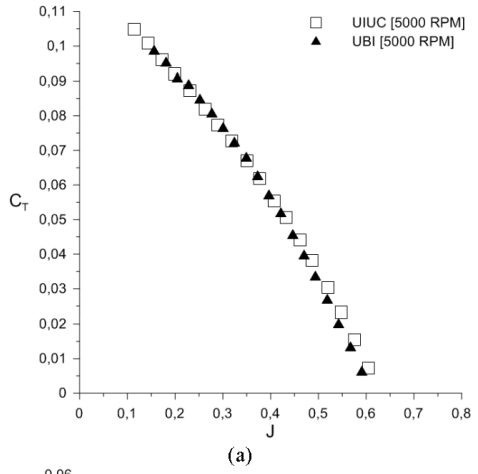

(a)

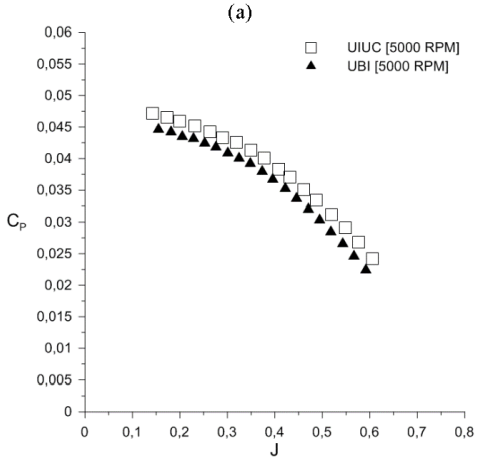

(b)

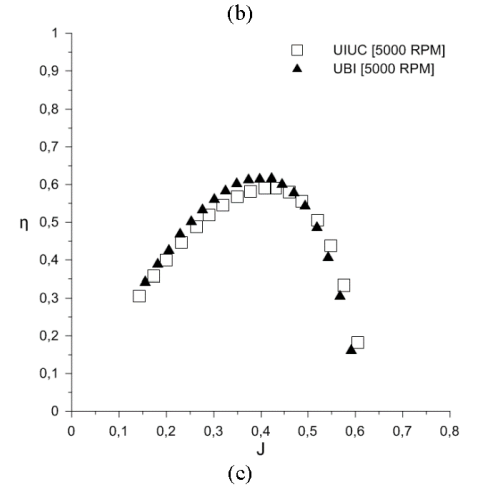

(c)

Fig. 10 APC 10"x4.7" Propeller data for 5000 *RPM*. (a) thrust coefficient (b) power coefficient (c) propeller efficiency.

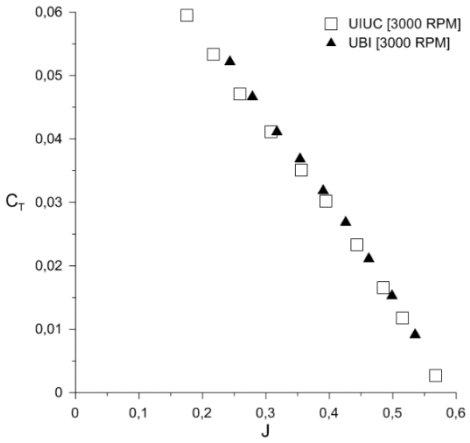

(a)

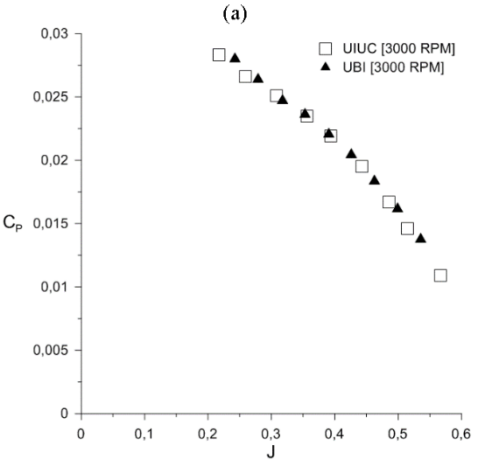

(b)

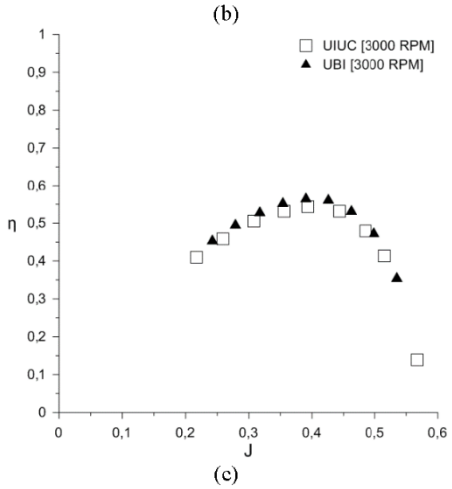

(c)

Fig. 11 APC 11"x5.5" Propeller data for 3000 *RPM*. (a) thrust coefficient (b) power coefficient (c) propeller efficiency.

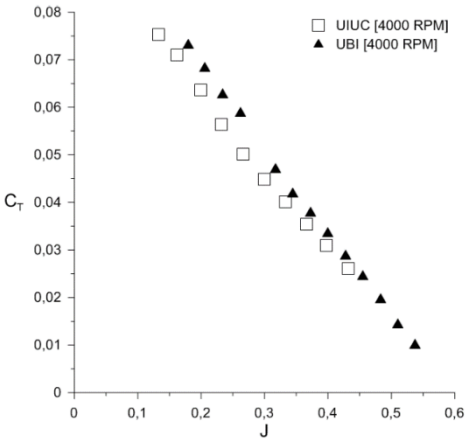

(a)

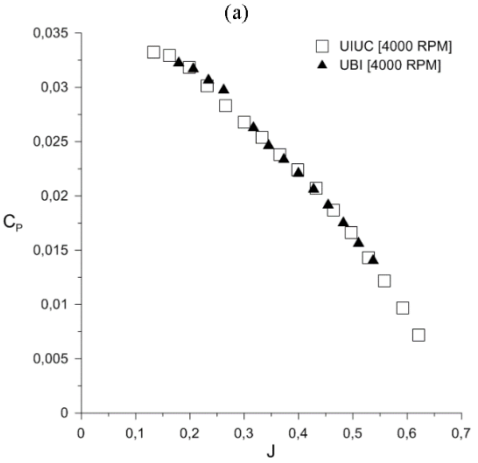

(b)

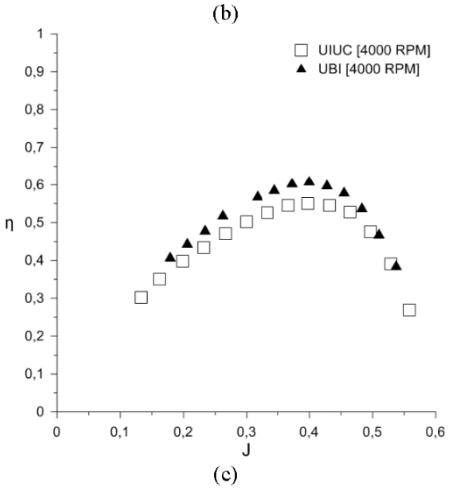

(c)

Fig. 12 APC 11"x5.5" Propeller data for 4000 *RPM*. (a) thrust coefficient (b) power coefficient (c) propeller efficiency.

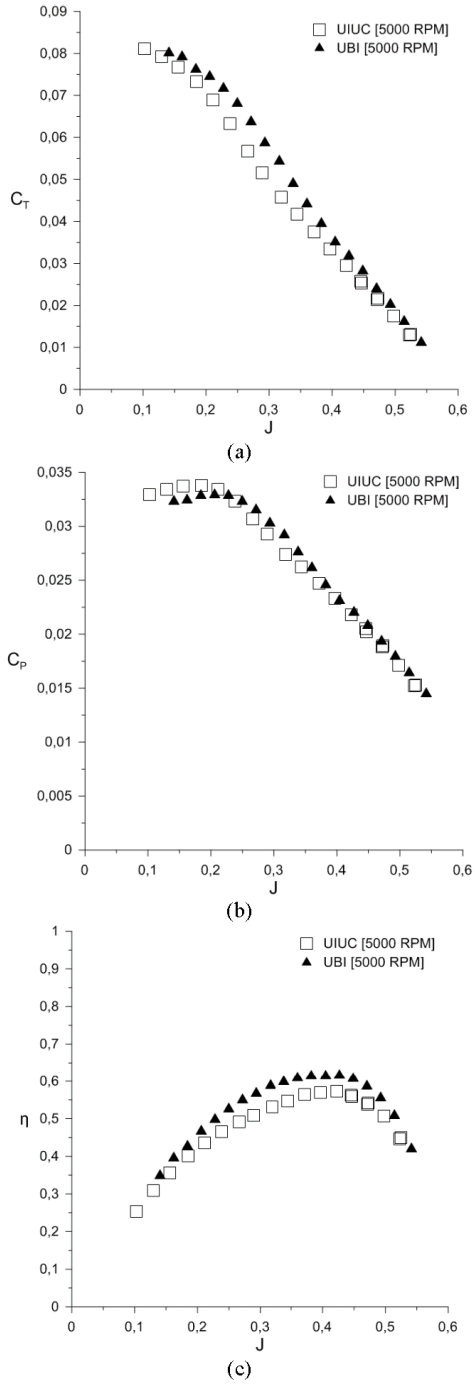

Fig. 13 APC 11"x5.5" Propeller data for 5000 *RPM*. (a) thrust coefficient (b) power coefficient (c) propeller efficiency.

Analyzing the results of the 10"x4.7" Slow Flyer propeller (see Fig. 9 and Fig. 10) it is seen that for the 4000RPM the measured thrust coefficient are slightly lower than those of UIUC, on the other hand, for 5000RPM this parameter closely matches the UIUC data points. Furthermore, for both rotational speeds UBI's coefficient of power shows a negative offset of approximately 6% comparing to UIUC. Regarding the efficiency plots for this propeller, the measured efficiency at 4000RPM was closely the same whereas for 5000RPM UBI measured a maximum higher efficiency for a slightly lower advance ratio.

Regarding the results obtained for the APC 11"x5.5" Thin Electric propeller (see Fig.11 to Fig. 13), it is possible to observe that for 3000*RPM*, the thrust coefficient from closely matches that of UIUC [28]. On the other hand, for 4000 and 5000*RPM* there is an offset on the thrust coefficient value, UBI showing a larger value. This difference is more pronounced at intermediate advance ratios. Regarding the power coefficient, the values measured by UBI are again in good agreement for 3000 and 4000*RPM* and a slight difference appears at 5000 *RPM*, with positive offset in the intermediate *J* values, gradually becoming negative towards the lower end of the advance ratio. Since the propeller efficiency is dependent on the thrust and power coefficients, the differences in thrust coefficients are also present in the propeller efficiency graph. In addition, it is possible to observe that both thrust and power coefficients increase with the increase in the propeller rotational speed. This is a typical LRN behavior and relates to the increase of the airfoil maximum lift coefficient throughout the blade at higher Reynolds number to increased rotational speed. Another airfoil characteristic that improves with the Reynolds number is the lift/drag ratio. This becomes evident observing the efficiency increase from 3000*RPM* to 5000*RPM*, where the UBI data shows a greater improvement than the UIUC data. Nevertheless, the curve trends that are a clear feature of the propeller model are alike.

The existing differences in the performance between UBI and UIUC data can be explained by the different propeller rotational speed controlling system used by UBI and UIUC. During the collecting data phase an effective rotational speed control mechanism is a key factor. There is a large coupling between the wind tunnel freestream velocity and the propeller rotational speed. So, the average propeller rotational speed value is not a representative number in terms of data accuracy in case there is significant *RPM* variance, σ. Considering the same average *RPM* value, the higher the fluctuations around the target *RPM*, the higher the power that will be consumed. As it is stated in Ref. [31], UIUC initially used a manual control of the throttle setting through the knob of a device called the ServoXciter EF. After testing this "open loop" controlling system it was observed the actual *RPM* values fluctuated up to 40 *RPM* around the target value for different freestream velocities. UBI uses a closed loop PID controller, showing maximum fluctuations of 5 *RPM* around the target *RPM* value during the data collection.

D. Propeller Performance Data

After validating the test rig, two uncatalogued propellers were tested. These propellers belong to two different UBI's Aerospace Science Department UAV projects: OLHARAPO and LEEUAV. The propeller used by OLHARAPO is a 12"x8" Aeronaut CAM Carbon Electric folding, with 3 blades. Regarding the LEEUAV, it uses a 13"x8" Aeronaut CAM Carbon Electric folding, 2-bladed propeller.

Aeronaut CAM Carbon Electric 12"x8" – 3 Blades

The results of the 3 bladed Aeronaut CAM Carbon Electric propeller are shown in Fig.14. The results show an increase in both thrust coefficient and power coefficient with an increase in the propeller *RPM*. However, since the increase in the thrust coefficient is higher than that of the power coefficient, it results in a higher propeller efficiency for higher *RPM's*. As mentioned in Section 3.3 this is due LRN detrimental effect fading away as the Reynolds number increases with the rotational speed.

The maximum efficiency of this propeller increases from about 65% for an advance ratio of 0.55 at 3000 *RPM* to 75% at an advance ratio of 0.65 and 7000 *RPM*.

Aeronaut CAM Carbon Electric 13"x8" – 2 Blades

Results for the Aeronaut Carbon Electric 13"x8" 2 bladed propeller are shown in Fig. 15. It is possible to observe an increase in the thrust coefficient with the Reynolds number, but no significant changes are visible in the power coefficient. Consequently, the thrust increase leads to the typical increase in the LRN propeller efficiency as the Reynolds number increases with propeller *RPM*.

E. Propeller Efficiency Comparison

The four propellers subjected to the performance tests presented in this work, can be divided in two categories, namely the fine pitch propellers, including the two from APC; and the coarse pitch propellers, including the two remaining Aeronaut propellers. In order to investigate the effect of the propeller pitch on the overall efficiency, two additional charts are plotted in Fig. 16 comparing the efficiency of the four propellers at 4000 RPM and 5000 RPM respectively.

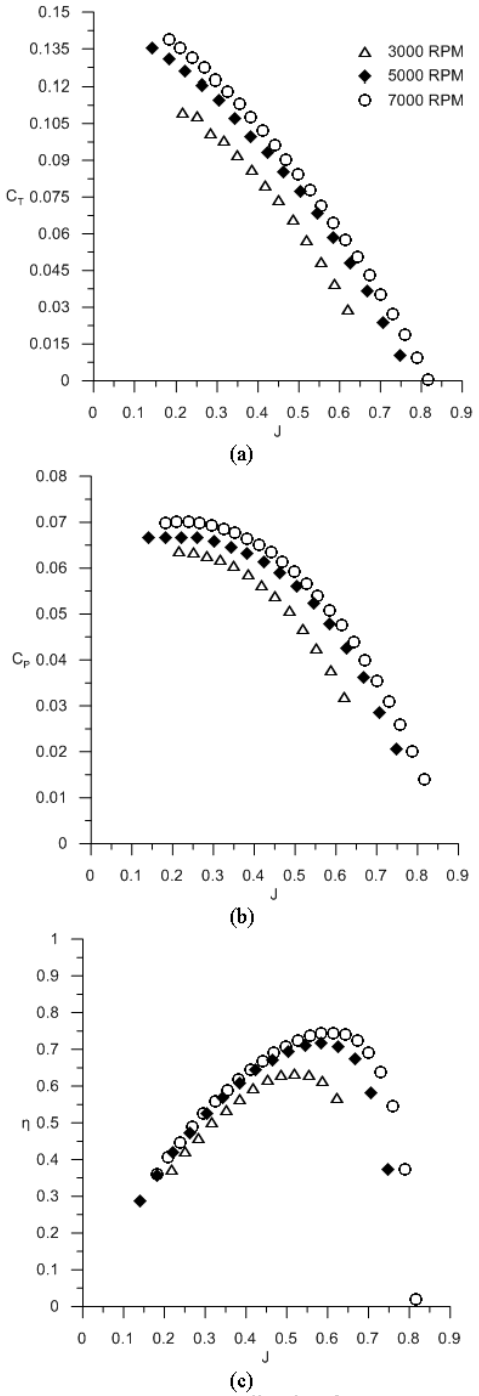

Fig. 14 Aeronaut 12x8" Propeller data for 3000 *RPM*, 5000 *RPM* and 7000 *RPM* (a) thrust coefficient (b) power coefficient (c) propeller efficiency.

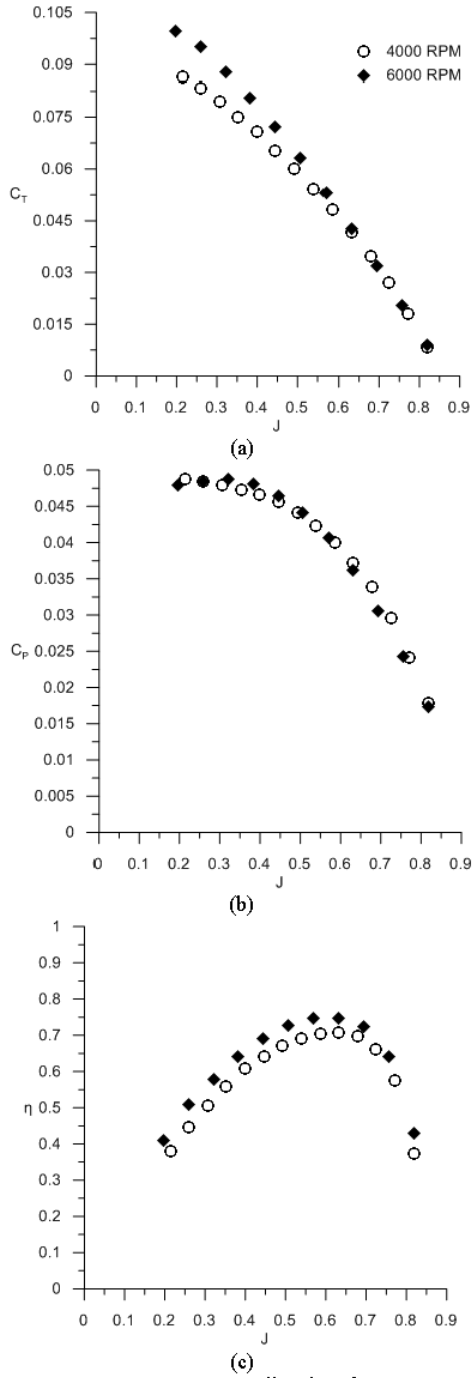

Fig. 15 Aeronaut 13"x8" Propeller data for 4000 *RPM* and 6000 *RPM* (a) thrust coefficient (b) power coefficient (c) propeller efficiency.

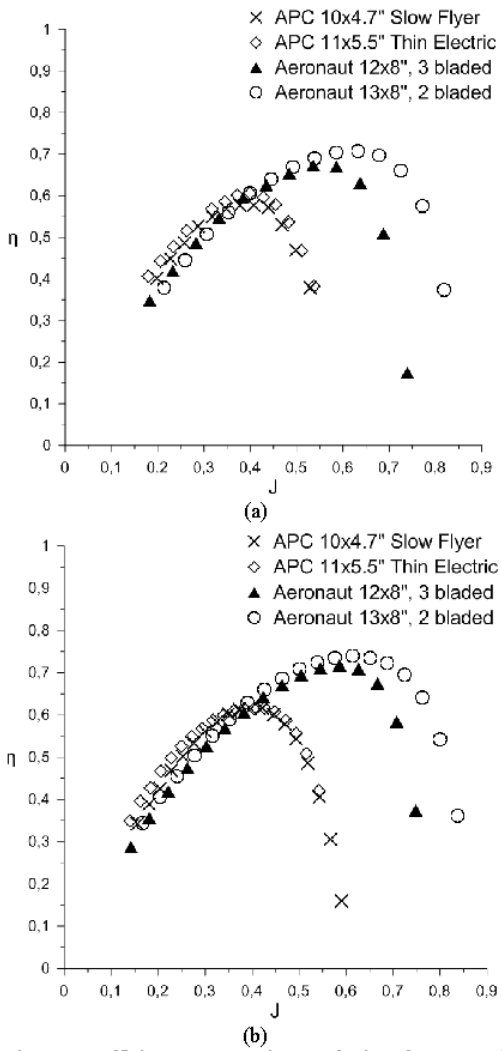

Fig. 16 Efficiency comparison of the four tested propellers. (a) 4000RPM (b) 5000RPM

Analyzing the results of the comparison between the tested propellers, it is possible to observe that:

- The two Aeronaut propellers, with their coarse pitch, have higher maximum efficiency;
- The two APC propellers shown a higher efficiency for advance ratios lower than 0.4;
- The maximum efficiency of the tested fine pitch propellers is around 60% for an advance ratio of 0.4. On the other hand, the maximum efficiency of the Aeronaut propellers is higher than 70%;
- At the maximum efficiency point of the APC propellers (*J=0.4*), there are no significant differences in the efficiency of all the tested propellers for both rotational speeds;

• Between both APC propellers, the APC 11"x5.5" Thin Electric shows to be more efficient in all presented conditions. The difference in efficiency between this two propellers appear to be more pronounced at lower RPM and may be attributed to the higher Reynolds number of the bigger propeller for a given rotational speed;

• Between both Aeronaut propellers, the 2 bladed Aeronaut 13"x8" shows to be more efficient in all presented conditions. The Aeronaut 13"x8" has a maximum efficiency of about 74% for an advance ratio of 0.6, while the 3 bladed Aeronaut 12"x8" shows a maximum efficiency of slightly above 70% for a lower advance ratio of 0.55. The difference in efficiency between this two propellers appear to be more pronounced at higher advance ratios ($J > 0.55$), this can be explained by the different number of blades between the two;

The fine pitch propellers show a smaller range of usable advance ratios (0.1 to 0.6) when compared with the coarse pitch propellers which show a wide range of operational advance ratios (0.1 to 0.85).

F. Uncertainty Analysis

The measurements error propagation begins with the primary quantities including thrust, torque, ambient pressure, ambient temperature and tunnel flow rate static ports differential pressure. The purpose of the error analysis is to determine the level of precision of the presented propeller performance results. In order to execute the analysis it was assumed that there is no error on the conversion from the sensor's voltages to the physical quantities; on the propeller diameter since it is given as a specification from the propeller manufacturer and on the wind tunnel sections dimensions since it is given as a specification from the manufacturer.7

Although the manufacturers provide this uncertainty information about the sensors, all the primary readings experience some level of fluctuations. If the fluctuations in the measurement of parameter X have a normal distribution, then 95% of the samples will fall within $\pm 2\sigma$ of the mean, so $\delta(X)=2\sigma$ can be applied [33]. The uncertainties analyzed include the wind tunnel freestream velocity, the propeller advance ratio, rotational speed, coefficients of thrust and power as well as the efficiency. A summary of the uncertainty analysis relative to the 12"x8" Aeronaut CAM Carbon folding 3-bladed propeller at 5000 *RPM* test is presented in the Table 3.

It can be noted that:

• For freestream velocities around 5-6 *m/s* interval there is an increased uncertainty in the results. By analyzing the raw data, this appears to be a result of higher fluctuations on the measurements around this velocity interval;

• For freestream velocities above 7 *m/s*, the uncertainty in this parameter is less than 1%;

• The uncertainty in C_T is typically less than 0.3%;

• The uncertainty in C_P is typically less than 0.6%;

• The uncertainty in η is typically less than 1%.

The observed uncertainties prove to be small and, as expected, they increase as the predominant primary measurement decreases such as the uncertainty in freestream velocity which increases as P_{diff} measurements decrease. This increased uncertainty can be found at the 5-6 *m/s* freestream velocity interval for all the tests.

Table 3 Aeronaut 12"x8", 3 bladed Propeller uncertainty for 5000 *RPM* data

	Uncertainty				
V'	V [%]	J [%]	C_T [%]	C_P [%]	η [%]
4	2.834	0.186	0.193	0.463	2.874
5	3.833	0.178	0.173	0.446	3.859
6	2.533	1.744	3.363	3.376	3.126
7	1.480	0.176	0.267	0.502	1.576
8	0.817	0.170	0.245	0.477	0.964
9	0.891	0.166	0.181	0.450	1.003
10	0.551	0.177	0.222	0.520	0.758
11	0.617	0.167	0.236	0.468	0.791
12	0.420	0.163	0.203	0.493	0.660
13	0.334	0.166	0.235	0.540	0.654
14	0.380	0.173	0.332	0.606	0.755
15	0.309	0.171	0.332	0.654	0.765
16	0.376	0.173	0.539	1.407	1.533
17	0.273	0.171	0.926	0.854	1.267

IV. Conclusions

This paper has presented the development and validation of a new test rig, suitable to test a wide range of low Reynolds number propellers up to a diameter of about 14".

Furthermore, the performance of two CAM Carbon Aeronaut propellers was measured over a range of propeller advance ratios for different rotational speeds.

It was shown that as the Reynolds number increases with the increase of propeller *RPM,* the propellers performance is significantly affected by increasing their thrust coefficient and efficiency.

The developed test rig can be used for several purposes, namely to improve the JBLADE Software.

Acknowledgment

The present work was performed as part of Project MAAT (Ref. No. 285602) supported by European Union through the 7th Framework Programme. Part of the work was also supported by C-MAST – Center for Mechanical and Aerospace Sciences and Technologies, Portuguese Foundation for Science and Technology Research Unit No. 151.

References

[1] Z. Zheng, W. Huo, Z. Wu, Autonomous airship path following control: Theory and experiments, *Control Engeneering Practices* Vol. 21, 2013, pp. 769–788.

[2] Q. Wang, J. Chen, G. Fu, D. Duan, An approach for shape optimization of stratosphere airships based on multidisciplinary design optimization, *Journal of*

Zhejiang University Science A. Vol. 10, 2009, pp. 1609–1616.
[3] E.H. van Eaton, Airships and the Modern Military, *U.S. Army War College*, Carlisle Barracks, 1991.
[4] L. Liao, I. Pasternak, A review of airship structural research and development, *Progress in Aerospace Sciences* Vol. 45, No. 4, 2009, pp. 83–96.
[5] J. Morgado, M.Â.R. Silvestre, J.C. Páscoa, Parametric Study of a High Altitude Airship According to the Multi-Body Concept for Advanced Airship Transport - MAAT, in: *IV Conferência Nacional em Mecânica Dos Fluidos, Termodinâmica e Energ*ia, Lisbon, 2012.
[6] Y.-G. Lee, D.-M. Kim, C.-H. Yeom, Development of Korean High Altitude Platform Systems, *International Journal of Wireless and Informatics and Networks*. Vol. 13, 2005, pp. 31–42.
[7] M.S. Smith, E.L. Rainwater, Applications of Scientific Ballooning Technology to High Altitude Airships, in: AIAA's *3rd Annual Aviation Technology Integration Operations and Technology Forum*, Denver, 1971: pp. 1–8.
[8] P. Martin, A. Milan., 2010, Switching Power Supply Unit For An Autonomous Monitoring System, WSEAS TRANSACTIONS on CIRCUITS and SYSTEMS, Issue 10, Vol. 9.
[9] A. Dumas, M. Trancossi, M. Madonia, I. Giuliani, Multibody Advanced Airship for Transport, in: *Society of Automotive Engineers Technical Paper* 2011-01-2786, 2011.
[10] G. Ilieva, J.C. Páscoa, A. Dumas, M. Trancossi, A critical review of propulsion concepts for modern airships, *Central European Journal of Engineering*. Vol. 2, 2012, pp. 189–200.
[11] Lockheed Martin, High Altitude Airship (HAA) *Persistent Communications and ISR for the Joint Warfighter Partnering to Meet Customers' Defining Moments*, Defense.
[12] A. Colozza, B. Park, Initial Feasibility Assessment of a High Altitude Long Endurance Airship, 2003.
[13] A.C. Gawale, R.S. Pant, Initial Sizing and Sensitivity Analyses of Stratospheric Airships for Psuedolite Based Precision Navigation System, in: *5th ATIO and 16th Lighter-Than-Air Systems Technologies and Balloon Systems Conference*, American Institute of Aeronautics and Astronautics, Arlington, 2000, pp. 1–15.
[14] Egrett II Brochure, E-Systems GreenVille Division, 1991
[15] A. Colozza, High Altitude Propeller Design and Analysis Overview, *Technical Report* Cleveland, 1998.
[16] Merlin, P. W., "Crash Course - Lessons Learned from Accidents Involving Remotely Piloted and Autonomous Aircraft", *Monographs in Aerospace History #44,* National Aeronautics and Space Administration, 2013.
[17] M.A. Silvestre, J.P. Morgado, J. Pascoa, JBLADE: a Propeller Design and Analysis Code, *2013 International Powered Lift Conference*, American Institute of Aeronautics and Astronautics, Reston, Virginia, 2013.
[18] J. Morgado, M.A.R. Silvestre, J.C. Páscoa, Validation of New Formulations for Propeller Analysis, Journal of Propulsion and Power. DOI: 10.2514/1.B35240
[19] Drela, M., "XFOIL - An Analysis and Design System for Low Reynolds Number Airfoils", *Proceedings of Low Reynolds Number Aerodynamics*, Berlin, Vol. 54, 1989, pp. 1–12.
[20] Prasetyo Edi, Nukman Yusoff, Aznijar Ahmad Yazid, 2008, The Design Improvement of Airfoil for Flying Wing UAV, WSEAS TRANSACTIONS on APPLIED and THEORETICAL MECHANICS, Issue 9, Vol. 3.
[21] M.S. Selig, Low Reynolds Number Airfoil Design Lecture Notes, *Von Kármán Institute,* 2003.
[22] T. Theodorsen, G.W. Stickle, M.J. Brevoort, Caracteristics of Six Propellers Including the High-Speed Range, *NACA Technical Report No. 594*, Langley, 1937.
[23] W. Gray, Wind-Tunnel Tests of Two Hamilton Standard Propellers Embodying Clark Y and Naca 16-Series Blade Sections, *NACA Technical Report No. 530*, Washington, 1941.
[24] Prasetyo Edi, Khairi Yusuf, Amir Radzi, Abdul Ghani, Hakim S. Sultan Aljibori., 2009, The Design of Light Jet Aircraft, WSEAS TRANSACTIONS on APPLIED and THEORETICAL MECHANICS, Issue 2, Vol. 4.
[25] R.W. Deters, G.K. Ananda, M.S. Selig, Reynolds Number Effects on the Performance of Small-Scale Propellers, *Procedings of 32nd AIAA Applied Aerodynamics Conference, A*merican Institute of Aeronautics and Astronautics, Atlanta, 2014.
[26] J.B. Brandt, M.S. Selig, Propeller Performance Data at Low Reynolds Numbers, (2011) 1–18.
[27] O.R. Shetty, M.S. Selig, Small-Scale Propellers Operating in the Vortex Ring State, in: 49th AIAA Aerosp. Sci. Meet. Incl. New Horizons Forum Aerosp. Expo., Orlando, Florida, 2011: pp. 1–16.
[28] Ananda, G., UIUC Propeller Database, Aerospace Engineering, *University of Illinois Champaign*, IL, http://aerospace.illinois .edu/m-selig/props/propDB.html [retrieved 25 September 2014].
[29] H. Glauert, Wind Tunnel Interference on Wings, Bodies, and Airscrews, 1933.
[30] A. Pope, J. Barlow, W. H. Rae, LOW-SPEED WIND TUNNEL TESTING, 1999.
[31] J.B. Brandt, SMALL-SCALE PROPELLER PERFORMANCE AT LOW SPEEDS, 2005.
[32] M.S. Selig, G. Ananda, Low Reynolds Number Propeller Perfomance Data : Wind Tunnel Corrections for Motor Fixture Drag, 2011.
[33] Hallauer W. L. Jr. and Devenport W. J., 2006, AOE 3054 Experimental Methods Course Manual. Experimental Error, A.O.E. Department, Virginia Tech. Blacksburg VA.

This page has been intentionally left blank
for double side copying

B.III – A Comparison of Post-Stall Models Extended for Propeller Performance Prediction

A Comparison of Post-Stall Models Extended for Propeller Performance Prediction

Abstract

Purpose – The purpose of the paper is to analyse different post-stall models, originally developed for use in wind turbine codes, and extend their use to the propeller performance prediction.
Design/methodology/approach – Different post-stall methods available in the literature were implemented in JBLADE Software. JBLADE contains an improved version of Blade Element Momentum (BEM) theory and it is appropriate for the design and analysis of different propellers in off-design conditions.
Findings – The preliminary analysis of the results shows that the propeller performance prediction can be improved using these implemented post-stall models. However, there is a lack of accuracy in the performance prediction of some propellers. Further comparisons including forces distribution along the blade may help to better understand this inaccuracy of the models and it will be studied on future work.
Originality/value – The work has extended the use of the post-stall models to the propeller performance prediction codes. It is shown that these models can be used to obtain an improved prediction of the propeller's performance.

Keywords JBLADE Software; Propeller Performance Prediction; Post-Stall Models Comparison;

Paper type Research paper.

Introduction

The Multibody Advanced Airship for Transportation (MAAT) project (Dumas et al. 2011; Dumas 2011) aims to investigate the possibility of a new global transport model which integrates next-generation airports, for transport of people and goods. Furthermore, new methods of airship's control (Pshikhopov, V. et al 2012 (a); Pshikhopov, V. et al 2012 (b); Pshikhopov, V. et al 2012 (c)) are being developed due to the complex shape and operation of the MAAT airships. The MAAT system is composed by three different modules: cruiser, feeder and the airport. The airport, named AHA (Airship Hub Airport) is a new concept that allows the loading and unloading of passengers and goods from ground to the feeder. The smaller airship, named Aerial Transport Elevator Network feeder (ATEN) (Dumas et al. 2012, Ilieva et al. 2015), should be capable to perform vertical take-off and landing and it will ensure the connection between the ground airports and the Photovoltaic Transport Aerial High altitude system (PTAH). ATEN can travel up and down changing its buoyancy and should be capable to move horizontally to join to the cruiser (Ceruti & Marzocca 2012). The bigger airship, PTAH, will travel mostly in horizontal paths at an altitude about 16 km, reducing the time needed to load/unload passengers and goods. Electrical propulsion systems are being studied (Smith et al. 2013) to overcome the problems related with the altitude. This airship (PTAH) is conceived to be a real logistic centre (Dumas et al. 2014), on which passengers and goods will change from one feeder to another (Vucinic et al. 2013), depending on their destination. Since PTAH will be mainly operated at stratospheric altitudes, propellers are a valid option to the airships' propulsion (Ilieva et al. 2012). However, at this altitude traditional propellers decrease their efficiency due to the atmosphere properties, requiring the development of new tools suitable for design and analyse propellers which will operate at these high altitudes. Design and optimization of propellers for such high altitude can be difficult (Monk 2002), making crucial the development of a new appropriate numerical tool.
One way to achieve an optimized propeller is comparing different designs and select the one with biggest relative merit. In order to perform these comparisons it is needed a low computational cost, but accurate numerical tool (Sarakinos et al. 2007; Koini et al. 2009; Wang 2014).
Although Blade Element Momentum (BEM) codes can be used to predict the propeller performance, this method has some limitations when the airfoil is stalled which happens mostly at low advance ratios. The accuracy of these codes is dependent on the input of the airfoil performance characteristics. Typically, BEM codes use two dimensional (2D) estimations to calculate the propeller performance. However, experimentally measured airfoil characteristics on rotating blades have found that these coefficients are significantly changed by three-dimensional (3D) effects. Therefore, a number of studies and methodologies have been developed to manage the post-stall effects mainly in the wind turbine industry (Tangler & Kocurek 2005). For propeller purposes there are some studies (Aviv & Gur 2005; Uhlig & Selig 2008) only presenting the effect of a specific post-stall model, however, there are no comparisons between the different post-

stall models for propeller performance analysis. In this paper, different post-stall models available on the literature (Snel et al. 1994; Du & Selig 1998; Dumitrescu & Cardos 2007; Chaviaropoulos & Hansen 2000; Corrigan & Schillings 1994) were implemented in a BEM Software and their ability to improve the propeller performance predictions was evaluated.

JBLADE Software

JBLADE (Silvestre et al. 2013; Morgado et al. 2013) is being developed as a numerical open-source propeller design and analysis tool written in the C++/QML programming language, compiled with Qt toolkit (Digia 2014). The software is based on QBlade (Marten et al. 2013; Marten & Wendler 2013) and XFLR5 (Deperrois 2011). JBLADE uses the classical Blade Element Momentum (BEM) theory modified to account for three dimensional flow equilibrium (Silvestre et al. 2013). The software has the capability to estimate the performance curves of a given propeller for off-design condition. The graphical user interface (GUI) makes easier to design and analyse the propeller simulations and helps the user to detect physical inconsistencies or minor mistakes in propeller's blade. Figure 1 shows the JBLADE code structure with the different sub-modules and their iteration routines in which the airfoil polars, blades, propellers and simulations are defined, executed and stored. Furthermore, it can be seen how the BEM module is coupled with XFOIL (Drela 1989) module.

Figure 1 JBLADE software structure representing the internal sub-modules interaction.

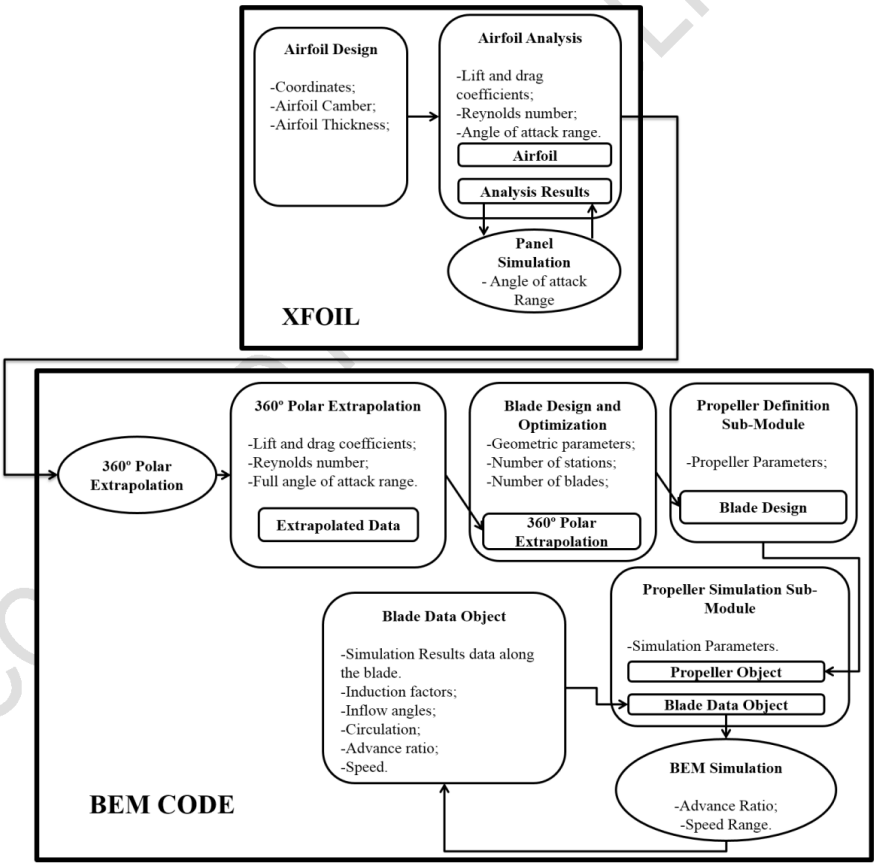

Airfoil Design and Analysis

To perform a propeller design or analysis it is necessary to import the needed airfoils which will be used along the blades sections. The airfoil performance data needed for the blades simulation come from original QBLADE's coupling with the XFOIL (Drela 1989) code through a direct analysis for each airfoil. Depending on the number of the points of imported airfoil, a global refinement of the airfoil's panels may be necessary to ensure good convergence during the airfoil analysis. Furthermore, the XFOIL sub-module allows the modifications of the airfoils by changing the airfoil thickness and its position as well as airfoil camber and its position. These analyses should be performed over the largest angle of attack range. In order to obtain accurate results with JBLADE it is essential that the correct Reynolds and Mach numbers are defined in the airfoil simulations. The achievement of correct Reynolds and Mach numbers along the blade may take some iteration until the propeller analysis process is finished. The data obtained in this sub-module will be used in the 360º Polar Extrapolation sub-module, where a full 360º range of angle of attack airfoil polar for each blade section airfoil will be built.

360º Polar Extrapolation

Similarly to the wind turbines, propellers may also achieve high angles of attack. In this sub-module the data previously calculated for each airfoil is extended to the full range of angle of attack. As referred by Montgomerie (1996) one of the key aspects during extrapolation process is the value of the drag coefficient at 90º of angle of attack. Different values of drag coefficient at 90º of angle of attack may lead to different extrapolated airfoil polars, which in turn, will lead to different final results. Originally, the method described by Montgmorie (2004) was used in JBLADE, but the extrapolation process was improved leading to a decrease of the errors introduced by the user. The value of the drag coefficient at 90 º is calculated according the correlation (Morgado et al. 2013) presented in Eqn (1):

$$C_{D_{90}} = 2.0772 - 3.978R_{LE} \tag{1}$$

Furthermore, a second method is also available in JBLADE for full 360º polars extrapolation. According to this method, the airfoil *y* coordinate at *x/c*=0.0125 was correlated with the airfoil C_{D90}, resulting in Eqn (2):

$$C_{D_{90}} = 2.086 - 4.6313(y/c)_{0.0125} \tag{2}$$

The airfoil polars used in this work were extrapolated using the method described in Eqn (1).
Blade Definition

The JBLADE software allows the introduction of the blade geometry as an arbitrary number of sections characterized by their radial position, chord, twist, airfoil and airfoil's associated polar. The user should specify the number of blades and the hub radius of the propeller. The software provides a 3D graphical representation of the blade/propeller to the user, helping the user to identify possible conflicts. In addition, JBLADE Software contains an inverse design methodology in which the user should specify the operating condition of the propeller, namely propeller's operating air density the free stream speed, the propeller rotational speed and the power (or torque) delivered to the propeller or thrust delivered by the propeller. After the introduction of previous mentioned parameters, the blade geometry is achieved.

Propeller Definition and Simulation

In the propeller definition and simulation sub-module the user can create new propellers composed by the previously defined blades. This sub-module allows simulations within a speed interval, for a fixed rotational speed and fixed pitch angle. To create and perform a simulation for a given propeller, the user should specify the number of elements along the blade, the convergence criteria, the density and viscosity of the fluid and maximum number of iterations (see Figure 2).

Figure 2 Simulation sub-module in JBLADE Software.

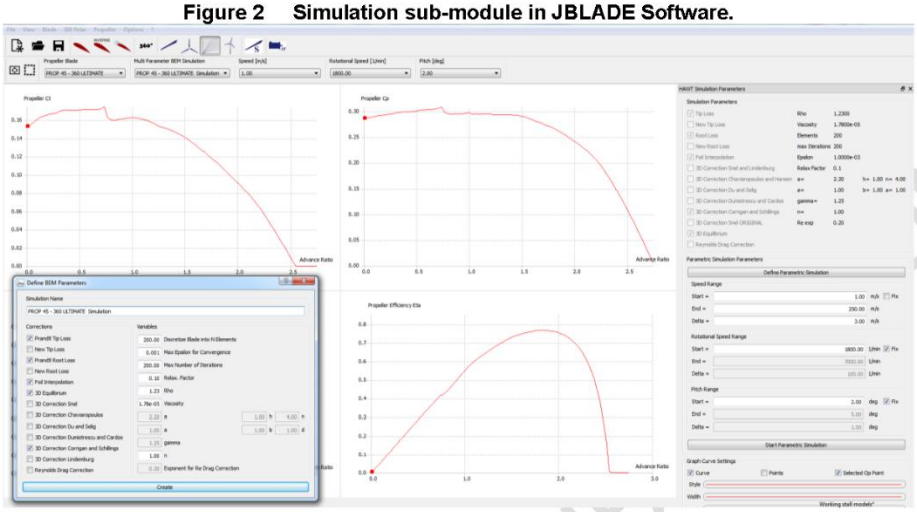

The propeller performance estimation is obtained with a BEM simulation routine (see Figure 3) and stored in the blade data object for each element along the blade. Furthermore, the user can improve the accuracy of the simulations using other tools also available in the JBLADE software such as: Root and Tip Losses, Post Stall Models, Foil Interpolation, 3D Equilibrium and Reynolds Drag Correction (Silvestre et al. 2013; Marten & Wendler 2013). When 3D Equilibrium formulation is enabled there is an additional layer of iterations in which $a_t = 0$. After solving that additional iteration procedure as described by Silvestre *et al.* (2013), the radial induction factor can be updated and the coefficients will be calculated again with the updated radial induction factor.

Figure 3 Flowchart of simulation procedure in JBLADE.

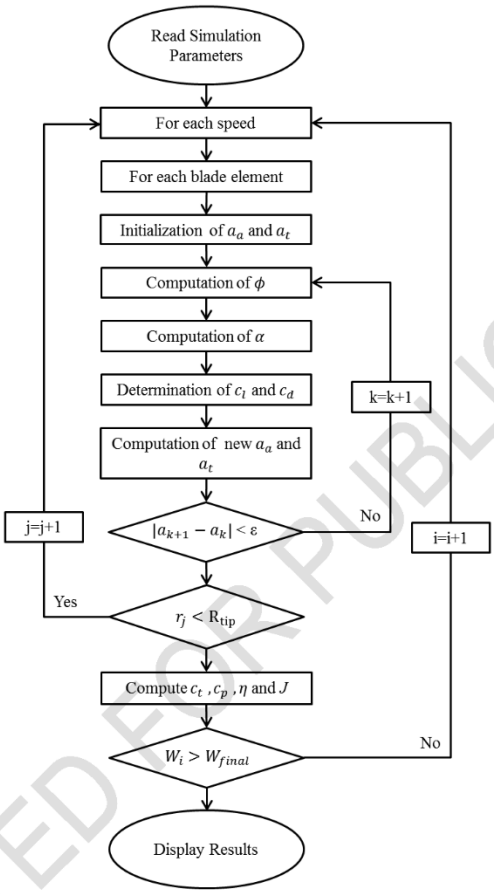

Post-Stall Models

The rotational motion of the blade affects the element's boundary layer such that the airfoil stall shifts to higher angles of attack. In order to complement the available tools in JBLADE, and make the predictions more accurate, some models to correct the airfoil characteristics after stall were implemented. Excluding the model developed by Corrigan & Schillings (1994), the corrections in the lift and drag coefficients were implemented as presented in Eqn (3) and Eqn (4):

$$c_{l_{3D}} = c_{l_{2D}} + g_{c_l} \Delta c_l \tag{3}$$

$$c_{d_{3D}} = c_{d_{2D}} + g_{c_d} \Delta c_d \tag{4}$$

Where g_{cl} and g_{cd} are the functions associated with each model, while Δc_l and Δc_d represents the difference between the obtained lift and drag coefficients in case of no separation occurs. The remaining $c_{l_{2D}}$ and $c_{d_{2D}}$ are the coefficients measured or calculated for 2D airfoil configuration.

Snel *et.al* Model

The model developed by Snel et al. (1994) emerged from the solution of a simplified form of the 3D boundary layer equations on a rotating blade presented in Eqn (5):

$$g_{c_l} = 3\left(\frac{c}{r}\right)^2 \tag{5}$$

This model only changes the lift coefficient, while 2D airfoil drag coefficient is maintained unchanged.

Du and Selig

This model (Du & Selig 1998) is an extension of the work done by Snel *et al.* (1994) which accounts also for changes in drag coefficient due to the rotation of the blade. The two dimensional coefficients are modified as presented in Eqn (6) and Eqn (7):

$$g_{c_l} = \frac{1}{2\pi}\left[\frac{1.6(c/r)a - (c/r)^{\frac{d}{\Lambda}\frac{R}{r}}}{0.1267b - (c/r)^{\frac{d}{\Lambda}\frac{R}{r}}} - 1\right] \tag{6}$$

$$g_{c_d} = \frac{1}{2\pi}\left[\frac{1.6(c/r)a - (c/r)^{\frac{d}{2\Lambda}\frac{R}{r}}}{0.1267b - (c/r)^{\frac{d}{\Lambda}\frac{R}{r}}} - 1\right] \tag{7}$$

Where:

$$\Lambda = \frac{\Omega R}{\sqrt{W^2 + (\Omega R)^2}} \tag{8}$$

In their original work, Du and Selig kept the constants *a=b=d=1*. The same values of *a*, *b* and *d* were used herein. Although it is possible to change the values of these constants in JBLADE, the user should have some knowledge about their possible values.

Dumistrecu and Cardos Model

The model proposed by Dumistrescu and Cardos (2007) presents a correction in lift coefficient. Similarly to the work of Snel *et al.* (1994) the function to correct the lift coefficient due to blade rotation came from analysis of the momentum equations for the three dimensional boundary layer.

$$g_{c_l} = 1 - \exp\left(-\frac{\gamma}{(r/c)-1}\right) \tag{9}$$

The correction presented in equation (9) assumes a viscous decay of the vortex lift in the spanwise direction. The authors concluded that the best comparisons with experimental data occurs for *γ=1.25*. The same value of *γ=1.25* is used in this study as well.

Chaviaropoulos and Hansen Model

The model presented by Chaviaropoulos & Hansen (2000) uses a system of simplified equations which were obtained by the integration of the three dimensional incompressible Navier-Stokes equations in the radial direction of the blade. This method was extended in order to account with the influence of the blade's twist.

$$g_{c_l} = a\left(\frac{c}{r}\right)^h \cos^n(\theta) \tag{10}$$

$$g_{c_d} = a\left(\frac{c}{r}\right)^h \cos^n(\theta) \tag{11}$$

The values used in the original work which best compare with the experimental data (Bouatem & Mers 2013) are: $a = 2.2, h = 1$ and $n = 4$ whereby the same values were used in the present simulations.

Corrigan and Schillings

The model developed by Corrigan and Schillings(Corrigan & Schillings 1994) correlates the stall delay to the ratio of the local blade chord to radial position. The authors analysed the pressure gradients in the boundary layer and combining it with the work of Banks & Gadd (ç1963) developed the correction function for the lift coefficient presented in Eqn (12):

$$c_{l\,rot} = c_{l\,non\_rot}\left(\frac{dc_{l_{pot}}}{d\alpha}\Delta\alpha\right) \tag{12}$$

The function is expressed as a shift in the angle of attack as presented in Eqn (13):

$$\Delta\alpha = \left[\left(\frac{K\left(\frac{c}{r}\right)}{0.136}\right)^n - 1\right]\left(\alpha_{C_{L_{max}}} - \alpha_{C_{L_0}}\right) \tag{13}$$

and the separation point is related with the velocity gradient, *K* through Eqn (14):

$$\left(\frac{c}{r}\right) = 0.1517K^{-1.084} \tag{14}$$

The authors recommend use a *n* value within 0.8 and 1.6. The value *n*=1 proved to give good results for different comparisons with experimental data (Corrigan & Schillings 1994). The same value of *n=1* was used along this work.

Results and Discussion

To verify the reliability of JBLADE software in predicting different propeller performance operating at different Reynolds number ranges the data from both numerical codes and experimental works were compared with JBLADE predictions in order to obtain the validation as complete as possible.

Adkins and Liebeck Propeller

The propeller presented by Adkins and Liebeck was analysed with JBLADE and the performance predictions were compared with the data found on the literature (Adkins & Liebeck 1994). The propeller has 2 blades and a diameter of 1.75 meters. The blade geometry (see Figure 4) was replicated inside JBLADE and analysed in off-design condition. This analysis was performed with JBLADE and compared with the numerical code of Adkins & Liebeck (1994).

Figure 4 Propeller geometry (Adkins & Liebeck 1994). The propeller has 2 blades and a diameter of 1.75meters.

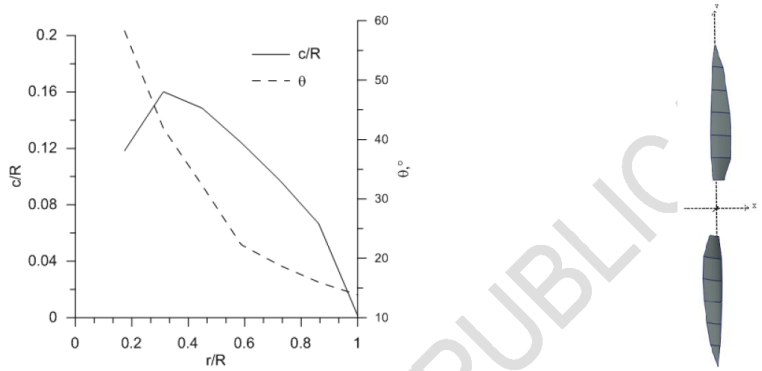

The agreement between JBLADE and Adkins & Liebeck code as it is shown in Figure 5 is good. The differences between both codes in the low advance ratio region come from the different approximation to the airfoil characteristics calculations done by different codes. The difference at Figure 5 (c) in the low advance region is a result of the different behaviour on thrust coefficient shown at Figure 5 (a).

Figure 5 Comparison between data predicted by JBLADE and data obtained from Adkins & Liebeck (1994). (a) thrust coefficient (b) power coefficient (c) propeller efficiency.

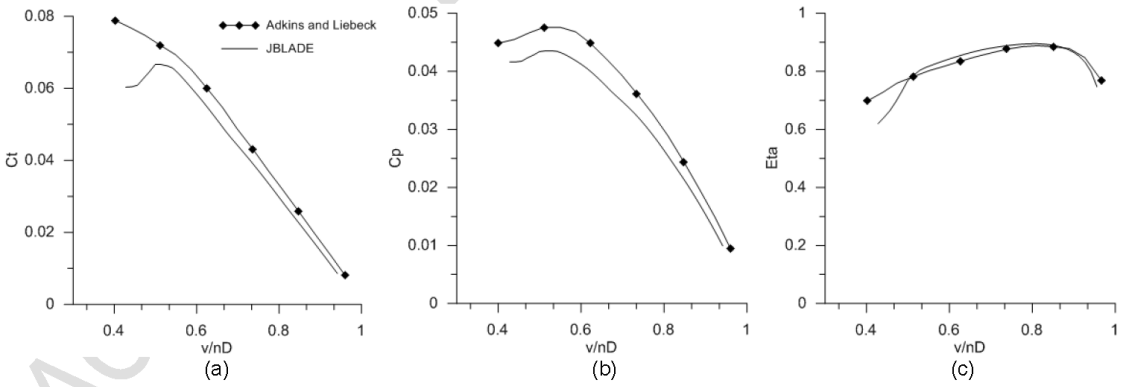

APC 10"x7" Propeller

An APC 10"x7" propeller was used to validate JBLADE for low Reynolds number predictions. The propeller was replicated according to the data (UIUC 2014). Figure 6 shows the chord and twist angle distribution along the blade radius.

Figure 6 APC 10"x7" propeller geometry (UIUC 2014). The propeller has 2 blades and a diameter of 0.254 meters.

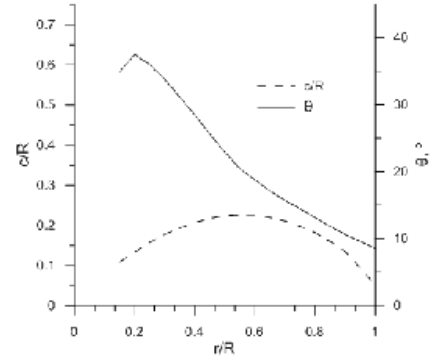

The comparison of the JBLADE's simulation against experimental data (UIUC 2014) is presented in Figure 7 and it is possible to observe that the simulation closely follows the measured thrust coefficient for high values of advance ratio. Regarding the power coefficient, the simulation gives close results at low advance ratio and the difference with the experiment increases moderately with the advance ratio. The highest values of the propeller efficiency, around 0.6, was also correctly predicted, as well as the advance ratio at which it occurs.

Figure 7 Comparison between data predicted by JBLADE and data obtained from UIUC database (UIUC 2014). (a) thrust coefficient (b) power coefficient (c) propeller efficiency.

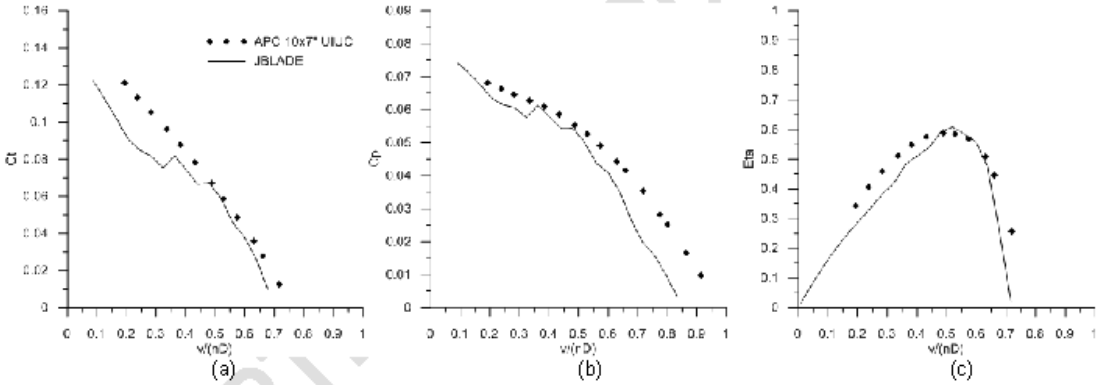

Post-Stall Models Comparison

To study the influence of different post-stall models in the propeller performance prediction, the propeller described in NACA Technical Report No. 594 (Theodorsen et al. 1937) was simulated using the above described formulation. This propeller corresponds to the configuration named "Nose 6 – Propeller C" and it has 3 blades and a diameter of 3.054 m (see Figure 8)

Figure 8 Propeller geometry presented in NACA Technical Report No. 594 (Theodorsen et al. 1937) and its shape after introduced in JBLADE. The propeller has 3 blades and a diameter of 3.054 meters.

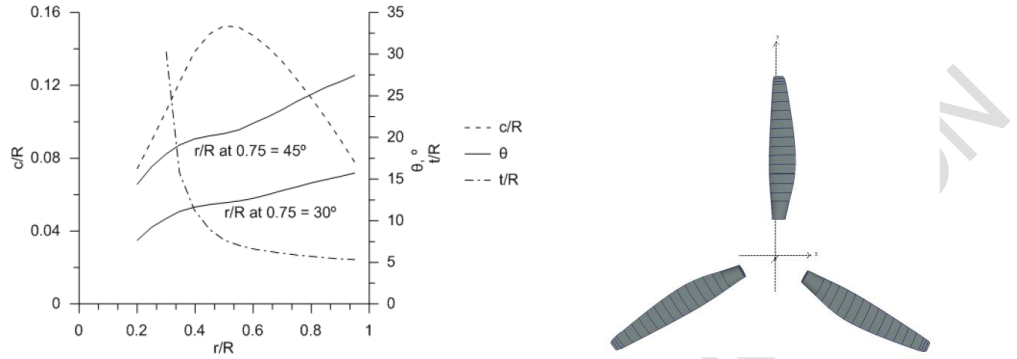

Figure 9 (a) shows that all the implemented models improve the thrust coefficient prediction when compared with a simulation in which no post-stall was used (Original BEM curve). The models show small discrepancies between the experimental and predicted thrust coefficient. Figure 9 (b) shows the effect of the post-stall models in the power coefficient prediction. Contrary to the thrust coefficients prediction, the power coefficient is significantly under predicted, even with the post-stall models correction. For both, thrust coefficient and power coefficient it is shown that the effect of the post-stall models is more pronounced on the low advance ratios regions. It was found that for this case the model developed by Corrigan and Schillings (Corrigan & Schillings 1994) performs best over the range of conditions studied, but still exhibited some limitations, especially in power coefficient prediction as mentioned.

Figure 9 Comparison between JBLADE predictions using different post-stall models and data from NACA TR No. 594 (Theodorsen et al. 1937) for $\theta_{75} = 30^o$. (a) thrust coefficient (b) power coefficient (c) propeller efficiency.

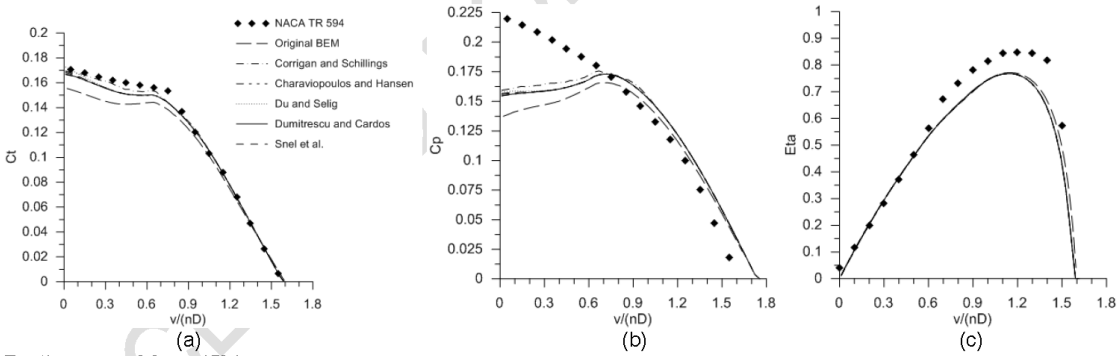

For the case of $\theta_{75} = 45^o$ (see

Figure 10 (a) to (c)), different models are predicting significantly different thrust coefficients. It happens since each model changes the lift coefficient in a different way and as higher the angle of attack, higher the differences on the lift coefficient at each blade's section. Besides the Dumitrescu & Cardos (2007) and Corrigan & Schillings (1994) models, the other post-stall models tend to overestimate the thrust coefficient(see Figure 10 (a)). The difference seen at low advance region on Figure 9 (b) and on Figure 10 (b) for all the predictions is very interesting, since it does not depend on the used model of post-stall since they do not improve the calculations in a considerable way at these advance ratios. It is clear that the analysed post-stall models fail to consistently improve the power coefficient prediction.

Figure 10 Comparison between JBLADE predictions using different post-stall models and data from NACA TR No. 594 (Theodorsen et al. 1937) for $\theta_{75} = 45^{o}$. (a) thrust coefficient (b) power coefficient (c) propeller efficiency.

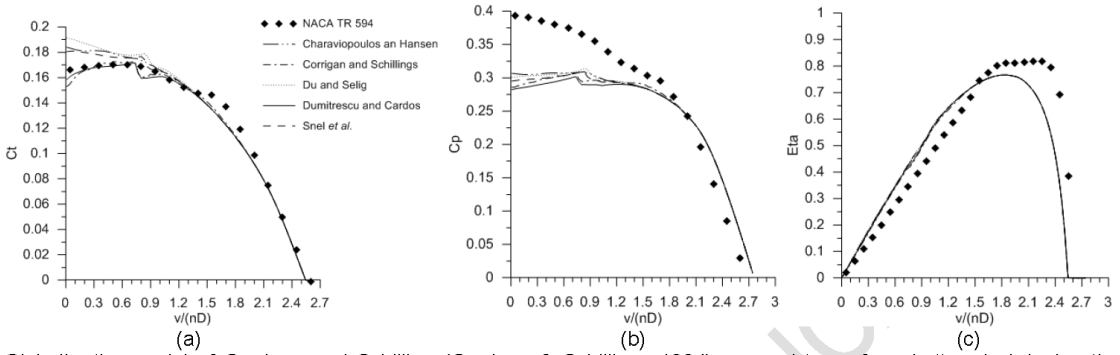

Globally, the model of Corrigan and Schillings(Corrigan & Schillings 1994) seemed to perform better in bringing the predictions closer to the test data when compared with other models. In general, the post-stall models have shown their ability to improve the performance prediction mostly in the thrust coefficient. The power coefficient is still significantly under predicted at low advance ratios. Further comparisons comprising forces distributions along the blade may help to better understand the lack of accuracy of the models and it will be the subject of future work.

Conclusion

This paper has presented JBLADE software which proved to be suitable for different propeller design and analysis. In addition, different propellers were analysed as a validation for the BEM formulation of JBLADE. Different validation cases have shown that the performance prediction done by JBLADE is in good agreement with both numerical and experimental data. Different post-stall models originally developed for wind turbines were herein extended to propeller performance predictions. They were implemented and compared with experimental data, and it was shown that they can improve the predictions of the propeller performance done by JBLADE software. However, some further work needs to be done. All the models implemented during this work are available in the JBLADE Software allowing the user to choose the most suitable method. In addition, the values of the original constants can be modified, although as mentioned above, the user should have some knowledge about the possible values of the constants. It was shown that JBLADE can be used as a tool for design and optimize the PTAH airship propellers since it was validated for analysing propellers operating at low Reynolds conditions, as it will occur at stratospheric altitudes.

Acknowledgments

The present work was performed as part of Project MAAT (Ref. No. 285602) supported by European Union through the 7th Framework Programme. Part of the work was also supported by both C-MAST - Center for Mechanical and Aerospace Sciences and Technologies, Portuguese Foundation for Science and Technology Research Unit No. 151.

References

Adkins, C.N. & Liebeck, R.H., 1994. Design of optimum propellers. Journal of Propulsion and Power, 10(5), pp.676–682. Available at: http://arc.aiaa.org/doi/abs/10.2514/3.23779

Aviv, R. & Gur, O., 2005. Propeller Performance at Low Advance Ratio. Journal of Aircraft, 42(2), pp.435–441. Available at: http://arc.aiaa.org/doi/abs/10.2514/1.6564

Banks, W.H.H. & Gadd, G.E., 1963. Delaying Effect of Rotation on Laminar Separation. AIAA Journal, (1), pp.941–942.

Bouatem, A. & Mers, A., 2013. Validation of Chaviaro Poulos and Hansen Stall Delay Model in the Case of Horizontal Axis Wind Turbine Operating in Yaw Conditions. Energy and Power Engineering, 05(01), pp.18–25. Available at: http://www.scirp.org/journal/PaperDownload.aspx?DOI=10.4236/epe.2013.51003

Ceruti, A. Marzzoca, P., 2012. Airship Research and Development in the Areas of Design, Structures, Dynamics and Energy Systems, Casey Stockbridge" International Journal of Aeronautical and Space Sciences, 13 (2), The Korean Society for Aeronautical & Space Sciences, Seoul, Korea, 01/06/2012, pp. 170–187, DOI:10.5139/IJASS.2012.13.2.170

Chaviaropoulos, P.K. & Hansen, M.O.L., 2000. Investigating Three-Dimensional and Rotational Effects on Wind Turbine Blades by Means of a Quasi-3D Navier Stokes Solver. Journal of Fluids Engineering, (122), pp.330–336.

Corrigan, J. & Schillings, J., 1994. Empirical Model for Blade Stall Delay Due to Rotation. In American Helicopter Society Aeromechanics Specialists. San Francisco.

Deperrois, A., 2011. Analysis of Foils and Wings Operating at Low Reynolds Numbers - Guidelines for XFLR5 v6.03, Digia, 2014. Qt Project. Available at: http://qt-project.org/ [Accessed February 18, 2014].

Drela, M., 1989. XFOIL - An Analysis and Design System for Low Reynolds Number Airfoils.pdf. In T. J. Mueller, ed. Low Reynolds Number Aerodynamics. Berlin: Springer-Velag, pp. 1–12.

Du, Z. & Selig, M., 1998. A 3-D stall-delay model for horizontal axis wind turbine performance prediction. In 1998 ASME Wind Energy Symposium. Reston, Virigina: American Institute of Aeronautics and Astronautics. Available at: http://arc.aiaa.org/doi/abs/10.2514/6.1998-21

Dumas, A., 2011. MAAT Project - Description of Work, Reggio nell'Emilia.

Dumas, A., Angeli, D., Trancossi, M., 2014. High Altitude Airship Cabin Sizing, Pressurization and Air Conditioning, Energy Procedia, Vol. 45, pp. 977-986

Dumas, A. et al., 2011. Multibody Advanced Airship for Transport. In SAE Technical Paper 2011-01-2786.

Dumas, A., Trancossi, M. & Madonia M., 2012. Energetic design and optimization of a large photovoltaic stratospheric unconventional feeder airship, SAE Technical Paper 2012-01-2166, DOI: 10.4271/2012-01-2166

Dumitrescu, H. & Cardos, V., 2007. A stall-delay model for rotating blades. In Proc. Appl. Math. Mech. 7. pp. 4100003–4100004. Available at: http://doi.wiley.com/10.1002/pamm.200700178

Ilieva, G. et al., 2012. A critical review of propulsion concepts for modern airships. Central European Journal of Engineering, 2(2), pp.189–200. Available at: http://www.springerlink.com/index/10.2478/s13531-011-0070-1

Ilieva, G. et al 2015. Unsteady Interaction Effects Between an Airship and Its Air-Jet Propulsion System, Engineering Applications of Computational Fluid Dynamics, pp. 127-143, Springer International Publishing, DOI: 10.1007/978-3-319-02836-1_9

Koini, G.N., Sarakinos, S.S. & Nikolos, I.K., 2009. A software tool for parametric design of turbomachinery blades. Advances in Engineering Software, 40(1), pp.41–51. Available at: http://linkinghub.elsevier.com/retrieve/pii/S0965997808000513

Marten, D. et al., 2013. QBLADE : An Open Source Tool for Design and Simulation of Horizontal and Vertical Axis Wind Turbines. International Journal of Emerging Technology and Advanced Engineering, 3(3), pp.264–269.

Marten, D. & Wendler, J., 2013. QBlade Guidelines v0.6, Berlin.

Monk, J.S., 2002. The Aerodynamic Design of an Optimised Propeller for a High Altitude Long Endurance UAV. In 23rd Congress of International Council of the Aeronautical Sciences. Toronto, pp. 1–10.

Montgomerie, B., 1996. Drag Coefficient Distribution on a Wing at 90 Degrees to the Wind, Petten.

Montgomerie, B., 2004. Methods for Root Effects, Tip Effects and Extending the Angle of Attack Range to +-180o, with Application to Aerodynamics for Blades on Wind Turbines and Propellers, Stockholm.

Morgado, J.P., Silvestre, M.A. & Pascoa, J., 2013. Full Range Airfoil Polars for Propeller Blade Element Momentum Analysis. In 2013 International Powered Lift Conference. Los Angeles, California: American Institute of Aeronautics and Astronautics. Available at: http://arc.aiaa.org/doi/abs/10.2514/6.2013-4379.

Pshikhopov, V.,. et al., 2012 (a). Impact of the Feeder Aerodynamics Characteristics on the Power of Control Actions in Steady and Transient Regimes, SAE Technical Paper 2012-01-2112, DOI:10.4271/2012-01-2112.

Pshikhopov, V., et al, 2012 (b). Stochastic processes estimations of stratospheric airship-feeder flight, Proceedings of Conference: Information technologies for control, St. Peters-burg, Russian Federation.

Pshikhopov, V., et al, 2012 (c). Probabilistic Approaches to Estimation of Flight Environment for Feeder of Multibody Transport Airship System", International SAE Journal, SAE International, USA, 22.10.2012", SAE 2012 Aerospace Electronics and Avionics Systems Conference, Phoenix, Arizona, United States".

Sarakinos, S.S., Valakos, I.M. & Nikolos, I.K., 2007. A software tool for generic parameterized aircraft design. Advances in Engineering Software, 38(1), pp.39–49. Available at: http://linkinghub.elsevier.com/retrieve/pii/S0965997806000792

Silvestre, M.A., Morgado, J.P. & Pascoa, J., 2013. JBLADE: a Propeller Design and Analysis Code. In 2013 International Powered Lift Conference. Reston, Virginia: American Institute of Aeronautics and Astronautics. Available at: http://arc.aiaa.org/doi/abs/10.2514/6.2013-4220.

Smith T., et al., 2013. Energy Harvesting for the MAAT High Altitude Cruiser-Feeder Airship Concept, JP Photovoltaic Materials and Devices, IJP, USA, Proceedings of the Institution of Mechanical Engineers, Part G: Journal of Aerospace Engineering, vol. 227, 4: pp. 586-598.

Snel, H., Houwink, R. & Bosschers, J., 1994. Sectional Prediction of Lift Coefficients on Rotating Wind Turbine Blades in Stall, Petten.

Tangler, J. & Kocurek, J.D., 2005. Wind Turbine Post-Stall Airfoil Performance Characteristics Guidelines for Blade-Element Momentum Methods. In 43rd AIAA Aerospace Sciences Meeting and Exhibit. Reno.

Theodorsen, T., Stickle, G.W. & Brevoort, M.J., 1937. Caracteristics of Six Propellers Including the High-Speed Range - Technical Report No. 594, Langley.

Uhlig, D. V & Selig, M.S., 2008. Post Stall Propeller Behavior at Low Reynolds Numbers. In 46th AIAA Aerospace Sciences Meeting and Exhibit. Reno: American Institute of Aeronautics and Astronautics.

UIUC, 2014. UIUC Propeller Data Site - Aerospace Engineering - University of Illinois. Available at: http://aerospace.illinois.edu/m-selig/props/propDB.html [Accessed July 10, 2014].

Vucinic, D., et al., 2013. MAAT Cruiser/Feeder Airship: Connection and Passenger Exchange Modes," SAE Technical Paper 2013-01-2113, doi:10.4271/2013-01-2113.

Wang, C., 2014. Integrated aerodynamic design and analysis of turbine blades. Advances in Engineering Software, 68, pp.9–18. Available at: http://linkinghub.elsevier.com/retrieve/pii/S0965997813001671

Nomenclature

Symbols

a_a = axial induction factor

a_t = tangential induction factor

B = number of blades

c = blade local chord, m

c_d = airfoil drag coefficient

$C_{D_{90}}$ = airfoil drag coefficient at 90°

c_l = airfoil lift coefficient

$c_{l_{rot}}$ = airfoil lift coefficient of rotating airfoil

$c_{l_{non\_rot}}$ = airfoil lift coefficient of non-rotating airfoil

c_p = power coefficient

c_t = thrust coefficient

D = propeller diameter, m

F = Prandtl's correction factor

L = lift force, N

P = Power, W

Q = Torque, Nm

r = radius of blade element position, m

R = blade tip radius, m

R_{LE} = airfoil leading edge radius

t = airfoil thickness

T = Thrust, N

W = element relative velocity, m/s

x/c = non dimensional *x* position

$(y/c)_{0.0125}$ = non dimensional *y* position at *x/c=0.0125*

Greek Symbols

α = angle of attack, deg

$\alpha_{CL_{max}}$ = angle of attack for maximum lift coefficient,

α_{CL_0} = angle of attack for zero lift coefficient, deg

ϕ = inflow angle, deg

σ_r = rotor solidity ratio

θ = incidence angle, deg

ρ = air density, kg/m^3

Ω = rotation speed, rad/s

B.IV - High altitude propeller design and analysis

Aerospace Science and Technology 45 (2015) 398–407

Contents lists available at ScienceDirect

Aerospace Science and Technology

www.elsevier.com/locate/aescte

High altitude propeller design and analysis

J. Morgado [a,*], M. Abdollahzadeh [b], M.A.R. Silvestre [a], J.C. Páscoa [b]

[a] University of Beira Interior, Aerospace Sciences Department, Edifício II das Engenharias, Calçada Fonte do Lameiro, no. 1, 6201-001 Covilhã, Portugal
[b] University of Beira Interior, Electromechanics Department, Edifício I das Engenharias, Calçada Fonte do Lameiro, no. 1, 6201-001 Covilhã, Portugal

ARTICLE INFO

Article history:
Received 17 December 2014
Received in revised form 7 June 2015
Accepted 9 June 2015
Available online 12 June 2015

Keywords:
JBLADE
Propeller inverse design
Propeller analysis
High altitude propeller
CFD propeller simulation

ABSTRACT

This paper presents the design and optimization of a new propeller to use on the MAAT cruiser airship. The inverse design methodology is based on minimum induced losses and was implemented in JBLADE software in order to obtain optimized geometries. In addition, the design procedure and the optimization steps of a new propeller to use at high altitudes are also described. The results of propellers designed with JBLADE are then analyzed and compared with conventional CFD results, since there is no experimental data for these particular geometries. Two different approaches were used to obtain the final geometries of the propellers. Instead of using the traditional lift coefficient prescription along the blade, the airfoil best $L^{3/2}/D$ and best L/D were used to produce different geometries. It is shown that this new design approach allows the minimization of the chord along the blade, while the thrust is maximized.

1. Introduction

The airships appeared in the end of 19th century and the first air transportation services were run by these controlled lighter-than-air vehicles. After a promising development in the beginning of 20th century, the crash of *LZ 129 Hindenburg* in May of 1937, led to the end of operations of the commercial airship transportation service and, thereafter, to almost 60 years of inactivity. Recently, the rapid progress of aerospace technologies [1,2], brought the airships back as a new platforms for undertaking multiple tasks [3]. In particular, stratospheric airships have been considered as an excellent platform for many different purposes such as aerial exploration, surveillance and monitoring or even as a solution for aerial transportation [4–9].

Multibody Concept for Advanced Airship for Transport (MAAT [10–12]) project is a collaborative European project which aims to develop a heavy lift cruiser-feeder airship system in order to provide middle and long range transport for passengers and goods. The MAAT airship will be composed by 3 different main modules: Airship Hub Airport (AHA) – located in the important logistic and near cities centers, where the airships will perform ground operations; Air Transport Efficient Network (ATEN) – feeder – an airship with its vertical take-off and landing capabilities used as connection between the ground and the cruiser; Photovoltaic Transport Airship for High-altitudes (PTAH) – cruiser – an airship to carry the cargo or passengers delivered by different feeders which remains airborne on stable routes on higher altitudes than civil aviation routes [11].

Propellers have been used as propulsion units in different types of aerial vehicles, including airships. In order to obtain an efficient propeller it is essential to have a reliable numerical tool to model its propulsive performance. The propeller optimization process can start from an inverse design method which gives us the blade geometric characteristics for a pre-determined operating point. This base blade geometry can then be used for a parametric/sensitivity analysis to judge its relative merit in the overall flight envelope.

The design of the propeller based on minimum induced losses started with Betz [13] and Goldstein [14] in the beginning of the 20th century. In 1936 Glauert [15] used the equations provided by Betz but without any organized procedure for designing the propellers. Also during 1936, Bierman [16] developed one of the first parametric studies, analyzing the influence of some parameters during propeller design. He analyzed the reduction in the design pitch angle in function of the propeller operating speed and the thrust and/or power increase. Theodorsen [17] showed that the Betz condition for minimum energy loss can also be applied for heavy disk loadings. Later in 1979, Larrabee [18] reviewed Glauert's work to produce a straightforward process to produce new propeller geometries. However, the method still has some problems: small angle of attack approximation, low disk loadings and does not include viscous terms in the induced velocity formulation. During 1990, Theodorsen's developments were later revisited by Riber and Foster [19]. Recently in 1994 Adkins and Liebeck [20] presented some improvements on the previous work bringing a new design method, without small angle of attack approximation

* Corresponding author. Tel.: +351 96 748 06 76.
E-mail address: jmorgado@ubi.pt (J. Morgado).

http://dx.doi.org/10.1016/j.ast.2015.06.011
1270-9638/

Nomenclature

a_a	Axial induction factor	R	Propeller tip radius ..... m
a_t	Tangential induction factor	Re	Reynolds number
B	Number of blades	T/A	Disk loading ..... N/m^2
C_D	Airfoil drag coefficient	V	Freestream velocity ..... m/s
C_f	Skin friction coefficient	x	Non-dimensional distance, $\Omega r/V$
C_L	Airfoil lift coefficient	y^+	Non-dimensional wall distance
C_p	Power coefficient	α	Angle of attack
C_t	Thrust coefficient	ε	Drag-to-lift ratio
Eta	Propeller efficiency	ζ	Displacement velocity ratio, v'/V
F	Prandtl's factor	θ	Incidence angle
G	Circulation function	λ	Speed ratio, $V/\Omega R$
L/D	Lift to drag ratio	ξ	Non-dimensional radius, r/R
M	Mach number	ϕ	Inflow angle
r	Radius of blade element position ..... m	ϕ_t	Tip inflow angle

Table 1
High-altitude propeller data.

Year	Aircraft name	Propeller thrust, N	Propeller diameter, m	T/A, N/m^2
1987	Egrett [21,22]	2773	3.04	305.42
1988	Condor [23]	1129	4.90	59.87
1993	Pathfinder [23,24]	23	2.01	7.25
1994	Perseus [25]	388	4.40	102.07
1995	Strato 2C [26]	2500	6.00	88.42
1996	Theseus [27]	409	2.74	69.36

and some of the light disk loading limitations, which better agrees with the analysis of the designed propeller.

Design and optimization of a high altitude propeller can be a challenging problem due to the extremely low air density. Even so, propellers are being used in many high altitude aircrafts such as: Egrett (1987) [21,22], Condor (1988) [23], Pathfinder (1993) [23,24], Perseus A (1993), Perseus B (1994) [25], Strato 2C (1995) [26], Theseus (1997) [27], Pathfinder Plus (1998), Centurion (1998) and Helios (1999). Although there is only little information about high altitude propeller design, a summary of the propellers characteristics is given in Table 1.

2. Methodology

2.1. JBLADE overview

JBLADE [28–32] is a numerical open-source propeller design and analysis software written in the C++/QML programming language [33]. The code is based on QBLADE [34,35] and XFLR5 [36] codes. It can estimate the performance of a given propeller geometry for off-design analysis and has a graphical interface making easier to build and analyze the propeller simulations.

With the coupling between a BEM formulation module and XFOIL [37], the airfoil characteristics needed for the blades simulation can be obtained through a direct analysis of each airfoil. The coupling between these modules allows the design of airfoils and the computation of their lift and drag polars. Furthermore, in order to improve the accuracy of the propeller analysis, the software allows the integration of airfoil data from experiments.

The simulation procedure starts by importing the blade's sections airfoils coordinates into the XFOIL module. An analysis of the performance for each airfoil over the largest possible angle of attack range is then executed. To ensure good accuracy in the propeller simulation results it is important to define the blade operational Reynolds and Mach numbers within XFOIL. Therefore, some iterations may be needed for a complete propeller simulation. These XFOIL airfoil performance polars are used to obtain a full 360° range of angle of attack airfoil polar. This polar extrapolation calculates the lift and drag coefficients of each airfoil for the complete range of angle of attack, removing any blade twist angle limitations.

The introduction of the blade geometry is made by specifying an arbitrary number of sections characterized by their radial position, chord, twist, length, airfoil and its associated 360° angle of attack range lift and drag polar. The propeller number of blades and hub radius must be specified as well.

The propeller performance results, which characterize the propeller, are then calculated and stored. It is possible to define different simulations for the same propeller, making easy to perform parametric studies. The density viscosity and speed of sound of the fluid can be modified according to the altitude in which the propeller will operate.

2.2. Propeller inverse design in JBLADE

Although the detailed description of the inverse design method can be found in Adkins and Liebeck [20] paper, a brief description of the method is given herein. To initiate the design, the user should specify the number of blades, the hub radius and define the position and airfoil of each section of the blade. The number of sections and their location can be arbitrarily chosen. Furthermore, to obtain an initial geometry of the propeller, the free stream speed, air density and the power that the propeller absorbs or the thrust that it needs to produce must be given. The implemented method requires the equivalence between momentum equations and circulation equations which results in the relation between ζ and the induction factors as presented in Eqs. (1) and (2):

$$a_a = \frac{\zeta}{2}\cos^2\phi(1-\varepsilon\tan\phi) \tag{1}$$

$$a_t = \frac{\zeta}{2x}\sin\phi\cos\phi\left(1+\frac{\varepsilon}{\tan\phi}\right) \tag{2}$$

After the determination of the drag-to-lift ratio and angle of attack for each station, the blade chord and blade twist angle are computed as presented in Eqs. (3) and (4) respectively:

$$c = \frac{4\pi\lambda G V R\xi/C_L B}{V(1+a_a)/\sin\phi} \tag{3}$$

$$\theta = \alpha + \phi \tag{4}$$

The four derivatives of I and J should be calculated and integrated along the radius in order to calculate the new ζ. Since the updated ζ is calculated, it is necessary to compare it with the previously calculated value to check for convergence. If it is not the case, the

Table 2
Atmosphere conditions for an altitude of 16 000 m.

Designation		Units
Air density	0.165	kg/m^3
Absolute viscosity	1.44×10^{-5}	kg/(m s)
Speed of sound	295.07	m/s

Table 3
Initial considerations for the study of number of propellers.

Designation		Units
Total thrust	339 650	N
Disk loading	300	N/m^2
Total area of actuator disk	1132.17	m^2

procedure needs to be repeated. The method takes into account the tip losses, according to Prandtl's formulation, as presented in Eqs. (5) and (6).

$$F = \frac{2}{\pi}\cos^{-1}\left(e^{-f}\right) \tag{5}$$

$$f = \left(\frac{B}{2}\right)\frac{1-\xi}{\sin\phi_t} \tag{6}$$

The inflow angle is calculated using ζ and the tip's inflow angle, as presented in Eqs. (7) and (8)

$$\tan\phi = \frac{\tan\phi_t}{\xi} \tag{7}$$

$$\tan\phi_t = \lambda\left(1 + \frac{\zeta}{2}\right) \tag{8}$$

2.3. Propeller design procedure

The main goal of the propeller is to transfer the power supplied to its shaft to the axial acceleration of the air stream as efficiently as possible. Propellers operating at high altitudes experience a number of unique design issues that must be addressed, namely the low dynamic pressure acting on the blades due to low air density and limited tip speed for reasonably low compressibility losses. The changes in the atmospheric conditions with altitude are herein assumed to correspond to the International Standard Atmosphere (ISA) [38]. The main properties of the atmosphere in which the propeller will operate are presented at Table 2.

The total thrust needed for the MAAT airship, which will be used as an input parameter for the propeller design is presented in Table 3. The disk loading was initially selected based on the data analysis of Table 1. After selecting the 305.42 N/m^2 as the disk loading, an initial study on the number of propellers needed to reach the total thrust was performed.

The implemented parametric study (see Fig. 1) shows that if 50 propellers are selected, each one needs to provide 6.79 kN of thrust. After some iteration between the inverse design method and the off-design analysis, it was decided to increase the diameter to 6 m, which had reduced the disk loading to around 240 N/m^2 (see Table 4). The rotation speed was computed using a fixed Mach number of 0.6 at the blade's tip.

2.3.1. Airfoil development

Since the L/D ratios are required as an input for the inverse design methodology, different airfoils were analyzed with the XFOIL module at the operating Reynolds and Mach numbers enabling an initial look at the airfoil characteristics. The L/D ratio has a small but noticeable effect on the final blade chord and twist and a significant effect on the propeller performance.

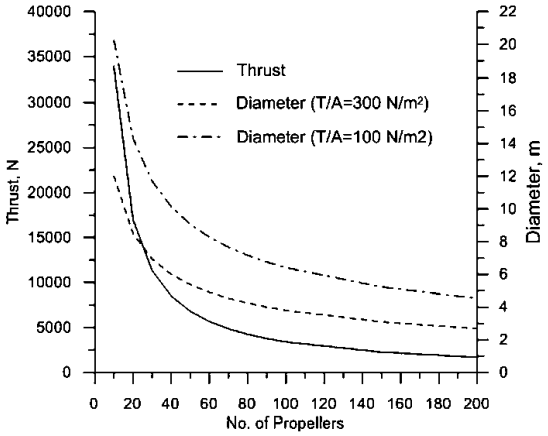

Fig. 1. Parametric study of the number of the propellers.

Table 4
MAAT cruiser propulsion.

Designation		Units
No. of propellers	50	
Propeller thrust	6.79×10^3	N
Rotation speed	550	rpm
Propeller diameter	6	m
Disk loading	240.15	N/m^2

The airfoil with highest $L^{3/2}/D$ from those that were analyzed (see Fig. 2) was then set as a base airfoil and improved [39] for a Reynolds number of 5.00×10^5. Thus, the airfoil's L/D within a useful angle of attack range was improved, allowing a reduction of the power required by the propeller for the selected disk loading and thrust. Since we are working at high altitudes, the blade chord calculated through the inverse design methodology tends to be large, leading to propellers with high solidity.

The comparison between the base and the improved airfoils shape and their pressure coefficient distribution along the chord are presented in Fig. 3. Their polars are presented in Fig. 4. It is possible to observe that the improved airfoil presents higher $L^{3/2}/D$ and L/D ratios and at the same time, these maxima ratios occur for higher lift coefficients, leading to a reduction of the blade chord needed to generate a given thrust.

2.3.2. Propeller geometry

A propeller operating design point consists of the airship's velocity, the thrust that the propeller needs to produce, the propeller hub and tip radius, the position of each intermediate section and the air properties at the desired altitude. The Reynolds number at $r/R = 0.75$ is then estimated for the selected operating point (see Tables 2 and 3). This was used to calculate the airfoil aerodynamic characteristics. The airfoil data were extrapolated and became available for full 360° angle of attack range. These data were then used by the inverse design sub-module of JBLADE, allowing the calculation of an optimal blade geometry.

A new approach for the propeller design was used herein. Instead of using a prescribed lift coefficient distribution, the software allows usage of the airfoil's best $L^{3/2}/D$ or best L/D for all sections, which leads to the minimization of the needed chord along the propeller's blade. Similarly, to some cases described in the literature [23,40] the same airfoil was used from root to tip. In the future, airfoils can be optimized for the respective position, which will allow even further improvement of the overall propeller

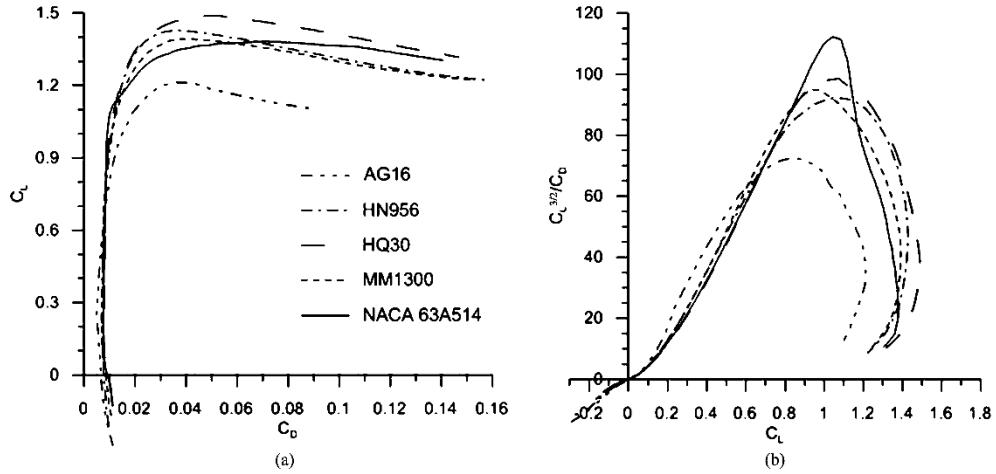

Fig. 2. Airfoils comparison performed in JBLADE's XFOIL sub-module for $Re = 5.00 \times 10^5$ and $M = 0.1$. (a) C_L vs C_D, (b) $C_L^{3/2}/C_D$ vs C_L.

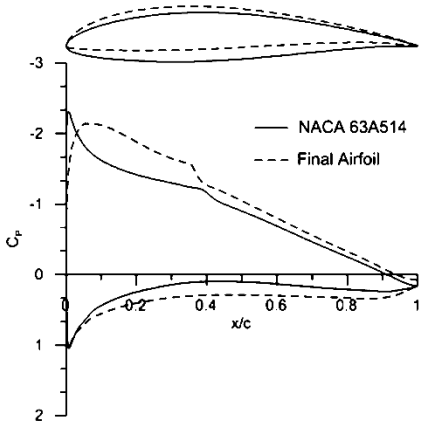

Fig. 3. Pressure coefficient distributions obtained with JBLADE's XFOIL sub-module for $Re = 5.70 \times 10^5$, $M = 0.41$ and $\alpha = 6.0°$.

performance. Since JBLADE does not contain any formulation to account with the sweep of the blades, the quarter chord of the airfoil was maintained coincident with the axis.

After obtaining the initial geometry, the off-design propeller performance was computed and the Reynolds and Mach numbers distributions along the blade radius were determined (see Fig. 5). The airfoil polars along the blade were updated for these actual Reynolds and Mach distributions and the inverse design methodology was applied again. This procedure was repeated until no evolution was observed in the blade's chord and twist.

Two different propellers were designed following the above described design procedure. One used the airfoil best L/D and the other was developed using the airfoil best $L^{3/2}/D$. These geometries are compared in Fig. 6. For both designs, the hub radius was fixed at 0.2 m and the tip radius was set to 3 m. The improved airfoil presented in Figs. 3 and 4 was used in the propellers blades.

2.4. Computational fluid dynamics

Since there is no experimental data for the presented blade, numerical simulations of the actual flow were performed to compare with the JBLADE software simulations. The computational fluid dynamics simulations were used to study the features of the flow structure and to obtain more detailed information such as parameters that affect the flow and the efficiency of the propeller.

The used airfoil was exported from JBLADE and imported in the CAD software with the respective chord and twist distribution along the blade radius. Each section was translated making the *xx* axis coincident with the 25% of the chord. The airfoils were then rotated for the respective section twist according to Fig. 6(a) and a multi-section body was built.

2.4.1. Mesh generation and boundary conditions definition

The computational domain was composed of about 2.7 million tetrahedral cells clustered around the blade surface as presented in Fig. 7. The boundaries of the domain representing the free stream conditions were set at 3 radius to the inlet and 10 radius to the outlet (see Fig. 7).

The blade (see Fig. 8) was defined by 300 nodes on the spanwise and 200 nodes on the chordwise direction.

Mesh independency tests were performed (see Fig. 9) to ensure that the obtained results are not dependent on the used mesh. As presented in Fig. 9, three different grids were used to ensure the results independency. The coarse mesh was composed by 1.65 million cells, the used mesh was made by 2.7 million and the refined mesh consisted in 4.18 million cells. The maximum discrepancy between the used mesh and the refined mesh was 3.9% for thrust coefficient and 4.2% for the power coefficient. Thus, since the result is not affected and in order to save computational time the mesh with 2.7 million was used in the remaining calculations. Furthermore, in order to reduce the computation time and facilitate the meshing process, periodic boundary conditions were also used. The y^+ was controlled by the external refinement of the mesh near the blade, through the creation of prismatic cells around the surface of the blade such that the first point above the blade surface had a value $y^+ < 1$. As presented in Fig. 7, the inlet, the outlet and the far domain were defined with a pressure far field boundary condition. At these boundaries the flow speed and direction are prescribed by inputting the value of the Mach number and the direction of the flow along the domain, together with the values of static pressure and temperature.

The values of the pressure and temperature were set according to ISA model to correspond to an altitude of 16 000 m above

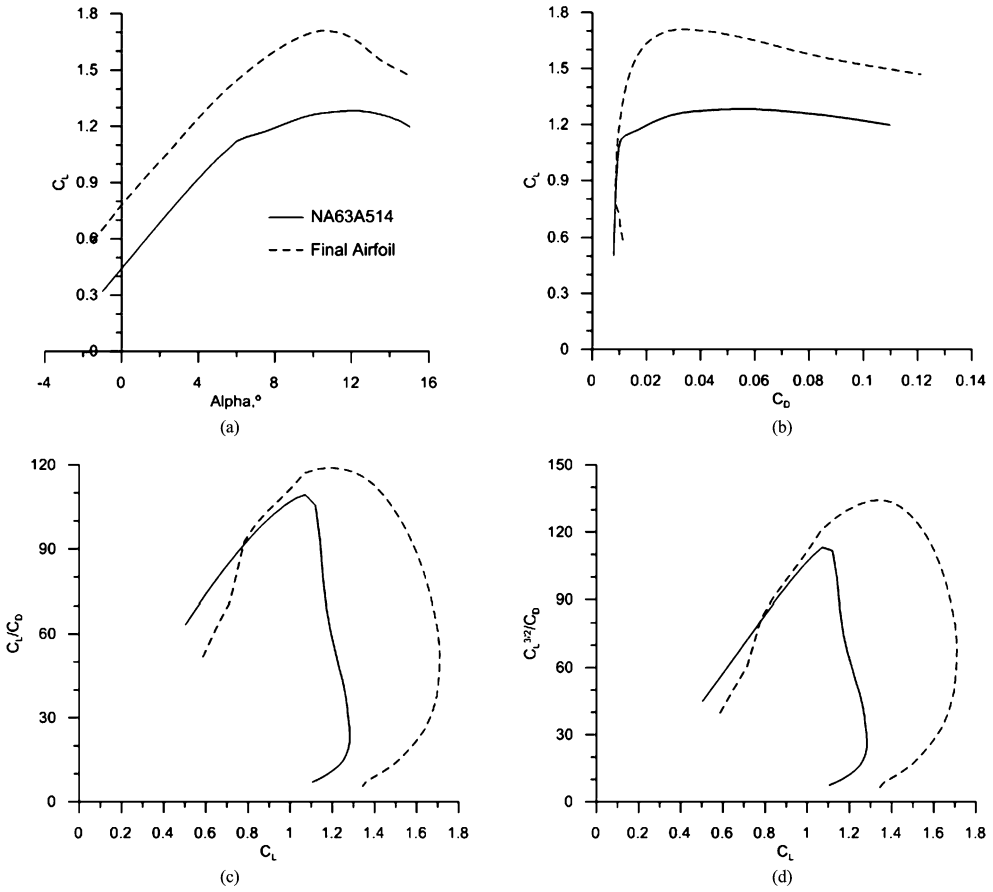

Fig. 4. Comparison between base and final airfoils for $Re = 5.70 \times 10^5$. (a) C_L vs α, (b) C_L vs C_D, (c) C_L/C_D vs C_L, (d) $C_L^{3/2}/C_D$ vs C_L.

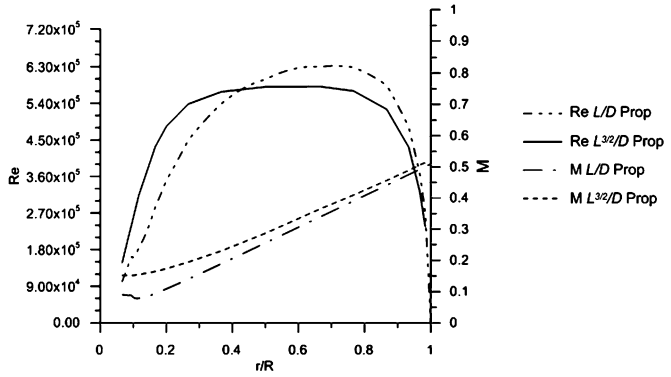

Fig. 5. Final Reynolds and Mach numbers distribution along the blades for $V = 28$ m/s.

mean sea level. The value of turbulent intensity and viscosity ratio assigned to these boundaries were 0.1% and 10 respectively. The blade surface was defined as a wall with no slip by considering the blade as a stationary wall with respect to the adjacent zone.

2.4.2. Numerical simulation procedure

Numerical simulation of steady compressible Reynolds-Averaged Navier–Stokes (RANS) equations and the turbulent mode with absolute velocity formulation was accomplished by discretizing the governing equations according the finite volume method (FVM) us-

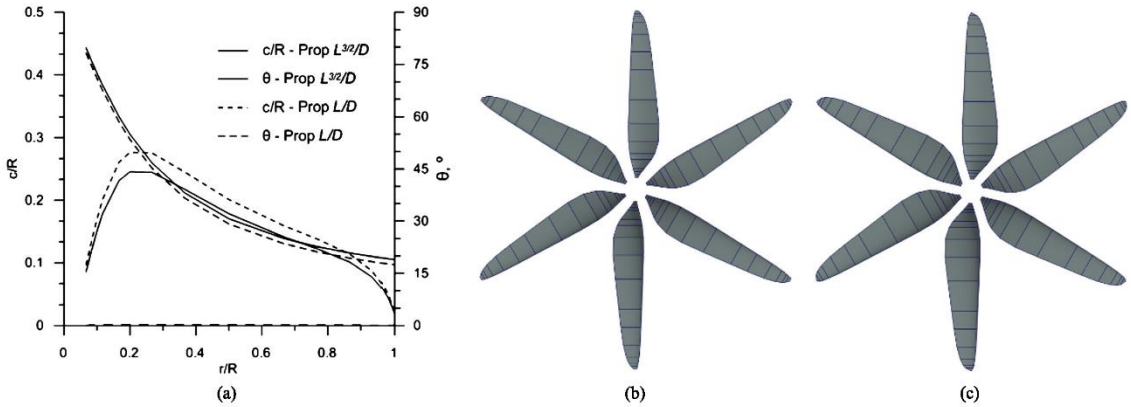

Fig. 6. (a) Comparison of propellers geometries, (b) $L^{3/2}/D$ propeller, (c) L/D propeller.

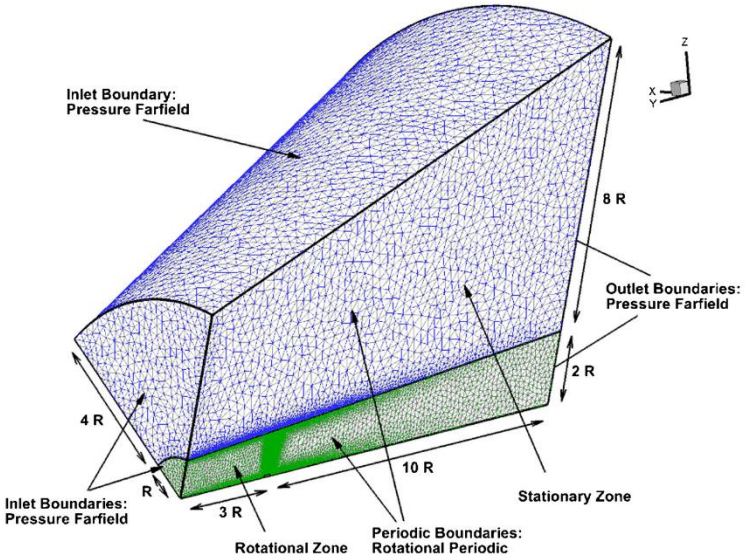

Fig. 7. Representation of the computational domain and its boundary conditions.

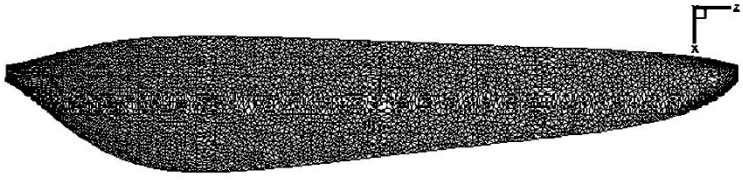

Fig. 8. Distribution of the cells on the blade surface.

ing a cell centered collocated arrangement of primitive variables. Moreover k–ω *SST* turbulence model [41] was used to deal with the time-averaging of the flow equations for simulating the turbulence.

The domain was divided in two regions: the rotating and stationary zones as presented in Fig. 7. The Multiple Reference Frame (MRF) method was chosen to accomplish the blade rotation, preventing the need to perform transient calculations by solving the governing equations in rotational reference frame considering the centrifugal and Coriolis acceleration. This method is better suited for steady state simulations where the unsteadiness of the problem can be ignored. Furthermore, the implicit coupled density based solver available in ANSYS Fluent® was selected for the coupling between momentum and continuity equations. Spatial discretization of the flow convective fluxes and turbulence variables was performed by high order advection upstream splitting method (AUSM)

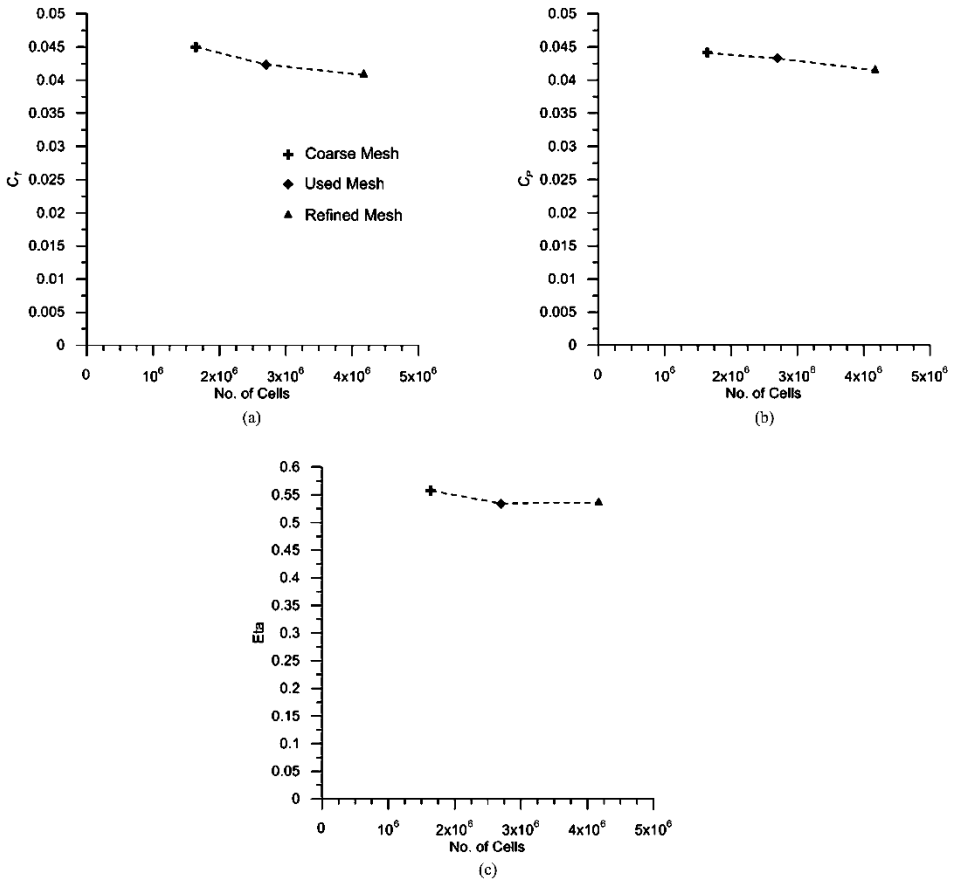

Fig. 9. Mesh independency study made for $L^{3/2}/D$ propeller at $V = 30$ m/s. (a) Thrust coefficient, (b) power coefficient, (c) propeller efficiency.

schemes and second order upwind scheme respectively. Moreover, least square cell based method was used for all the gradients. The CFD solution corresponds to a rotating domain speed of 550 rpm. To facilitate the convergence of the solution during the simulation, the rotational speed was increased gradually from 100 rpm to the final rotational speed of 550 rpm. The convergence of the numerical solution is controlled by assigning 1 to the Courant number for the iterative solution and considering suitable under relaxation factors for the turbulent variables. The convergence of the solution is also guaranteed by monitoring the relative numerical error of the solution drop below 1.0×10^{-7}. In order to compare the results of the numerical simulation with the obtained results from the JBLADE software, the propellers were simulated over a range of velocity between 10 m/s and 65 m/s.

3. Results and discussion

3.1. Inverse design integration validation

In order to validate the inverse design implementation in JBLADE, the light aircraft propeller presented by Adkins and Liebeck [20] was obtained using the implemented method. The required data for propeller inverse design are described in Table 5 and the resulting geometry is presented in Fig. 10.

Table 5
Input data for propeller inverse design.

Designation		Units
Power	52	kW
Rotation speed	2400	rpm
Hub diameter	1	ft
Tip diameter	5.75	ft
Aircraft velocity	49	m/s
Lift coefficient	0.7	
No. of blades	2	

Observing Fig. 10 is possible to conclude that JBLADE is in good agreement with original implementation done by Adkins and Liebeck [20]. The implementation was checked also against QMIL [42] since it uses a different approach for introducing the airfoil characteristics. The results have shown that similar geometries are obtained for the given propeller design point.

3.2. Propeller performance comparison

The performance of the propellers is presented in Fig. 11 in function of the advance ratio. On the left, Fig. 11(a) presents the thrust coefficient versus advance ratio, Fig. 11(b) the power coefficient, Fig. 11(c) presents the propeller efficiency.

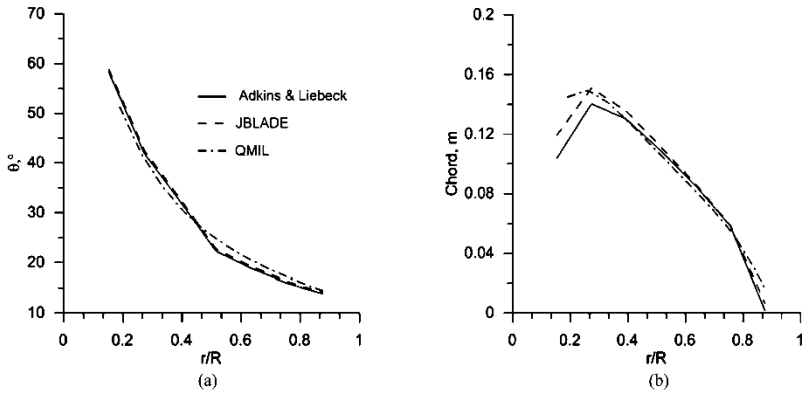

Fig. 10. Comparison between data predicted by JBLADE [26,28] and QMIL [38] and Adkins and Liebeck [18] for the inverse design methodology validation. (a) Blade twist angle, (b) chord distribution.

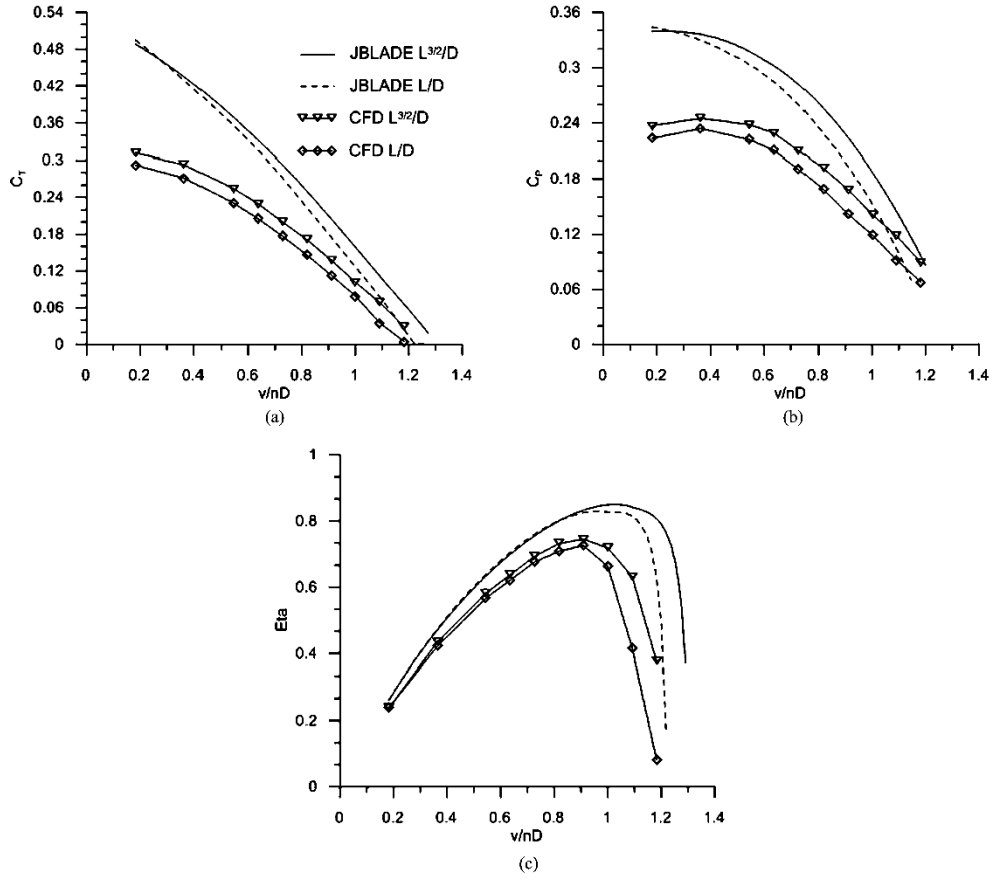

Fig. 11. Comparison between data predicted by JBLADE and CFD for the optimized propeller: (a) thrust coefficient, (b) power coefficient, (c) propeller efficiency.

Since there is no experimental data, the JBLADE results were compared with the CFD simulations. Observing Fig. 11 it is possible to conclude that JBLADE is in fair agreement with CFD calculations. JBLADE predicts a slightly bigger thrust coefficient than CFD in the higher advance ratio region. The results also show that the power coefficient is over estimated by JBLADE at low advance ratios when compared with CFD simulations. Due to the small differences presented in thrust and power coefficient, the propeller

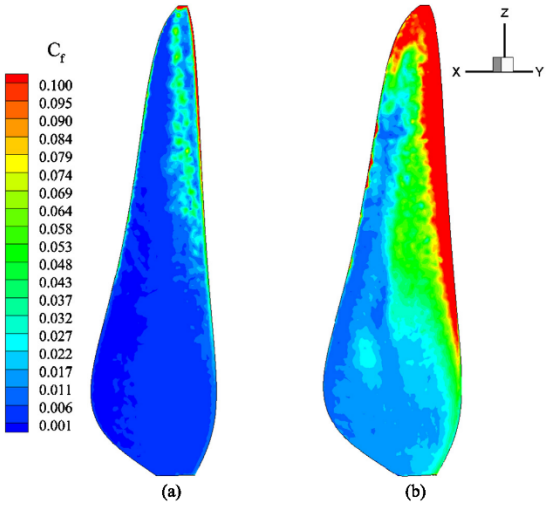

Fig. 12. Comparison of skin friction coefficient distribution on upper surfaces for $V = 30$ m/s and 550 rpm. (a) $L^{3/2}/D$ propeller, (b) L/D propeller.

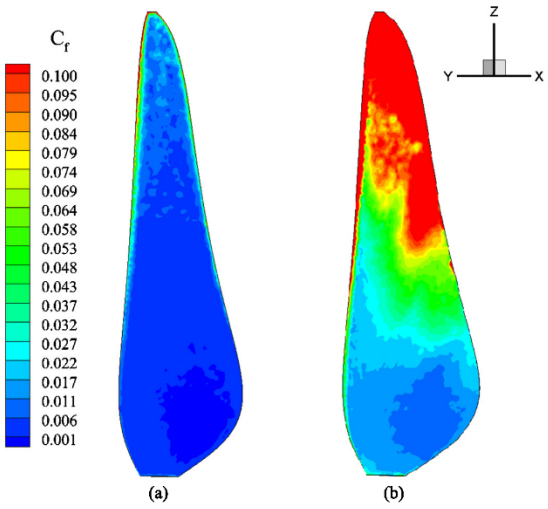

Fig. 13. Comparison of skin friction coefficient distribution on lower surfaces for $V = 30$ m/s and 550 rpm. (a) $L^{3/2}/D$ propeller, (b) L/D propeller.

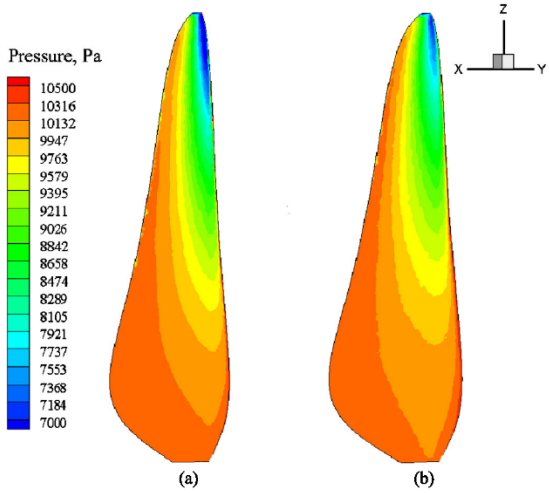

Fig. 14. Comparison of pressure distribution on upper surfaces for $V = 30$ m/s and 550 rpm. (a) $L^{3/2}/D$ propeller, (b) L/D propeller.

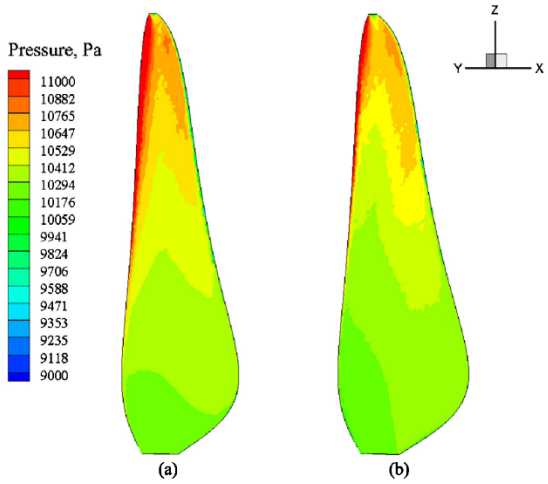

Fig. 15. Comparison of pressure distribution on lower surfaces for $V = 30$ m/s and 550 rpm. (a) $L^{3/2}/D$ propeller, (b) L/D propeller.

efficiency is slightly under predicted by JBLADE in the low advance ratio regions. The advance ratio for the maximum efficiency closely matches the CFD values but the maximum efficiency is estimated to be 10% higher than the CFD simulations values. This is related to the JBLADE's over prediction of the thrust coefficient at high advance ratios. Besides comparing JBLADE results with the CFD simulations, Fig. 11 also shows that JBLADE correctly predicts the difference between the two different design methodologies. This difference also appeared in CFD simulations and it is possible to conclude that JBLADE can be used to produce different propeller geometries and select the propeller with better performance.

In order to understand the influence of the different design concepts on the performance of the propellers, the skin friction on the blades is compared in Figs. 12 and 13. These figures clearly show that the skin friction coefficient of the blade designed using the concept of best L/D is higher than the skin friction coefficient on the blade designed using the airfoil's best $L^{3/2}/D$. This means that there is a larger viscous loss on the L/D blade's surface, which is not beneficial for the performance of the blade, since the input power will be partly used to overcome the extra drag caused by the blade shape. Most of these losses are occurring near the leading edge of the airfoil and mostly in the tip region of the blade.

Another parameter that could be used for analyzing the blade design is the pressure distribution on the blades surfaces (see Figs. 14 and 15). The thrust is originated mostly from pressures forces, which means that the larger the difference of pressure between the sides of the blade, the greater the thrust generation capability of the blade in the same operating condition.

When the blade is rotating, the upper surface of the blade presents lower pressure and the lower surface of the blade has

higher pressure. The biggest difference of pressure distributions appears on the blade tip while at the blade's root the difference is small. The comparison of the blades reveals that the $L^{3/2}/D$ propeller provides higher pressure differences all over the blade radius, which, together with lower friction along the surfaces, means higher thrust.

4. Conclusions

This paper reports the work conducted to design and analyze two different propellers for application on MAAT high altitude cruiser airship. The propellers were designed to propel the cruiser at a steady-level flight of 16 000 m above sea level. A convenient airfoil was selected and a new airfoil was developed. Its aerodynamic performance was computed with XFOIL. The inverse design methodology applied to the selected operating point produced the propeller geometry for minimum induced losses according to two different design concepts. The propeller designed with the concept of maximum $L^{3/2}/D$ generates bigger pressure differences between upper and lower surfaces with less friction which mean more thrust than the blade designed with the concept of maximum L/D.

Conflict of interest statement

The authors declare that there is no conflict of interests regarding the publication of this article.

Acknowledgements

The present work was performed as part of Project MAAT (Ref. No. 285602) supported by European Union Seventh Framework Programme. Part of the work was also supported by both C-MAST – Center for Mechanical and Aerospace Sciences and Technologies, Portuguese Foundation for Science and Technology Research Unit No. 151.

References

[1] M. Abdollahzadeh, F. Rodrigues, J.C. Páscoa, P.J. Oliveira, Numerical design and analysis of a multi-DBD actuator configuration for the experimental testing of ACHEON nozzle model, Aerosp. Sci. Technol. 41 (2015) 273–295.
[2] M. Abdollahzadeh, J.C. Páscoa, P.J. Oliveira, Modified split-potential model for modeling the effect of DBD plasma actuators in high altitude flow control, Curr. Appl. Phys. 14 (2014) 1160–1170.
[3] Z. Zheng, W. Huo, Z. Wu, Autonomous airship path following control: theory and experiments, Control Eng. Pract. 21 (Jun. 2013) 769–788.
[4] Q. Wang, J. Chen, G. Fu, D. Duan, An approach for shape optimization of stratosphere airships based on multidisciplinary design optimization, J. Zhejiang Univ. Sci. A 10 (2009) 1609–1616.
[5] E.H. Van Eaton, Airships and the Modern Military, Carlisle Barracks, 1991.
[6] L. Liao, I. Pasternak, A review of airship structural research and development, Prog. Aerosp. Sci. 45 (May 2009) 83–96.
[7] J. Morgado, M.Â.R. Silvestre, J.C. Páscoa, Parametric study of a high altitude airship according to the multi-body concept for advanced airship transport – MAAT, in: IV Conferência Nacional em Mecânica dos Fluidos, Termodinâmica e Energia, Lisbon, 2012.
[8] Y.-G. Lee, D.-M. Kim, C.-H. Yeom, Development of Korean high altitude platform systems, Int. J. Wirel. Inf. Netw. 13 (Dec. 2005) 31–42.
[9] M.S. Smith, E.L. Rainwater, Applications of scientific ballooning technology to high altitude airships, in: AIAA's 3rd Annual Aviation Technology, Integration, and Operations Technical Forum, Denver, 1971, pp. 1–8.
[10] A. Dumas, MAAT Project – Description of Work, Reggio nell'Emilia, 2011.
[11] A. Dumas, M. Trancossi, M. Madonia, I. Giuliani, Multibody advanced airship for transport, SAE Technical Paper 2011-01-2786, 2011.
[12] G. Ilieva, J. Páscoa, A. Dumas, M. Trancossi, MAAT – Promising innovative design and green propulsive concept for future airship's transport, Aerosp. Sci. Technol. 35 (2014) 1–14.
[13] A. Betz, L. Prandtl, Schraubenpropeller mit Geringstem Energieverlust, Gött. Nachr. (1919) 193–217.
[14] S. Goldstein, On the vortex theory of screw propellers, Proc. R. Soc. A, Math. Phys. Eng. Sci. 123 (Apr. 1929) 440–465.
[15] H. Glauert, Airplane propellers, in: W.F. Durand (Ed.), Aerodynamic Theory, Berlin, 1935.
[16] D. Biermann, Compromises in propeller design, J. Aeronaut. Sci. 3 (Feb. 1936) 142–144.
[17] T. Theodorsen, Theory of Propellers, McGraw–Hill Book Company, New York, 1948.
[18] E.E. Larrabee, Practical design of minimum induced loss propellers, SAE Technical Paper 790585, 1979.
[19] H.S. Ribner, S.P. Foster, Ideal efficiency of propellers – Theodorsen revisited, J. Aircr. 27 (Sep. 1990) 810–819.
[20] C.N. Adkins, R.H. Liebeck, Design of optimum propellers, J. Propuls. Power 10 (Sep. 1994) 676–682.
[21] G-520 Egrett – the Perfect Platform for High Altitude Reconnaissance and Surveillance, Grob Company, 1991.
[22] Egrett II Brochure, E-Systems GreenVille Division, 1991.
[23] A. Colozza, High altitude propeller design and analysis overview, Technical Report, Federal Data Systems, Cleveland, 1998.
[24] J.S. Monk, A propeller design and analysis capability evaluation for high altitude application, MSc Thesis, University of Witwatersrand, Johannesburg, 2010.
[25] NASA Facts – Perseus B, Dryden Flight Research Center, National Aeronautics and Space Administration, Edwards, 1999.
[26] D. Schawe, C. Rohardt, G. Wichmann, Aerodynamic design assessment of Strato 2C and its potential for unmanned high altitude airborne platforms, Aerosp. Sci. Technol. 6 (2002) 43–51.
[27] P.W. Merlin, Crash Course – Lessons Learned from Accidents Involving Remotely Piloted and Autonomous Aircraft, Monographs in Aerospace History, vol. 44, National Aeronautics and Space Administration, 2013.
[28] M.A.R. Silvestre, J.P. Morgado, J.C. Pascoa, JBLADE: a propeller design and analysis code, in: 2013 International Powered Lift Conference, Los Angeles, American Institute of Aeronautics and Astronautics, 2013.
[29] J.P. Morgado, M.A.R. Silvestre, J.C. Pascoa, Full range airfoil polars for propeller blade element momentum analysis, in: 2013 International Powered Lift Conference, Los Angeles, American Institute of Aeronautics and Astronautics, 2013.
[30] J.P. Morgado, M.A.R. Silvestre, J.C. Pascoa, Validation of new formulations for propeller design, J. Propuls. Power 31 (2014) 467–477, http://dx.doi.org/10.2514/1.B35240.
[31] J.P. Morgado, M.A.R. Silvestre, J.C. Pascoa, A comparison of post-stall models extended for propeller performance prediction, Aircr. Eng. Aerosp. Technol. (2015), http://dx.doi.org/10.1108/AEAT-07-2014-0119.R1.
[32] M.A.R. Silvestre, J. Morgado, P. Alves, P. Santos, P. Gamboa, J.C. Páscoa, Propeller performance measurements at low Reynolds numbers, Int. J. Mech. (ISSN 1998-4448) 9 (2015) 154–166.
[33] Digia, Qt Project, http://qt-project.org/ [cited: 10 July 2014].
[34] D. Marten, J. Wendler, G. Pechlivanoglou, C.N. Nayeri, C.O. Paschereit, QBLADE: an open source tool for design and simulation of horizontal and vertical axis wind turbines, Int. J. Emerg. Technol. Adv. Eng. 3 (2013) 264–269.
[35] D. Marten, J. Wendler, QBlade Guidelines v0.6, Berlin, 2013.
[36] A. Deperrois, Analysis of foils and wings operating at low Reynolds numbers – guidelines for XFLR5 v6.03, 2011.
[37] M. Drela, XFOIL – an analysis and design system for low Reynolds number airfoils, in: Proceedings of Low Reynolds Number Aerodynamics, Berlin, in: Lecture Notes in Engineering, vol. 54, 1989, pp. 1–12.
[38] U.S. Standard Atmosphere URL: http://ccmc.gsfc.nasa.gov/modelweb/atmos/us_standard.html, Washington D.C. [cited 25 September 2014].
[39] P.V. Gamboa, M.A.R. Silvestre, Airfoil optimization with transition curve as objective function, in: VI International Conference on Adaptive Modeling and Simulation ADMOS 2013, Lisbon, 2013.
[40] L.D. Koch, Design and performance calculations of a propeller for very high altitude flight, NASA/TM 1998-206637, Lewis Research Center, Cleveland, 1998.
[41] F.R. Menter, Two-equation eddy-viscosity turbulence models for engineering applications, AIAA J. 32 (Aug. 1994) 1598–1605.
[42] M. Drela, QPROP formulation, 2006.

B.V - XFOIL *vs* CFD performance predictions for high lift low Reynolds number airfoils

Aerospace Science and Technology 52 (2016) 207–214

Contents lists available at ScienceDirect

Aerospace Science and Technology

www.elsevier.com/locate/aescte

XFOIL *vs* CFD performance predictions for high lift low Reynolds number airfoils

J. Morgado [a,*], R. Vizinho [b], M.A.R. Silvestre [a], J.C. Páscoa [b]

[a] University of Beira Interior, Aerospace Sciences Department, Edifício II das Engenharias, Calçada Fonte do Lameiro, no. 1, 6201-001 Covilhã, Portugal
[b] University of Beira Interior, Electromechanics Department, Edifício I das Engenharias, Calçada Fonte do Lameiro, no. 1, 6201-001 Covilhã, Portugal

ARTICLE INFO

Article history:
Received 16 December 2015
Received in revised form 24 February 2016
Accepted 26 February 2016
Available online 4 March 2016

Keywords:
XFOIL
Airfoil analysis
$k-kl-\omega$ modified transition model
$k-\omega$ SST turbulence model

ABSTRACT

Blade Element Momentum (BEM) theory is an extensively used technique for calculation of propeller aerodynamic performance. With this method, the airfoil data needs to be as accurate as possible. At the same time, Computational Fluid Dynamics (CFD) is becoming increasingly popular in the design and optimization of devices that depend on aerodynamics. For fixed and rotary wing applications, the airfoil lift over drag coefficient is the dominant airfoil performance parameter. Selecting a suitable computational tool is crucial for the successful design and optimization of this ratio. The XFOIL code, the Shear Stress Transport $k-\omega$ turbulence model and a refurbished version of $k-kl-\omega$ transition model were used to predict the airfoil aerodynamic performance at low Reynolds numbers (around 2.0×10^5). It has been shown that the XFOIL code gives the overall best prediction results. Also, it is not clear that CFD turbulence models, even with boundary layer transition detection capability, can compute better airfoil performance predictions data.

1. Introduction

The technological developments in aeronautics, astronautics and material industries, together with the increase in oil prices caused by the world-wide oil crisis, brought a new focus on airship vehicles [1,2]. The Multibody Advanced Airship for Transportation (MAAT [3–6]) concept aims to develop a new global transportation form for people and goods. Generally, the propulsion system for these advanced low-dynamic vehicles is based on high power DC motor-driven propeller systems [1,7]. Nevertheless, at this altitude traditional propellers have a dramatically reduced efficiency caused by the high altitude atmosphere properties. When compared with lower altitude conditions, an airship operating in the stratosphere will find smaller air density and pressure as well as a reduced air kinematic viscosity and speed of sound. This makes the Reynolds number range of the propeller airfoils under study fall in the 10^5 order of magnitude and, simultaneously, limits the tip speed for a given limit Mach number. Thus, computational methods suitable for design and analysis of airfoils and propellers for high altitude operation are required. Blade Element Momentum theory (BEM) is commonly used to calculate the performance of propellers due to its low computational costs. However, the correct predictions from BEM codes depends on the reliability of the airfoil performance data [8]. Therefore, the correct estimation of the airfoil performance on the low Reynolds number regime found at high altitudes will have a decisive impact on the development of propellers for the MAAT airships. Airfoil performance at low Reynolds numbers is highly dependent on the boundary layer transition onset position [9]. So, it is essential to accurately predict the transition region on the surface of the airfoil to predict its actual performance. In order to analyze airfoils and make the coefficients available for use in the propeller performance prediction there are two main methods that can be applied. One is the solution of the Reynolds Averaged Navier Stokes (RANS) equations and closure models using structured or unstructured meshes. The second method is based on an inviscid flow solution coupled with a boundary-layer formulation. In order to study the accuracy of the above mentioned methods, a conventional $k-\omega$ SST turbulence model [10,11], a $k-kl-\omega$ transition closure [12] and XFOIL [13] were used to predict the performance of different airfoils at low Reynolds number.

The Shear Stress Transport $k-\omega$ model, is a two equation eddy-viscosity model developed by Menter et al. This SST formulation was devised to effectively blend the robust and accurate formulation of the $k-\omega$ model in the near wall region with the free-stream correct behavior of the $k-\varepsilon$ turbulence closure. The $k-kl-\omega$ transition model presents an interesting division of the turbulence scale introduced by Walters and Leylek [14]. The original model was implemented in OpenFoam and some modifications

* Corresponding author. Tel.: +351 96 748 06 76.
E-mail address: jmorgado@ubi.pt (J. Morgado).

http://dx.doi.org/10.1016/j.ast.2016.02.031
1270-9638/

Nomenclature

c	Airfoil local chord	L	Lift force, N
C_D	Airfoil drag coefficient	L'	Component of lift force on the original system of coordinates
C_L	Airfoil lift coefficient	P_{kl}	$k-kl-\omega$ model laminar fluctuations kinetic energy production term
D	Drag force, N	$P_{k_{t,s}}$	$k-kl-\omega$ model turbulent kinetic energy production term
D'	Component of drag force on the original system of coordinates	R_{BP}	$k-kl-\omega$ model bypass transition energy transfer function
D_L	$k-kl-\omega$ model laminar fluctuations kinetic energy destruction term	R_{NAT}	$k-kl-\omega$ model natural transition energy transfer function
D_T	$k-kl-\omega$ model turbulent kinetic energy destruction term	S_k, S_ω	Dissipation of k and ω
D_ω	Cross diffusion term	t	Airfoil thickness
f_ω	$k-kl-\omega$ model kinematic wall effect damping function	α	Angle of attack
G_ω	Generation of ω	ρ	Air density, kg/m^3
$\tilde{G}_k$	Turbulence kinetic energy generation due to mean velocity gradients	Γ_k, Γ_ω	Effective diffusivity of k and ω
k	Turbulent kinetic energy	μ	Dynamic viscosity, Pa s

were proposed [12]. The other used code was XFOIL. The XFOIL code [13] combines a panel method and an integral boundary layer formulation for the analysis of potential flow around the airfoils. The code was developed to rapidly predict the airfoil performance at low Reynolds numbers and its accuracy is well recognized [15].

2. Theoretical formulation

2.1. Shear stress transport (SST) $k-\omega$ model

As previously mentioned, the Shear Stress Transport (SST) $k-\omega$ model [10,11] is a two-equation eddy-viscosity closure. This Menter's *SST* formulation was developed to effectively blend the robust and accurate formulation of the standard $k-\omega$ turbulence model in the near wall region with the $k-\varepsilon$ model behavior as the model switches to the latter away from the wall. The authors decided to choose the SST $k-\omega$ model due to its accuracy for a wide class of low Reynolds number airfoil flows on which low Reynolds number airfoils are inserted, as suggested in the literature [16]. The SST $k-\omega$ model has similar formulation to the Standard $k-\omega$ model. The transport equations are defined as presented in Eq. (1) and Eq. (2):

$$\frac{\partial}{\partial t}(\rho k)+\frac{\partial}{\partial x_i}(\rho k u_i)=\frac{\partial}{\partial x_j}\left(\Gamma_k\frac{\partial k}{\partial x_j}\right)+\tilde{G}_k-Y_k+S_k \tag{1}$$

$$\frac{\partial}{\partial t}(\rho\omega)+\frac{\partial}{\partial x_i}(\rho\omega u_i)=\frac{\partial}{\partial x_j}\left(\Gamma_\omega\frac{\partial\omega}{\partial x_j}\right)+G_\omega-Y_\omega+D_\omega+S_\omega \tag{2}$$

The $\tilde{G}_k$ represents the generation of turbulence kinetic energy due to the mean velocity gradients, calculated according Eq. (3):

$$G_k=-\rho\overline{u_i'u_j'}\frac{\partial u_j}{\partial x_i} \tag{3}$$

The effective diffusivities for the $k-\omega$ model are given by Eq. (4) and Eq. (5):

$$\Gamma_k=\mu+\frac{\mu_t}{\sigma_k} \tag{4}$$

$$\Gamma_\omega=\mu+\frac{\mu_t}{\sigma_\omega} \tag{5}$$

where σ_k and σ_ω are the turbulent Prandtl numbers for k and ω respectively and they are calculated as presented in Eq. (6) and Eq. (7):

$$\sigma_k=\frac{1}{\frac{F_1}{\sigma_{k,1}}+\frac{(1-F_1)}{\sigma_{k,2}}} \tag{6}$$

$$\sigma_\omega=\frac{1}{\frac{F_1}{\sigma_{\omega,1}}+\frac{(1-F_1)}{\sigma_{\omega,2}}} \tag{7}$$

The turbulent viscosity μ_t (see Eq. (4) and Eq. (5)) is computed as follows:

$$\mu_t=\frac{\rho k}{\omega}\frac{1}{\max[\frac{1}{\alpha^*},\frac{SF_2}{a_1\omega}]} \tag{8}$$

where S represents the strain rate magnitude.

2.1.1. Low Reynolds correction

The low Reynolds correction implemented in Ansys Fluent® modifies the α^* coefficient (see Eq. (8)). This coefficient damps the turbulent viscosity and it is given by Eq. (9):

$$\alpha^*=\alpha^*_\infty\left(\frac{\alpha^*_0+Re_t/R_k}{1+Re_t/R_k}\right) \tag{9}$$

where:

$$Re_t=\frac{\rho k}{\mu\omega} \tag{10}$$

$$R_k=6 \tag{11}$$

$$\alpha^*_0=\frac{\beta_i}{3} \tag{12}$$

$$\beta_i=0.072 \tag{13}$$

Note that in the high-Reynolds-number form of the $k-\omega$ model, $\alpha^*=\alpha^*_\infty=1$.

2.2. $k-kl-\omega$ transition model

The work of Mayle and Schulz [17], was responsible for setting the foundations for the laminar kinetic energy theory. The latter theory accounts for the kinetic energy of the velocity fluctuations that occur within the laminar boundary layer pre-transitional region. These velocity oscillations were measured for the first time in 1937 as a result of the pioneer experimental work of Dryden

[18]. It was concluded that the free-stream turbulence was responsible for the occurrence of such boundary layer perturbations. Taylor [19] made an interesting observation regarding these pre-transitional laminar velocity fluctuations. It was acknowledged that these oscillations were related to thickening and thinning of the boundary layer. Later in 1971, the experimental work of Klebanoff [20], explicitly identified these streamwise fluctuations, naming them as breathing modes. However, through the work of Kendall [21] these velocity oscillations were renamed as Klebanoff modes in honor of their original discoverer.

Based on this new transition theory, many novel RANS transition models have been developed since then. In 2004, the numerical work of Walters and Leylek [14] presented a locally formulated laminar fluctuation kinetic energy transition model. The turbulence transition closure was named $k-kl-\omega$, and was implemented in the commercial software Ansys Fluent®. Later in 2008, Walters and Cokljat [22] presented an improved version of the original 2004 transition model, the $k-kl-\omega$. Besides the change in the turbulence length scale variable from ϵ to ω some model constants and functions were also modified. The $k-kl-\omega$ transition model can be resumed down to three transport equations. One for the laminar fluctuations kinetic energy, kl, another for the turbulent kinetic energy, k, and the last one for the specific turbulent kinetic energy dissipation rate, ω. The incompressible transport equations are disclosed in Eq. (14) to Eq. (16):

$$\frac{Dk}{Dt} = P_k + R_{BP} + R_{NAT} - \omega k - D_T + \frac{\partial}{\partial x_j}\left[\left(\nu + \frac{\alpha_t}{\sigma_k}\right)\frac{\partial k}{\partial x_j}\right] \quad (14)$$

$$\frac{Dkl}{Dt} = P_{kl} + R_{BP} - R_{NAT} - D_L + \frac{\partial}{\partial x_j}\left[\nu\frac{\partial kl}{\partial x_j}\right] \quad (15)$$

$$\frac{D\omega}{D}t = C_{\omega_1}\frac{\omega}{k}P_k + \left(\frac{C_{\omega_R}}{f}w - 1\right)\frac{\omega}{k}(R_{BP} + R_{NAT}) - C_{\omega_2}\omega^2 + C_{\omega_3}f_\omega\alpha_T f_W^2\frac{\sqrt{k}}{y^3} + \frac{\partial}{\partial x_j}\left[\left(\nu + \frac{\alpha_t}{\sigma_\omega}\right)\frac{\partial\omega}{\partial x_j}\right] \quad (16)$$

The production terms in Eq. (14) and Eq. (15) are based on velocity strain rate and are presented in Eq. (17) and Eq. (18)

$$P_k = \nu_{T,s}S^2 \quad (17)$$

$$P_{kl} = \nu_{T,l}S^2 \quad (18)$$

One of the most interesting features of this transition model is the turbulence scale division. Introduced in the work of Walters and Leylek [14], this was also applied in the 2008 $k-kl-\omega$ version [22]. This concept has been shown to be present in fully turbulent boundary layers by Moss and Oldfield [23] and Thole and Bogard [24]. As such, turbulence is divided in large and small scales. The large scale is related to the laminar fluctuation kinetic energy production through the "splat mechanism", as suggested by Volino [25] and mentioned by Bradshaw [26]. The small scale is related to regular turbulence. Far from wall surfaces the small scale turbulent kinetic energy is equal to the free-stream turbulent kinetic energy. The definition of the limiting length scale is obtained from Eq. (19), where λ_T is the turbulent small length scale defined in Eq. (20):

$$\lambda_{eff} = \min(C_{\lambda y}, \lambda_T) \quad (19)$$

$$\lambda_T = \frac{\sqrt{k}}{\omega} \quad (20)$$

The small scale turbulent kinematic viscosity is calculated as presented in Eq. (21). This makes use of a collection of damping functions that attempt to simulate various mechanisms, such as the shear-sheltering effect (see Eq. (22)), the turbulence intermittency (see Eq. (23)) and the kinematic and viscous wall effect as presented in Eq. (24) and Eq. (25). The last damping function is based on effective turbulent Reynolds number (see Eq. (26)). Furthermore, in order to satisfy realizability, C_μ is calculated according to Eq. (27). In the work of Walters et al. [14,22], C_μ is a simplified version of its original form according to the work of Shih and Zhu [27] and Shih et al. [28].

$$\nu_{T,s} = f_v f_{INT} C_\mu \sqrt{k_{T,s}}\lambda_{eff} \quad (21)$$

$$f_{SS} = e^{[-(\frac{C_{ss}\nu\Omega}{k})^2]} \quad (22)$$

$$f_{INT} = \min\left(\frac{k_L}{C_{INT}k_{TOT}}, 1\right) \quad (23)$$

$$f_W = \frac{\lambda_{eff}}{\lambda_T} \quad (24)$$

$$f_v = 1.0 - e^{-\frac{\sqrt{Re_T}}{A_v}} \quad (25)$$

$$Re_T = \frac{f_W^2 k}{\nu\omega} \quad (26)$$

$$C_\mu = \frac{1}{A_0 + A_s(\frac{S}{\omega})} \quad (27)$$

The remaining $k-kl-\omega$ transition model description can be found in the work of Walters and Cokljat [22]. The described transition model was implemented in the open-source software OpenFoam. After a systematic analysis and testing of the transition model some modifications were proposed. Application of such modifications yielded improved results. One of the applied changes to the model was made to the turbulence intermittency damping function f_{INT} (see Eq. (23)). This modification avoids the fact that the original model predicts zero turbulent viscosity in the free-stream. This is so since k_L exists only near wall surfaces. Therefore the proposed term is then calculated as presented in Eq. (28).

$$f_{INT}^{new} = \min\left(\frac{k}{C_{INT}k_{TOT}}, 1\right) \quad (28)$$

Another relevant change in relation to the original model is the definition of turbulence Reynolds number, Re_T presented in Eq. (26). The classical literature definition of turbulence Reynolds number as used by several turbulence models such the ones presented at Refs. [29–31] was applied also in the present modified transition model. This will result in an improved asymptotic skin-friction coefficient behavior along the fully turbulent region of the flow. The altered term is presented in Eq. (29):

$$Re_T^{new} = \frac{k}{\nu\omega} \quad (29)$$

The original model's turbulence specific dissipation rate destruction term is $-C_{\omega 2}\omega^2$. It was observed that the latter had an excessive effect near the wall. Also, in the work of Craft et al. [32] the presented turbulence model has a set of equations resembling the presented turbulent kinetic energy, k, and the specific turbulent kinetic energy dissipation rate, ω, of the $k-kl-\omega$ transition model. In the just presented work, instead of ω, the transported quantity is the turbulent kinetic energy dissipation rate, $\tilde{\epsilon}$. The function of interest is $C_{\epsilon 2}$. This is multiplied by the term responsible for the destruction of the turbulent kinetic energy dissipation rate. Near the wall, its influence is reduced. The proposed hypothesis is then the imposition of a damping function, f_ω (see Eq. (24)) multiplied to the $-C_{\omega 2}\omega^2$ term. The resulting term is given in the third element on the right side of Eq. (30):

$$\frac{D\omega}{Dt} = C_{\omega 1}\frac{\omega}{k}P_k + \left(\frac{C_{\omega R}}{f_W} - 1\right)\frac{\omega}{k}(R_{BP} + R_{NAT}) - C_{\omega 2}\omega^2 f_W + C_{\omega 3}f_\omega\alpha_T f_W^2\frac{\sqrt{k}}{y^3} + \frac{\partial}{\partial x_j}\left[\left(\nu + \frac{\alpha_t}{\sigma_\omega}\right)\frac{\partial\omega}{\partial x_j}\right] \quad (30)$$

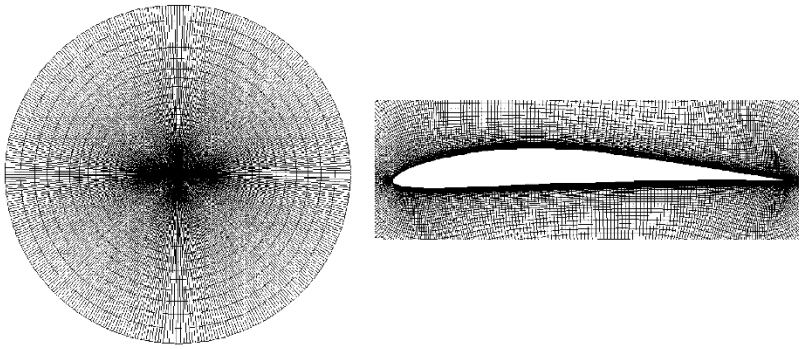

Fig. 1. (a) General view of the used mesh for the CFD simulations. (b) Detail of the mesh around the airfoil.

A more detailed description of the modified $k-kl-\omega$ turbulence transition model version is available in the work of Vizinho et al. [12].

2.3. XFOIL code

The XFOIL [13] code combines a potential flow panel method and an integral boundary layer formulation for the analysis of the flow around airfoils. The code was developed to rapidly predict the airfoil performance at low Reynolds numbers and its convergence is achieved through the iteration between the outer and inner flow solutions on the boundary layer displacement thickness. Thus, the XFOIL code calculates the viscous pressure distribution and captures the influence of limited trailing edge separation and laminar separation bubbles. The XFOIL uses an approximate e^N envelope method to calculate transition. With this method the code tracks only the most amplified frequency at a given point on the airfoil downstream from the point of instability to obtain the amplitude of that disturbance. Transition is assumed when this integrated amplitude reaches an empirically determined value. The appropriate N to use into XFOIL calculations, can be calculated by Eq. (31) as presented by van Ingen [33].

$$N = -8.43 - 2.4\ln(T_u) \tag{31}$$

where T_u represents the absolute turbulence intensity. In the present work N was set to the default value of 9, which corresponds to a smooth wing surface in a low turbulence intensity freestream.

3. Numerical procedure

3.1. Mesh generation

In order to simulate the airfoils and compare the different Computational Fluid Dynamics (CFD) models, a completely structured O-type mesh was used. The mesh had the outer boundaries placed 30 chords away from the airfoil. The airfoil was defined with 250 points around its contour and special attention was given to the boundary layer regions in order to ensure that the first point of the mesh corresponds to a $y^+ < 1$. The used mesh is shown in Fig. 1.

3.2. Boundary conditions

To simulate the airfoils at the desired chord-based Reynolds number, corresponding to those of the available experimental results given by the literature ($Re = 2.0 \times 10^5$), a density based solver was applied. The far boundary was represented by a pressure farfield using the Mach number input to prescribe the flow speed. The desired angle of attack was obtained using the appropriate flow direction vector components. The airfoil top and bottom surfaces were defined as wall boundary conditions and the fluid inside the domain was defined as air with $\rho = 1.225$ kg/m^3 and $\mu = 1.79 \times 10^{-5}$ Pa s. These procedures give the advantage to simulate all angles of attack using only a single mesh [34]. To correctly compute the lift and drag coefficients, the decomposition of the flow direction vector was used as presented in Eq. (32) and Eq. (33)

$$L = L'\cos(\alpha) - D'\sin(\alpha) \tag{32}$$

$$D = L'\sin(\alpha) + D'\cos(\alpha) \tag{33}$$

where L and D are lift and drag, respectively, and L' and D' represent the components of the aerodynamic force based on the mesh system of coordinates of Ansys Fluent®.

3.3. CFD simulation procedure

Both Computational Fluid Dynamics simulations were performed using a steady state solver. The pressure based solver, SIMPLE, was used together with a Green-Gauss cell based discretization scheme. On Ansys Fluent®, a second order upwind (SOU) scheme was used for the momentum and turbulence equations discretization. Regarding the OpenFoam simulations, the second order linear-upwind stabilized transport (LUST) discretization scheme was chosen. The Laplacian terms and the pressure equations were discretized using a linear discretization. The convergence of the numerical solution is controlled considering suitable under relaxation factors for the turbulent variables. Convergence is also guaranteed by monitoring the relative numerical error of the solution, as it drops below 1.0×10^{-8}. In order to compare the results of the numerical simulations with the obtained results from the JBLADE software, the airfoils were simulated for a given Reynolds number, over a range of angles of attack.

3.4. XFOIL simulation procedure

The influence of the number of points used to define the airfoil inside XFOIL was analyzed. Fig. 2 presents the different polars obtained using different number of points in XFOIL. It was concluded that for more than 150 points, XFOIL does not show a significant difference in the airfoil polars. However, as the XFOIL is requiring less than a minute of elapse time per polar on an average desktop computer, each airfoil was defined with 250 points.

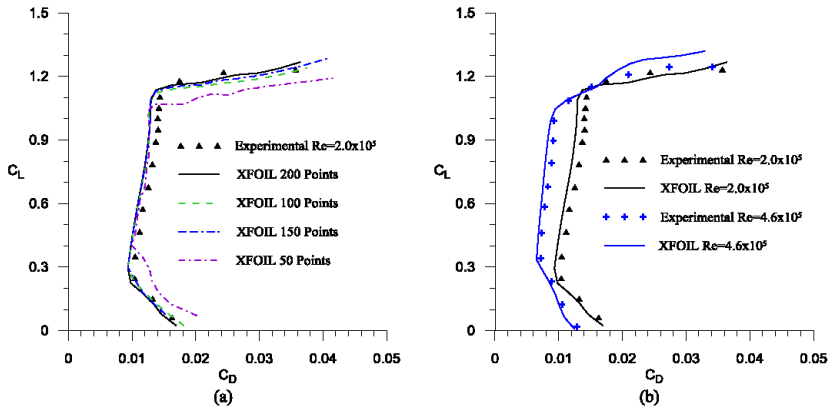

Fig. 2. (a) Validation of polar calculation using different number of points to define an airfoil in XFOIL. (b) Comparison between XFOIL and experimental studies [35] for E387 airfoil at different Reynolds numbers.

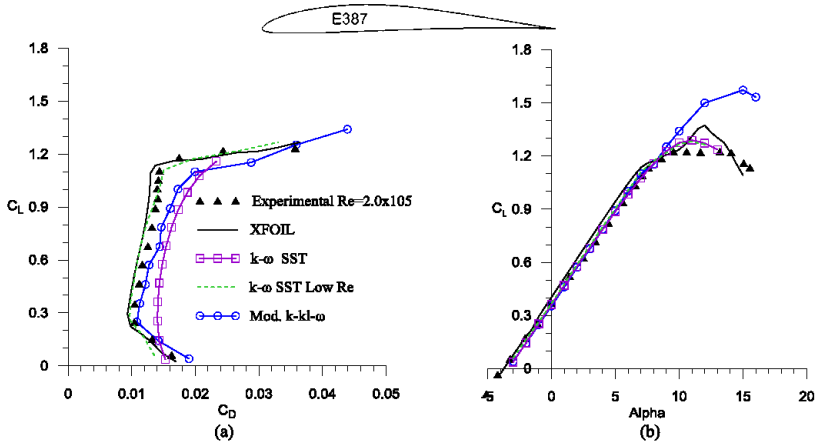

Fig. 3. Aerodynamic characteristics of the E387 airfoil measured at Penn State wind tunnel [37] compared with the numerical simulation results. (a) C_L *vs* C_D. (b) C_L *vs* α.

4. Results and discussion

4.1. E387 airfoil

The *E*387 airfoil was designed during 1960s by Richard Eppler. Since the airfoil was specifically designed to use on model sailplanes, it had represented a significant improvement over other airfoils available at that time. The airfoil performance predicted for $Re = 2.0 \times 10^5$ by XFOIL, $k-kl-\omega$ transition model and $k-\omega$ *SST* turbulence model (with and without low Reynolds corrections) are compared to the University of Illinois Urbana–Campaign (UIUC) [35] wind-tunnel measurements in Fig. 3(a) and (b).

The results presented at Fig. 3(a) show that all the predictions are in good agreement with the experiments. The XFOIL and $k-SST$ turbulence model with the low Reynolds corrections ($k-\omega$ *SST Low Re*) are capable to accurately predict the corners of the low drag region, although they are predicting a slightly higher maximum lift coefficient. Regarding the $k-\omega$ *SST* without low Reynolds corrections, since it is unable to predict transition, it does not replicate the sharp corners, although the maximum lift coefficient is well computed.

The refurbished version of $k-kl-\omega$ transition model presents better agreement with the experimental data than *SST* $k-\omega$ turbulence model without low Reynolds corrections. For the lower corner of the low drag bucket this model can correctly predict the values of both lift and drag coefficients. In the direction of the top corner of the low drag region as the lift coefficient increases $k-kl-\omega$ transition model predicts a slightly higher drag coefficient for a given lift coefficient, making the curve appear to the right when compared with the measurements.

Fig. 4(a) and (b) shows the pressure distribution for an angle of attack of 0 and 4 degrees, respectively. The results obtained from the described numerical methods are compared with the measurements provided in Ref. [36].

At an angle of attack of 0°, XFOIL and $k-\omega$ *Low Re* turbulence model are in a perfect agreement with experiments, while the modified $k-kl-\omega$ transition model slightly under predicts the pressure coefficient in the upper surface of the airfoil. At the angle of attack of 4°, the behavior of different used methods remain the same, with a slightly under prediction in the $k-kl-\omega$ transition model until $x/c = 0.6$.

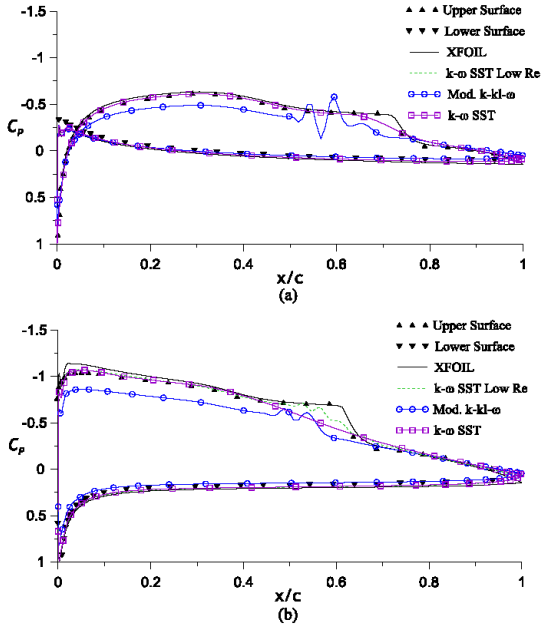

Fig. 4. Comparison of E387 airfoil pressure distributions for $Re = 2.0 \times 10^5$ [36]. (a) $\alpha = 0°$. (b) $\alpha = 4°$.

In Fig. 5(a) the transition position versus lift coefficient is plotted with the airfoil's drag polar in order to observe the parallelism between the position of the transition and the laminar bucket limits. It is clear that the less steep part of the transition curves correspond to the limits of the laminar bucket of the drag polar as shown in Fig. 5.

In particular, one can note the lift coefficient of the transition ramps as the corners of the low drag bucket of the airfoil. The lower surface transition ramp at lift coefficient of about 0.3 as the lower corner and the upper surface transition ramp at lift coefficient of about 1.15 as the upper corner of the low drag bucket. The turbulence model *SST* $k-\omega$ with low Reynolds corrections and XFOIL give a close prediction but the latter estimates a larger laminar flow extent at lower lift coefficients. The modified $k-kl-\omega$ transition model shows the same trend but only matches closely the other models around a lift coefficient of 1.18, overestimating the laminar flow extent at higher lift coefficients. The relation between transition position and laminar bucket of the drag polar demonstrates the importance of the transition location prediction during the development of a new airfoil.

4.2. S1223 airfoil

The S1223 airfoil was designed by M. Selig [35] to achieve a Cl_{max} greater than 2 at $Re = 2.0 \times 10^5$. The S1223 airfoil has 11.93% thickness and camber of 8.67%. The UIUC [35] experimental data give a maximum lift coefficient of approximately 2.2 with moderate stall characteristics as shown in Fig. 6(a) and (b).

Fig. 6(a) shows the predictions for the S1223 airfoil drag polar. For the $k-\omega$ *SST* turbulence model with low Reynolds corrections, the agreement with experimental data is good up to an angle of attack of approximately 10°. Contrary to the predictions presented for the E387 airfoil, the $k-kl-\omega$ transition model does not predict the lower corner of the low drag bucket accurately. However, the agreement for higher angles of attack is even better than the XFOIL predictions. For XFOIL, the maximum lift coefficient is well predicted although it occurs in a lower angle of attack, as it is possible to observe in Fig. 6(b). At higher angles of attack XFOIL underestimates, by a significant extent, the drag coefficient value.

Fig. 7(a) shows the pressure distribution at $\alpha = 4°$ and it is possible to observe that, according to the comparison provided in Fig. 4 (a) and (b) the $k-\omega$ *SST Low Re* represents the most accurate approximation to the experiments. While the $k-kl-\omega$ transition model is slightly underestimating the correct pressure distribution, the XFOIL code is overestimating the pressure distribution around the airfoil for this angle of attack. At Fig. 7(b) the pressure distribution for $\alpha = 8°$ shows the same above mentioned behavior of each model.

5. Conclusions

Analyzing the comparisons between the experimental measurements and the predictions obtained using different numerical methods, it is clear that the XFOIL remains an excellent airfoil design and analysis tool. It shows the capability to predict the airfoil performance as good as any of the other used methods. The ease of use of XFOIL compared to the more complex CFD performed in ANSYS Fluent® and OpenFoam encourages its use at low speeds

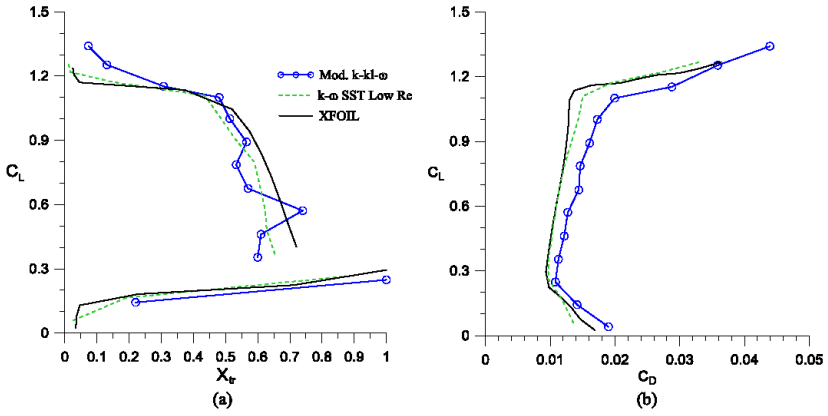

Fig. 5. (a) Transition position of the E387 airfoil. (b) Drag polar of E387 for $Re = 2.0 \times 10^5$.

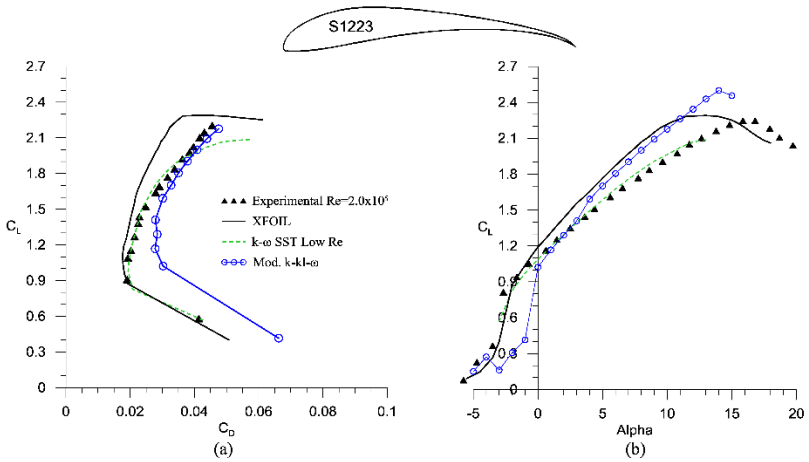

Fig. 6. S1223 airfoil polar for $Re = 2.0 \times 10^5$. UIUC measurements from Ref. [35] (a) C_L *vs* C_D. (b) C_L *vs* α.

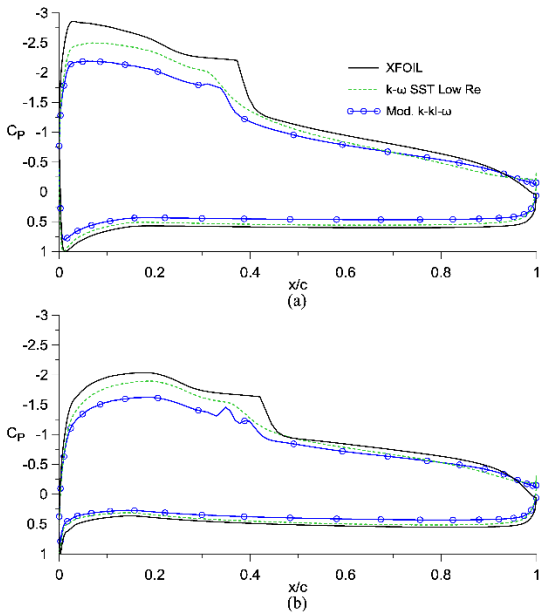

Fig. 7. Comparison of S1223 airfoil pressure distributions for $Re = 2.0 \times 10^5$. (a) $\alpha = 4°$. (b) $\alpha = 8°$.

and for single-element airfoils. XFOIL predictions are comparable to those of other turbulence and transition methods. Although only two cases were considered, the changes made in the $k - kl - \omega$ transition model shows promising results in predicting accurate C_L and C_D values. It was clear that a number of existing methods can predict the aerodynamic characteristics of airfoils with sufficient accuracy for most engineering applications. While XFOIL can provide sufficient accuracy for the conceptual design phase of the propellers, the importance of being able to account for transition with Navier–Stokes solvers is of high importance, not only for steady-state two-dimensional calculations, but also for the three-dimensional and/or unsteady-state cases.

Conflict of interest statement

The authors declare that there is no conflict of interests regarding the publication of this article.

Acknowledgements

The present work was performed as part of Project MAAT (Ref. No. 285602) supported by European Union through the Seventh Framework Programme. Part of the work was also supported by C-MAST – Center for Mechanical and Aerospace Sciences and Technologies, Portuguese Foundation for Science and Technology Research Unit No. 151.

References

[1] R. Ma, B. Zhong, P. Liu, Optimization design study of low-Reynolds-number high-lift airfoils for the high-efficiency propeller of low-dynamic vehicles in stratosphere, Sci. China, Technol. Sci. 53 (2010) 2792–2807, http://dx.doi.org/10.1007/s11431-010-4087-0.
[2] B.E. Prentice, A. Phillips, R.P. Beilock, J. Thomson, The rebirth of airships, J. Transp. Res. Forum 44 (2005) 173–190.
[3] G. Ilieva, J.C. Páscoa, A. Dumas, M. Trancossi, A critical review of propulsion concepts for modern airships, Cent. Eur. J. Eng. 2 (2012) 189–200, http://dx.doi.org/10.2478/s13531-011-0070-1.
[4] A. Dumas, M. Trancossi, M. Madonia, I. Giuliani, Multibody advanced airship for transport, in: SAE Technical Paper 2011-01-2786, 2011.
[5] J. Morgado, M.Â.R. Silvestre, J.C. Páscoa, Parametric study of a high altitude airship according to the multi-body concept for advanced airship transport – MAAT, in: IV Conferência Nacional Em Mecânica Dos Fluidos, Termodinâmica E Energia, Lisbon, 2012.
[6] J. Morgado, M. Abdollahzadeh, M.A.R. Silvestre, J.C. Páscoa, High altitude propeller design and analysis, Aerosp. Sci. Technol. 45 (2015) 398–407, http://dx.doi.org/10.1016/j.ast.2015.06.011.
[7] M. Young, S. Keith, An overview of advanced concepts for near-space systems, in: 45th AIAA Joint Propulsion Conference & Exhibit, American Institute of Aeronautics and Astronautics, Denver, Colorado, 2009.
[8] L.D. Koch, Design and performance calculations of a propeller for very high altitude flight, Case Western Reserve University, 1998.
[9] P.V. Gamboa, M.A.R. Silvestre, Airfoil optimization with transition curve as objective function, in: VI International Conference on Adaptive Modeling and Simulation ADMOS 2013, 2013, pp. 1–12.
[10] F.R. Menter, Two-equation eddy-viscosity turbulence models for engineering applications, AIAA J. 32 (1994) 1598–1605, http://dx.doi.org/10.2514/3.12149.
[11] F.R. Menter, Influence of freestream values on k-omega turbulence model predictions, AIAA J. 30 (1992) 1657–1659, http://dx.doi.org/10.2514/3.11115.
[12] R. Vizinho, J.C. Pascoa, M. Silvestre, High altitude transitional flow computation for a propulsion system nacelle of MAAT airship, SAE Int. J. Aerosp. 6 (2013) 714–720, http://dx.doi.org/10.4271/2013-01-2268.

[13] M. Drela, XFOIL – an analysis and design system for low Reynolds number airfoils, in: T.J. Mueller (Ed.), Low Reynolds Number Aerodynamics, Springer-Verlag, Berlin, 1989, pp. 1–12.
[14] D.K. Walters, J.H. Leylek, A new model for boundary layer transition using a single-point RANS approach, J. Turbomach. 126 (2004) 193, http://dx.doi.org/10.1115/1.1622709.
[15] M.S. Selig, Low Reynolds number airfoil design lecture notes, VKI Lect. Ser. (2003) 24–28.
[16] J. Bardina, P. Huang, T. Coakley, J. Bardina, P. Huang, T. Coakley, Turbulence modeling validation, in: 28th Fluid Dynamics Conference, American Institute of Aeronautics and Astronautics, Reston, Virigina, 1997.
[17] R.E. Mayle, A. Schulz, The path to predicting bypass transition, in: Volume 1: Turbomachinery, ASME, 1996, pp. 405–411.
[18] H. Dryden, Air flow in the boundary layer near a plate, NACA report 562, 1937.
[19] G. Taylor, Some recent developments in the study of turbulence, in: Fifth International Congress for Applied Mechanics, Cambridge, Massachusetts, 1939.
[20] P. Klebanoff, Effects of free-stream turbulence on a laminar boundary layer, Bull. Am. Phys. Soc. 16 (1971) 1323.
[21] J. Kendall, Studies on laminar boundary layer receptivity to freestream turbulence near a leading edge, in: Boundary Layer Stability and Transition to Turbulence, in: Proceedings of the Symposium, ASME and JSME Joint Fluids Engineering Conference, 1991.
[22] D.K. Walters, D. Cokljat, A three-equation eddy-viscosity model for Reynolds-averaged Navier–Stokes simulations of transitional flow, J. Fluids Eng. 130 (2008) 121401, http://dx.doi.org/10.1115/1.2979230.
[23] R. Moss, M. Oldfield, Effect of free-stream turbulence on flat-plate heat flux signals: spectra and eddy transport velocities, J. Turbomach. 118 (1996) 461–467.
[24] K. Thole, D. Bogard, High freestream turbulence effects on turbulent boundary layers, J. Fluids Eng. 118 (1996) 276–284.
[25] R.J. Volino, A new model for free-stream turbulence effects on boundary layers, J. Turbomach. 120 (1998) 613–620.
[26] P. Bradshaw, Turbulence: the chief outstanding difficulty of our subject, Exp. Fluids 16 (1994) 203–216, http://dx.doi.org/10.1007/BF00206540.
[27] T. Shih, J. Zhu, J. Lumley, A new reynolds stress algebraic equation model, NASA TM 106644, Ohio, 1994.
[28] T.-H. Shih, W.W. Liou, A. Shabbir, Z. Yang, J. Zhu, A new $k-\epsilon$ eddy viscosity model for high Reynolds number turbulent flows, Comput. Fluids 24 (1995) 227–238, http://dx.doi.org/10.1016/0045-7930(94)00032-T.
[29] K.C. Chang, W.D. Hsieh, C.S. Chen, A modified low-Reynolds-number turbulence model applicable to recirculating flow in pipe expansion, J. Fluids Eng. 117 (1995) 417–423, http://dx.doi.org/10.1115/1.2817278.
[30] T.J. Craft, B.E. Launder, K. Suga, Prediction of turbulent transitional phenomena with a nonlinear eddy-viscosity model, Int. J. Heat Fluid Flow 18 (1997) 15–28, http://dx.doi.org/10.1016/S0142-727X(96)00145-2.
[31] S. Lardeau, M.A. Leschziner, N. Li, Modelling bypass transition with low-Reynolds-number nonlinear eddy-viscosity closure, Flow Turbul. Combust. 73 (2004) 49–76, http://dx.doi.org/10.1023/B:APPL.0000044367.24861.b7.
[32] T.J. Craft, B.E. Launder, K. Suga, Development and application of a cubic eddy-viscosity model of turbulence, Int. J. Heat Fluid Flow 17 (1996) 108–115.
[33] J. van Ingen, The eN method for transition prediction. Historical review of work at TU delft, in: 38th Fluid Dynamics Conference and Exhibit, American Institute of Aeronautics and Astronautics, Reston, Virigina, 2008.
[34] D. Silva, M. Avelino, M. De-Lemos, Numerical study of the airflow around the airfoil S1223, in: II Congresso Nacional de Engenharia Mecânica, João Pessoa, 2002.
[35] M.S. Selig, J.J. Guglielmo, High-lift low Reynolds number airfoil design, J. Aircr. 34 (1997) 72–79, http://dx.doi.org/10.2514/2.2137.
[36] R. McGee, B. Walker, B. Millard, Experimental results for the eppler 387 airfoil at low Reynolds numbers in the langley low-turbulence pressure tunnel, Hampton, Virginia, 1988.
[37] M.D. Maughmer, J.G. Coder, Comparisons of theoretical methods for predicting airfoil aerodynamic characteristics, Pennsylvania State University, 2010.